Wettability Patterning in Microfluidic Systems and Applications in the Petroleum Industry

Marc Schneider

To cite this version:

Marc Schneider. Wettability Patterning in Microfluidic Systems and Applications in the Petroleum Industry. Fluid Dynamics [physics.flu-dyn]. Université Pierre et Marie Curie - Paris VI, 2011. English. NNT : . pastel-00568996

HAL Id: pastel-00568996
https://pastel.hal.science/pastel-00568996

Submitted on 24 Feb 2011

THESE DE DOCTORAT DE
L'UNIVERSITE PIERRE ET MARIE CURIE

Spécialité

La Physique de la Particule à la Matière Condensée
(ED 389)

Présentée par

Marc SCHNEIDER

Pour obtenir le grade de

DOCTEUR de l'UNIVERSITÉ PIERRE ET MARIE CURIE

Sujet de la thèse :

Mouillabilité texturée dans les systèmes micro fluidiques et applications dans l'industrie pétrolière

Wettability Patterning in Microfluidic Systems and Applications in the Petroleum Industry

soutenue le 1er février 2011

devant le jury composé de :

M. Patrick TABELING Directeur de thèse
Mme. Anne-Marie GUÉ Rapporteur
Mme. Annie VIALLAT Rapporteur
Mme. Valérie CABUIL Examinatrice
M. Lyderic BOCQUET Examinateur
M. Ludovic JULLIEN Examinateur
M. Martin LÜLING Invité
M. Fadhel REZGUI Invité

Acknowledgements

It is a pleasure to thank the many people who made this thesis possible.

It is difficult to overstate my gratitude to my thesis director, Patrick Tabeling, and to my manager at Schlumberger, Fadhel Rezgui. Throughout my thesis work, they provided encouragement, sound advice, good teaching, good company, and lots of good ideas. I would like to thank them very much for guiding me through the last three years.

I would like to show my gratitude to Anne-Marie Gué, Annie Viallat, Valérie Cabuil, Lyderic Bocquet and Ludovic Jullien for being integral members of my thesis committee and for accepting to judge my work.

I am very grateful to have been supported for my PhD work by Schlumberger. I would like to thank Martin Lüling for his support and his valuable insight and I would also like to thank Alain Buisson and Eric Parot, who helped and supported me continuously throughout the last three years.

I would also like to thank all members of the MMN lab at ESPCI, who worked with me and helped me there during the last three years. Thank you, Annick, Aurélien, Avin, Benjamin, Binqing, Boris, Caroline, Clémence, Delphine, Emmanuel, Fabrice, Florent, Hervé, Magalie, Mathilde, Nicolas, Pascaline, Philippe, Rafaële, Yves, Zhen Zhen, and Zhuo! Special thanks go to Avin Babataheri and Boris Kozlov for the many fruitful discussions and their invaluable support.

I want to thank Hélène Berthet and Isabelle Etchart for their valuable help with the manuscript.

Also many thanks to the student interns Aymen, Florian, Franco, Kaouthar, and Radouan, with whom I had the pleasure to work together at Schlumberger.

Lastly, I would like to thank my parents, my brother and numerous friends who endured this long process with me, always offering support.

Table of Contents

Chapter 1

Introduction

Understanding multiphase flow in porous media is of great importance for many industrial and environmental applications at various spatial and temporal scales [**1**]. Displacement processes in natural porous media, such as oil and natural gas reservoirs, play a crucial role during waterflooding, enhanced oil recovery (EOR) or CO_2 sequestration [**2**], [**3**], which are of key importance to the petroleum and energy industries, and displacement processes in aquifers and geothermal reservoirs are a major topic in soil science and hydrology [**2**], [**4**]. Examples for multiphase flow in synthetic porous matrices range from applications in classical chemistry [**2**] such as filtration or flow in packed columns to gas–liquid transport in fuel cells [**5**], [**6**], which are of major interest for energy applications [**7**]. It is thus necessary to identify and understand multiphase flow processes at the microscopic scale in order to describe their manifestation at the macroscopic level.

Since the 1980s, microfluidic networks (micromodels) are frequently used as laboratory models for porous media in order to identify and study multiphase flow phenomena in detail [**8**], [**9**]. These micromodels, made of transparent materials such as glass or transparent polymer, allow for detailed visual observations of the fluid phases [**7**], [**10**] as they propagate within the microfluidic pores and channels [**11**]. Detailed studies have been conducted for the two fundamental cases of immiscible–fluid displacement: (1) drainage, i.e. invasion of the non–wetting phase [**12**], [**13**], [**14**], and (2) imbibition, i.e. invasion of the wetting phase [**15**], [**16**], [**17**]. The influence of various parameters such as injection speed, fluid viscosities, etc. could be identified [**18**], [**19**], [**20**], which significantly affect the fluid displacement. Detailed studies on micromodels led to the identification of phase–diagrams, which provide flow pattern predictions as function of capillary number and viscosity [**21**], [**22**], [**23**]. Micromodel experiments revealed the underlying physics of fluid movement in pores and together with the gathered experimental data allowed for development and validation of a variety of simulation tools [**24**], [**25**], [**26**], [**27**], [**28**], [**29**].

This progress in understanding multiphase flow on a pore–level scale through micromodels was of key significance, in particular for the oil industry [**30**], and led from simple compact flow assumptions to more sophisticated and accurate flow descriptions in the 1980s and 90s [**9**], [**31**], [**32**]. New simulations and flow predictions were a great success for the field [**33**], [**34**], [**35**], due to their increased predictive power of multiphase flow in oil reservoirs.

However, despite this progress, studies and applications were limited to systems and cases with homogeneous, uniform surface properties, i.e. wettability. Wettability is the relative adhesion of two fluids to a solid surface. With respect to two immiscible fluids in porous media, wettability is the measure of the preferential tendency of one of the fluids to wet the surface of the porous medium in the presence of the other fluid [**36**]. The assumption of uniform surface properties across the entire porous medium only yields fluid flow predictions which strictly accord to the fundamental cases: drainage and imbibition, depending on whether the invading phase is wetting the porous medium or not. In general, however, the surface properties along interstitial surfaces frequently vary and the porous media can possess heterogeneous or patterned wettability [**37**], [**38**]. If a parameter f_w is introduced describing the fraction of wetting surface with respect to the invading fluid, then it becomes apparent that the two fundamental cases of fluid displacement in porous media describe only singular points, i.e. drainage for $f_w = 0$ and imbibition for $f_w = 1$, and the entire range of fractional wettability is neglected.

In particular the oil industry realized in recent years that consideration of mixed or fractional wettability is of utmost importance since displacement effectiveness and ultimate oil recovery by drive fluids (e.g. water) are governed by the wettability of the reservoir rock [**39**], [**40**], [**41**]. It is said that maximizing the recovery of known hydrocarbon reserves remains perhaps the biggest challenge facing the petroleum industry. Although waterflooding has been used for decades to recover oil, the recovery mechanisms at the pore scale remain uncertain [**42**]. Significant effort was made to include the effects of mixed or fractional wettability in flow simulators [**43**], [**44**], [**45**], [**46**], although they suffer significantly from a lack of predictive power [**47**]. Consequently it has become evident that a detailed understanding of the multiphase displacement mechanism at a pore level for mixed–wet media is essential [**48**]. However, due to a lack in appropriate technology so far, detailed experimental investigations of multiphase flow in porous media with patterned wettability remained elusive [**42**], [**49**].

It is apparent that detailed studies of multiphase flow behavior in porous media with patterned wettability are needed, both as a scientific contribution to the fields of physics and fluid mechanics as well as providing crucial underlying data for applications, e.g. in the petroleum industry. Such studies demand a significant technological progress, which allows for the fabrication and preparation of micromodels with well controlled wettability patterning of high surface quality and high spatial resolution. The present work focuses on both, the technology to prepare the micromodels as well as the investigation of flow phenomena in wettability–patterned porous media with a main focus on applications for the oil industry.

1.1 Multiphase Flow in Micromodels

Micromodels, typically made of transparent materials, provide a planar network with two–dimensional pore connectivity, and are therefore well suited for detailed observations of the fluid interfaces at pore level. Such micromodels have been frequently used in the past in order to study fundamental properties of multiphase flow in porous media, as previously mentioned. However, studies were limited to micromodels of uniform wettability. Uniform surface properties (i.e. wettability) allow for the study of the two fundamental cases of immiscible fluid displacement: drainage and imbibition. Drainage describes the case where the invading (displacing) fluid is non–wetting, i.e. repelled by the solid, with respect to the initial (displaced) fluid, while imbibition describes the opposite case, where the invading fluid is wetting, i.e. attracted by the solid, with respect to the initial fluid [**50**]. For both cases, drainage and imbibition, several different flow behaviors, or regimes, as functions of various flow conditions and parameters were identified and experimentally investigated [**22**], [**23**], [**21**]. Two dominant parameters are the capillary number:

$$\mathrm{Ca} = \frac{V\mu_{\mathrm{injected}}}{\gamma} \qquad (\ 1.1\ )$$

which describes the relative effect between viscous forces and surface tension, and the viscosity ratio:

$$M = \frac{\mu_{\mathrm{injected}}}{\mu_{\mathrm{initial}}} \qquad (\ 1.2\ )$$

where V is the characteristic (mean) velocity of the injected fluid, γ the interfacial tension between the two fluid phases, and μ_{initial} and μ_{injected} are the viscosities of the initial (displaced) and injected (displacing) fluid, respectively.

Based on these parameters phase diagrams for micromodels were established, which describe distinctive flow patterns or regimes. While surface tension and viscosities are inherent fluid properties the capillary number is also dependent on the characteristic velocity and can easily be varied in an experiment by changing the injection rate. For the assessment of a phase diagram various viscosity ratios are typically realized by the choice of appropriate fluid pairs.

Figure 1.1 shows a phase diagram for the drainage case as function of capillary number Ca and viscosity ratio M according to Lenorman [**21**] and identifies several distinct flow regimes. For large capillary numbers (i.e. high flow rate) the flow patterns are dominated by viscous effects. For large M, (i.e. low viscosity and therefore low pressure drop in the initial, displaced phase) stable displacement occurs, while for small M (i.e. low viscosity of the injected displacing fluid) viscous fingering occurs due to Saffman–Taylor instabilities [**51**]. For small capillary numbers (i.e. slow flow rate, viscous forces negligible), the emerging flow pattern shows capillary fingering, also referred to as invasion percolation, where at each intersection a path of least capillary resistance (i.e. largest cross–section) is chosen by the invading fluid.

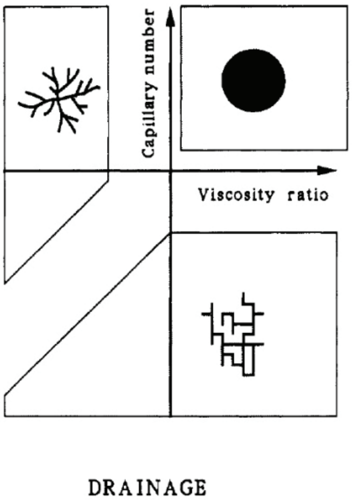

Figure 1.1: Phase diagram for drainage [**21**].

Figure 1.2 shows phase diagrams for the imbibition case. Again, for large capillary numbers, the flow patterns are governed by viscous forces, which yield viscous fingering for small M and stable displacement for large M. For fairly small capillary numbers the flow pattern shows a flat frontal advance if the aspect ratio between individual pores is reasonably small. For excessive aspect ratios between individual pores, capillary fingering can also emerge in the imbibition case. In this case, however, the wetting fluid favors the invasion of the smaller pores first and large pores are avoided due to capillary pressure. For very small capillary numbers the invading fluid penetrates the network by flowing as a film along the walls, leaving the initial phase in the center of the channels. By this mechanism, pores and channels within the network are filled by the invading fluid without bulk connections to the injection point. If large differences in channel sizes are present then the smallest channels are predictably filled first, otherwise filling occurs as random clusters.

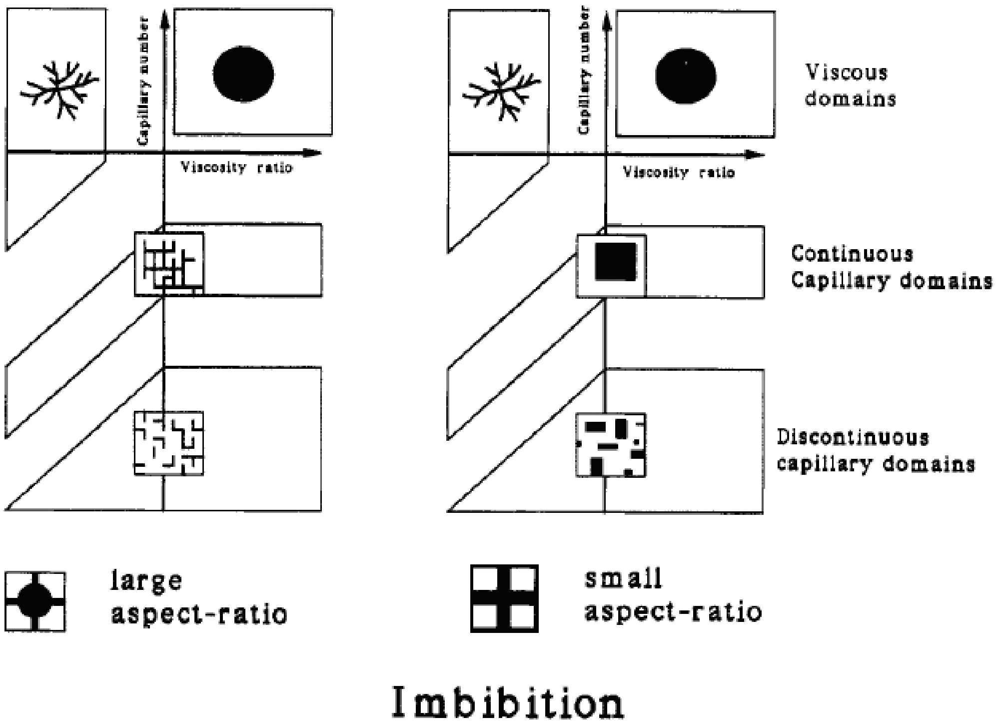

Figure 1.2: Phase diagrams for imbibition: left–hand figure, large aspect ratio; right–hand figure, small aspect ratio [**21**].

If additional parameters or initial conditions are considered, for example partial initial saturation with the invading fluid, then addition regimes may appear, especially in the imbibition case [**24**], [**18**].

1.2 Wettability in Microfluidic Systems

Wettability describes the ability of a fluid to maintain contact with a solid surface with respect to a second immiscible fluid [**36**]. Wettability is a result of the competition between adhesive forces between a liquid and a solid, which cause the liquid to spread across the solid surface, and cohesive forces within the liquid, which try to minimize its surface area and keep it in a compact form (e.g. sphere) [**52**], [**53**]. A means of quantifying wettability is the contact angle θ, which represents the angle at which the fluid/fluid interface meets the solid surface. For a drop of liquid deposited on a solid surface (Figure 1.3) the contact angle follows from the Young equation [**54**]:

$$\gamma_{SG} - \gamma_{SL} - \gamma_{LG}\cos\theta = 0 \qquad (1.3)$$

where γ_{SG}, γ_{SL}, and γ_{LG}, are the interfacial tensions between solid/gas (air), solid/liquid, and liquid/gas, respectively. Subscripts are frequently dropped for the fluid/fluid interfacial tension ($\gamma_{LG} \equiv \gamma$). Eqn. 1.3 describes the force balance at the triple line (between gas, liquid, and solid, c.f. Figure 1.3b) which needs to be satisfied in order to obtain static conditions. For very strong liquid–solid affinity complete wetting or spreading occurs, which represents the limit of the contact angle $\theta = 0$ (Figure 1.3a). For surface angles smaller than 90° the liquid has a high wettability (Figure 1.3b), while for contact angles larger than 90° the liquid has a low wettability (Figure 1.3c). For very weak liquid–solid affinity, complete non–wetting or repulsion occurs, which is represented by a contact angle of 180° (Figure 1.3d).

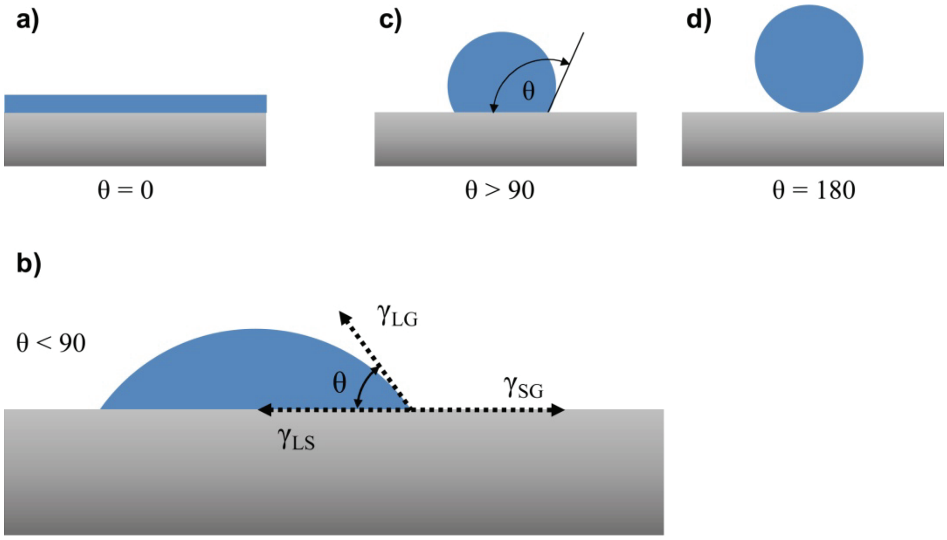

Figure 1.3: Idealized examples of contact angle and spreading of a liquid (blue) on a flat, smooth solid (gray). Different wetting states are shown: (a) complete wetting or spreading, (b) high wettability, (c) low wettability, and (d) complete non–wetting (repulsion).

If water shows a strong affinity towards the solid surface ($\theta < 90°$) the solid is said to be hydrophilic, otherwise ($\theta > 90°$) it is hydrophobic. However, this terminology typically implies that the second fluid phase is a gas (e.g. air). In general, however, eqn. 1.3 and the definition of the contact angle are also valid if the second fluid is a liquid (e.g. oil). In a system of water, oil and solid, the solid is described as 'water–wet' for $\theta_{\text{water}} < 90°$ and 'oil–wet' for $\theta_{\text{water}} > 90°$. For contact angles in the range of $80° < \theta_{\text{water}} < 100°$ the solid is sometimes described as 'neutrally–wet' or 'intermediate–wet' [**55**]. For solid/liquid/gas systems, the contact angle is always measured between the liquid and the solid and therefore unambiguous (c.f. Figure 1.3). Special attention, however, needs to be paid to the definition of the contact angle if the second fluid is a liquid as well. The liquid for which the contact angle measurement applies needs to be clearly stated. In this text the contact angle typically refers to the water phase or an appropriate subscript is introduced.

Capillary pressure, or Laplace pressure, describes a pressure difference across a fluid/fluid interface [**56**]:

$$\Delta p = p_c = p_{nw} - p_w \qquad (1.4)$$

where p_c is the capillary pressure and p_{nw} and p_w are the pressures in non–wetting and wetting phase, respectively (Figure 1.4). The capillary pressure is a result of the surface tension in a curved surface and defined by the Young–Laplace law as [**56**]:

$$p_c = \gamma C \qquad (1.5)$$

where C is the mean curvature of the meniscus. For a spherical meniscus in a cylindrical tube as shown in Figure 1.4, the curvature is given as:

$$C = \frac{2}{R} = \frac{2\cos\theta}{r} \qquad (1.6)$$

with the radius of the curvature R or the radius of the cylindrical tube r.

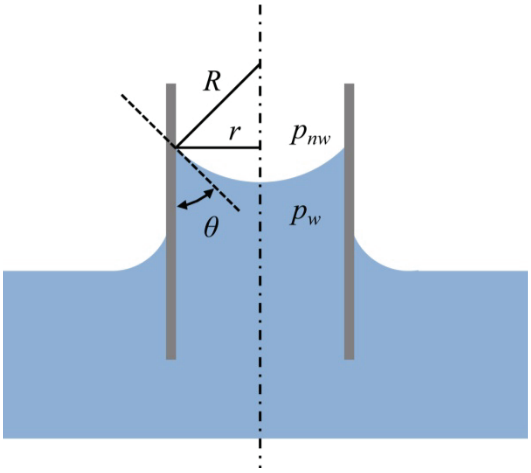

Figure 1.4: Capillary rise in a cylindrical tube of radius *r*. The tube (gray) shown in cross–section is dipped in water (blue). Water is wetting the tube material and a spherical meniscus of radius *R* is formed.

The shape of fluid interfaces in rectangular microchannels was studied in detail by Lenormand et al. [**11**] and is shown in Figure 1.5. A completely non–wetting fluid forms a slug and small amounts of wetting fluid remain in the corners. However, it was shown that the mean curvature of the fluid interface can be expressed in good approximation by the two main radii of curvature. For a fluid pair with complete wetting/non–wetting (θ = 180°, c.f. Figure 1.5), the curvature is therefore given as [**11**], [**57**]:

$$C = 2\left(\frac{1}{w} + \frac{1}{h}\right) \qquad (1.7)$$

for a channel of width w and height h. For partial wetting, the mean curvature in a rectangular microchannel is given as [**58**]:

$$C = 2\left(\frac{\cos\theta}{w} + \frac{\cos\theta}{h}\right) \qquad (1.8)$$

As eqns. 1.5 to 1.8 show, capillary pressure is closely related to wettability through the contact angle.

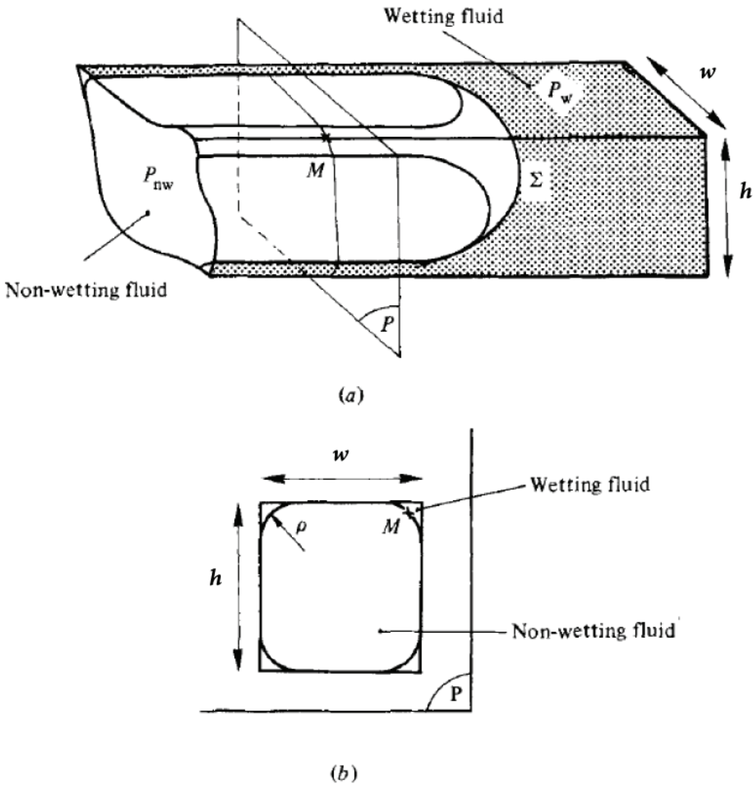

Figure 1.5: Fluid interface in a rectangular microchannel: (a) perspective view, (b) cross–sectional view in the plane P [**11**].

In microfluidic systems, both for continuous microflows as well as for droplet–based microfluidics, the liquid streams or droplets need to be guided through the system in a controlled fashion [**59**], [**60**]. Since the fluid types are typically dictated by the application itself, proper flow guidance needs to rely on channel geometry and surface properties (i.e. wettability) of the microfluidic device. Microfluidc devices are typically made from glass or transparent polymers with various surface properties [**61**], [**62**]. For example PDMS, one of the most commonly used polymers for microfluidic applications [**63**], possesses a hydrophobic surface ($\theta = 108°$ [**64**]), and is the material employed in this work. In many cases wettability needs to be modified and tailored to specific needs in order for the devices to provide the desired functionalities [**65**]. For example, filling of hydrophobic systems with aqueous solutions might be challenging, in particular for small channel geometries, due to large capillary pressures (eqn. 1.5), and requires homogeneous wettability alterations towards surface hydrophilicity. In the case of droplet–based microfluidics, wettability properties need to be carefully considered as well: stability requirements dictate good wettability between the continuous phase and the channel walls [**66**], [**67**]. Other applications require much more sophisticated surface modifications, such as patterned wettability which is a requirement for multiple emulsion encapsulation [**68**], [**69**]. A continued, more detailed review and discussion of surface treatment, patterning and functionalization in microfluidic systems for cross–discipline general applications is provided in Chapter 2.

Particular interest of wettability patterning in the present work was focused towards the investigation of multiphase flow in micromodels with patterned wettability. As mentioned previously, despite the urgent need for careful investigations on flow behavior in networks with factional (patterned) wettability, detailed experimental results have remained elusive [**42**]. The absence of convincing experimental results is mainly due to the lack of technology to pattern wettability in micromodels.

A few approaches were made in recent years to fabricate micromodels with heterogeneous wettability properties. One method consists of packing glass and polymer beads in a single layer between two glass plates [**37**], [**38**]. If beads of different wettability are used, heterogeneities can be created; however, control over pore geometry is not possible. In a modified method, glass beads of various sizes were packed in multiple layers to also vary pore space [**70**], but fluid propagation in multiple layers does not allow for detailed pore–level observations. A different approach was made by using classical micromodels etched and sealed in glass, which provide strongly water–wet surfaces in their native state. Wettability was then altered by aging in either crude oil [**71**] or with a specific silicate gel [**72**]. Wettability heterogeneities could be induced by partial filling with the agent, but there was no spatial control over the heterogeneities. All techniques suffer from either poor control over the wettability pattern or poor control over the pore space. One approach as reported by Laroche et al. [**73**] describes a promising concept: a classical micromodel was etched into glass followed by silanization with octadecyltrichlorosilane (OTS) to provide oil–wet surfaces. OTS could then be selectively etched away by acid to locally recover initial water–wet properties. However wettability patterning needed to be performed on the open halves, which made proper sealing of the system impossible and spatial resolution was limited to coarse patches with centimetric resolution.

It is obvious that progress on this subject of study is limited by lacking technology. The development of a wettability patterning technique of high quality and high spatial resolution applicable within sealed microfluidic devices is required in order to continue progress on multiphase flow studies in micromodels with fractional wettability.

1.3 Wettability in the Oil Industry

Rock wettability is a major factor in oil recovery, controlling the location, flow, and distribution of fluids in a reservoir. Wettability affects most of the petrophysical properties of reservoir rocks including capillary pressure, relative permeability, waterflood behavior, electrical properties, and enhanced oil recovery (EOR). [**74**], [**75**], [**76**]. However, only in recent years has wettability been fully recognized as an important factor, while for most parts of the last century common reservoir engineering practices were based on the assumption that oil reservoirs are homogeneously water–wet [**41**], [**77**].

Reservoir rock wettability is generally classified as either homogeneous or heterogeneous. For the homogeneous case the entire rock surface exhibits uniform wettability of a certain type. The rock might be water–wet (Figure 1.6a), oil–wet (Figure 1.6c) or at some intermediate wettability state [**41**], [**55**], [**78**]. On the other hand, for the heterogeneous case, different, distinguishable surface regions within the rock exhibit different wettability. Two different types of heterogeneous wetting states are commonly recognized [**36**]: fractional wettability and mixed wettability. Fractional wettability (Figure 1.6b) provides a generalized definition and is typically used to describe random wettability distribution from single pore scale to clusters of pores [**79**]. Mixed wettability describes a particular case where a network of large pores exhibits oil–wet surfaces while small pores are water–wet [**80**]. The notion of this very specific definition of mixed wettability is based on a particular mechanism for this pattern to form in oil reservoirs as discussed below. In some literature, fractional wettability is further distinguished and labeled, for example as dalmatian[1] or speckled[2] wettability, based on other distinct patterns [**81**].

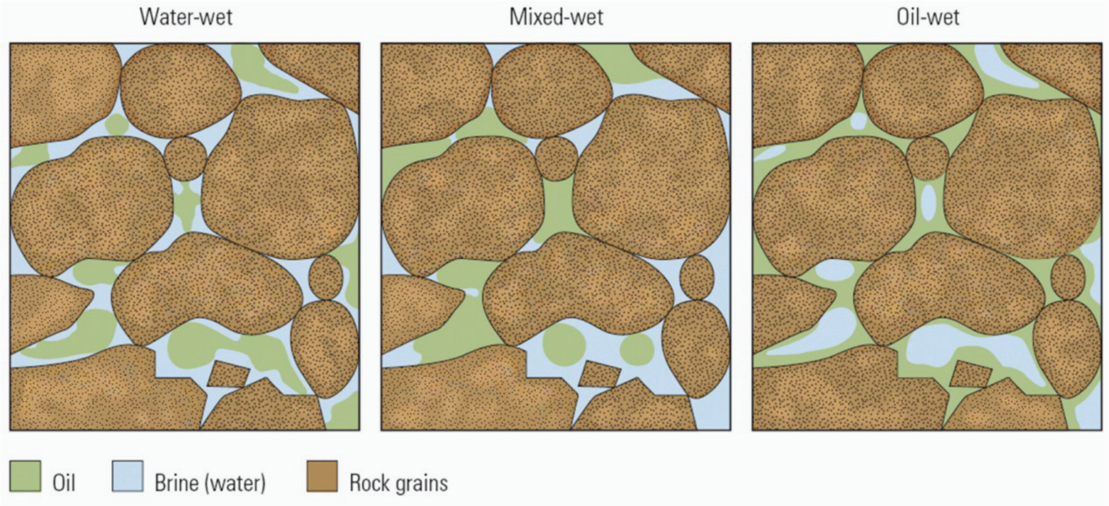

Figure 1.6: Wetting in pores [**82**].

Reservoir rocks are complex structures comprised of a variety of different minerals, where each mineral might have a different wettability [**82**]. In addition, the surface wettability can be altered by adsorption of polar compounds or film deposition of organic material [**55**], [**81**], [**83**], [**84**]. Most of the pure minerals present in reservoir rock are hydrophilic, which would make a clean rock strongly water–wet [**85**]. For this reason all oil reservoirs were assumed to be water–wet in the past. However, wettability is oftentimes permanently altered by adsorption or deposition of organic material present in the crude oil [**55**], [**86**], [**87**]. Typically, the wettability altering molecules are contained within the heavy fraction of the crude oil, the asphaltenes [**88**], [**89**]. Mechanisms of wettability alteration by crude oils strongly

---

[1] Water-wet and oil-wet surfaces both distributed as discontinuous patches.

[2] Patches of oil-wet areas within a continuous water-wet surface.

depend on oil composition, rock and mineral type, as well as on the water (brine) properties [**81**], [**90**]. Water is present in a reservoir in the form of brine at a certain salinity and various levels of acidity or alkalinity. The stability of residual water films is a critical factor in allowing or preventing asphaltene molecules from the oil phase to reach and adhere to the mineral surface and thereby alter the rock wettability [**91**], [**92**]. It is also evident that mineral composition of the reservoir rock promotes or prevents such wettability alterations. While a large number of silicate reservoirs (e.g. sandstone) are believed to be water–wet, most of the carbonate reservoirs are oil–wet or mix–wet [**55**], [**39**], [**81**].

Oil reservoirs evolve by oil migration into initially brine–filled pore space of naturally water–wet rock [**41**]. Oil as the non–wetting phase preferentially invades the large pores, leaving water in the small pores and as a film along the mineral surface. Depending on rock surface roughness and brine composition, residual water films in the large pores might collapse, allowing for direct oil/rock contact, which alters the local rock wettability permanently [**93**]. At the same time, water remains in the small pores and sharp corners and prevents direct oil/rock contact hence retaining initial water–wet conditions. Such mechanisms lead to the development of fractional or mixed wettability in oil reservoirs [**41**], [**80**], [**36**].

Detailed knowledge of reservoir wettability conditions is crucial for the development of optimal production strategies. However, proper wettability assessment is challenging and definitive conclusions frequently remain elusive, particularly in the case of heterogeneous wettability [**42**], [**90**]. Reservoir wettability is determined from laboratory analysis of core samples [**94**]. Extracting a core and providing samples to the laboratory in pristine conditions is not an easy task and can often generate significant alterations to the core sample. Wettability alterations of the core samples from their reservoir state during cutting, surfacing and subsequent handling can occur for a number of reasons such as drilling fluid contamination, oxidation, drying and, most importantly, temperature and pressure reduction effects on crude oil composition such as asphaltene precipitation or wax deposition [**77**], [**88**]. Several methods are available to measure wettability in core samples based on contact angle or capillary pressure measurements [**94**], [**95**]. Measurements based on capillary pressure employ imbibition and drainage cycles to gauge the bulk wettability of the sample and provide a wettability index ranking between water–wet and oil–wet. Such methods provide sound results for homogeneous wettability but heterogeneous wettability conditions cannot be identified and are indistinguishable from intermediate homogeneous wettability [**95**]. Contact angle measurements, such as the sessile drop technique, are challenging to apply on rough, porous surfaces and the validity of the wetting state of the freshly cut rock surface is questionable. A continued and more detailed review and discussion of wettability measurements in core samples is provided in Chapter 3.

Extraction and recovery of crude oil from a reservoir can be classified in three main stages: primary, secondary, and tertiary recovery. During primary recovery typically 5 – 15% of the original oil in place is produced by the overburden pressure through the oil wells drilled into the reservoir. Another 15 – 30% of oil can be produced by forced water injection, known as water flooding or secondary recovery [**96**], [**97**]. A variety of additional techniques, generally referred to as enhanced oil recovery (EOR) or tertiary recovery, can be employed to extract another 5 – 15%, yielding an overall recovery of 30 – 60% of the original oil in place [**93**], [**97**]. Such techniques aim for the recovery of oil retained by to capillary forces or immobilized due to high viscosity and include injection of miscible fluids, chemical floods, surfactant or polymer injection, steam injection, etc. [**98**], [**99**].

Precise knowledge of reservoir wettability is essential for accurate predictions of several factors, such as residual oil saturation or relative permeability, which in turn are major factors for economic evaluations during waterflooding and EOR [**100**], [**101**]. Water flooding is a common practice in oil recovery and has been employed for many years [**102**], [**103**]. Figure 1.7 shows the principle of a typical waterflood operation.

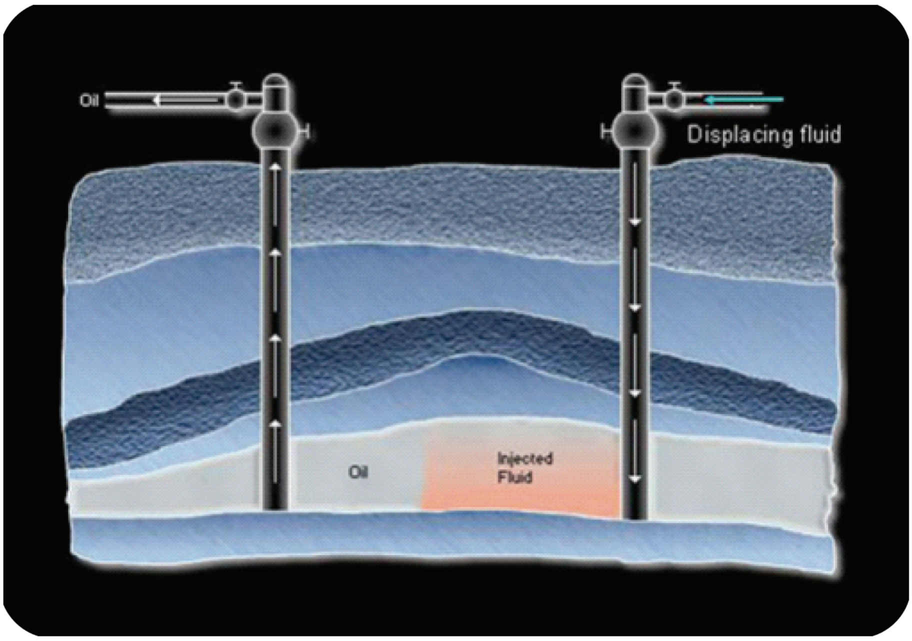

Figure 1.7: Secondary oil recovery by waterflooding: the displacing fluid (water) is injected in to the reservoir through the injector well (right) and displaced oil is recovered at the production well (left) [**104**].

During waterflooding of a water–wet reservoir, water advances through the porous medium in a fairly flat front [**105**]. Despite a fairly uniform water front on a macro–scale, a considerable oil fraction is trapped due to entrapment mechanisms on the micro–scale [**106**]. Figure 1.8a shows an example of oil entrapment by a snap–off mechanism where water as the wetting phase can advance as surface films while oil still remains in the center of large pores [**107**]. For large aspect ratios, where a wide pore is connected through very small throats, water films in the throats frequently coalesce and cut off globules of oil from the continuous oil phase. Since oil is the non–wetting phase (large contact angles θ_{oil}) the large pressure required to overcome the capillary pressure (eqn. 1.4) and move the oil globules through the narrow throats effectively traps the disconnected oil in the large pores [**105**], [**108**], [**109**]. After the water front passes almost all the remaining oil is immobile. Due to this immobilization in the water–wet case there is little or no oil production after water breakthrough at the production well, and waterflooding can be stopped [**40**]. Figure

1.9 shows oil recovery as a function of injected water volume for a laboratory experiment on a core sample (solid curve) [**107**]. Oil recovery ceases shortly after water breakthrough, which occurs at slightly less than one times the pore volume of injected water.

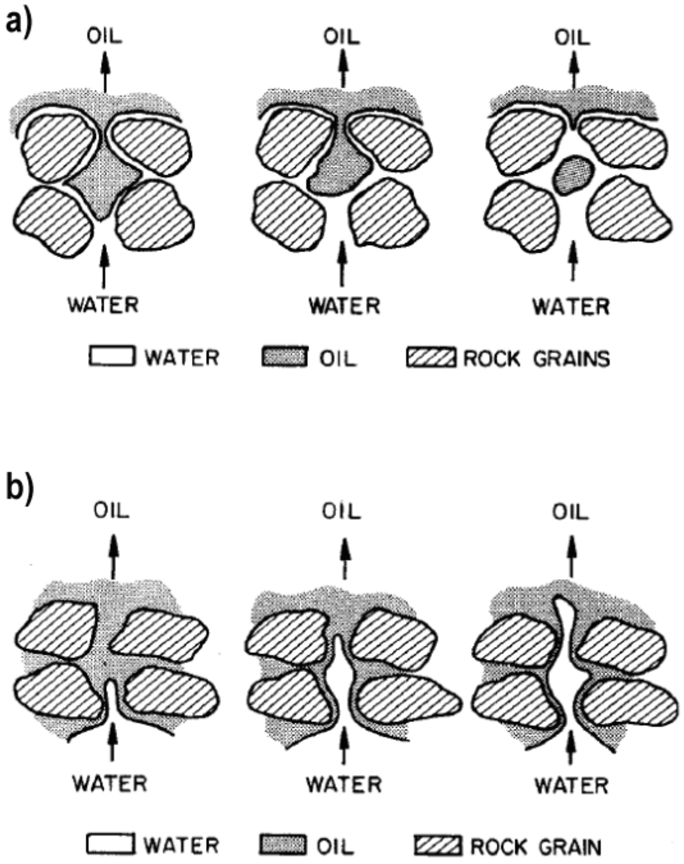

Figure 1.8: Water displacing oil from a pore in (a) a strongly water–wet rock, and (b) a strongly oil–wet rock [**107**].

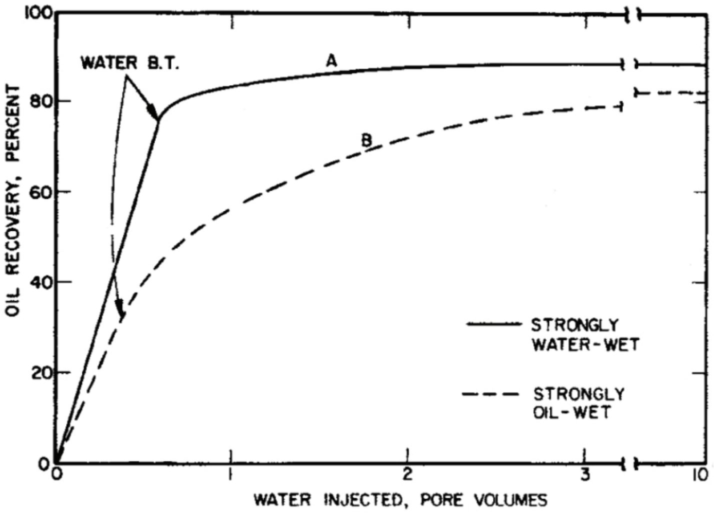

Figure 1.9: Typical waterflood performance in water–wet and oil–wet sandstone cores at moderate oil/water viscosity ratios [**107**].

In the case of waterflooding in an oil–wet reservoir, on the other hand, the rock preferentially remains in contact with the oil and waterflooding in this case is much less efficient [**40**]. The advancing water develops large fingers and invades only a network of larger pores, while oils remains in smaller pores and as a film along the rock surfaces of the large pores (Figure 1.8b). Water breakthrough at the production well occurs quickly with much less water volume injected than in the water–wet case. As water injection continues, more oil is recovered as water continues to invade more pores and additional continuous channels are formed. Residual oil remains connected through continuous films and can therefore continuously be produced; however, recovery rate falls to very low levels when water has formed enough continuous channels in order to flow nearly unrestricted [**105**], [**40**]. A waterflood experiment on an oil–wet core sample shows this early water breakthrough with continued oil recovery during injection of many pore volumes of water (Figure 1.9, dashed curve) [**107**]. A water flood in an oil–wet reservoir is less efficient compared to a water–wet reservoir since many pore volumes of water need to be injected over a significant period of time, and during flooding large amounts of water are produced together with oil in the production well. Additional complications and decrease in efficiency can occur in fractured reservoirs. It is believed that during flooding, water mainly flows in the fractures along the path of least resistance and efficient oil recovery occurs only if water spontaneously imbibes into the matrix blocks and thereby displaces the oil into the network of fractures [**110**], [**111**], [**112**]. Spontaneous imbibition of water, however, can only occur in water–wet rock.

In the case of fractional wettability, it was experimentally shown that waterflood efficiency drops with increasing oil–wet fraction [**40**], [**113**], [**114**]. However, for the particular case of mixed wettability, waterflooding is consistently reported to be very efficient and yield residual oil saturations much lower than for the water–water case [**15**], [**42**], [**80**], [**115**]. The particular configuration of the mixed–wet state, with a continuous oil–wet surface along the large pores and water–wet small pores, combines the advantages of both oil–wet and water–wet mechanisms. Water easily invades the porous medium due to the water–wet surface areas, however, snap–off mechanisms typical for water–wet rock (c.f. Figure 1.8a) are largely eliminated since oil can continuously be drained through surface films along the oil–wet surfaces [**40**].

The significance of the reservoir wettability state is evident from the discussion on secondary recovery (waterflooding) and it plays an equally important role for fluid injection during tertiary recovery (EOR) [**116**]. In particular, heterogeneous wettability, which can have the highest impact (e.g. on waterflooding), is the least understood wettability class. Detailed knowledge of the rock wettability is key, yet often remains elusive [**42**], [**90**]. A lack in appropriate wettability measurement techniques is apparent; new methods and tools for reservoir wettability assessment are needed.

1.4 Outline

The present study focuses on wettability effects in porous media and their influence on multiphase flow behavior with a particular focus on applications for the petroleum industry.

Chapter 2 is dedicated to studies on micromodels. A large part of the work was focused on the technological progress required to fabricate micromodels with well controlled wettability patterns. Micromodels were fabricated in PDMS by soft lithography, which is reviewed in section 2.1. Surface treatment in these systems was achieved by selective graft photo–polymerization, which presents a key technology required for wettability patterning in micromodels. The surface treatment technique is presented in section 2.2. A study of multiphase flow behavior in micromodels of patterned wettability is presented in section 2.3. Further applications of the wettability patterning technique are also outlined.

Chapter 3 is dedicated to applications for the oil industry. A new wettability measurement technique for rock samples based on visual imaging is investigated in section 3.1. The measurement technique is based on flow regime predictions established by studies on micromodels. A novel instrument for microscopic imaging of rock samples is presented in section 3.2 and characterized in detail. This imager instrument allows for multiphase fluid observations on the pore level of a rock and might become a new tool for wettability assessment.

Chapter 2

Wettability Patterning in PDMS

The field of microfluidics has made significant progress and experienced great success during the last three decades [**117**], [**118**], although the field is still at an early stage of development [**119**]. Microfluidics has great impact across many disciplines such as chemistry, biology, and live science [**120**], [**121**], [**122**], [**123**], [**124**], and also in fluid mechanics and physics [**125**], [**126**], [**127**], both for applications [**128**] as well as for fundamental research. Microfluidic systems are typically made from various materials such as glass or silicon but polymers have become increasingly popular [**61**] due to their significantly lower costs, les complicated and faster fabrication, as well as their unique chemical, structural and biological functionalities [**62**]. In particular PDMS is a popular material widely used for microfluidic applications [**129**], [**130**], [**131**]. A detailed review of PDMS microfluidic systems and their fabrication is given in section 2.1.

In many cases the material properties of the host microfluidic devices are not sufficient and applications require modified surface properties and functionalized surfaces, carefully tailored to the task at hand [**132**], [**133**]. For example, systems made of hydrophobic PDMS frequently require surface modifications of the microfluidic channel in order to obtain hydrophilic surface properties. Several different techniques for surface modifications are available [**134**], [**135**]: oxygen plasma treatment and adsorbed surfactant coatings have been proven to work well for certain types of applications but suffer from a lack of long–term stability [**136**], [**64**]. Alternatively, covalent surface modifications such as self–assembled monolayers, or surface grafted polymer chains, provide much better long–term stability [**136**], [**137**].

In particular, surface modification by grafting of functional polymers is a versatile and powerful tool, which allows for careful tailoring of the desired surface properties [**138**]. A number of different surface grafting techniques exist for liquid or vapor phase systems with graft polymerization initiation by plasma discharge, oxidation through ozone, UV initiation, etc. [**139**], [**140**]. In particular, UV–induced surface graft polymerization is widely applied to modify open surfaces [**141**] such as polymer sheets or membranes [**142**], [**143**]. Treatments within enclosed microfluidic structures, on the other hand, pose significant challenges and suffer in many cases from low yield and poor quality [**144**], [**145**]. In addition, many applications require the ability to pattern surface properties: the surface modifications need to be applied locally with high spatial control while maintaining high surface quality of both original and patterned parts [**146**].

Surface–directed UV–initiated graft polymerization is a technique well suited to pattern functionalized polymers within microfluidic structures enclosed in PDMS at high spatial resolution. This technique is presented in detail in section 2.2. Applications for this wettability patterning technique are presented and discussed in section 2.3.

2.1 Microfluidic Systems Made of PDMS

PDMS is one of the most widely used polymers for fabrication of microfluidic systems [**62**]. The use of a PDMS elastomer for microfluidic systems has numerous advantages over silicone or glass. Systems made of PDMS can be easily and quickly fabricated at low cost by rapid prototyping techniques such as soft lithography [**147**], [**148**], and when PDMS is cast from a mold it replicates the features of the master with high fidelity (tens of nanometers) [**63**]. PDMS is optically transparent over a wide wavelength range down to UVB (280 nm) [**129**] and therefore compatible with many optical detection methods. It is also a non–toxic, biocompatible material which is impermeable to water and permeable to gases [**131**], [**149**]. Furthermore, PDMS provides a hydrophobic surface with a water contact angle of 108° in air [**64**].

The PDMS cast containing the microstructures can readily form a reversible seal with a plane counterpart (e.g. flat sheet of PDMS) due to van der Waals forces [**63**]. Irreversible seals with significantly higher bonding strengths can also easily be realized by bonding due to plasma oxidation of the surface [**64**] or by an alternative technique with partial pre–curing, bonding, and post–curing of two PDMS halves [**150**].

A detailed description of the fabrication process for PDMS microfluidic devices, as employed in this research, is presented in the following sub–sections.

2.1.1 *Fabrication of Microfluidic Systems*

The general process of the fabrication of a PDMS microfluidic device by soft lithography is shown in Figure 2.1. In short, a photolithographic process is used to transfer the desired structure to a photoresist deposited on a silicon waver in order to create a silicon master (Figure 2.1a). PDMS devices are then cast from the master by pouring liquid PDMS prepolymer onto the master and allowing for curing at elevated temperatures (Figure 2.1b). The cured, solidified PDMS is then peeled off from the master and bonded to a flat counterpart in order form an enclosed microfluidic system (Figure 2.1c). The silicon master can be reused and any number of PDMS devices can be produced in a fast and easy way by repetition of the final two stages.

A detailed description of the process is given below, including a description of the materials and methods used in the present work.

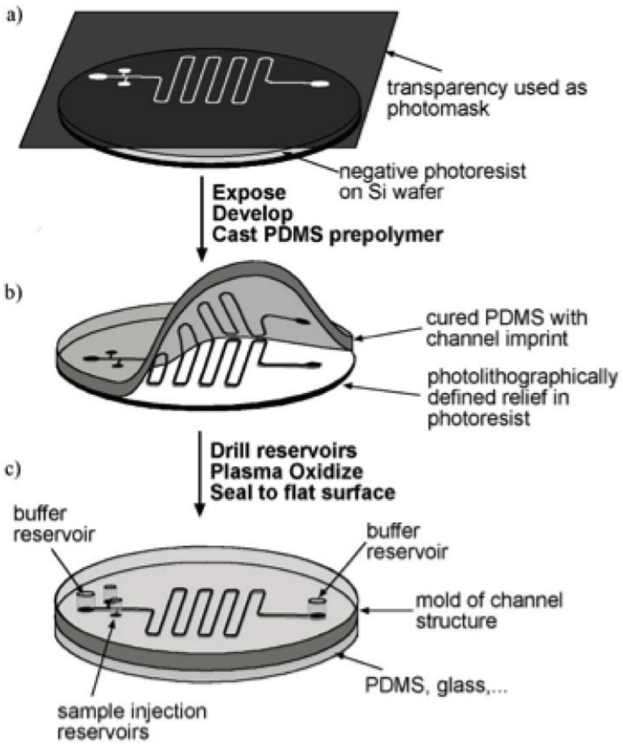

Figure 2.1: General process of PDMS device fabrication. (a) Fabrication of silicon master: Desired structures are transferred to photoresist on silicon waver via photolithography. (b) Cast from the silicone master transfers the embossed master structures as grooves to the PDMS device. (c) PDMS device is bonded against a flat counterpart in order to create enclosed microfluidic structures [**151**].

2.1.2 *Fabrication of Silicon Master*

As mentioned in the previous sub–section, the first step in making a new microfluidic device is the fabrication of a silicon master by photolithography (c.f. Figure 2.1a). A schematic of the fabrication process is shown in Figure 2.2. In a first step, the photoresist SU8[3] was spun on a pre–cleaned silicon wafer on a spin coater and a soft bake was performed according to the manufacturer's specifications [**152**] in order to remove the solvent. By variation of SU8 solvent content (viscosity) and spinning speed the desired film thickness of the photoresist could be achieved (Figure

---

[3] SU-8 2000 photoresist series, MicroChem Corporation, Newton, Massachusetts.

2.2a). Typically, film thicknesses from 0.5 µm to 200 µm and more can be achieved in a single coating [**152**].

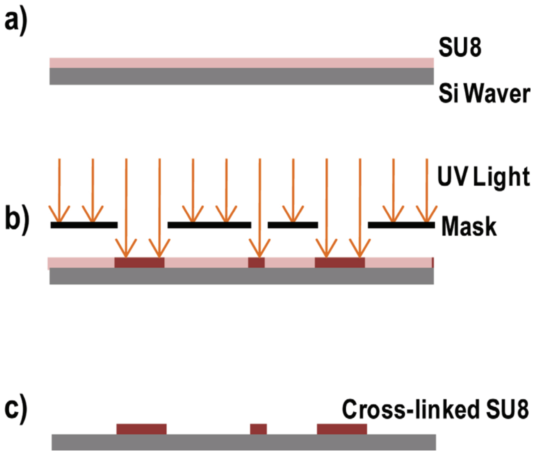

Figure 2.2: Silicon master fabrication process. (a) SU8 photoresist is spun onto a silicon waver at a desired thickness. (b) Microstructures are transferred to the photoresist by UV exposure through a mask. (c) Developed photoresist provides the microfluidic structures on the silicon master.

The desired microstructures were transferred to the photoresist by UV exposure on a mask–aligner[4] at at wavelentgh of 365 nm (Figure 2.2b). The applied UV energy dose was determined as a function of the photoresist thickness according to the manufacturer's specifications [**152**]. After exposure the waver was subjected to a post–bake in order to allow for cross–linking in the exposed SU8 areas followed by a developing step, where non–exposed SU8 was removed by the developer solvent (Figure 2.2c). An optional hard bake [**152**] was typically performed as well in order to further increase the durability of the master. Final dimensions of the fabricated structures were verified with a mechanical needle profiler[5].

The structures of the microfluidic system were custom–designed with CAD software and corresponding masks were obtained, either as ink–printed foil masks or etched chrome masks on glass substrate. The resolution of the foil masks was limited

---

[4] MJB4 mask-aligner, Süss MicroTec AG, Garching, Germany.

[5] DekTak 6M Stylos Profiler, Vecco High Performance Engineering Inc, Columbia Station, Ohio.

by the printer to 3600 dpi (7 µm per dot) while chrome masks provided nanometric resolution. However, if resolution was not critical, foil masks were chosen by default since they were faster to produce at significantly lower cost.

2.1.3 *Fabrication of PDMS Devices*

The fabrication of the PDMS chip itself consists in casting a PDMS slab from the silicone master and bonding it against a second, flat PDMS slab (c.f. Figure 2.1b–c). A schematic representation of the process is shown in Figure 2.3. First, PDMS pre–polymer[6] was prepared for casting: a PDMS base (linear polymer chains) was thoroughly mixed with curing agent (cross–linker) at a ratio of 10:1 (w/w) and poured onto the silicon master placed in a disposable Petri dish (Figure 2.3a). The cast was allowed to cure in an oven at 65°C for 2 hours before it was peeled from the silicon master. The PDMS slab containing the impression of the microfluidic structure was then cut to size and via holes were punched into the slab in order to provide chip–to–world fluid connections in the final device (Figure 2.3b).

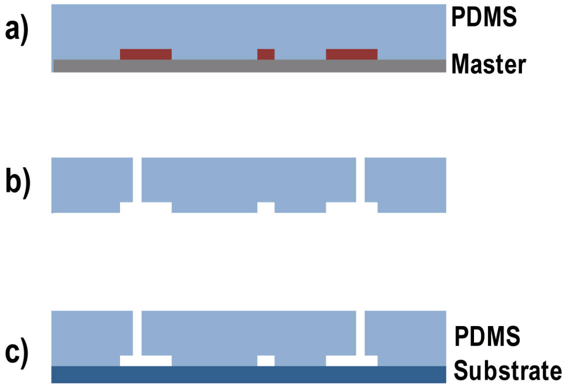

Figure 2.3: Fabrication of microfluidic PDMS chip. (a) PDMS pre–polymer is poured onto the silicon master and allowed to cure. (b) The cured PDMS slab is peeled off from the silicon master and via holes are created. (c) The micro–structured PDMS half is bonded against a flat substrate (e.g. PDMS) to seal the microfluidic structures.

---

[6] Sylgard 184 Silicone Elastomer Kit (Base and Curing Agent), Dow Corning Corporation, Midland, Michigan.

In parallel, a flat PDMS slab was prepared by casting from a flat surface (disposable Petri dish) and following the same protocol. Both halves were then bonded against each other in order to produce a device with enclosed microfluidic structures (Figure 2.3c). Bonding was achieved by activating the surfaces of the two halves in oxygen plasma[7] for 30 seconds at 400 mTorr and a power of 30 W applied to the RF–coil. After the plasma treatment both halves were immediately brought in contact in order to allow for irreversible bonds to form, which sealed the device permanently. The devices were then typically annealed in an oven at 90°C for two days in order to reverse the plasma–induced surface changes and recover the native water contact angle of PDMS of 108° [**153**].

2.2 Surface Treatment in Microfluidic Systems

Covalent polymer coatings are oftentimes superior to other surface modification methods in terms of mechanical and chemical robustness and also provide a high degree of flexibility towards the introduction of a variety of functional groups [**154**]. These covalent polymer coating techniques can be classified in two categories: (1) "grafting–to", where end–functionalized polymers are covalently tethered onto the target surface, and (2) "grafting–from", where polymerization of monomers is initiated on the target surface and polymer brushes are grown [**136**]. While both techniques are commonly used for modifications on open surfaces, application within enclosed capillaries and microfluidic channels is extremely challenging, in part due to the problem of bulk polymerization and subsequent clogging of the channels during treatment. The "grafting–from" technique is favorable since only small monomers need to be introduced into the micro–channels. Following work related to PAA grafting on open PDMS surfaces [**155**], [**156**], [**157**], the first success of graft polymerization of PAA within simple micro–channels was reported by the same group in 2004 [**158**]. However, many parameters for the surface treatment were neglected, overlooked, or misinterpreted, which caused the treatments in many cases to be unreliable and of low quality, and significant improvements were required.

---

[7] PDC-002 Plasma Cleaner, Harrick Plasma, Ithaca, New York.

Based on this obvious need, a significant part of the present work was dedicated to a careful study of surface treatments in order to provide a reliable protocol yielding high quality surface patterning.

In the next section (2.2.1), a detailed study on surface treatment for wettability patterning within enclosed PDMS microfluidic structures is presented and discussed. The specific method employed is surface–directed UV–initiated graft polymerization of PAA on PDMS, based on a two–step protocol published by Hu et al. [**158**]. Significant improvements have been made which allow for reliable wettability pattering of high quality at high spatial resolution, which is applicable even in complex microfluidic networks. A brief outline of the process is given below.

The surface treatment consists of the two main steps: priming and graft polymerization. Figure 2.4 shows the treatment process on a schematic cross–section of a single channel (white) in a PDMS chip (blue). The priming step serves to deposit BP photoinitiator along the PDMS walls. Therefore, a solution of BP in acetone (red) is injected into the microsystem[8] as shown in Figure 2.4b. During photoinitiator injection BP molecules diffuse into the PDMS matrix and form a reservoir of photoinitiator in proximity to the channel walls, even after the solution is removed (shown as light red in Figure 2.4c). In a second step, the channel is filled with an aqueous solution of AA monomers[9] (shown as green in Figure 2.4d) and the system is exposed to UV light [10] (Figure 2.4e). During UV exposure, BP molecules are excited, and relax by hydrogen abstraction typically from the PDMS methyl groups thus creating free radical sites. From these free radical sites, AA starts to polymerize and PAA grows on and within the PDMS walls. After cleaning, a covalently tethered PAA coating remains along the channel walls (dark green) as shown in Figure 2.4e. In contrast to native, hydrophobic PDMS, the PAA coating is strongly hydrophilic, providing a large contrast in wettability (surface energy). The two–step protocol ensures that photoinitiator and monomers are in contact only along the walls where

---

[8] Solution of 10 wt% BP in acetone injected for typically 5 min.

[9] Typically 20 wt% AA in pure water, for more details see section 2.2.1.

[10] UV exposure at 365 nm for typically 5 min at 35-50 mW/cm^2.

surface treatment is desired, hence reducing or eliminating interfering bulk polymerization within the channel.

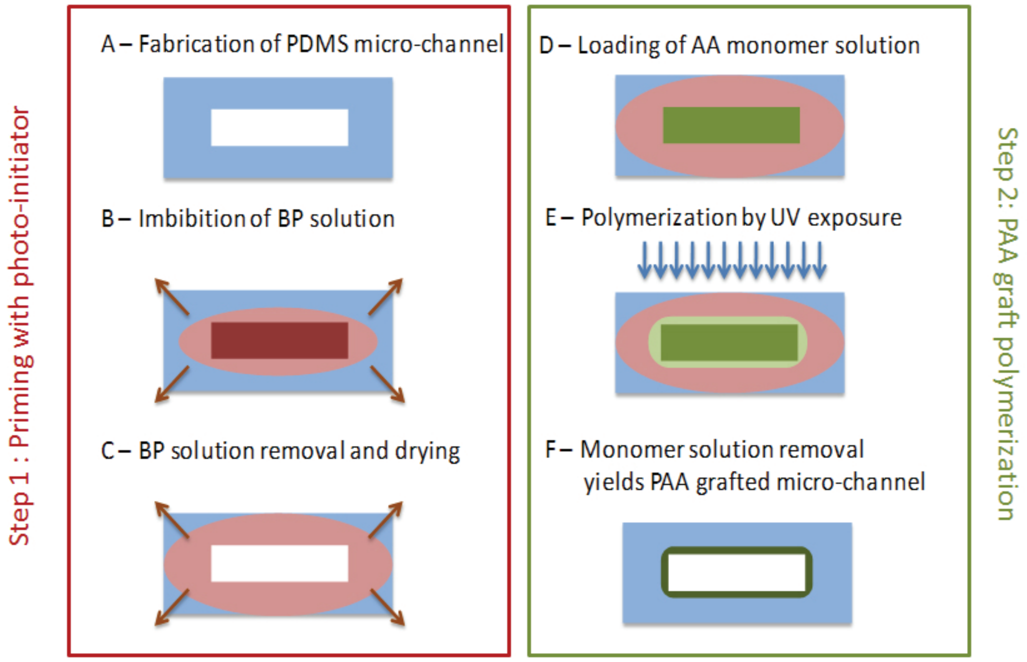

Figure 2.4: Schematic treatment process for surface–directed UV–initiated graft polymerization of PAA on PDMS surfaces. A cross–section of a single channel in PDMS (blue) is shown. First, during priming, BP solution (red) is injected and BP is allowed to diffuse into PDMS walls (light red). In a second step, AA monomer solution (green) is filled into the channel and exposed to UV light, which yield a coating of grafted PAA (dark green).

Patterning of the treatment can easily be realized by selective UV exposure through a mask as shown in Figure 2.5: a schematic PDMS chip with multiple channels is depicted in Figure 2.5a. After priming and filling the channels with monomer solution (c.f. Figure 2.4) certain areas can then be selectively exposed to UV light through a mask (Figure 2.5b). Treatment is only applied in the exposed segments hence providing a microfluidic system with patterned surface properties (Figure 2.5c).

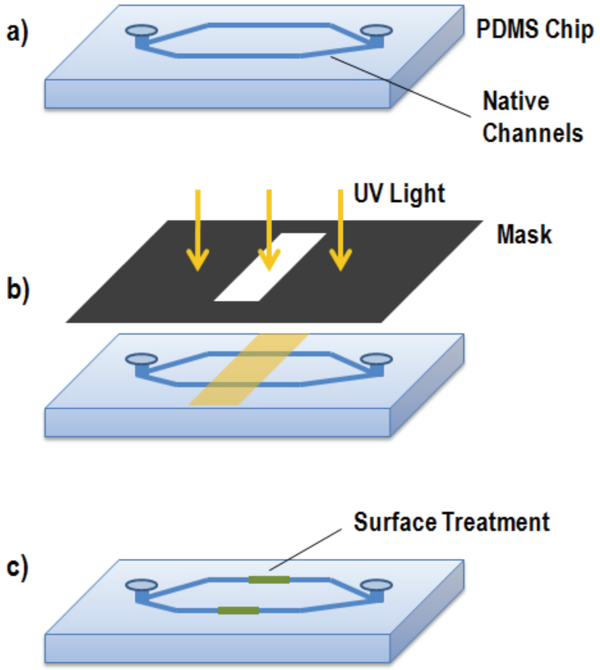

Figure 2.5: Schematic of the patterning process. (a) A microfluidic device is prepared for surface treatment (primed with BP and filled with AA monomer solution). (b) Graft initiation is selectively initiated by UV exposure through a mask. (c) The final system contains a patterned surface treatment as defined by the mask.

The photochemical process during UV exposure is schematically shown in Figure 2.6. The predominant reaction scheme for the photoinitiator BP is outlined[11] in Figure 2.6a. UV radiation excites BP and quickly produces triplet BP. If in proximity to a hydrogen donor site, triplet BP is relaxed via hydrogen abstraction to BP ketyl radical, thus forming a free radical at the donor site. BP ketyl radicals typically combine with each other to form benzopinacol. Within the PDMS matrix, methyl groups are favorable donor sites for hydrogen abstraction (Figure 2.6b). After radicalization, PAA starts to grow from the PDMS chain as illustrated in (Figure 2.6c).

---

[11] For details see Appendix A.

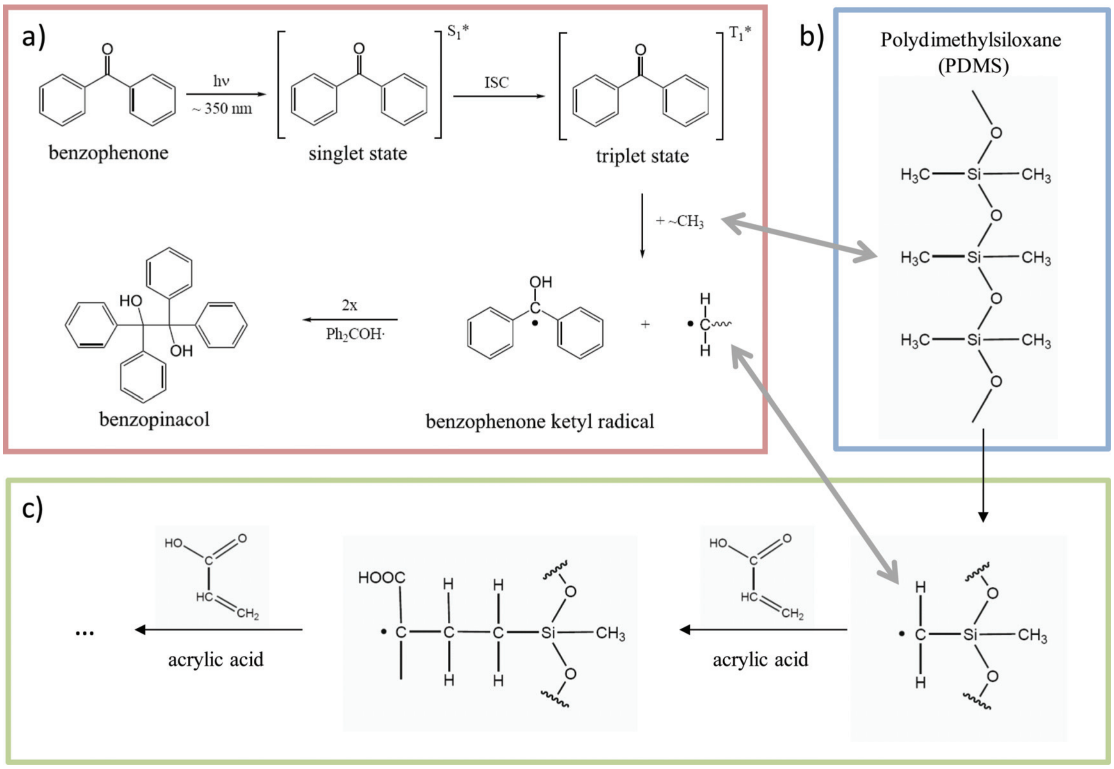

Figure 2.6: Schematic outline of the photochemical process involved in surface treatment showing (a) BP photoinitiation, (b) PDMS, and (c) PAA graft polymerization.

Significant effort was dedicated to the investigation of the priming process itself. In particular the diffusion properties of BP within PDMS were studied in detail, a critical factor for successful surface treatment which seems to have been neglected in literature so far. The results, surprisingly fast BP migration in acetone–swollen PDMS together with a new in–situ visualization technique, will be published in *Langmuir* as presented in Appendix A.

The entire surface treatment process was carefully studied as well and every step of the treatment process was rigorously investigated in order to identify the key parameters required to perform a stable and reliable treatment of high quality. The influence of each parameter was carefully investigated and recommended values were identified. This detailed understanding of the treatment process and the effects of the critical parameters on it allowed for significant improvements in quality and reliability of the process. These new results and the deepened understanding of a significantly improved surface–directed UV–initiated graft polymerization process, together with a ‘recipe’ of detailed step–by–step instructions, were published in *Analytical Chemistry* in order to make them available to the field. The full article is presented in the following section.

2.2.1 *Article:* *Wettability Patterning by UV–Initiated Graft Polymerization of Poly(acrylic acid) in Closed Microfluidic Systems of Complex Geometry*

Anal. Chem. **2010**, *82*, 8848–8855

Wettability Patterning by UV-Initiated Graft Polymerization of Poly(acrylic acid) in Closed Microfluidic Systems of Complex Geometry

Marc H. Schneider,[*,†,‡] **Hervé Willaime,**[†] **Yvette Tran,**[†] **Fadhel Rezgui,**[‡] **and Patrick Tabeling**[†]

ESPCI, 10 Rue Vauquelin, 75005 Paris, France, and Schlumberger, 1 Rue Henri Becquerel, 92140 Clamart, France

Ⓦ **This paper contains enhanced objects available on the Internet at http://pubs.acs.org/ac.**

Many microfluidic applications require modified surface wettability of the microchannels. Patterning of wettability within enclosed microfluidic structures at high spatial resolution has been challenging in the past. In this paper, we report an improved method for altering the surface wettability in poly(dimethylsiloxane) (PDMS) microchannels by UV-induced graft polymerization of poly(acrylic acid). Our method presents significant improvements in terms of wettability contrast and spatial resolution of the patterned structures as compared to recent literature and is in particular applicable to complex microfluidic structures with a broad range of channel sizes and aspect ratios. A key part of our work is the clear description of the surface treatment process with the identification of key parameters, some of which have been overlooked, neglected, or misinterpreted in previous works. We have studied these key parameters in detail and provide recommended values for each parameter supported by experimental results. This detailed understanding of the treatment process and the effects of the critical parameters on it allowed us to significantly improve quality and reliability of the treatment process.

Microfluidic devices made with rapid prototyping techniques, especially soft lithography,[1] have given rise to an enormous amount and versatility of applications across many fields. A favorite material frequently used for such devices is poly(dimethylsiloxane) (PDMS), which provides a number of advantageous properties such as its flexibility, durability, transparency, and chemical inertness to name a few. Casting PDMS from a mold and subsequent bonding to a flat PDMS counterpart provides a very rapid fabrication method for enclosed microfluidic devices,[2,3] which can provide elaborate channel structures of varying depth. For many applications, PDMS devices in their native, hydrophobic state are readily utilizable and well suited for the particular task. Other applications, however, demand different surface properties such as hydrophilic walls, e.g., in order to facilitate the filling of such devices with aqueous solutions.[4] Common hydrophilization techniques include oxygen plasma treatment[4] and adsorbed surfactant coatings, and both techniques have been proven to work well for certain types of applications but suffer frequently from a lack of long-term stability[2] and might not be practical if a patterned treatment is required.[5] A widely used surface modification technique in polymer science is the surface-attached polymerization, which provides chemically stable surfaces due to the covalent attachment of the polymer chains to the substrate.[4,6−9] Such surface modification can be initiated by a number of different techniques,[6] e.g., plasma discharge, oxidation through ozone,[10] and UV irradiation,[11] which can be applied either to liquid phase systems or vapor phase systems.[9,5] Since plasma discharge and ozone methods typically start the initialization on all accessible surfaces, patterned surface modifications can be achieved only by partially covering the substrate surface. In contrast, the UV irradiation method has the inherent advantage that polymerization is only initiated in areas exposed to UV light, which is a well suited method if spatially patterned surface modifications are required.

In 2002, the first successful grafting of poly(acrylic acid) (PAA) on PDMS based on a liquid phase system with UV irradiation was reported by Hu et al.,[12] which was previously used for surface modifications on poly(ethylene) substrates.[13] This early protocol was based on a one-step process with long, intensive UV exposure of open PDMS systems in order to directly initialize polymerization on the surface. After several improvements,[14,15] the first success of graft polymerization of PAA in closed PDMS channels was

---

[*] To whom correspondence should be addressed. E-mail: mschneider@slb.com.

[†] ESPCI.

[‡] Schlumberger.

(1) Xia, Y.; Whitesides, G. M. *Annu. Rev. Mater. Sci.* **1998**, *28*, 153–184.

(2) Duffy, D. C.; McDonald, J. C.; Schueller, O. J. A.; Whitesides, G. M. *Anal. Chem.* **1998**, *70*, 4974–4984.

(3) McDonald, J. C.; Duffy, D. C.; Anderson, J. R.; Chiu, D. T.; Wu, H.; Schueller, O. J. A.; Whitesides, G. M. *Electrophoresis* **2000**, *21*, 27–40.

(4) Liu, J.; Lee, M. L. *Electrophoresis* **2006**, *27*, 3533–3546.

(5) Wong, I.; Ho, C.-M. *Microfluid. Nanofluid.* **2009**, *7*, 291–306.

(6) Kato, K.; Uchida, E.; Kang, E.-T.; Uyama, Y.; Ikada, Y. *Prog. Polym. Sci.* **2003**, *28*, 209–259.

(7) He, D.; Susanto, H.; Ulbricht, M. *Prog. Polym. Sci.* **2008**, *34*, 62–98.

(8) Nie, Z.; Kumacheva, E. *Nat. Mater.* **2008**, *7*, 277–290.

(9) Deng, J.; Wang, L.; Liu, L.; Yang, W. *Prog. Polym. Sci.* **2009**, *34*, 156–193.

(10) Diaz-Quijada, G. A.; Wayner, D. D. M. *Langmuir* **2004**, *20*, 9607–9611.

(11) Uyama, Y.; Kato, K.; Ikada, Y. *Surface Modification of Polymers by Grafting*; Springer Verlag: Heidelberg, Germany, 1998; Vol. 137, pp 1−39.

(12) Hu, S.; Ren, X.; Bachman, M.; Sims, C. E.; Li, G. P.; Allbritton, N. *Anal. Chem.* **2002**, *74*, 4117–4123.

(13) Richey, T.; Iwata, H.; Oowaki, H.; Uchida, E.; Matsuda, S.; Ikada, Y. *Biomaterials* **2000**, *21*, 1057–1065.

(14) Hu, S.; Ren, X.; Bachman, M.; Sims, C. E.; Li, G. P.; Allbritton, N. *Electrophoresis* **2003**, *24*, 3679–3688.

(15) Hu, S.; Ren, X.; Bachman, M.; Sims, C. E.; Li, G. P.; Allbritton, N. *Langmuir* **2004**, *20*, 5569–5574.

10.1021/ac101345m

reported in 2004.[16] The main factor for a successful treatment within a closed microchannel was the incorporation of the photoinitiator benzophenone (BP) as a two-step protocol. Application of an efficient photoinitiator such as BP helps in general to decrease UV exposure time from several hours to several minutes and to employ longer wavelengths and therefore minimizes UV induced damage of the PDMS substrate significantly.[10,17,18] Otherwise, if the PDMS device is exposed to short wavelength UV or broadband illumination for extended periods of time, photoinduced modification within the entire PDMS matrix accompanies the grafting process at the surfaces, causing oxidation, chain scission, unsaturation, and degradation of the PDMS backbone structure, as known from other treatment techniques.[19−24] Furthermore adsorption of BP on the PDMS surface in a first step and application of the monomer solution in a second step provide a surface-directed polymerization and help to significantly minimize bulk polymerization in the monomer solution and subsequent channel clogging, which is a major problem of one-step protocols in closed channels. Hu et al.[16] reported the successful PAA grafting for simple channel geometries enclosed in PDMS at a spatial resolution of about 100 μm. While being a success to the field without doubt, many applications such as multiple emulsion synthesis,[25−30] continuous flow liquid−liquid extraction,[31−34] etc. demand a much better control of spatial resolution and require the treatment to be applicable to systems of complex geometries.

In recent years, a lot of work has been performed in order to improve both spatial resolution as well as the contrast in wettability.[17,35−39] For the treatment of a single PDMS surface (open system), significant improvements have been reported for spatial resolution down to a few micrometers.[35,36,38] However, these improvements are based on bringing the photo mask in close proximity to the surface, physically covering the surface with an attached mask, or focusing a light pattern onto the surface and are therefore only applicable to open systems or flat substrates. Also, because of its simplicity in terms of system preparation, the protocol has been used for surface attachment of different polymers such as poly(acrylamide) or poly(ethylene glycol)diacrylate (PEGDA) in order to increase the contrast in wettability between native PDMS and the grafted polymer.[14,35,37,38] Investigators found that PAA surface grafts typically yield the smallest water contact angles of about 60−70°,[15,17] close to the value of 58° as found on pure PAA thin films.[40] PEGDA is added by some investigators in small quantities as a cross-linker. However, both acrylate bonds of PEGDA possess a large propagation rate but low termination rate constants[41] and therefore yield rapid polymerization into the bulk solution[42] and hence cause severe clogging problems with treatment in closed systems. Apart from UV-induced polymerization, other PAA deposition techniques have been developed, such as deposition by ion exchange reactions[43] or by plasma induced polymerization.[44] However, such techniques are applied to the open system and subsequent sealing of the device becomes challenging.

Abate et al.[45] have recently shown successful graft polymerization of PAA in a closed channel with the best results regarding spatial resolution and wettability contrast yet reported. Although the investigators start out with a PDMS device they use the PDMS matrix in their approach only as a structural skeleton, which is entirely masked by a sol−gel coating of functionalized silanes in a first step before additional treatments are applied. Consequently, for such technique with additional difficulties, the protocol for polymerization on such surfaces needs to differ substantially from the grafting directly on PDMS.

Controversial results have been presented in literature concerning the final localization and appearance of the grafted layer. While in many cases the PAA grafted layer is considered to be a dense layer of PAA growing predominantly on top of the PDMS substrate,[16,36] other data suggest that the PAA chains grow mainly inward into the PDMS substrate and form a network of entangled chains of PAA and PDMS.[35] In addition, the adsorption process of the photoinitiator BP seems to not yet be well understood. In many cases, little or no supporting data is published for the chosen application time and solution formulation, yet the particular parameters used differ significantly from each other.

In this paper, we present an improved method for wettability patterning by UV-induced graft polymerization of PAA directly in enclosed PDMS microfluidic structures. We identify and discuss

---

(16) Hu, S.; Ren, X.; Bachman, M.; Sims, C. E.; Li, G. P.; Allbritton, N. *Anal. Chem.* **2004**, *76*, 1865–1870.

(17) Hu, S.; Brittain, W. J. *Macromolecules* **2005**, *38*, 6592–6597.

(18) Xiao, D.; Van Le, T.; Wirth, M. J. *Anal. Chem.* **2004**, *76*, 2055–2061.

(19) Efimenko, K.; Wallace, W. E.; Genzer, J. *J. Colloid Interface Sci.* **2002**, *254*, 306–315.

(20) Waddell, E. A.; Shreeves, S.; Carrell, H.; Perry, C.; Reid, B. A.; McKee, J. *Appl. Surf. Sci.* **2008**, *254*, 5314–5318.

(21) Schnyder, B.; Lippert, T.; Kotz, R.; Wokaun, A.; Graubner, V.-M.; Nuyken, O. *Surf. Sci.* **2003**, *532−535*, 1067–1071.

(22) Berdichevsky, Y.; Khandurina, J.; Guttman, A.; Lo, Y.-H. *Sens. Actuators, B* **2004**, *97*, 402–408.

(23) Olah, A.; Hillborg, H.; Vancso, J. G. *Appl. Surf. Sci.* **2005**, *239*, 410–423.

(24) Tsougeni, K.; Tserepi, A.; Gogolides, E. *Microelectron. Eng.* **2007**, *84*, 1104–1108.

(25) Hennequin, Y.; Pannacci, N.; Pulido de Torres, C.; Tetradis-Meris, G.; Chapuliot, S.; Bouchaud, E.; Tabeling, P. *Langmuir* **2009**, *25*, 7857–7861.

(26) Abate, A. R.; Weitz, D. A. *Small* **2009**, *5*, 2030–2032.

(27) Tabeling, P. *Lab Chip* **2009**, *9*, 2428–2436.

(28) Pannacci, N.; Bruus, H.; Bartolo, D.; Etchart, I.; Lockhart, T.; Hennequin, Y.; Willaime, H.; Tabeling, P. *Phys. Rev. Lett.* **2008**, 101.

(29) Chu, L.-Y.; Utada, A. S.; Shah, R. K.; Kim, J.-W.; Weitz, D. A. *Angew. Chem., Int. Ed.* **2007**, *46*, 8970–8974.

(30) Seo, M.; Paquet, C.; Nie, Z.; Xu, S.; Kumacheva, E. *Soft Matter* **2007**, *3*, 986–992.

(31) Tokeshi, M.; Minagawa, T.; Uchiyama, K.; Hibara, A.; Sato, K.; Hisamoto, H.; Kitamori, T. *Anal. Chem.* **2002**, *74*, 1565–1571.

(32) Aota, A.; Hibara, A.; Kitamori, T. *Anal. Chem.* **2007**, *79*, 3919–3924.

(33) Aota, A.; Nonaka, M.; Hibara, A.; Kitamori, T. *Angew. Chem., Int. Ed.* **2007**, *46*, 878–880.

(34) Aota, A.; Mawatari, K.; Kitamori, T. *Lab Chip* **2009**, *9*, 2470–2476.

(35) Wang, Y.; Lai, H.-H.; Bachman, M.; Sims, C. E.; Li, G. P.; Allbritton, N. L. *Anal. Chem.* **2005**, *77*, 7539–7546.

(36) Patrito, N.; McCague, C.; Chiang, S.; Norton, P. R.; Petersen, N. O. *Langmuir* **2006**, *22*, 3453–3455.

(37) Ebara, M.; Hoffman, J. M.; Stayton, P. S.; Hoffman, A. S. *Radiat. Phys. Chem.* **2007**, *76*, 1409–1413.

(38) Sugiura, S.; Edahiro, J.-i.; Sumaru, K.; Kanamori, T. *Colloids Surf. B* **2008**, *63*, 301–305.

(39) Fiddes, L. K.; Chan, H. K. C.; Lau, B.; Kumacheva, E.; Wheeler, A. R. *Biomaterials* **2010**, *31*, 315–320.

(40) Kaczmarek, H.; Szalla, A.; Chaberska, H.; Kowalonek, J. *Surf. Sci.* **2004**, *566−568*, 560–565.

(41) Decker, C. *Macromol. Rapid Commun.* **2003**, *23*, 1067–1093.

(42) Lin, H.; Kai, T.; Freeman, B. D.; Kalakkunnath, S.; Kalika, D. S. *Macromolecules* **2005**, *38*, 8381–8393.

(43) Lahav, M.; Narovlyansky, M.; Winkelman, A.; Perez-Castillejos, R.; Weiss, E. A.; Whitesides, G. M. *Adv. Mater.* **2006**, *18*, 3174–3178.

(44) Barbier, V.; Tatoulian, M.; Li, H.; Aref-Khonsari, F.; Ajdari, A.; Tabeling, P. *Langmuir* **2006**, *22*, 5230–5232.

(45) Abate, A. R.; Krummel, A. T.; Lee, D.; Marquez, M.; Holtze, C.; Weitz, D. A. *Lab Chip* **2008**, *8*, 2157–2160.

parameters for each step of the treatment, which have significant influence on the quality of the treatment.

EXPERIMENTAL SECTION

Materials. Sylgard 184 Silicone Elastomer Kit was purchased from Dow Corning. Silicon wafers were purchased from Wafer World, and SU8 2000 series photoresist was obtained from MicroChem. Acrylic acid (AA), benzophenone (BP), benzyl alcohol, sodium periodate ($NaIO_4$), tolonium chloride (TC), and sodium hydroxide were purchased from Sigma-Aldrich and used without further purification. Organic solvents and lab supplies were purchased from VWR. Deionized (DI) water was produced in-house by a Synergy Ultrapure water system from Millipore (resistivity $\geq$ 18.2 MΩ cm).

Device Fabrication and Preparation. Microfluidic channel structures were created on a silicon wafer by a photolithography patterning process of SU8 photoresist. The desired microstructures were transferred to the photoresist by UV exposure on a MJB4 mask-aligner from Süss MicroTec. The photoresist was processed according to the parameters given by the manufacturer[46] for the desired thickness. Final dimensions of the mold were verified with a DekTak 6 M Stylos Profiler from Vecco. Sylgard 184 PDMS base was mixed with curing agent at a ratio of 10:1 (w/w) and cast against the silicon master as well as against a flat reference surface in order to create both the structured part and the flat counterpart of the microfluidic device, each about 2 mm in thickness. The cast was allowed to cured at 65 °C for 2 h before the two halves where bonded against each other in order to produce a closed microfluidic system. Bonding was achieved by activating the surfaces of the two halves with oxygen plasma in a Harrick Plasma Cleaner for 30 s at a 400 mTorr oxygen atmosphere. Both halves were brought into contact immediately after the plasma treatment so that irreversible bonds could form at the interface, sealing the device permanently. The devices were then annealed in an oven at 90 °C for 2 days in order to reverse the plasma-induced surfaces changes and recover the native water contact angle of PDMS of 108°.[2,23]

UV-Initiated Wettability Patterning. Wettability pattering within the microfluidics network was achieved by UV-initiated graft polymerization of AA through an appropriate mask. In a first step, the microfluidic device was primed with the photoinitiator BP. A solution of 10 wt % BP in acetone was flowed through the microchannels at 200 μL/min for typically 5−10 min before the solution was flushed out with air. Because of the acetone-induced swelling of the PDMS matrix, the hydrophobic BP molecules can easily diffuse into the PDMS and provide high concentrations of photoinitiator along the channel walls. The systems were then vacuum-dried for 10 min unless stated otherwise.

Monomer solution was prepared prior to the experiments by mixing AA monomer in DI water and degassing the solution for several hours under vacuum in order to remove dissolved oxygen. The typical mix consisted of 20 wt % AA in water without additional supplements. However some experiments were conducted with solution with varying amounts of monomer or with additional supplements such as benzyl alcohol or $NaIO_4$. The monomer solution was then loaded into the primed microfluidic device. For complex networks with the tendency to trap air bubbles during injection, an overpressure of about 500 mbar for about 1 min was applied to the solution during injection in order for the degassed PDMS to absorb the trapped gas bubbles and promote optimal filling. The monomer solution was sealed into the microfluidic device by closing the fluid inlets with adhesive tape.

The microfluidic device was then exposed to UV radiation through an ink-printed foil-mask, directly in contact with the PDMS surface. The distance between the mask was therefore governed by the thickness of the PDMS layer. A detailed discussion on optical resolution is provided in the Supporting Information. As the UV light source, the Lightningcure LC8 lamp with a 200 W mercury−xenon arc lamp with beam homogenizer and collimator from Hamamatsu was used. An additional 365 nm band-pass filter was added to the optical path to further restrict the optical output to the desired wavelength and therefore minimize sample heating. The effective (measured) UV intensity in the exposure plane was 64 mW/cm^2 at 100% lamp power. Unless stated otherwise, exposure was performed at 50% lamp power (32 mW/cm^2) for several minutes as indicated.

After UV exposure, the monomer solution was flushed out and the system was typically rinsed with ethanol for 1 h followed by a rinse of water at pH 10 for another hour. The purpose of the thorough rinsing sequence is to remove unreacted AA monomers as well as BP and its reaction products as well as to deprotonate the PAA for optimum hyrophilicity. All processes described above were performed at ambient temperature (22 °C). Because of the effective suppression of light outside the 365 nm line, sample heating during UV exposure was found to be negligible.

Visualization of the Graft Polymerization. Since PAA is a polyelectrolyte with negative charge units in aqueous solution, staining with TC was used to identify the PAA grafts. A solution of 1 wt % TC in DI water was loaded into the microfluidic device and allowed to rest for 10 min. After, the solution was removed and the system was flushed with water. The TC cations complex the PAA and mark it deep blue but will not stain native PDMS. Typically a small amount of sodium hydroxide was added to the TC solution (pH 10) in order to promote proton dissociation and charge buildup in the PAA grafts.[47,48]

In order to study the depth profile of the applied graft, thin sections of the treated microfluidic devices were taken with a razor blade, stained after dissection with TC, and observed under a microscope at high magnification.

RESULTS AND DISCUSSION

The basic steps of the surface treatment are schematically shown in Figure 1. For each step we have identified one or more critical parameters, which are crucial to a successful treatment. These critical parameters together with recommended values are listed in Table 1. In the following, each step will be discussed in detail and the critical parameters and their optimal values will be highlighted.

The surface treatment process starts with a microfluidic channel structure enclosed in PDMS as depicted in Figure 1A. The microfluidic device is fabricated as two halves, enclosed via

---

[46] MicroChem. Datasheet, SU-8 2000 Permanent Epoxy Photoresist-Processing Guidelines for SU-8 2100 and SU-8 2150; MicroChem: Newton, MA, 2007.

[47] Uchida, E.; Uyama, Y.; Ikada, Y. *Langmuir* **1993**, *9*, 1121–1124.

[48] Kang, E. T.; Tan, K. L.; Kato, K.; Uyama, Y.; Ikada, Y. *Macromolecules* **1996**, *29*, 6872–6879.

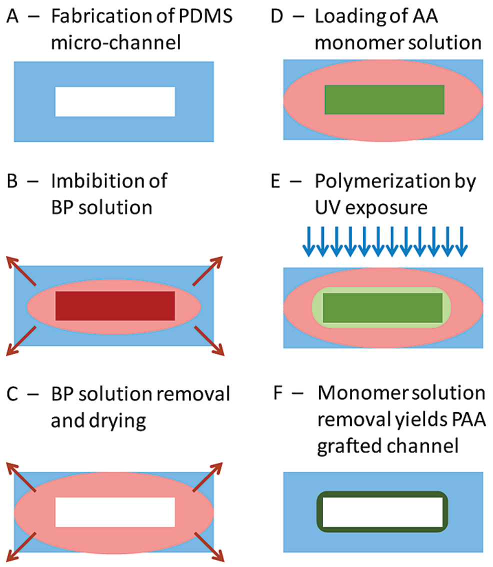

Figure 1. Schematic of UV-induced graft polymerization treatment. (A) Cross-sectional view of a microfluidic channel enclosed in PDMS (blue). (B) Solution of photoinitiator BP in acetone (dark red) is flowed through the channel and BP diffusion into PDMS matrix (light red) is depicted. (C) BP solution is removed from channel but diffusion into PDMS continues. (D) Aqueous AA monomer solution (green) is loaded into the channel. (E) UV exposure generates free radicals where BP is present (light red) and initiates AA polymerization as monomers diffuse into PDMS (light green). (F) Monomer solution is removed after UV exposure and a covalently bound PAA grafted layer is left behind (dark green).

plasma bonding and annealed afterward in order to regain native PDMS hydrophobicity. The fabrication process is described in detail in the Experimental Section.

Application of Photoinitiator. Proper priming of the microfluidic system with the photoinitiator BP plays a crucial part in the polymerization process and is described in the Experimental Section. In short, in a first step a solution of 10 wt % BP in acetone is flowed through the microfluidic system for at least 5 min (cf. Table 1). Supported by the imbibition of the solvent acetone into the PDMS matrix, hydrophobic BP molecules adhere to and diffuse through the channel walls into the PDMS matrix in vicinity of the channel as depicted in Figure 1B. In a subsequent step, the photoinitiator solution is flushed out of the system by air injection and the system is dried under vacuum for typically 10 min (cf. Table 1). During drying time, BP continues to diffuse into the PDMS matrix, which leads to a homogenized layer of primed PDMS around the channels.

A detailed study on the diffusion behavior of BP in PDMS based on a novel visualization technique developed in our laboratory was recently conducted.[49] In short, for this study we used strong UV excitation and a green emission filter to capture a weak photoluminescence signal emitted by an intermediary product (In) in the relaxation process of the BP radicals. This photoluminescence signal is produced after activated BP molecules have successfully undergone hydrogen abstraction and provides direct evidence for the presence of BP. Aided by this study, we revealed several critical parameters and their optimum values as listed in Table 1.

We also found the waiting time between priming and graft initiation to be a critical parameter as listed in Table 1. Further, contradictory to other reports found in literature, we refrain from flushing BP solution with water as significant BP precipitation can occur. Results and an additional discussion on these issues are provided in the Supporting Information.

Photoinitiator Quenching by Oxygen. We have identified molecular oxygen as a major cause for failed or inhomogeneous treatment. Measures need to be taken during treatment to keep oxygen away from the reaction sites along the channel walls of the microfluidic system. For a typical setup without any precaution, there are two pathways on which molecular oxygen can reach the reaction sites and disturb the grafting process: (1) Atmospheric oxygen can diffuse through PDMS, which has a high gas permeability, and reach the channel wall from the back side. (2) Dissolved oxygen in the monomer solution is brought into the channels and can easily diffuse toward the channel walls.

A detailed discussion about the influence of oxygen is given in the Supporting Information. In summary, we want to point out that the presence of oxygen significantly affects and disturbs the efficiency of PDMS radicalization (graft initiation). In order to keep a simple benchtop process, we favor the deep implantation of BP in order to screen the oxygen influx through PDMS as compared to treatment under nitrogen atmosphere. We recommend BP dissolved in pure acetone, which favors strong imbibition. We also recommend an application time (imbibition time) of 5 min or longer under constant flow in order to ensure sufficient uptake

Table 1. Significant Parameters for the Polymerization Treatment and Recommended Values As Determined in Our Study

parameter	recommended value
photoinitiator solution formulation	10 wt % benzophenone in acetone[a]
photoinitiator imbibition	5 min or longer under constant flow[a]
photoinitiator solution removal	acetone solution removal by air only followed by immediate vacuum drying;[b] drying time typically 10 min but less than 30 min
monomer solution formulation	20 wt % acrylic acid (AA) in deionized water (10 wt % AA for systems with small restrictions below 50 μm)
monomer solution additives	none[c] (0.5 wt % benzyl alcohol for systems with small restrictions below 50 μm)
oxygen removal	degassing of monomer solution for at least 1 h prior to use;[d] no special treatment of PDMS substrate
UV exposure time and energy	5 min UV exposure at 365 nm at an intensity of 35−50 mW/cm^2 resulting in an energy dose of 10−15 J/cm^2 (higher dose for low AA concentration and added benzyl alcohol)
final cleaning	flushing for 1 h with ethanol followed by up to 2 h of water (pH 10)

[a] Longer imbibition times were shown to significantly improve treatment quality in contradiction to other literature stressing the need for very short imbibition times,[16] and photoinitiator dilution with water[35] was found to be unnecessary. [b] Flushing with water[16] should be avoided as it might cause BP crystals to fall out of solution in large quantities if mixing of photoinitiator solution and water occurs. [c] We found the commonly proposed addition of $NaIO_4$[16,26,35,36] unnecessary at best and showed that it limits and suppresses graft polymerization. [d] Quenching by molecular oxygen has a significant impact on the graft polymerization and might cause buried layers or suppress polymerization completely. However, impact and proper mitigation were neglected in related literature so far.

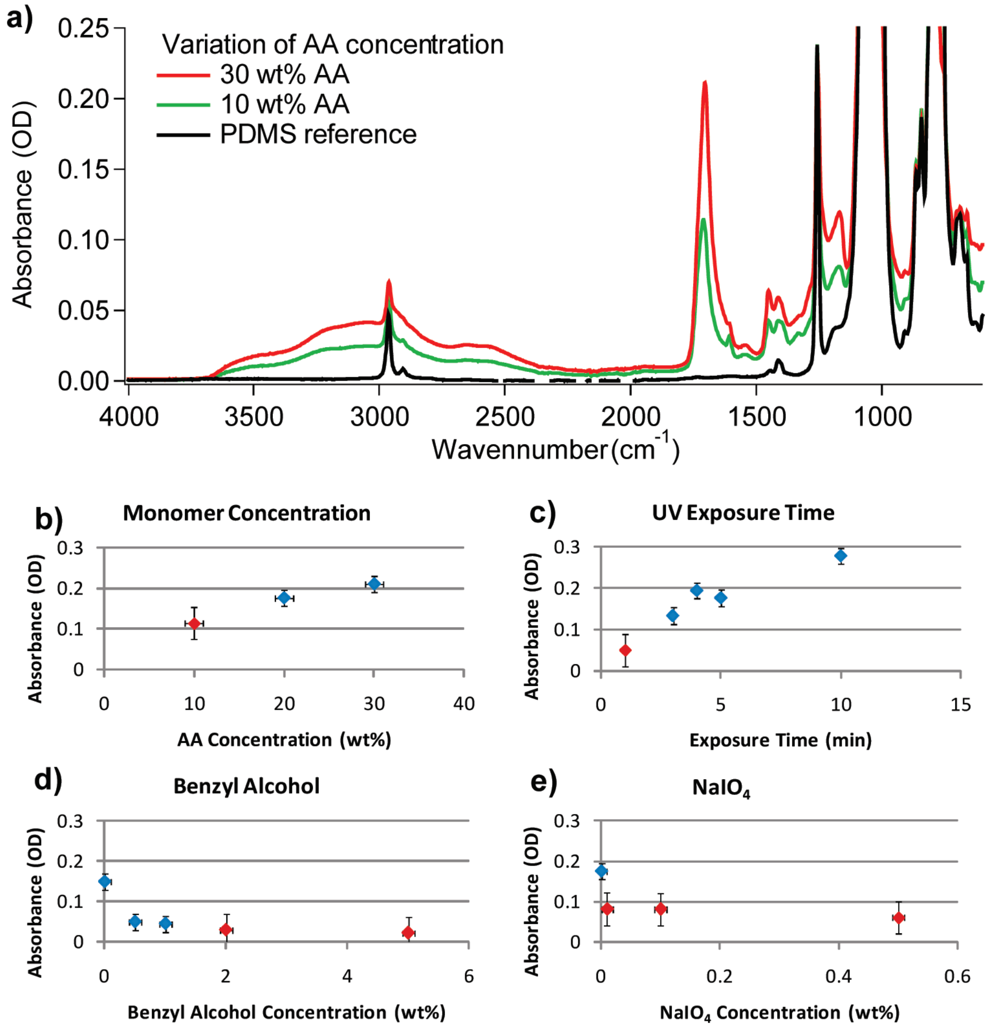

Figure 2. (a) FT-IR-ATR absorption spectra of native PDMS as well as grafted PAA with different parameters. The spectra clearly reveal the presence of carboxylic acid groups with broad absorption bands of the O−H stretch as well as a sharp carbonyl peak. Peak absorption values of the carbonyl stretch representing grafting densities are reported in parts b−e as functions of different grafting parameters. Grafting was performed on large channel cavity-type systems. The blue dots indicate homogeneous treatment over the cavity, while red dots indicate grafting results with only partial coverage.

of BP into the PDMS matrix. In the subsequent step of vacuum-drying for 10 min, BP continues to diffuse into the PDMS matrix, which forms a deep and homogeneous layer of PDMS primed with BP. However, it is crucial to remove dissolved oxygen in the monomer solution prior to injection (Figure 1D) in order to stop the oxygen supply through the second pathway. We therefore recommend oxygen removal by degassing under vacuum in Table 1.

Graft-Polymerization Properties. The formulation of the monomer solution, which is loaded into the channels (Figure 1D) as well as the settings for the subsequent UV exposure (Figure 1E) are critical parameters for the treatment process as listed in Table 1. We have conducted a series of experiments in order to investigate the influence of each parameter and characterized the resulting graft with Fourier transform-infrared (FT-IR) spectroscopy.

After the microfluidic systems were primed with BP, they were loaded with monomer solution and exposed to UV light in order to induce surface-directed graft polymerization at the channel walls. Monomer solution consisted of AA diluted in DI water at various concentrations. Resulting PAA graft efficiency was tested on cavity systems and analyzed via FT-IR-attenuated total reflectance (ATR); details on the employed method are provided in the Supporting Information. Figure 2a shows IR spectra of PAA grafts obtained with different monomer solutions as well as a PDMS reference spectrum. The carbonyl absorption peak is used as characteristic measure for the grafting quality and represents a qualitative measure for graft density as discussed in the Supporting Information. Unless noted otherwise, the standard monomer concentration in Figure 2 is 20 wt % AA and the standard exposure time is 5 min at 32 mW/cm^2.

Figure 2b shows the absorbance for varying monomer concentrations while the absorbance as a function of UV exposure time is shown in Figure 2c. We found that higher monomer concentrations yield higher absorbance values (grafting densities) and also minimize depletion effects in large channel systems. However, with higher monomer concentrations, the risk of polymerization around impurities within the solution increases, which caused small PAA clusters to form and can potentially cause blockage, especially in small channel systems. However, we never observed true gel formation in the solution at any of the used concentrations. UV exposure time increases the absorbance (grafting density) significantly for exposures up to 5 min at the given UV power of 32 mW/cm^2 but yields only minimal improvements for longer exposures. We therefore recommend a UV dose of 10−15 J/cm^2 (Table 1). A qualitative study of PAA penetration depth by investigation of stained cross sections showed a clear dependency on the exposure time. For constant UV dose, exposure at maximum power (and one-quarter of the exposure time) generated PAA layers of about half the depth than compared to exposure at 25%. The square root relationship between PAA layer thickness and exposure time seems to indicate a process limited by AA monomer diffusion.

Additives to the monomer solution as commonly proposed in the literature[12−16,35−37,45] were also tested. Benzyl alcohol is typically added as a chain transfer agent, limiting polymer brush size and suppressing polymerization around nucleation seeds within the solution.[13,50] However, high concentrations of chain transfer agent significantly reduce the grafting density[6] (Figure 2d). Addition of NaIO$_4$ is frequently proposed in the literature in order to act as an oxygen scavenger.[13,12,4] In our tests, we found that with properly degassed monomer solutions and with BP acting as an oxygen scavenger in the PDMS matrix beneficial effects from NaIO$_4$ are very limited. On the contrary NaIO$_4$ seems to negatively affect the graft polymerization both in terms of grafting density as well as in homogeneity (Figure 2e). We therefore refrain from adding NaIO$_4$ to the monomer solution.

In summary, we found that optimum grafting results for large channel structures can be achieved with a 20 wt % AA monomer solution, either pure or with minute quantities of benzyl alcohol, and an UV exposure for 5 min at about 30 mW/cm^2. For very small channels or narrow restrictions within the systems, if contaminants and their subsequent polymerization are present, the protocol can be adjusted by increasing the amount of benzyl alcohol or decreasing the monomer concentration accordingly (cf. Table 1).

Characterization of Grafted Layer. After UV exposure (Figure 1E), the monomer solution is flushed out and thoroughly rinsed, which leaves the PDMS channels with a grafted layer of hydrophilic PAA in the exposed areas, as depicted in Figure 1F. In this section, we report our findings on the achievable spatial resolution of the treatment, on the resulting surface quality, as well as on wettability.

We investigated the edge resolution of grafted PAA layers on a 100 μm square channel (Figure 3a). The mask was placed to cover the first 75 μm of the channel; the PAA graft was performed according to standard protocol and stained blue with TC. Figure 3a shows a blue-level plot along the channel where blue values are assumed to correlate with the grafting density. The grafted layer starts precisely at 75 μm where the masked area ended but the grafting density increases within the next 25 μm along the channel. It has been speculated in literature that activated triplet BP might diffuse into the dark regions and cause radical initialization in the masked area, hence creating a graft density gradient into the shadow area.[35] Although this process might occur on very small length scales, we deduce from our experiments that the major effect is oxygen diffusing into the exposed area from the dark regions and inhibiting radical initialization, hence creating a grafting density gradient beginning at the mask edge into the illuminated structure.

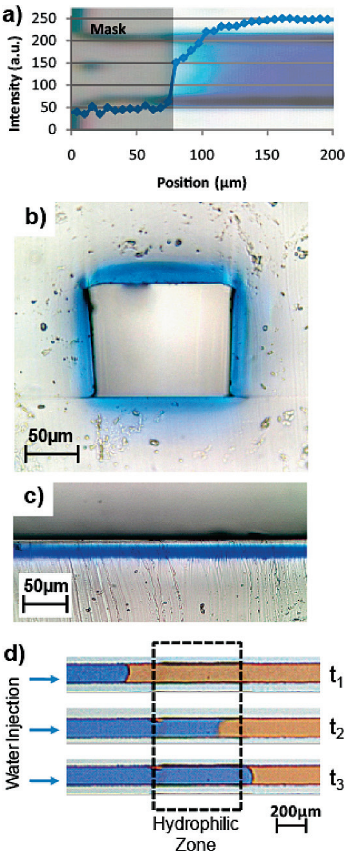

Figure 3. S(a) Partially grafted channel with PAA stained blue (background). Blue level plot along channel shows the start of the treatment precisely where mask was placed (at 75 μm). (b) Stained cross-section of PAA treated microchannel with proper protocol. (c) Treatment on large-cavity sample without degassing of monomer solution causes formation of buried PAA layer. (d) Time sequence of microchannel showing contrast in wettability between treated and untreated parts. Hydrophilic PAA grafts applied inside marked region. Water (blue) is slowly injected to replace oil (red). Time evolution clearly shows meniscus inversion inside treated zone.

We analyzed the penetration depth of the PAA graft on a stained cross-section as shown in Figure 3b. Standard treatment was performed on a 100 μm square channel with an UV dose of about 40 J/cm^2. The cross-section shows a deep penetration of PAA within the PDMS to depths up to 20 μm and more. It also shows a very good uniformity of the treatment on the top, bottom, and side walls (UV illumination from top). The uniform thickness of the grafted layer shows that the screening effect of the first layer of BP is negligible with the used illumination, which confirms our previous arguments (cf. the Supporting Information). Typically grafted layers of a few micrometers in depth are sufficient, which can be achieved already with a UV dose of only 15 J/cm^2. Cross-sectional studies were also performed on large-cavity samples. Figure 3c shows a sample treated with the standard protocol at an enhanced UV dose of 40 J/cm^2 but without degassing the monomer solution. As the figure shows, dissolved oxygen from the monomer solution has diffused into PDMS and inhibited grafting initialization before it was used up by BP. PAA graft formation occurred

---

(49) Schneider, M. H.; Tran, Y.; Tabeling, P. Benzophenone Absorption and Diffusion in PDMS and Its Role in Graft Photo-Polymerization for Surface Modification. Unpublished work, 2010.

(50) Kumlangdudsana, P.; Dubas, S. T.; Dubas, L. *J. Met., Mater. Miner.* **2007**, *17*, 67–74.

therefore only at a region about 6−7 μm below the surface, creating a buried layer with no effect on surface wettability. With a degassed monomer solution however, a grafted layer up to the surface can be easily achieved. Judging from Figure 3 it appears that PAA grows predominantly within the PDMS network. This hypothesis is supported by the FT-IR measurements (cf. Figure 2a), where the PDMS signature is still clearly visible in the top layer (methyl stretching band), despite a high grafting density of PAA. A surface study performed by optical profiling (see the Supporting Information) shows a small increase of up to 1 μm in surface height, probably cause by a bulging effect due to the increase in polymer density.

We measured the water contact angle to be 63 ± 7° on the dry PAA graft, which correlates well with the values reported in the literature between 58° and 65° for PAA chains grafted on PDMS[15,17,36,44] as well as for pure PAA thin films[40] under initially dry conditions. The resulting wettability contrast between treated areas and native PDMS has been investigated in a channel with patterned wettability as shown in Figure 3d. The figure shows the system at three discrete time intervals. The PAA graft has been applied within the dashed area. Water (blue) was slowly injected displacing the oil (red). The shape of the meniscus clearly shows that oil is wetting the native PDMS outside the treated area, as expected. However, wettability is instantly inverted inside the treated zone and causes the oil to dewet very rapidly until wettability reverts again outside the treated zone. Also, oil−water−PDMS contact angles were measured on larger PDMS samples immersed in water. Oil contact angles (hexadecane) for untreated PDMS were found to be 30 ± 10° while on PAA grafted surfaces oil was completely repelled (i.e., 180°). Contact angles were also verified on aged samples. For a PDMS sample with PAA treatment, which was stored under dry conditions for 6 months, we obtained an oil contact angle of 155 ± 10°. Although the contact angle is a little smaller as compared to a fresh sample, the PAA graft seems to be a very durable treatment, even after extended time periods. Additionally, the system shown in Figure 3d was left to age in oil for 1 month. After a thorough cleaning cycle (acetic acid, ethanol, water), the same meniscus inversion could qualitatively be observed, providing further evidence for the durable nature of covalently attached PAA brushes.

Application: Parallel-Flow Stabilization. As demonstration of the achievable resolution and quality, we show an example of the treatment used for parallel-flow stabilization. Such stabilized flow of a liquid next to another immiscible liquid is required for the application of liquid−liquid extraction. Figure S2 in the Supporting Information shows our system for parallel-flow stabilization; the treatment is applied along the wall guiding the aqueous phase while the remaining channel area is left hydrophobic to guide the oil. The system was tested for a number of different pressures. As shown in Figure S2 in the Supporting Information, the untreated system develops quick flow instabilities while the system with surface treatment allows a stable parallel flow for the same flow rates. Such stable flow is essential for applications like liquid−liquid extraction, and the example clearly shows the benefit of a well controlled wettability treatment with precise patterning capability.

Application: Double Emulsions. Another application which requires wettability patterning with precise spatial control is the synthesis of double or multiple alternate emulsions. Figure 4a shows an example for successful synthesis of water in fluorinated oil in water (W/O/W) double emulsions. In order for a stable emulsion to form, the continuous phase needs to wet the surface of the microchannel.[28,51] From the second flow-focusing structure on, the channel surface needs to be hydrophilic in order for water to form a stable outer phase, which was achieved by our treatment. Oil stops to wet the channel at the transition to the hydrophilic area (second flow-focusing structure), and water begins to form the outer phase allowing a stable double emulsion to form. More detailed information is given in Figure S3 in the Supporting Information.

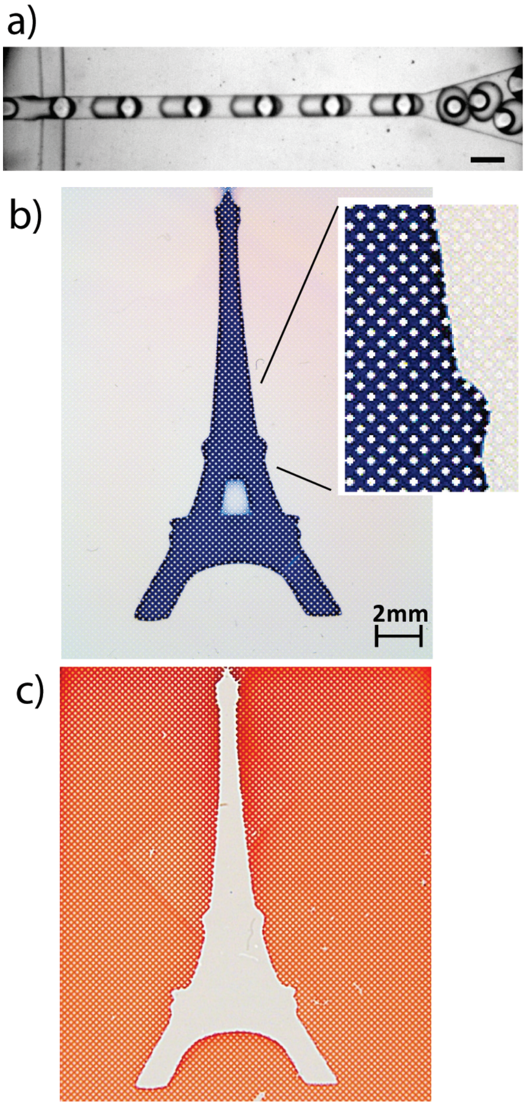

Figure 4. (a) Double-emulsion synthesis (water in oil in water) as an example for a simple dynamic system. Hydrophilic treatment from the second encapsulation on allows water to form a stable outer phase (black bar represents 200 μm). (b) Microfluidic channel network with hydrophilic PAA treatment pattern as a complex system example. Channels with hydrophilic treatment are revealed by blue stain. (c) Oil (red) injected into the network imbibes only untreated hydrophobic channels and thereby revealing the shape of the hydrophilic pattern. A video of the experiment showing the oil slowly imbibing the hydrophobic zones but sparing the treated channels appears in the HTML version of this paper.

---

(51) Dreyfus, R.; Tabeling, P.; Willaime, H. *Phys. Rev. Lett.* **2003**, *90*, 144505.

Application: Microfluidic Networks. Complex channel networks can be easily realized in PDMS in order to simulate porous media such as oil reservoir rock, for example. With such microfluidic networks it is then easy to study multiphase flow behavior and related parameters as the fluids can be observed directly in the channels (pores). Studies thus far were limited however to microfluidic systems of homogeneous wettability, while in real reservoir rock wettability is oftentimes heterogeneous and might even vary from pore to pore. We could successfully demonstrate patterning (i.e., wettability alteration) of selected channels and areas within the network. Figure 4b,c shows a network system containing a regular lattice of 20 000 individual channels ($80 \times 80 \times 220\ \mu m^3$) where an area in the shape of the Eiffel tower was subjected to hydrophilic treatment. The channels with hydrophilic PAA treatment are revealed in Figure 4c by the blue color of the TC stain. Oil (red) injected into the network does not enter the hydrophilic treated channels, hence revealing the shape of the treated area (Figure 4b). A more detailed view is given in Figure S1 in the Supporting Information. As this example shows, our treatment technique easily provides the required resolution to selectively change wettability of small structures within complex geometries.

CONCLUSIONS

We have identified a set of significant parameters which are crucial to successful wettability patterning by PAA graft polymerization of high quality. We have studied each parameter in detail in order to understand its influence and to provide a recommended value for optimum treatment (see Table 1). Some of the parameters were not considered or not mentioned in previously published works, and for some other parameters we could add detailed understanding of their influence and therefore identify more suitable values. Understanding the grafting process in detail is a key part to create a reliable and repeatable process. Our examples demonstrate that the technique can be easily and reliably applied to treat systems of complex geometry while yielding excellent spatial resolution and a high wettability contrast.

SUPPORTING INFORMATION AVAILABLE

Additional information as noted in text. This material is available free of charge via the Internet at http://pubs.acs.org.

Received for review June 9, 2010. Accepted September 21, 2010.

AC101345M

Wettability Patterning by UV-Initiated Graft Polymerization of Poly(acrylic acid) in Closed Microfluidic Systems of Complex Geometry

Marc H. Schneider[1,2,*], *Hervé Willaime*[1], *Yvette Tran*[1], *Fadhel Rezgui*[2],
Patrick Tabeling[1]

[1] *ESPCI, 10 rue Vauquelin, 75005 Paris, France.*
[2] *Schlumberger, 1 rue Henri Becquerel, 92140 Clamart, France.*
[*] *Corresponding Author*

Supporting Information

ABSTRACT

In the following supporting information we provide additional details on photo-initiator properties, on poly(acrylic acid) (PAA) graft layer characterization, and on optical resolution. In the 'photo-initiator properties' section we discuss and employ UV spectroscopy to investigate benzophenone (BP) adsorption, discuss BP application and diffusion as well as the effect of oxygen on the photo-initiation process. In the 'PAA graft layer characterization' section we discuss the employment of Fourier-transform infrared (FTIR) spectroscopy as a measurement tool for PAA graft density evaluation as well as optical surface profiling as a measurement tool for surface characterization. In the 'optical resolution" section we discuss the diffraction limit of the achievable resolution. In the figure section we present two additional examples for the application of the wettability patterning treatment: patterned wettability in microfluidic channel networks, and parallel-flow stabilization in micro-channels for liquid-liquid extraction. We also present more detailed material on double emulsion synthesis.

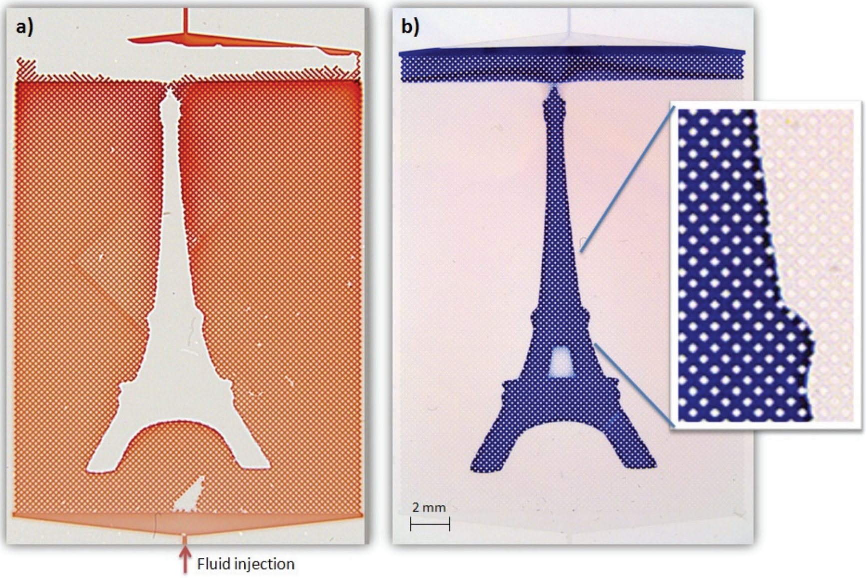

Figure S1: Microfluidic channel network composed of 20,000 individual channels (80 x 80 x 220 μm^3). An area in the shape of the Eiffel tower has been subjected to hydrophilic treatment. (a) The network is initially filled with water and oil (red) is slowly injected. As oil imbibes into the hydrophobic parts but is rejected from the hydrophilic zone, the shape of the Eiffel tower emerges. (b) After the experiment the system is flushed with a solution of TC in order to visualize the hydrophilic channels (blue). Channels filled with a transparent fluid lack sufficient contrast to be distinguished from the surrounding PDMS.

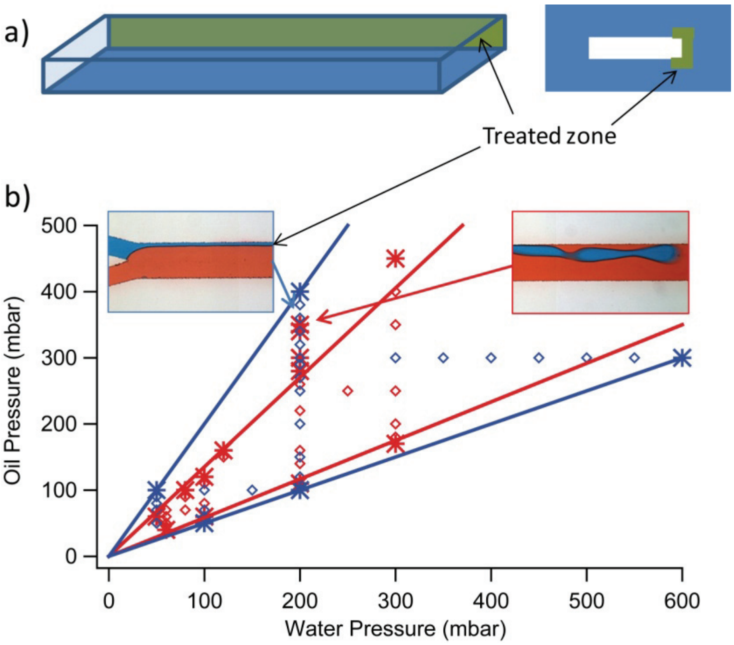

Figure S2: Parallel-flow stabilization in a PDMS micro-channel. (a) Schematic of the applied treatment: one of the sidewalls contains a hydrophilic PAA treatment in order to stabilize the aqueous phase. (b) Experimental results on parallel-flow stabilization for various applied water and oil pressures. Diamonds represent experiments where stable parallel-flow of the water- and oil phase occurred (c.f. left insert) while an asterisk marks an experiment with developing instabilities (c.f. right insert). Data obtained for a treated system (patterned wettability) are shown in blue while red data point represent experiments with an untreated system. Wettability treatment clearly expands the range of the stable parallel-flow regime.

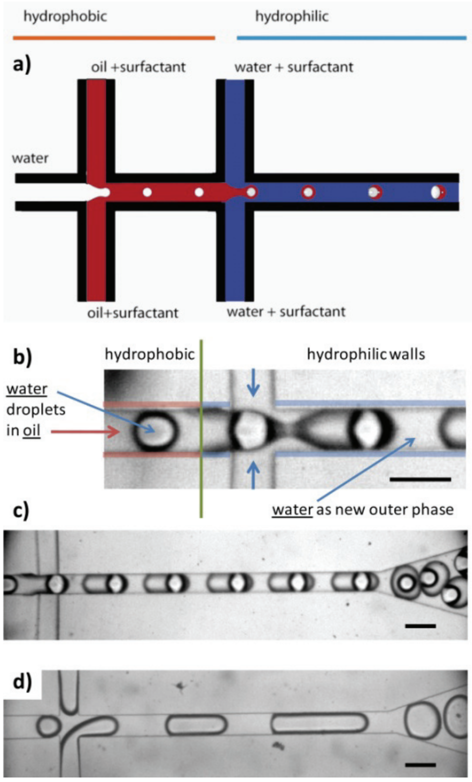

Figure S3: Double emulsion synthesis (water in oil in water). (a) Schematic layout of the microfluidic device: Two flow-focusing structures perform subsequent encapsulation. First, water (white) is encapsulated in oil (red) and then both are encapsulated in water again (blue). Micro channels up to the second flow-focusing structure need to be hydrophobic in order to support oil as continuous phase. From the second flow-focusing structure on, channels need to be hydrophilic in order for water to from the new continuous phase. Altered channel wettability is also indicated in the microscopic image of a real system shown in (b). (c) Shows the stable formation of double emulsion in a wettability-patterned system with the following experimental parameters: 5 µl/min pure water (white), 10 µl/min fluorinated oil + surfactant (red), and 15 µl/min water + surfactant (blue). (d) Control experiment of the same system with the same experimental parameters, but without patterned wettability (no surface treatment). As can be seen, a stable second encapsulation cannot be achieved. Black bars represent 200 µm.

PHOTO-INITIATOR PROPERTIES

UV spectroscopy.

UV absorption measurements were conducted on an 8453 UV-visible spectrometer from Agilent. Spectral data for each sample were recorded between 190 nm and 1100 nm with a resolution of 1 nm. Liquid samples were introduced into the spectrometer in a quartz cuvette with 2 mm path length. A background reference spectrum was taken prior to each measurement with the empty cuvette in the beam path. PDMS samples were introduced directly into the spectrometer as flat stripes of 2 mm thickness. Background reference spectra for these samples were taken with an empty sample chamber. PDMS samples were typically handled as larger pieces during sample preparation, e.g. during immersion in BP solution. A center part was then cut out afterwards and used for spectroscopic analysis in order to avoid artifacts caused by additional imbibition along the original edges of the sample.

Benzophenone adsorption and diffusion.

Detailed understanding of BP adsorption and diffusion in PDMS is crucial for a successful surface treatment protocol. We employed UV spectroscopy as well as a new visualization technique to study the interactions of

BP with PDMS. BP possesses an absorption band overlapping with the mercury i-line (365 nm) which makes it an ideal candidate for UV activation with a mercury lamp. In addition, this band lies outside of the absorption range of acetone and therefore acetone can be used as solvent without negative screening effects (Figure S4). Since PDMS is transparent for wavelength down to 300 nm and below, UV spectroscopy can be used to detect and quantify the amount of adsorbed BP as the spectra in Figure S4 show.

In addition we studied the spatial location (depth profile) of the absorbed BP and its diffusion over time. For this study we used strong UV excitation and a green emission filter to capture weak photoluminescence signal emitted by an intermediary product (In) in the relaxation process of the BP radicals. This photoluminescence signal is produced after activated BP molecules have successfully undergone hydrogen abstraction and provides direct evidence for the presence of BP. The technique was recently developed in our laboratory, a detailed discussion about the technique and more general results will be published elsewhere[1]. Table S1 lists the results of an imbibition study of BP into PDMS. A solution of 10 wt% BP in acetone was applied to a micro-channel under constant flow for 10 minutes. Imbibition depth was probed at discrete time steps and the reported depth values represent the distance from the channel wall into the PDMS where the phosphorescence signal of the BP intermediary could be observed. Solution application was stopped and the channel was flushed with air after 10 minutes. However, BP diffusion was monitored for another hour. While the absolute error is estimated to be up to 10%, relative deviations within a series of measurements are small and the data points follow tightly a square-root law. After BP application is stopped (after 10 minutes) diffusion continues at a significant rate as can be seen in Table S1. This diffusion causes the BP concentration to decrease drastically, which manifests in a decrease in photoluminescence in our experiments and in a decrease of free radical generation during the grafting process in general. After one hour, the obtained phosphorescence signal was already very weak. It is therefore absolutely essential to consider BP diffusion and limit the waiting time between priming and graft initialization in the surface treatment protocol.

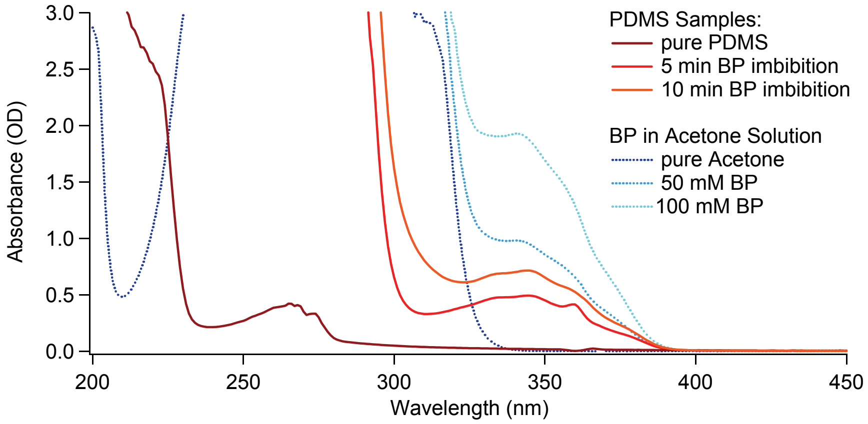

Figure S4: UV absorption spectra for samples of 2 mm path length. The dotted set of curves shows BP solutions in acetone and pure acetone as reference. The solid curves show a native PDMS sample as well as samples imbibed with BP solution.

Table S1: Benzophenone imbibition into PDMS from a 10 wt% solution injected into a micro-channel. The imbibition depth measures the distance from the channel wall into the PDMS where the phosphorescence signal of the BP intermediary could be observed. The first six data points were taken while BP solution was continuously applied; for the last three data points BP solution was removed and the channel kept dry.

Time (s)	Depth (µm)	Condition
30	121	Constant flow of BP solution
60	176	
120	245	
180	304	
300	390	
600	549	BP solution removed
660	580	1 min after
2400	1061	30 min after
4200	1328	60 min after

Application of photo-initiator.

One critical parameter related to the priming process is the waiting time between priming and graft initiation, which needs to be well controlled and kept at short time intervals (less than half an hour) in order to ensure a sufficiently high BP concentration close to the surface. However, we found that a certain waiting time (typically 10 minutes during vacuum drying) is beneficial as it allows the BP concentration to homogenize through diffusion, and in addition, degassing of the PDMS matrix facilitates filling the system with monomer solution in the subsequent step, in particular for complex systems (networks) where trapping of air bubbles can occur. Moreover, we have observed that even small crystalline BP deposits, which might occur during flushing, diffuse into the PDMS matrix during vacuum drying. However, contradictory to other reports found in literature we refrain from flushing BP solution with water. In particular in large cavities, if water is used for flushing, mixing can occur between the BP solution and the injected water, which causes BP to crystallize and fall out of solution in large quantities. This uncontrolled BP precipitation can best be avoided if BP is dissolved in pure acetone and flushed out by air injection only.

Photo-initiator quenching by oxygen.

The presence of molecular oxygen significantly lowers or completely inhibits the hydrogen abstraction of BP depending on its concentration[2,3], as it quenches triplet BP very efficiently[4,5], and can also cause photo-bleaching of BP[6,7]. However, by quenching and photo-bleaching BP, oxygen is consumed at a significant rate as well[8]. If BP is present at sufficiently high concentrations it acts therefore as oxygen scavenger during initial exposure and creates an oxygen sink before PDMS radicalization through hydrogen abstraction starts. However, if BP concentration is too low or if oxygen is replenished through diffusion quickly enough, radicalization of PDMS will be completely inhibited and graft polymerization does not take place. It is therefore obvious that the supply of fresh oxygen through the both pathways mentioned above needs to be blocked or at least limited in order to obtain good grafting results. Oxygen diffusing through PDMS towards the oxygen sink is certainly causing constant radicalization inhibition in a certain border area. However, we can easily implant BP at significant depths within the PDMS. Then, the portion of BP buried deep behind the channel wall consumes or screens the oxygen well before it reaches the reaction site and therefore effectively shuts down oxygen influx through the PDMS matrix.

More critical, on the other hand, is the presence of dissolved oxygen in the monomer solution as in this case the oxygen limits or inhibits PDMS radicalization right at the surface where graft polymerization is desired. We have performed experiments of the entire graft process with identical parameters but the monomer solution with or without degassing prior to use. We found that the removal of dissolved oxygen from the monomer solution prior to use through degassing provided a significant increase in grafting efficiency.

CHARACTERIZATION OF PAA GRAFT LAYER

ATR-FTIR spectroscopy.

Infrared absorption spectroscopy was performed on a Tensor27 Fourier Transform Infrared (FTIR) spectrometer from Bruker with a diamond crystal Attenuated Total Reflection (ATR) probe head. Large rectangular channels (cavities) of dimension 0.3 x 5 x 15 mm^3 were prepared, graft polymerization was performed according to protocol, and cut-outs from the cavity were used as samples for analysis and brought into contact with the diamond ATR crystal at the area of interest. The spring-loaded fixation bold was always fully closed in order to achieve constant terminal pressure between sample and crystal probe. The spectral data for each sample were recorded between 4000 cm^{-1} and 950 cm^{-1} in steps of 2 cm^{-1} as an average of 50 individual measurements. Sample preparation through treatment within large channel cavities was chosen in order to mimic the treatment in closed systems with limited and sealed-off monomer solution and the simultaneous treatment of multiple walls while at the same time the samples were large enough to be easily and reliably placed on the ATR crystal probe.

Graft-polymerization characterization via ATR-FTIR spectroscopy.

Resulting PAA graft efficiency was tested on cavity systems and analyzed via FTIR-ATR. Starting from large wavenumbers PDMS has its first significant absorption band at 2950-2970 cm^{-1}, which corresponds to asymmetric –CH3 stretching in ≡Si-CH3 group, and is then transparent down to the symmetric –CH3 deformation band in ≡Si-CH3 group at 1245-1270 cm^{-1} [9]. PAA can be easily detected on and distinguished from PDMS substrate due the characteristic absorption of the carboxylic acid groups. The broad absorption band of the -OH stretch in -COOH at 3350-2500 cm^{-1} [10] gives a clear indication of the presence of hydrophilic carboxylic acid groups. Quantification can then be done easily for the sharp and intense band at 1725-1700 cm^{-1}, which corresponds to the -C=O stretch in –COOH [11]. This carbonyl absorption peak is therefore used as a characteristic measure for the grafting quality. Stained cross-sections have revealed that the formation of PAA within the PDMS matrix is typically significantly deeper than 1 µm. Since the ATR probe of the spectrometer is probing only the first micron below the sample surface, we consider the IR absorbance at the carbonyl band to be a qualitative measure for graft density rather than for graft thickness. Therefore, absorbance values are used to indicate grafting density in the following study.

FTIR measurements for each graft-polymerization treatment (each data point in Figure 2, main text) were obtained at three different spots. For homogeneous treatment results (indicated by blue markers) the variation in the measured absorption values was less than ±5% in all cases (indicated by error bars). For some choices of parameters the resulting treatment was inhomogeneous and patchy (indicated by red markers), with variations in the FTIR absorption of ±10% (error bars) or even patches without any treatment. Subsequent visualization of treatment via staining confirmed the inhomogeneous, patchy nature for treatments indicated by red markers (Figure 2, main text). Horizontal error bars indicate the uncertainty in the mixing ratio of the prepared monomer solutions.

Optical surface metrology.

Surface topology of grafting results was characterized with a Wyko NT9100 Optical Profiling System from Vecco. This non-contact three-dimensional surface metrology technique allows for quick analysis of the surface topology of the grafted samples even at the bottom of the structured channels due to microscopic objectives with long working distances. Possible optical magnifications of the instrument are 5.5X, 10X, 27.5X and 50X. The samples were typically measured in high definition vertical-scanning interferometry (HDVSI) mode, which is a phase demodulation single-measurements technique based on white light interferometry. With the 50X magnification the HDVSI mode provided a depth resolution of 50 nm. Subsequent data analysis was performed with the software package Vision 4.10 also supplied by Vecco.

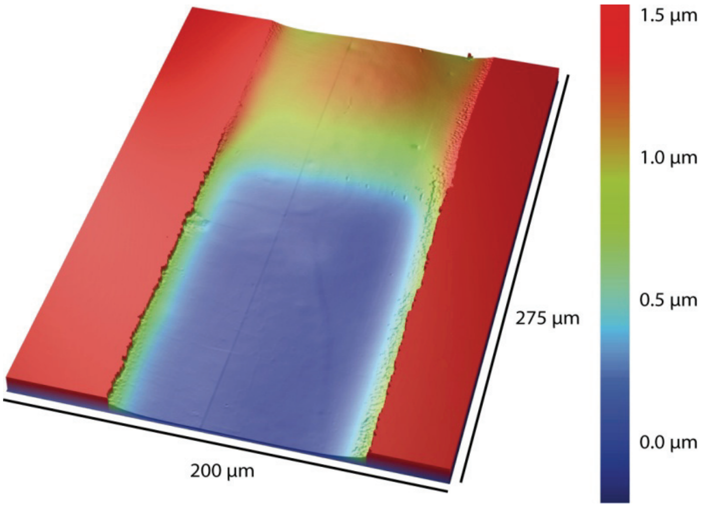

Figure S5: Surface topology of a microfluidic channel measured by optical surface profiling around the border between treated and native PDMS.

Graft-polymerization treatment on a partially masked 100 × 100 µm^2 channel was performed (c.f. Figure 3). The channel was cut open and the border area between the treated and untreated part was investigated in detail by optical surface profiling. Figure S5 shows the optical surface profile: The surface profile changes in the treated area; the height of the channel floor increases by about 1 µm at the center of the channel wall. Judging from the shape it appears to be a bulging effect caused by the increased polymer density due to the added PAA chains. However, compared to the channel dimensions the chance in height is less than 1%, and probably does not affect most applications.

OPTICAL PERFORMANCE

The main focus of the present study lies on surface treatment within enclosed microfluidic capillaries and structures. If the surface wettability of a segment of a microfluidic channel shall be modified, a critical parameter is the achievable resolution between the treated and untreated part of the channel. This edge resolution needs to be achieved evenly on all four surfaces of the channel: bottom, top, and side walls. If the channels and microstructures have a substantial depth (e.g. 100 µm channel, c.f. Figure 3, main text), the best approach is UV exposure with collimated light in order to achieve a uniform treatment edge both at the bottom and the top surface of the structure. For very shallow structures a focused exposure might be considered as well, which provides the option of placing the mask within the lens assembly of the focusing device. However, for all our experiments we have employed collimated UV exposure for compatibility with deep structures.

For exposure with a collimated beam through a mask the distance between the mask and the object plays an important role since diffraction effects cause the resolution to degrade. If we assume a monochromatic light source and the illumination with a collimated uniform beam (i.e. plane wave of unit amplitude) we can model the resulting light intensity behind an aperture with a Fresnel diffraction model. For a slit of width $2w$ and infinite length the intensity distribution in a plane behind the slit at a distance z is given by[12]:

$$I(x) = \frac{1}{4}\{[C(\alpha_2) - C(\alpha_1)]^2 + [S(\alpha_2) - S(\alpha_1)]^2\} \qquad \text{(S1)}$$

with the Fresnel integrals $C(\alpha)$ and $S(\alpha)$, and the arguments $\alpha_1 = -\sqrt{2/\lambda z}\,(w + x)$ and $\alpha_1 = \sqrt{2/\lambda z}\,(w - x)$ with the wavelength λ. The Fresnel integrals are defined as $C(a) = \int_0^a \cos(\pi \cdot t^2/2)dt$ and $S(a) = \int_0^a \sin(\pi \cdot t^2/2)dt$.

The UV light source employed in our study contained a beam homogenizer and collimator and a band-pass filter around the mercury i-line (λ = 365 nm). With this particular wavelength and an assumed slit width of $2w$ = 1 mm, eq. S1 was evaluated for several mask distances z as shown in Figure S6. For our studies we typically fabricated microstructures embedded in 2 mm PDMS on either side and placed the photo mask in direct contact with the PDMS chip (i.e. mask distance z = 2 mm) which results in an UV intensity gradient of about 20 µm in width around the edge of the mask. This intensity gradient is a main cause for our typical resolution of 25 µm (c.f. Figure 3a, main text). However, in many cases the thickness of the PDMS layer at least on one side can be significantly lowered and resolution increased (c.f. Figure S6). In particular for systems containing small channels, less PDMS support structure is required, which allows for thinner systems and increased resolution.

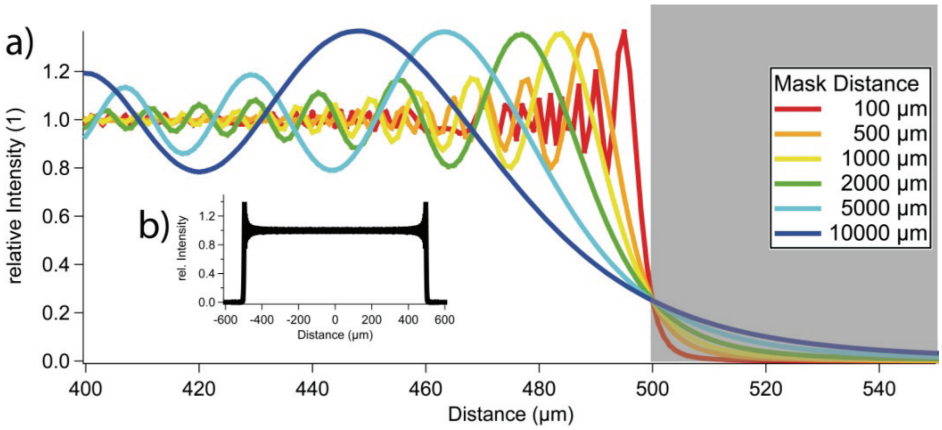

Figure S6: Calculated light intensity distribution behind a wide slit mask at several distances behind the mask (mask distance) for collimated illumination at a wavelength of 365 nm. (a) Detail view close to one of the edges. The beginning of the masked area is outlined in grey. (b) Intensity profile for 100 µm mask distance showing the full slit width of 1 mm.

References

1. Schneider, M. H.; Tran, Y.; Tabeling, P. Benzophenone Absorption and Diffusion in PDMS and Its Role in Graft Photo-Polymerization for Surface Modification. *Langmuir* **2010**, DOI: 10.1021/la103345k.
2. Gorman, A. A.; Rodgers, M. A. J. *J. Am. Chem. Soc.* **1986**, *108*, 5074-5078.
3. Drake, J. M.; Levitz, P.; Turro, N. J.; Nitsche, K. S.; Cassidy, K. F. *J. Phys. Chem.* **1988**, *92*, 4680-4684.
4. Arai, T.; Nishimura, Y.; Sasaki, M.; Fujita, H.; Matsuo, I.; Sakuragi, H.; Tokumaru, K. *Bull. Chem. Soc. Jpn.* **1991**, *64*, 2169-2173.
5. Nau, W. M.; Scaiano, J. C. *J. Phys. Chem.* **1996**, *100*, 11360-11367.
6. Hutchinson, J. A.; DiBenedetto, J.; Rentzepis, P. M. *J. Am. Chem. Soc.* **1986**, *108*, 6517-6521.
7. Coyle, J. D. Introduction to Organic Photochemistry; John Wiley & Sons: Great Britain, 1986; pp 69-72, Chapter 2.
8. Goerner, H. *Photochem. Photobiol.* **2006**, *82*, 801-808.
9. Efimenko, K.; Wallace, W. E.; Genzer, J. *J. Colloid Interface Sci.* **2002**, *254*, 306-315.
10. Pretsch, E.; Buehlmann, P.; Affolter, C. Structure Determination of Organic Compounds - Tables of Spectral Data, 3rd ed.; Springer Verlag: Heidelbewrg Germany, 2000; pp 286-303, Chapter 6.
11. Gokel, G. W. Dean's Handbook of Organic Chemistry, 2nd ed.; McGraw-Hill: New York USA, 2004; pp 30-35, Chapter 6.
12. Goodman, J. W. Introduction to Fourier Optics, 2nd ed.; McGraw-Hill: New York USA, 1996; pp 84-87, Chapter 4.

2.2.2 *Additional Comments on PDMS Devices and Surface Treatment*

During surface treatment PAA seems to grow predominantly within the PDMS matrix as mentioned in the previous section. The thickness, or penetration depth, of the treatment is controlled by UV intensity and exposure time. An example is shown in Figure 2.7 for PAA treatment with various exposure times. In the cross–sections stained with toluidine blue, the presence of PAA is revealed by the blue color, showing a clear increase in penetration depth with UV exposure time. In general, UV exposure time needs to be sufficiently long in order for a homogeneous closed PAA coating to form (c.f. sub–section 2.2.1), which provides the desired surface properties (e.g. hydrophilicity). Reasonable overexposure can help to ensure a closed coating although increased penetration depth does not further alter the surface properties.

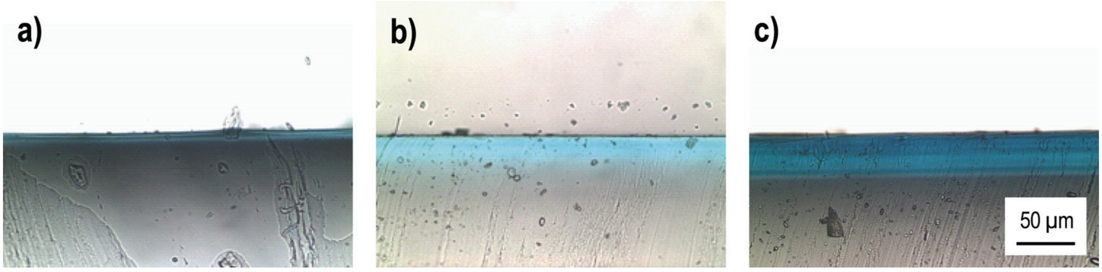

Figure 2.7: Stained cross–sections of treated PDMS showing different penetration depths of the PAA treatment. The presence of PAA is revealed by the blue color of the stain. Treatment was performed by UV exposure at 55 mW/cm^2 for (a) 2 min, (b) 5 min, (c) 10 min.

Excessive overexposure, however, can have a negative impact on the surface properties and needs to be avoided. It was found that for very long exposures yielding very deep PAA penetration, micro–cracks appear on the treated surface, in particular if treatment is applied to a large area. Treatment on a flat PDMS surface with 10 min UV exposure yielding almost 50 μm penetration depth (c.f. Figure 2.7c) was closely inspected with a 3D optical surface profiler[12] as shown in Figure 2.8. The 3D profile shows a rough surface covered with micro–cracks (Figure 2.8a), around 100 µm in size and up to 3 µm deep (Figure 2.8b). A micrograph obtained by an optical microscope with dark field illumination is shown in Figure 2.8c.

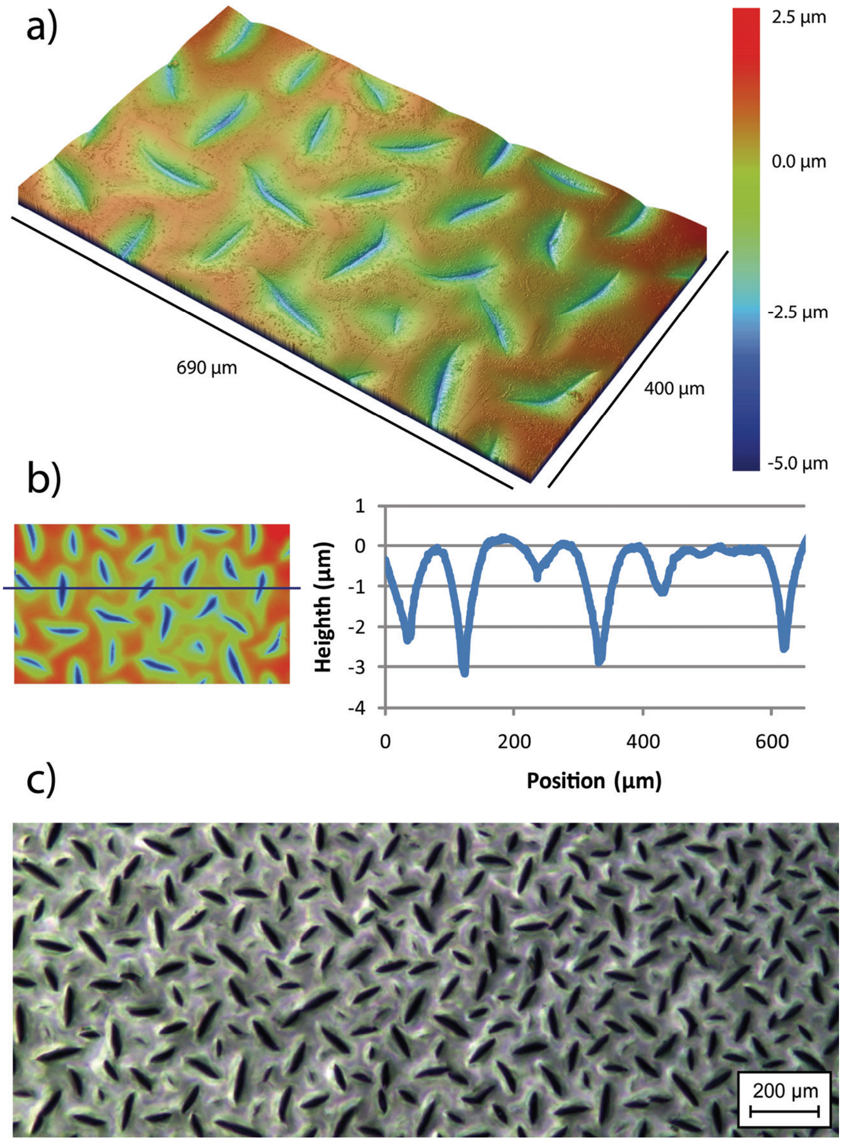

Figure 2.8: Surface analysis of excessively treated PDMS surface showing micro cracks. (a) 3D surface profile plot. (b) Depth profile across the surface as indicated by the black line. (c) Optical dark–field image of the surface.

---

[12] Wyko NT9100 Optical Profiling System, Vecco High Performance Engineering Inc., Columbia Station, Ohio.

These micro–cracks imply significant tensile stress within the treated surface. PAA is grafted on (i.e. covalently tethered to) PDMS while immersed in an aqueous phase. It is speculated that tensile stress is caused by the shrinkage of the graft layer during drying after the treatment. However, with reasonably long exposure times thick coatings of uniformly high quality can be created without the risk of micro–cracking.

Native, untreated PDMS surfaces can also show significant roughness as shown for example in Figure 2.9a. This ‘roughness’ of the channel sidewalls originates in the resolution limit for the ink–printed foil masks (dot matrix printing). The fuzzy edges on the foil masks are then reproduced by the soft lithography process and cause surface roughness as shown in the figure. Such surface roughness or surfaces defects are known to cause pinning of the contact line [**57**], [**66**], [**67**], e.g. for water injected into a dry channel (Figure 2.9a). In particular ridges perpendicular to the flow direction as present due to mask defects are known to cause significant pinning [**159**].

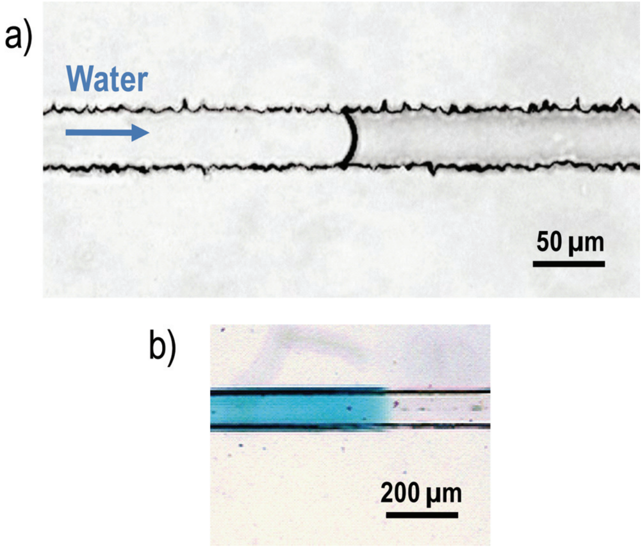

Figure 2.9: PDMS microchannels. (a) Water is injected in a 40 × 40 μm^2 channel in a PDMS chip with ‘rough’ walls. (b) 100 × 100 μm^2 channel with partial hydrophilic surface treatment (blue).

These pinning effects can significantly interfere with the desired fluid front behavior controlled by wettability pattering. A partially treated channel as shown in Figure 2.9b for example, can be seen as a type of capillary burst valve (CBV) [**58**], [**160**], [**161**], based on the change of surface energy (wettability) [**162**]. The efficiency of the stop valve is given by capillary pressure at the wettability transition zone according to eqn. 1.5 for a mean curvature according to eqn. 1.8. For an initially dry system as shown in Figure 2.9b, water would imbibe spontaneously into the treated, hydrophilic part (blue) for a contact angle of θ_w = 60°. The water front would stop at the beginning of the non–wetting untreated part as now a positive driving pressure is required according to eqns. 1.5 & 1.8 (positive curvature) for θ_{nw}= 108°.

For typical channel sizes in the range of several tenths of microns, this pressure difference is small[13] (several mbar) and pressure differences required to overcome pinning were found to be in the same range for systems made with foil masks. However, systems made with chrome mask yield smooth walls and show no or only little disturbance due to pinning. It was experimentally verified that the required driving pressures in PDMS channels made from chrome masks follow theoretical values within a 10% error margin.

In order to avoid any unnecessary disturbances from excessive pinning phenomena, the microfluidic networks as introduced in section 2.3.1 were made with chrome masks. As an example, Figure 2.10 shows a comparison of a microfluidic network segment made with (a) an ink–printed foil mask and (b) a high–resolution chrome mask (b).

---

[13] E.g.: $\Delta p = 6\text{mbar}$ for $w = h = 40\mu\text{m}$ and $\gamma = 72\,\text{N/cm}$.

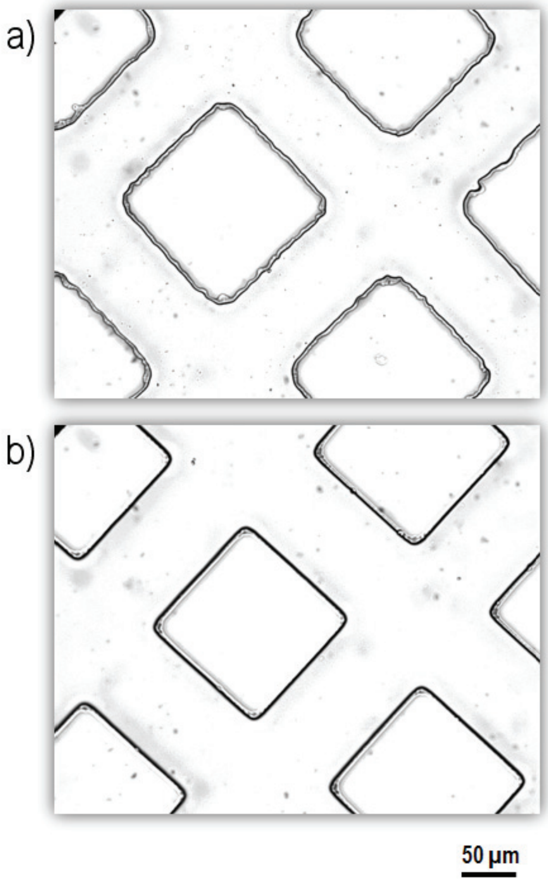

Figure 2.10: Microscopic images of a PDMS microfluidic network. PDMS was cast from a master made with (a) ink–printed foil mask and (b) chrome mask. The sections show 6 pillars with the surrounding channels.

2.3 Application of Surface Patterning

Applications for surface patterning are vast. In the field of biology, biochemistry and life science, functionalized, patterned surfaces are of great interest for applications requiring the separation or immobilization of biomolecules, such as enzyme microreactors, immunoassays, genomic analysis, and cell manipulations to name a few [**135**], [**122**]. A recent review on patterned surfaces for biomolecular manipulation [**163**] compares eleven manipulation techniques and lists classical microfluidics (without sophisticated patterning) as one of the two dominant techniques[14] with the only disadvantage being limited pattern geometries. It is apparent that well controlled surface patterning within microfluidic systems, i.e. the combination of surface chemistry, patterning and microfluidics, will have a powerful impact in the field [**164**].

Great demand for precise surface patterning in microfluidic systems exists in the field of chemistry as well. For separation, synthesis, processing or in the field of analytical chemistry, microfluidic devices are frequently used, employing both continuous microflows and droplet based (digital) microfluidics [**59**]. In both cases surface patterns are essential for many applications in order to stabilize and guide the flow properly. For continuous microflows, for example, parallel–flow stabilization supported by surface patterning is essential for continuous–flow liquid–liquid extraction applications [**165**], [**166**], [**167**], [**168**], [**169**], as already discussed in the article reproduced in (section 2.2.1). Another example for parallel–flow stabilization is shown in Figure 2.11 where water is flowing in between two streams of oil, providing twice the surface area for extraction. Wettability patterning is also an effective measure to create or significantly improve an existing capillary stop valve [**58**], [**162**], which allows for pressure controlled movement of fluid slugs in the microfluidic device. In particular the applicability of wettability treatment for complex microfluidic structures might be of great potential to microfluidic large–scale integration chips as well [**170**].

In droplet based microfluidics, wettability pattering plays a crucial role for multiple emulsion encapsulations [**171**], [**172**], [**173**], droplet fusion [**174**], etc. The requirement for stable droplet transport is a wetting condition of the continuous phase with respect to the channel walls [**66**], [**67**]. An example of successful water–oil–water double–emulsion encapsulation was shown in the article (section 2.2.1), enabled by patterning channel wettability along the different encapsulation stages [**68**], [**69**], [**175**].

---

[14] Ranking by number of references is 2008: ‘Contact and non-contact printing’ with 6032 references, ‘Microfluidics’ with 1824 references followed by ‘Photolithography’ with 328 references [**163**].

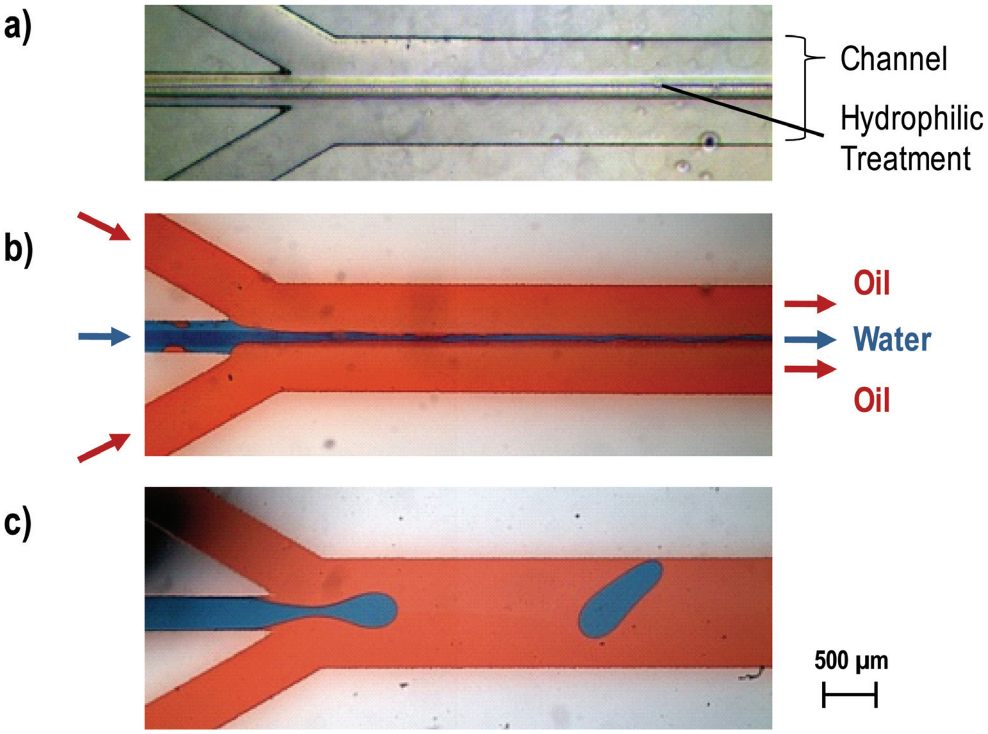

Figure 2.11: Parallel–flow stabilization example for liquid–liquid extraction. (a) Phase contrast image of microfluidic channel (empty) showing a strip of hydrophilic treatment along the center top and bottom wall. (b) Fluid injection of oil (red), water (blue), and oil show a stable parallel flow due to surface treatment. (c) Experiment performed under the same condition but without surface treatment shows severe instabilities.

Wettability patterning is also of significant importance for fundamental research in the field of physics and fluid mechanics, which is the main application of this work. Multiphase flow behavior is studied in microfluidic networks with patterned wettability and the influence and the impact of such wettability patterns on the flow behavior are investigated in detail, as described in the following section.

2.3.1 *Main Application: Wettability Patterning in Micromodels*

Microfluidic channel networks (micromodels) have been used for many years for experimental studies on multiphase flow phenomena in porous media [**11**], [**14**], [**7**], [**176**]. Detailed understanding of fluid transport, in particular for water–oil systems is of great interest for the petroleum industry, as discussed in the introduction. However, studies were limited to porous media of uniform wettability due to technological limitations, and experiments were performed for either wetting case (imbibition) or non–wetting case (drainage) with respect to the invading phase [**21**]. With the new wettability pattering technique, multiphase flow behavior can now be investigated for the first time in microfluidic networks of patterned wettability with well controlled geometry and surface properties at high spatial resolution.

The capabilities for wettability pattering in complex systems with high spatial resolution are shown in Figure 2.12. A microfluidic network composed of a square lattice of microchannels between 50 – 100 µm in size (Figure 2.12b) is subjected to wettability patterning treatment. A custom–designed UV mask (Figure 2.12c) provides a set of particular openings (yellow areas) allowing for exposure of individual channels (Figure 2.12a). Successful treatment of the exposed channels is revealed by the blue stain in the microscopic image (Figure 2.12d).

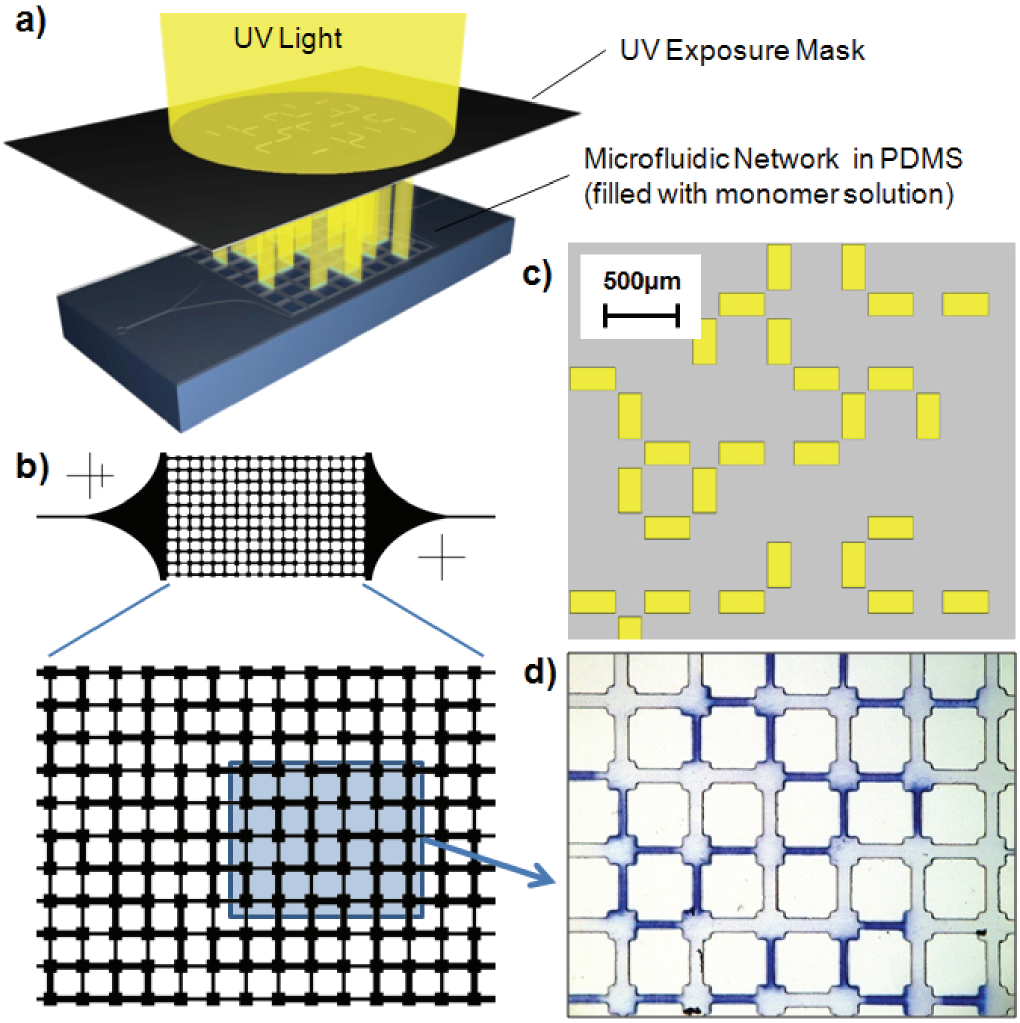

Figure 2.12: High–resolution wettability patterning in microfluidic channel networks. (a) Schematic outline of the treatment process: individual channels are exposed to UV light through a particularly designed slit mask. (b) Schematic of the employed network. (c) Schematic of the employed mask: yellow areas indicate openings in the mask. (d) Microscopic image of a real network with patterned wettability on an individual channel level. Hydrophobic channels appear blue due to staining.

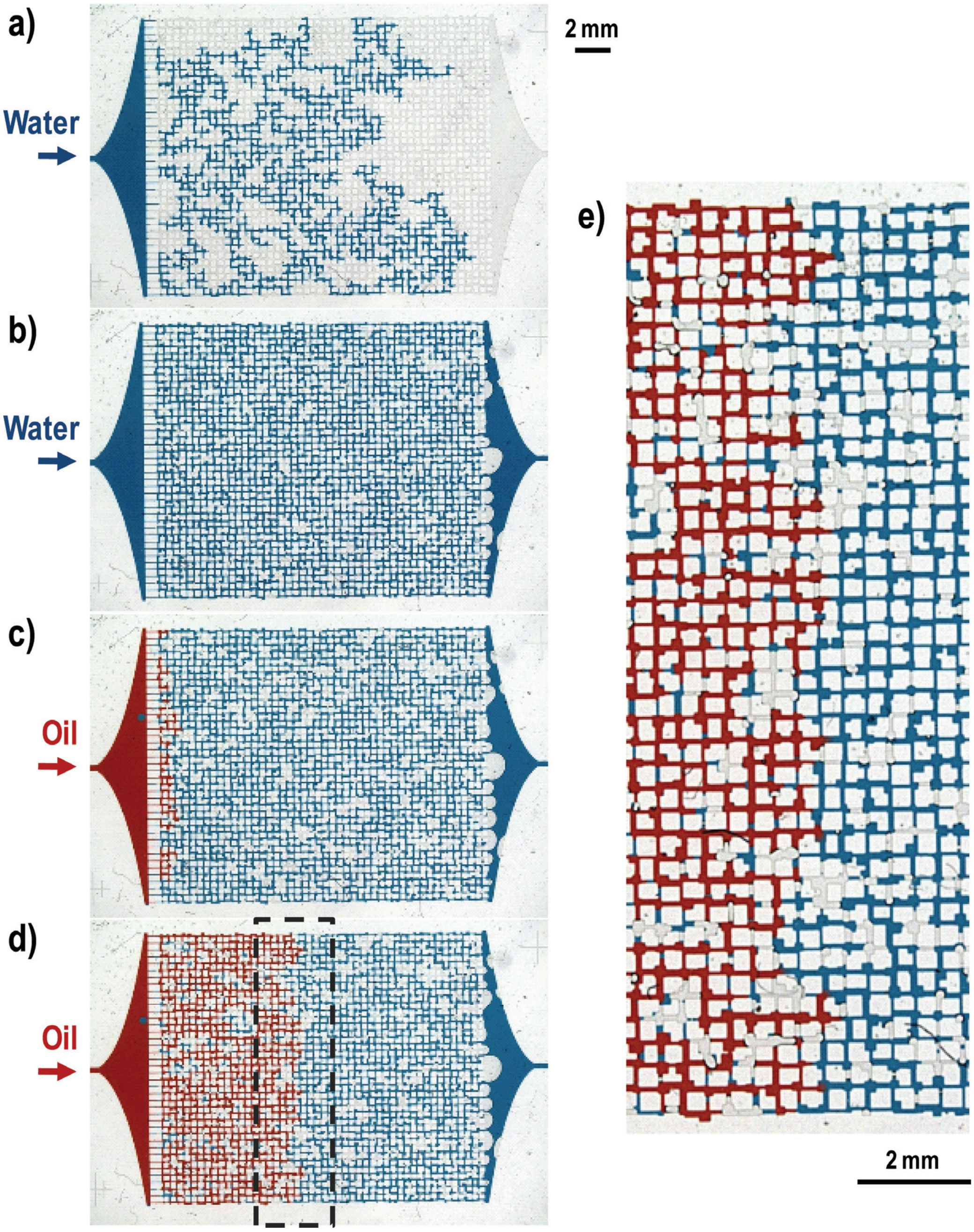

Figure 2.13: Fluid injection in a hydrophobic, oil–wet micromodel made of PDMS. Water (blue) is injected first, followed by oil (red). Some gas (air) remains trapped in the channels during the experiment.

Figure 2.13 shows a ‘classical example’ for multiphase flow in a complex micromodel with homogeneous wetting properties. Briefly, the micromodel is composed of 4000 microchannels with random width distribution between 50 – 150 µm and a depth of 75 µm. The micromodel is made of untreated PMDS, which is hydrophobic and oil–wet. Aqueous phase dyed with brilliant blue is slowly injected into the network (Figure 2.13a). Since water is the non–wetting phase, a percolation–like flow pattern emerges, caused by capillary fingering. After steady state flow is established, most of the pores are filled with the aqueous phase; however some air remains trapped (Figure 2.13b). The injection cycle is continued by injection of mineral oil dyed with the dye Oil Red (also known as Sudan IV) at the same flow rate (Figure 2.13c). Since oil is the wetting phase, invasion occurs as a flat frontal advance (Figure 2.13d). Even for imbibition with flat frontal advance, trapping of the initial phase (here: water and air) can occur to some degree (Figure 2.13e). In this particular example the viscosity ratio was balanced ($M = 1$) by adding glycerol to the water phase in order to match the oil viscosity of 15 cP.

One of the main applications for wettability patterning in complex micromodels was the study of multiphase flow behavior in such systems with respect to the fraction of treated channels f_w. Figure 2.14 shows a segment of a water–filled micromodel during oil injection (red) at two discrete time steps. 60% of the channels are oil–wet (bright shades) while 40% of the area has been rendered water–wet by surface treatment ($f_w = 0.4$). The experiment shows oil quickly invading accessible oil–wet areas (light shades) while avoiding water–wet channel clusters (dark shades).

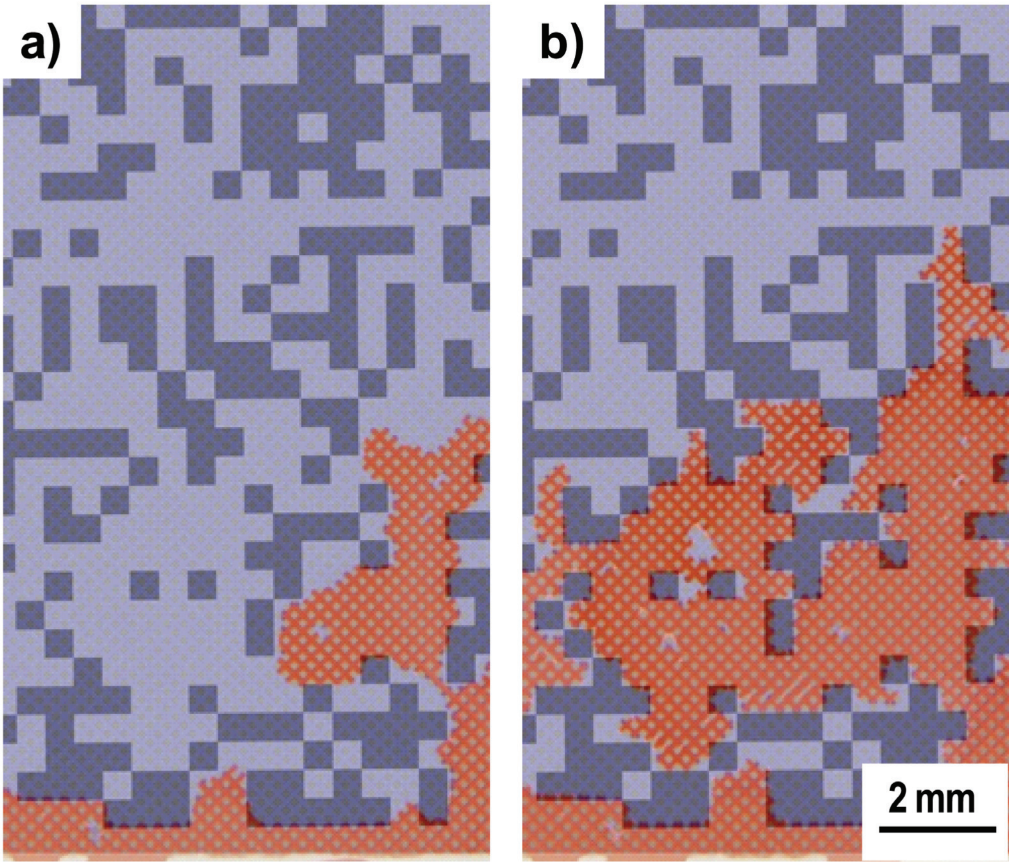

Figure 2.14: Segment of a micromodel with patterned wettability at different time steps during oil (red) injection. The micromodel composed of a regular crisscross channel lattice is initially filled with water (transparent). The images show an overlay of the actual microscopic images with an indication map of the applied surface treatment. Dark shades indicate water–wet areas.

The micromodel shown in Figure 2.14 is made of a regular lattice composed of uniform channels in a crisscross arrangement (Type I). Other network types with geometric irregularities are used as well. Figure 2.15 shows an overview of the three main network types as used in the present work. More detailed information on the different network types and their properties is given in Appendix B.

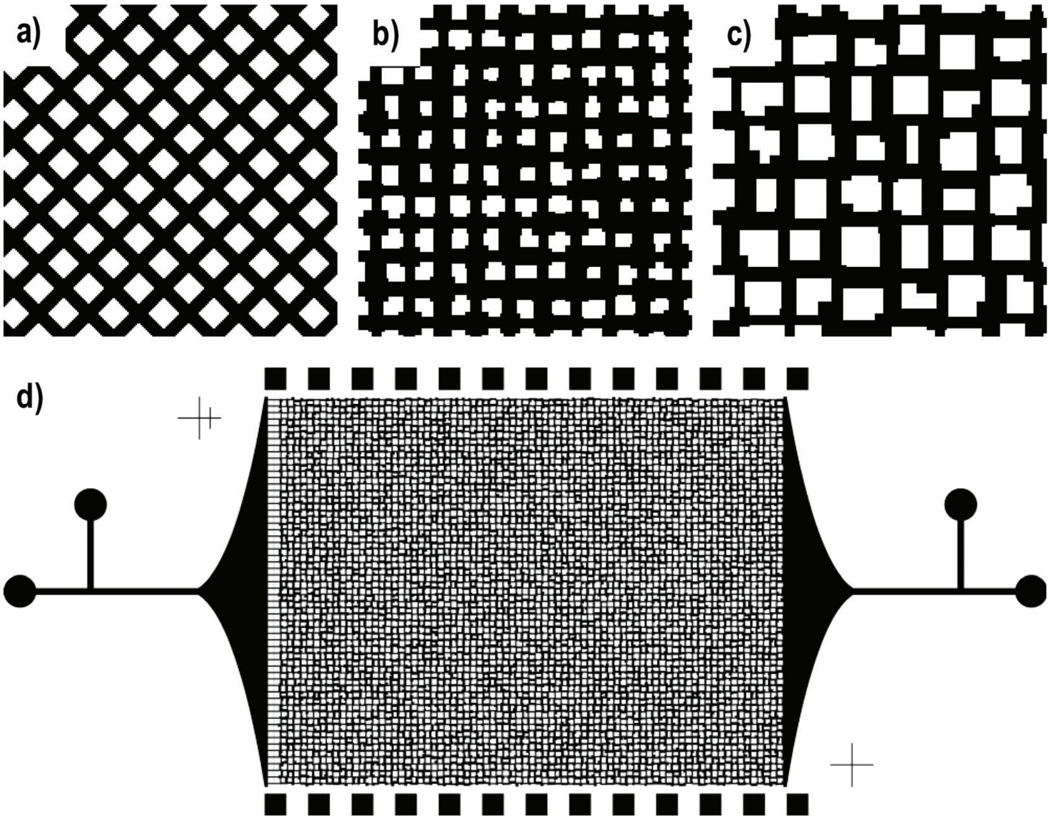

Figure 2.15: Design of the three main network types as used in this work: (a) Type I, (b) Type II, (c) Type III. (d) Overall network design with fluid inlets and alignment structures.

The influence of patterned wettability on multiphase flow behavior was studied in detail, with special focus on residual oil or water saturation as well as on fractal behavior. Results on this experimental study were reported in a short publication. The publication including supporting information is presented in the next section.

2.3.2 ***Article:*** ***Multiphase Flow in Porous Media with Patterned Wettability***

Wettability Patterns and Their Impact on Fluid Displacement in Porous Media

Marc Schneider, Patrick Tabeling

According to estimates nearly 2 trillion barrels of conventional oil and another 5 trillion barrels of heavy oil will remain in reservoirs worldwide after conventional recovery methods have been exhausted [Tho08], a significant amount of oil which corresponds to more than 200 years of world oil supply at current consumption rates. Significant effort is focused on the production of these residual reserves by enhanced oil recovery (EOR) techniques, based on injection of additional fluids into the reservoirs.

Reservoir wettability is a crucial factor in oil recovery, as is governs flow behavior during immiscible fluid displacement within the porous reservoir rock [Don08]. The wettability state of reservoir rock oftentimes presents as very complex with wettability variations at the pore scale, which makes it a very difficult quantity to properly understand and assess [Sah93]. Nowadays it is widely accepted that most of the world's oil is locked in mixed-wet reservoirs, i.e. reservoir rock with wettability variations down to the pore level [Don08]. Mixed or fractional wettability is known to impact oil recovery during waterflooding or EOR, but progress is needed to better understand flow phenomena induced by these wettability patterns.

Reservoir assessment and evaluation by simulation based on pore-level modeling, strongly relying on a detailed understanding of mixed wettability effects, is significantly lacking in predictive power [Blu01] as detailed experimental investigations remain elusive [Mor01], [Kum10].

Micromodels, i.e. porous rock models made of glass or polymer, revealed multiphase flow properties for systems of homogeneous wettability in the past [Sah93]. A need for such micromodels with patterned wettability is emerging, both to study fundamental flow behavior as basis for simulation well as to provide a tool for end user research on EOR improvements in mixed-wet conditions. However, a lack in suitable technology prevented studies on micromodels of mixed wettability so far.

Recent breakthrough in technology [Sch10] allows us for the first time to produce micromodels with local wettability alterations on the pore level by selective UV exposure as illustrated in Fig. 1A. The micrograph shows a micromodel where small pore throats were selectively rendered hydrophilic (water-wet) while the large pores and pore throats remain oil-wet, thus replicating precisely controlled mixed-wet conditions of reservoir rock in a micromodel for the first time.

Our experiments on micromodels (Fig. 1B) with patterned wettability reveal new flow regimes at various hydrophilic (water-wet) wettability fractions f_w. Micromodels with uniform channel size (♦) show a very fast increase of the residual water saturation S_{rw} with increasing f_w (Fig. 1C, top). Even very small f_w induce significant S_{rw}, much more than only the water fraction trapped in the water-wet pores, as the ration S_{rw} / f_w reveals (Fig. 1C, bottom). Characteristic for this regime are continuous pathways of oil-wet pores, which allows oil to invade the network by circumventing water-wet pore clusters. On the other end, at large f_w, another regime emerges where S_{rw} increases with decreasing f_w. This regime is characterized by a combination of oil bursting through non-wetting zones and the spontaneous imbibition of isolated, discontinuous oil-wet structures. Details are provided in Fig. S1. At $f_w \approx 0.5$ the two regimes are separated by a discontinuity, the percolation threshold, where oil-wet and water-wet paths change from continuous to isolated and vice versa. For systems with channel size distribution (□), the second regime is masked by geometry-induced percolation effects.

As our results reveal, wettability patterns have a large impact on multiphase flow behavior and show an entirely different behavior as compared to either completely wetting or non-wetting case. Although the location of the percolation threshold at 50% wettability fraction is specific to 2D network connectivity, the observed regimes are generic and must also exist in 3D porous media. The very large influence on S_{rw} in 2D suggests that the phenomenon to prevail in real reservoir rock as well.

We have now reached a level of technology, which enables us to generate precise tools for experimental research, allowing for detailed investigation of mixed wettability and its influence on multiphase flow in porous media. With most of the world's oil reserves trapped in mixed-wet reservoirs we anticipate our presented tool for experimental end user research to be of major interest for the petroleum industry, as it allows for the development of improved EOR methods for mixed-wet reservoirs

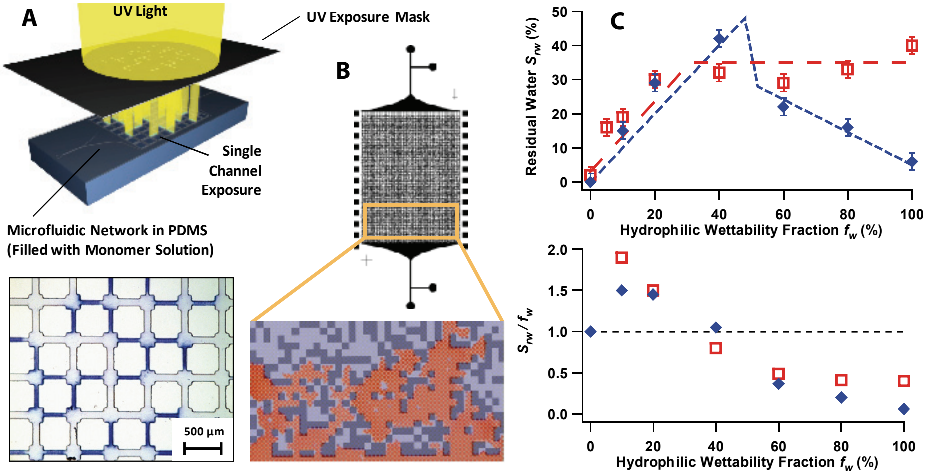

Fig. 1. (**A**) Precision wettability pattering in micromodels by UV-initiated graft polymerization provides wettability alteration of individual pores (schematic, top). The micrograph (bottom) reveals selective hydrophilic treatment of individual channels by blue stain. (**B**) Micromodel composed of 20,000 channels as employed in our work. The detail view (bottom) shows a segment of the network during an injection experiment, where oil (red) invades water-filled pores. Dark shades indicate hydrophilic regions. (**C**) Residual water saturation S_{rw} (top) and saturation relative to hydrophilic zones (bottom) for different wettability fractions f_w. Experiments were performed on micromodels with uniform (♦) and distributed (□) channels

References

1. Donaldson E.C., Alam W., *Wettability* (Gulf Publishing Company, Houston, TX, 2008)
2. Blunt M. J., *Current Opinion in Colloid & Interface Science*, **6**, 197 (2001)
3. Morrow N. R., Mason G., *Current Opinion in Colloid & Interface Science*, **6**, 321 (2001)
4. Kumar M., Fogden A., *Langmuir*, **26**, 4036 (2010)
5. Berejnov V. et al., *Lab Chip*, **8**, 689 (2008)
6. Sahimi, M., *Reviews of Modern Physics*, **65**, 1393 (1993)
7. Schneider, M. H. et al., *Analytical Chemistry*, **82**, 8848, (2010)
8. Thomas S., *Rev. IFP*, **63**, 9 (2008)

SUPPORTING MATERIAL

WETTABILITY PATTERNS AND THEIR IMPACT ON FLUID DISPLACEMENT IN POROUS MEDIA

Figures

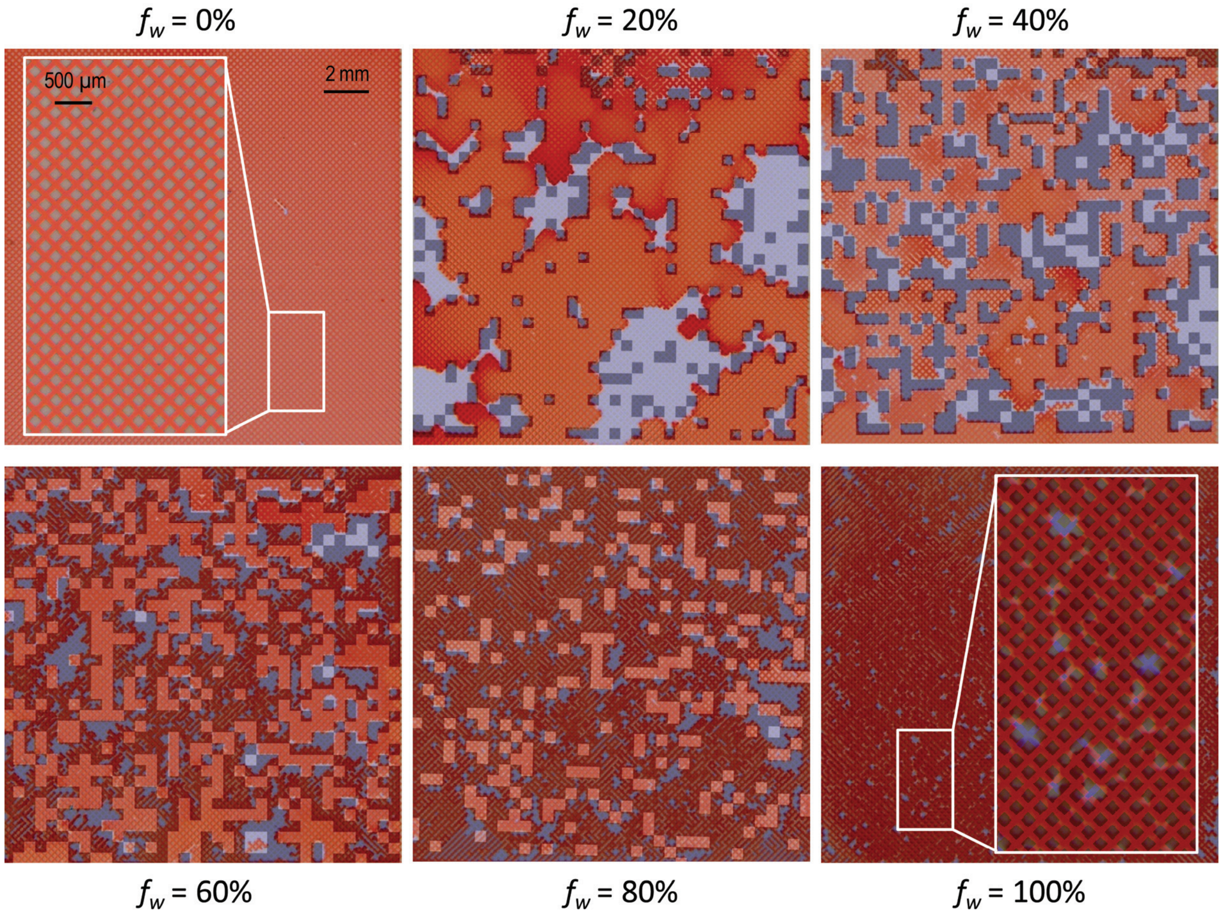

Figure S1: Water-saturated micromodels with uniform channel size show oil invasion as a function of hydrophilic wettability fraction f_w. Hydrophilic (water-wet) pore clusters are indicated by dark shades while bright shades represent hydrophobic (oil-wet) zones. For a uniformly oil-wet system ($f_w = 0$) complete filling occurs with no residual water. The first flow regime for wettability fractions smaller than 50% ($f_w < 0.5$) is characterized by oil invading along continuous oil-wet pathways while circumventing water-wet patches. During this invasion process significant amounts of water are trapped, even in oil-wet zones. In the second flow regime for larger wettability fractions (($f_w > 0.5$), no continuous oil-wet pathways exist. The invasion is characterized by a combination of oil bursting through oil-wet pores and spontaneously imbibing oil-wet clusters. For a uniformly water-wet system (f_w = 100), fairly uniform oil invasion occurs again, although water-trapping in individual pores occurs easily as oil is now the non-wetting fluid.

Materials and Methods

Micromodel Fabrication. Micromodels were fabricated from poly(dimethylsiloxane) according to a rapid prototyping technique based on soft lithography [Xia98]. In short, microfluidic channel structures were created on a silicon waver by a photolithographic pattering process of SU8 photoresist. Chrome-based photomasks were fabricated according to the channel design, the structures were transferred to the photoresist by UV exposure and the photoresist was developed to yield a silicon wafer with an embossed pattern of microchannel structures in SU8 serving as a mold. PDMS was cast by pouring a mix of pre-polymer and cross-linker (Sylgard 184 PDMS kit) on the mold, thoroughly degassing the melt under vacuum, and allowing PDMS to reticulate for 2 h at 65°C. After solidification, the PDMS cast was removed from the mold, trimmed in shape, and bonded against a flat PDMS counterpart to form a microfluidic system with closed channel structures. Bonding was achieved by surface activation in oxygen plasma at 400 mTorr for 30 s in a Harrick Plasma Cleaner. Both halves were brought in contact immediately after plasma treatment so that irreversible bonds could form at the interface, thus sealing the device permanently. The devices were then annealed in an oven at 90°C for 2 days in order to reverse the plasma-induced surface changes and recover native PDMS hydrophobicity [Ola05].

Wettability Patterning. Wettability patterns within the micromodels were achieved by UV-initiated graft polymerization of poly(acrylic acid) (PAA) [Sch10]. In short, micromodels were primed with photoinitiator benzophenone (BP) by driving a solution of 10% (wt) BP in acetone through the device for 5 minutes, allowing BP to diffuse into the PDMS matrix in vicinity of the channel walls. After vacuum drying for 15 minutes, the channels were loaded with a degassed solution of 20% (wt) acrylic acid (AA) in water and the system was exposed to UV light (365 nm) through a photomask for 3–4 minutes at an intensity of 30 mW/cm^2. After completion of graft photo-polymerization the system was thoroughly rinsed with ethanol and water to remove all adsorbed material leaving behind only the hydrophilic PAA coating covalently tethered to the PDMS surface in the desired regions.

Micromodel Specifications. Two different types of micromodels were used. Micromodel type one consisted of a regularly spaced lattice with 20,000 channels of uniform size ($80 \times 80 \times 220\ \mu\text{m}^3$) with a node connectivity of 4 and no enlarged cavities at the nodes. The other micromodel type was composed of 10,000 channels of variable size ($(50\text{–}120) \times 80 \times 300\ \mu\text{m}^3$) representing throats with an enlarged cavity ($(70\text{–}140)^2 \times 80\ \mu\text{m}^3$) at each node representing pores. Hydrophilic (water-wet) treatment was applied through UV exposure masks, which contained randomly placed square openings ($500 \times 500\ \mu\text{m}^2$) at sufficient numbers to create the desired wettability fraction f_w, where each square opening yielded a cluster of 3–5 water-wet pores.

Laboratory Setup. Micromodels were placed on a light table and imaged from above with 6.6 Megapixel color CCD camera through a high-resolution zoom lens. The resolution of the image sensor was sufficiently high to capture the entire network while providing good resolution (10 µm pixel resolution) in each individual channel to observe individual fluid interfaces. Fluids were slowly injected by a high-precision syringe pump (neMESYS, centoni) at a rate of 10 µl/min.

Experimental Procedure. Micromodels were initially filled with mildly alkaline water (pH 10) and hexadecane stained with oil red was injected, representing a low viscosity mineral oil (3 cP). Hexadecane was predominantly invading the oil-wet native PDMS surfaces, while water retained on PAA grafted areas. Wettability was verified on samples for the water (pH 10) / hexadecane fluid system: In the presence of water, hexadecane is completely repelled from PAA grafted surfaces (oil contact angle $\theta_{\text{oil}} = 180°$) while hexadecane is strongly wetting native PDMS at $\theta_{\text{oil}} = 30°$. An image sequence of each injection process was recorded at 3 frames per second and each frame was automatically analyzed by a custom-designed image processing routine.

References

[Xia98]	Xia, Y. and Whitesides G.M., *Annu. Rev. Mater. Sci.*, **28**, 153 (1998)
[Ola05]	Olah, A. et al, *Appl. Surf. Sci.*, **239**, 410 (2005)
[Sch10]	Schneider, M.H. et al., *Anal. Chem.*, **82**, 8848 (2010)

2.3.3 *Additional Comments on Micromodel Experiments*

Residual fluid saturations provide a practical measure for flow behavior evaluation, which is commonly used. Other commonly used measures, in particular for conceptual studies on micromodels, introduce the concept of fractals. Typically, the invading fluid front is characterized by its fractal dimension or mass or volume fractals are considered, where the fractal number for the invaded fluid volume is calculated [**177**].

In general, to quantitatively characterize a self–similar system, an embedding dimension D_e is defined, which describes the smallest Euclidean dimension of the space in which a given object can be embedded. Then, in order to decide on the fractality of an object, the Hausdorff dimension is measured. [**178**]. The volume $V(l)$ of an arbitrary object can be measured by covering it with cubes of edge length l and volume l^{D_e}:

$$V(l) = N(l) \times l^{D_e} \qquad (2.1)$$

where $N(l)$ is the number of cubes required. For a geometric object, the volume does not change if the unit of measure is changed, thus $N(l) \sim l^{-D_e}$. However, fractals are characterized by [**178**]:

$$N(l) \sim l^{-D} \qquad (2.2)$$

where D is the fractal dimension with $D < D_e$.

In micromodels with two–dimensional connectivity the third physical dimension (depth of the systems) is constant and can be removed (i.e. $D_e = 2$) for the consideration of mass or volume fractals. The fractal dimension for regular percolation is known to be $D = 1.89$ [**179**], [**180**]. In the drainage case, i.e. the injection of the non–wetting phase in a micromodel of uniform wettability, the invading fluid follows a pattern governed by capillary fingering (invasion percolation) for slow injection speed (small Ca). Fractal dimensions for invasion percolation patterns are typically reported in the range of $1.80 < D < 1.90$, with large uncertainties due to limited network size [**181**]. More precise values around $D = 1.82$ are reported from studies on very large networks by simulation [**182**] and experiments [**12**]. At higher injection speeds (larger Ca) flow patterns created by viscous fingering yield an even lower fractal dimension of about $D = 1.62$ [**183**], [**184**]. On the other hand, if invasion of the wetting phase causes complete filling of the micromodel, the fractal dimension equals the embedding dimension $D = D_E = 2$.

For the experimental series on micromodel type I (uniform channel size) with various wettability fractions f_w as reported in the previous section, fractality was analyzed in addition to the residual water saturation. After breakthrough at steady state flow, the fractal mass of the oil phase was analyzed. The fractal dimension was determined by a common technique, where starting from the center of the network the number of oil–filled channels N within a square area of edge length L is counted for increasingly large squares [**12**], [**13**]. In contrast to eqn. 2.2, this particular method follows the inverse scaling relationship $N \sim L^D$, but yields the same fractal dimension. The counts of oil–filled channel N for each box of size $L \times L$ were plotted as logarithmic values versus $\log_{10} L$ and the fractal dimension was determined from a line fit according to:

$$D = \frac{\log_{10} N}{\log_{10} L} \qquad (2.3)$$

Figure 2.16 show the fractal dimension according to eqn. 2.3 for type I micromodels at various wettability fractions. Complete filling with oil in the imbibition case ($f_w = 0$) yields a fractal dimension $D = 2$, i.e. no fractality of the system, as expected. In regime I up to 50% water–wet area ($f_w = 0.5$) even small water–wet fractions f_w induce significant fractality to the systems with fractal dimensions as low as $D = 1.85$. The discontinuity between regime I and II as already observed for the behavior of residual saturations (section 2.3.2) is also clearly visible in Figure 2.16. For water–wet fractions above 50% ($f_w > 0.5$), oil still exhibits fractal behavior but with much larger fractal dimensions ($D > 1.93$). In the drainage case, i.e.

for a completely water–wet system (f_w = 1), the fractal dimension almost returns to the embedding dimension (D = 1.98) for this network type. Although the invading oil is the non–wetting phase, capillary fingering (invasion percolation) does not occur since all channel cross–sections are of the same size. For drainage (f_w = 1) at small capillary numbers in a network type with channel size distribution, a fractal dimension of D = 1.82 would be expected due to capillary fingering. For micromodel type I, fractality is induced (e.g. by fingering) purely by wettability effect and not by network geometry, as all channels are of same size.

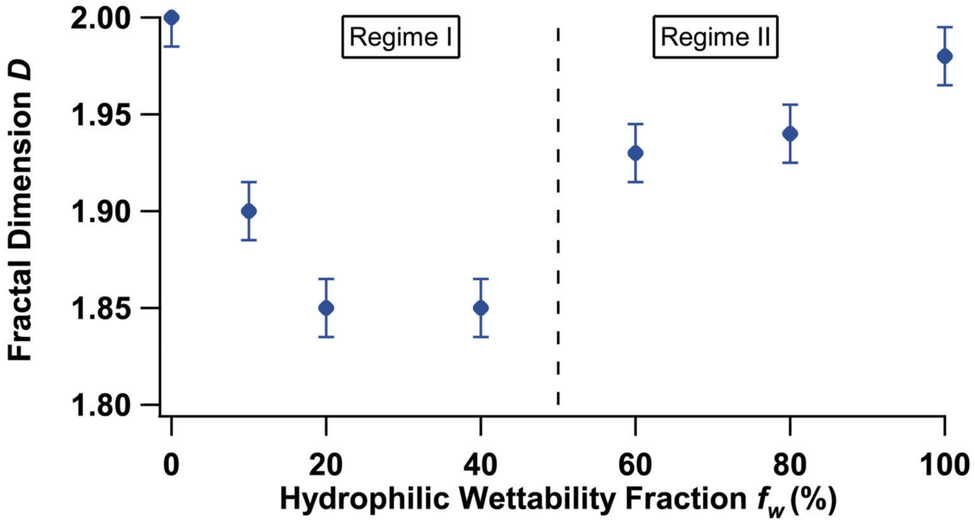

Figure 2.16: Fractal dimension D of the oil phase after breakthrough at steady–state flow conditions as a function of wettability fraction f_w for micromodel type I (uniform channel size).

Pressures across the micromodels were monitored during injection at constant flow rate. As expected, for imbibition and small f_w, driving pressures were low since invasion of the wetting phase is assisted by capillary forces. For large f_w, required driving pressures were significantly higher since the invading oil in this case was the non–wetting phase and needed to overcome the capillary pressure of each pore. Typical driving pressures close to the wetting case (f_w = 0) were at around 15 mbar while required pressures close to the non–wetting case (f_w = 1) were about twice as high (30 mbar).

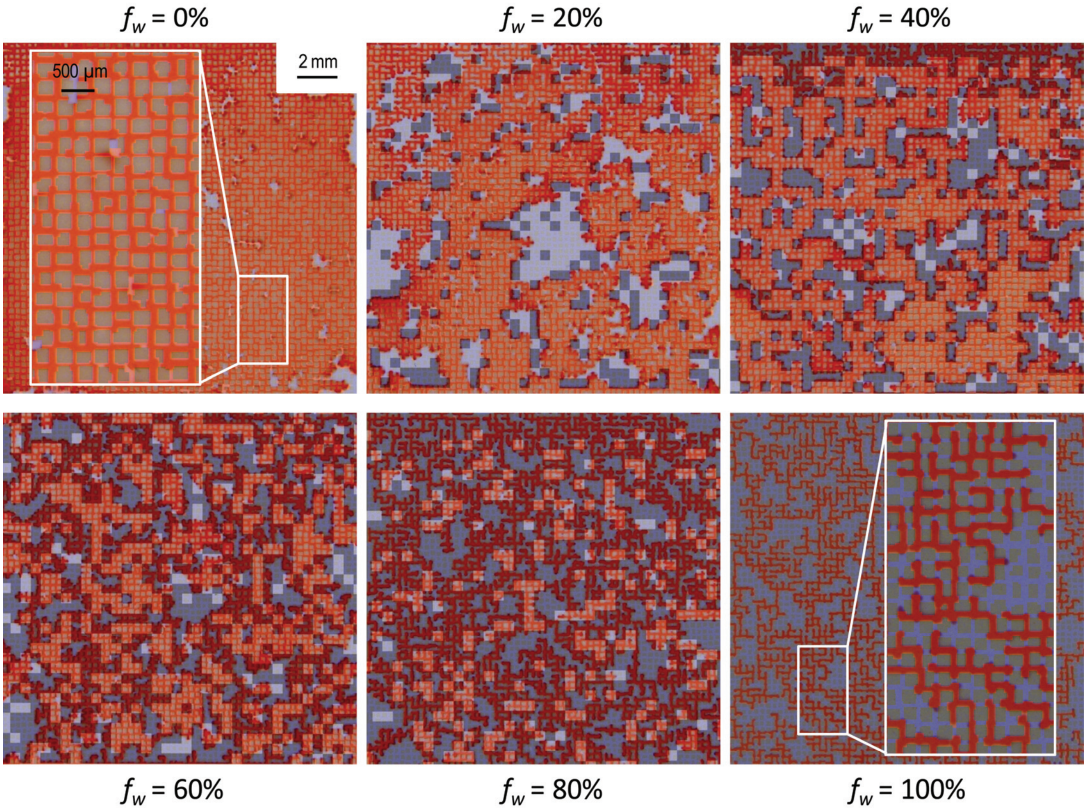

Figure 2.17: Water–saturated micromodels with channel size distribution (Type III) at various hydrophilic wettability fractions f_w showing oil invasion after breakthrough. Hydrophilic (water–wet) pore clusters are indicated by dark shades while bright shades represent hydrophobic (oil–wet) zones.

Images of oil invasion after breakthrough for micromodels with uniform channel size (Type I) were shown in section 2.3.2 for various wettability fractions. Figure 2.17 shows such images for micromodels with channel size distribution (Type III). For $f_w = 0$ the micromodel is almost completely filled by oil imbibition, however, some amount of water is trapped due to snap–off effects caused by variable channel sizes. For small f_w, displacement behavior as seen in Figure 2.17 is comparable to networks with uniform channel size: oil invades the network along oil–wet pathways while circumventing water–wet pore clusters and thereby trapping significant amounts of water. In the case of distributed channel size at large water–wet fractions ($f_w > 0.5$)

residual water saturations remain significant due to geometry–induced trapping effects by capillary fingering (invasion percolation).

Chapter 3

Applications for the Oil Industry

Two–phase flow behavior in micromodels was studied in Chapter 2 and the appearance of different flow patterns was investigated as a function of wettability. These fundamental studies on immiscible fluid displacement in porous media and the identification and classification of distinct flow regimen prove vital to applications in the oil industry as they can provide the foundation for the development of new reservoir simulators with improved predictive power [**42**], [**47**] as well as for new measurement techniques.

A new method for wettability assessment in core samples was developed. The method, as presented in sub–section 3.1.3, judges wettability from optical observation of the shape of the fluid front during fluid invasion, which relies on the presence of particular flow regimes as determined by micromodel experiments. A general review on wettability measurements in core samples is provided below.

A novel microscopic imager instrument is introduced in section 3.2, which allows for optical observations of rock/fluid interactions down to the pore scale. The imager was developed to provide reliable imaging of rock samples at sufficiently high quality and to overcome particular imaging challenges related to difficult sample conditions in order to allow for new, optics–based measurements such as the proposed wettability assessment.

3.1 Wettability Measurements in Core Samples

Several evaluation methods for wettability are commonly used in the oil industry, which are either based on contact angle or capillary pressure curves [**85**], [**55**], [**185**]. Contact angles are commonly measured by the classical sessile drop method [**186**], [**187**], [**188**], or by modified forms of the method [**189**], [**190**], [**191**], where a drop of liquid is brought in contact with the rock surface and contact angles are determined by visual inspection (c.f. Figure 1.3). Such methods only work well for flat, polished mineral crystals. Although contact angle determination on porous surfaces is possible [**192**], [**193**], the measured values are subjected to large uncertainties and hysteresis due to surface roughness and heterogeneities [**77**], [**194**]. Furthermore, wettability of reservoir rock is determined in part by deposits of organic molecules, such as asphaltenes, which can accumulate in the presence of crude oil along the surfaces within the pore space [**195**], [**90**]. Contact angle measurements on freshly cut surfaces, e.g. the outside of a core sample, cannot provide conclusive results as these surfaces represent a mix of the true wettability within the pores and wettability of freshly exposed minerals. Some methods exist, which attempt to restore native state wettability of core samples by solvent cleaning and subsequent aging of the rock in the original crude oil [**196**], [**197**], [**198**], [**199**]. However, it remains questionable if and when the original wettability state of the core recovers [**191**], [**200**], and contact angle results oftentimes deviate significantly form wettability measurements established by capillary pressure techniques [**201**], [**202**].

3.1.1 *Wettability Measurements Based on Capillary Pressure*

The two most widely used techniques used by oil and service companies to determine core sample wettability [**85**] are the Amott–Harvey method [**203**], [**204**], and the United State Bureau of Mines (USBM) method [**205**], which are based on imbibition and centrifuge capillary pressure measurements [**95**]. Figure 3.1b shows schematically a typical capillary pressure curve, which plots the capillary pressure as a function of water saturation during drainage (black curve, arrows pointing left) and imbibition (black curve, arrows pointing right) cycles[15], and identifies four distinct saturations of particular interest. The residual (irreducible) water saturation $S_{iw} = S_1$ denotes the lowest possible water saturation and therefore the largest possible oil

---

[15] Strictly speaking, the terms imbibition and drainage refer to the invasion of wetting and non-wetting phase, respectively. However, since it was historically common practice to consider all reservoir rock as water-wet, the terms imbibition and drainage are frequently used to describe the increase and decrease in water saturation, even in the case of an oil-wet rock [**82**].

saturation, which can be reached by water/oil displacement. The residual water is the amount of water trapped in the rock at any capillary pressure. The residual oil saturation $S_{or} = 1 - S_4$ denotes the lowest achievable oil saturation after water imbibition, i.e. the oil trapped in the rock [**206**]. The points S_2 and S_3 indicate points of zero capillary pressure. From a point of low water saturation up to point S_2, water imbibes spontaneously into the rock. From high water saturation (low oil saturation), water is expelled (oil imbibes) spontaneously down to point S_3.

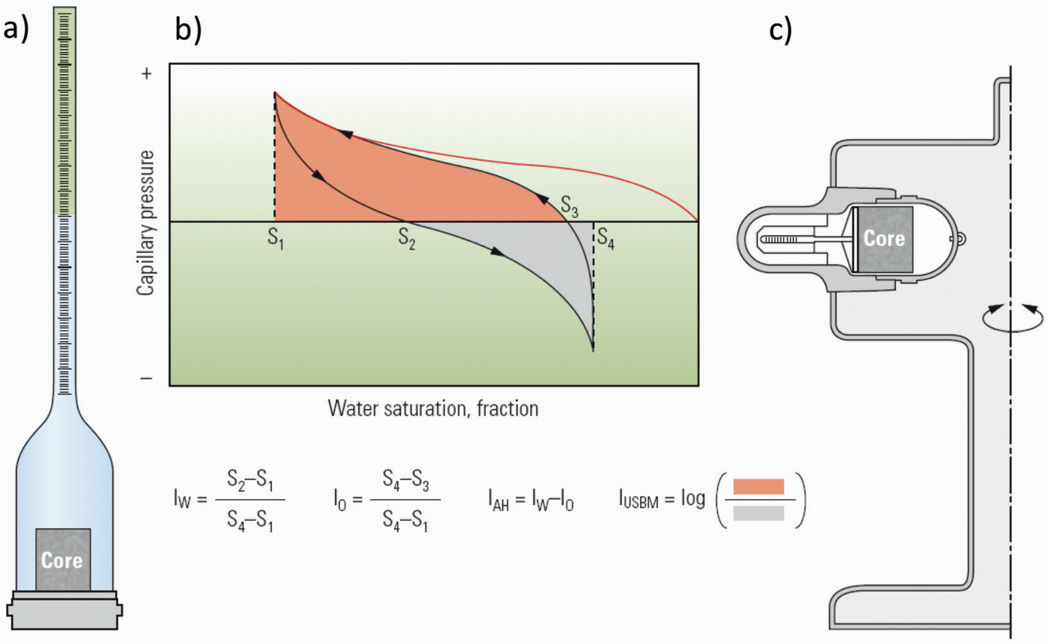

Figure 3.1: Wettability measurement on core samples. (a) Spontaneous imbibition of water can be measured by the amount of expelled oil in a graduated tube. Inverse arrangement allows for measurement of expelled oil. (b) Typical capillary pressure curves as recorded during drainage and imbibition cycles. Saturations of particular interest are indicated in the diagram. (c) Arrangement of a core sample in a centrifuge for water drainage. Inverse placement of the core holder allows for water imbibition [**82**].

Imbibition indices can be defined, which compare the amount of spontaneously imbibing fluid to the total amount of displaceable fluid. With respect to the particular water saturation points, the water imbibition index can be defined as:

$$I_w = \frac{\mathrm{S}_2 - \mathrm{S}_1}{\mathrm{S}_4 - \mathrm{S}_1} = \frac{V_{osp}}{V_{osp} + V_{of}} \qquad (3.1)$$

where V_{osp} and V_{of} are the amounts of oil expelled by spontaneous imbibition and forced injection of water, respectively. The imbibition index for oil follows to:

$$I_o = \frac{\mathrm{S}_4 - \mathrm{S}_3}{\mathrm{S}_4 - \mathrm{S}_1} = \frac{V_{wsp}}{V_{wsp} + V_{wf}} \qquad (3.2)$$

where V_{wsp} and V_{wf} are the amounts of water expelled by spontaneous imbibition and forced injection of oil, respectively.

For the Amott–Harvey imbibition test, a core sample at irreducible water saturation S_{iw} is placed in a water–filled tube and the amount of expelled oil by spontaneous water imbibition V_{osp} over a period of at least 10 days is measured (Figure 3.1a). Afterwards, the sample is placed in a flow cell and water is forced through, in order to reach residual oil saturation S_{ro}. The additional, forced amount of displaced oil V_{of} during flowing is also measured. The core sample at residual oil saturation S_{ro} is then placed in an oil–filled tube for the reverse experiment and the amount of displaced water by spontaneous oil imbibition V_{wsp} is determined. Forced oil–flooding in a flow cell reveals the additional, forced amount of displaced water V_{wf}. The two imbibition indices I_w and I_o for water and oil can be calculated according to eqns. 3.1 and 3.2 and the Amott–Harvey wettability index follows to:

$$I_{AH} = I_w - I_o \qquad (3.3)$$

The result is a number between +1 (strongly water–wet) and -1 (strongly oil–wet) [**207**].

The USMB method is based on the complete measurement of the capillary curve. Therefore a core sample at S_{wi} is placed in a centrifuge within a water–filled tube and centrifuged at stepwise–increasing speeds. Each spin rate subjects the core sample to a particular pressure and expels a corresponding amount of oil, which is recorded. After the imbibition curve is recorded, the sample is placed in a second, oil–filled cell and the centrifuging procedure is repeated to determine the drainage curve (Figure 3.1c). The areas between drainage and imbibition curve and the zero capillary pressure line are integrated, and the logarithm of the ratio between the two areas forms the USMB index (Figure 3.1b). The measurement range extends from -∞ (strongly water–wet) to +∞ (strongly oil–wet), although most measurements result in an index between -1 and +1. The USMB method is fast but the recorded saturations need to be corrected for the nonlinear pressure gradient in the centrifuge [**82**].

3.1.2 *Wettability Effects on Capillary Pressure and Relative Permeability*

The Amott–Harvey method as well as the USBM method characterizes wettability based on the capillary pressure curve. Figure 3.2 compares the different behaviors of the capillary pressure curve for the water–wet and the mixed–wet cases. In a water–wet case (Figure 3.2a), the entire capillary curve principally lies in the positive pressure range. I.e. water spontaneously imbibes if the rock is at low water saturation but oil does not exhibit spontaneous imbibition in the opposite case, which is the expected result for a water–wet rock. In the mixed–wet case (Figure 3.2b), the situation is different and the capillary curve extends both towards negative and positive pressures. At low water saturation spontaneous imbibition into the water–wet pores occurs; however, water imbibition stops well before residual oil saturation is reached since water cannot imbibe spontaneously into oil–wet pores. On the other hand, at high water saturation spontaneous oil imbibition into oil–wet pores does occur in this case [**108**], [**208**]. Imbibition and drainage capillary pressure curves typically do not line up with each other; this hysteresis effect is cause in parts by the hysteresis between the advancing and receding contact angle [**105**], which in turn can be attributed in large parts to the surface roughness and surface heterogeneities of the porous medium [**95**], [**209**], [**210**], [**211**].

Figure 3.2 also indicates the primary drainage curves (dotted). Primary drainage of water (first invasion of oil) refers to the very first time oil is migrating into clean reservoir rock, before wettability has been altered by aging. For a real oil reservoir these curves are of theoretical nature only, but in a core flood experiment the primary drainage can be measured as the very first oil invasion after the core has been rendered water–wet by thorough cleaning.

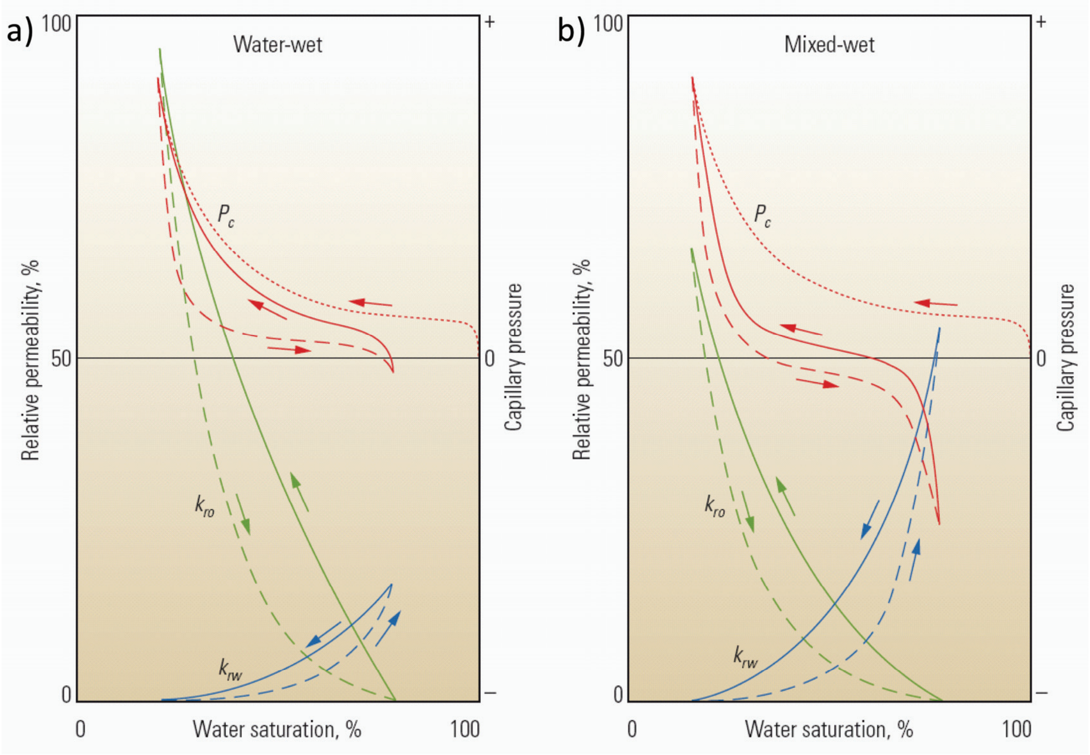

Figure 3.2: Capillary pressure and relative permeability for (a) water–wet and (b) mixed–wet rock. Capillary pressure evolution (red) is shown for primary drainage (dotted) and subsequent cycles of drainage (dashed) and imbibition (solid). Relative permeability is shown for water (blue) and oil (green), both for imbibition (solid) and drainage (dashed) [**82**].

In interaction with the capillary pressure, wettability also strongly affects relative permeability. For a single phase, fluid flow through a porous medium in one dimension is described by Darcy's law [**212**]:

$$q = \frac{k}{\mu} \nabla P \tag{3.4}$$

where q is the volume flux, ∇P is the pressure gradient, k is the permeability of the porous medium and μ is the viscosity of the fluid. The volume flux q, sometimes also called the filtration velocity, is not the velocity at which the fluid is travelling through the pores [**213**]. The average fluid velocity $\bar{v}$ by which the fluid is travelling through the pores is related to the volume flux by:

$$\bar{v} = \frac{q}{\phi} \tag{3.5}$$

with the porosity ϕ . The permeability k is the intrinsic permeability of the porous solid. In a two–phase flow or multiphase flow situation, Darcy's law can still be used to describe the flow, however each fluid experiences an additional resistivity caused by the presence of the other fluids, expressed by the introduction of the additional relative permeability term k_r [**214**]:

$$q = \frac{k_r k}{\mu} \nabla P \tag{3.6}$$

The relative permeability for one fluid phase assumes values between $0 \leq k_r \leq 1$ as a function of the amount and distribution of other phases [**50**].

Relative permeability for water (k_{rw}) and oil (k_{ro}) is shown in Figure 3.2 as a function of water saturation. In the mixed–wet case (Figure 3.2b), at low water saturations water permeability is low and oil permeability is high, due to the large quantities of oil present in the rock. If water saturation is high, water permeability is consequently also high while small quantities of oil lead to only a low oil permeability. Water permeability at the irreducible water concentration S_{iw} decreases to zero since at this point the remaining water volume is trapped and all continuous pathways through the porous medium are severed. The same argument applies for zero oil permeability at the residual oil saturation S_{ro} [**105**], [**215**].

In the water–wet case (Figure 3.2a), oil permeability is very high at low water saturations because oil invades mainly the largest pores in a water–wet rock and therefore provides a large cross–section for oil flow through the porous medium. Water permeability at high water saturations, on the other hand, remains surprisingly low, which is a particular phenomenon for (strongly) water–wet rocks. Although large quantities of water are present, the water phase is manly located in the small pores while the residual non–wetting oil is trapped in the center of the large pores (c.f. Figure 1.8a), which significantly restricts the water flow [**105**], [**216**].

3.1.3 *Article:* *Wettability Determination of Core Samples Through Visual Rock and Fluid Imaging During Fluid Injection*

Wettability Determination of Core Samples Through Visual Rock and Fluid Imaging During Fluid Injection

Marc Schneider[1,3,], Florian Osselin[3], Ballard Andrews[2], Fadhel Rezgui[1], Patrick Tabeling[3]*

[1]Etudes et Production Schlumberger, 1 rue Henri Becquerel, 92140 Clamart, France
[2] Schlumberger-Doll Research, 1 Hampshire Street, Cambridge, MA 02139 USA
3 ESPCI, 10 rue Vauquelin, 75005 Paris, France
**Corresponding Author*

Abstract. Reservoir rock wettability is a key factor in oil recovery, as it controls the location, flow, and distribution of reservoir fluids. However, proper assessment of wettability is not an easy task and provides a number of challenges. Wettability is in parts determined by the history of the oil reservoir through mechanisms such as aging and fouling. Hence measurements on freshly exposed rock surfaces (e.g. on core plugs), are unreliable indicators and frequently do not represent the true wettability within the sample. Therefore wettability of core plugs is typically assessed by fluid injection techniques such as the USBM index. In this article we present a novel and fast method for wettability determination based on the optical observation of injected fluids, independent from the surface wettability state of the sample. Fluid behavior within the boundaries of the capillary regime is driven by capillary forces and thus by wettability, which is exploited for our method. A combined optical white-light and fluorescence imaging technique provides excellent contrast for reliable observations.

Keywords. Wettability, Core Samples, Displacement in Porous Media, Fluid Front, Imbibition and Drainage

1 Introduction

Wettability is a key property of reservoir rock that affects rock-fluid properties such as residual oil saturation, relative permeability, and capillary pressure (Anderson, 1987), (Anderson, 1987), (Djebbar & Donaldson, 2004), (Zhou et al., 2000), all crucial parameters with direct influence on oil recovery. Despite its significance, wettability of reservoir rock still remains very difficult to measure and for many considerations or calculations only wettability estimates are used. For pure smooth solids, wettability is easily measurable by simple techniques such as contact angle measurements. However, for heterogeneous rough materials the wettability assessment is made more difficult by local variations. In addition, the wettability of reservoir rock is in many cases governed by surface alterations resulting from aging and fouling rather than by the underlying mineral composition (Al-Maamari & Buckley, 2003), (Buckely et al., 2003). Therefore the wettability state of freshly exposed surfaces, such the surface of a core plug, does not reliably represent the true wettability within the core. It is clear that reliable assessment requires a proper measurement technique for bulk wettability, independent of the surface conditions. Several are available to evaluate the wettability of a core sample in a laboratory environment, such as the Amott or USBM methods (Anderson, 1986), (Donaldson et al., 1969). However, both these methods require a time-consuming series of imbibition and drainage cycles.

This paper presents a new method to determine bulk wettability based on optical microscopy, independent of the rock surface conditions. Previously, we reported on a microscopic imaging device and its application to probe local fluid mobility (Schneider et al., 2009). Following the methodology of observing rock-fluid interactions by optical means, we focused on wettability measurements. For a certain range of capillary numbers (i.e., injection speeds), a fluid follows distinct flow patterns when driven through a porous medium; these patterns depend on the medium's wettability (Lenormand et al., 1988), (Lenormand, 1990). While in the nonwetting case invasion percolation is expected to produce distinct finger structures on a local scale, imbibition of a wetting liquid results in a fairly flat fluid front. On fluid breakthrough at the exit surface of the rock sample, a cross-sectional view of the arriving fluid front can be observed; from that we determined the bulk wettability of the core independent of its current surface conditions. We combined traditional white-light images with fluorescence excitation of the natural fluorescence in crude oils in order to significantly enhance the optical contrast and detect minute quantities of oil.

2 Theory and Concept

2.1 Theoretical Background

By definition, wettability represents the affinity of a fluid to spread on the surface of a solid in the presence of another fluid (Djebbar & Donaldson, 2004), (Hirasaki, 1991). Let us consider water and oil. If water wets the solid with respect to oil, the contact angle will be small (θ < 90°) and the solid is called water-wet: The water will spread on the surface of the rock. On the contrary, if it does not wet, the contact angle will be larger (θ > 120°) and the solid is called oil-wet. The water will stay as a spherical drop and will minimize its contact area with the rock. If the system presents an angle between these two limits, the wettability is called intermediate.

Capillary pressure, related to wettability by the surface tensions, is the key part of our experiments. Let us consider a curved interface between two immiscible fluids. There is some pressure across the interface. The variation of pressure is called capillary pressure (Anderson, 1987):

$$P_\mathrm{c} = p_\mathrm{nw} - p_\mathrm{w} \qquad (1)$$

where p_nw is the pressure inside the nonwetting fluid and p_w is the pressure inside the wetting fluid. The curvature radii determine this capillary pressure with the Laplace law:

$$P_\mathrm{c} = \sigma(1/R_1 + 1/R_2) \qquad (2)$$

where σ is the interfacial tension between the two fluids, and R_1 and R_2 the curvature radii. Finally, the case of a thin pore and a meniscus leads to an equation linking the capillary pressure and the contact angle:

$$P_\mathrm{c} = 2\sigma\cos\theta/r \qquad (3)$$

where r is the radius of the tube and θ is the contact angle. Eq. 3 shows that the pressure needed to make a fluid penetrate a pore is directly related to the wettability of the fluid for this pore and to the radius of the pore. If the fluid wets the pore, it will be easy for the fluid to penetrate, and the fluid may even be actively soaked up if the radius is small enough. On the contrary, if the liquid does not wet the pore, pressure is required for penetration, and the smaller the pore the higher the pressure needed.

Immiscible two-phase displacement in porous media down to the pore scale has been the subject of detailed studies based on experiments and simulation ranging from considerations of individual pores and throats to 2D and 3D network models and real porous media (Sahimi, 1993). Displacement can occur in two fundamental forms: drainage and imbibition. While drainage describes the process where the nonwetting phase is pushed into the porous medium to displace the wetting fluid, imbibition describes the opposite case, in which the wetting fluid imbibes the porous medium, displacing the nonwetting phase. For both drainage and imbibition, different types of displacement behavior has been classified as different regimes (Lenormand et al., 1988), (Lenormand, 1990), (Lenormand, 1986), (Vizika et al., 1994), (Blunt & Scher, 1995), (Xu et al., 1998), (Hughes & Blunt, 2000), (Ovdat & Berkowitz, 2007). In the presence of both viscous and capillary forces, two dimensionless numbers are typically used to characterize the displacement, the capillary number:

$$Ca = q\mu_\mathrm{injected}/\sigma \qquad (4)$$

and the viscosity ratio:

$$M = \mu_\mathrm{injected}/\mu_\mathrm{initial} \qquad (5)$$

where q is the injection velocity, and μ_initial and μ_injected are the viscosities of initial (displaced) and injected (displacing) phase, respectively. In the drainage case three particular regimes can be recognized: (i) capillary fingering or invasion percolation (IP) for small capillary numbers (low injection speeds), (ii) stable displacement for faster injection speeds and low viscosity of the displaced phase (large M), and (iii) viscous fingering for faster injection speeds and low viscosity of the injected phase (small M) (Lenormand et al., 1988), (Lenormand, 1990). In the imbibition case, particular regimes can be identified as well: (I) bond percolation for very small capillary numbers and strong wetting where the wetting fluid imbibes as a thin film along the channel walls while the nonwetting phase remains in the bulk channels, (II) flat frontal advance for small to large capillary numbers, and (III) compact cluster growth again for very small capillary numbers but for intermediate wetting properties (Hughes & Blunt, 2000), (Blunt & Scher, 1995), (Lenormand, 1986).

More distinct regimes appear for imbibition if initial partial saturation of the wetting phase exists (Hughes & Blunt, 2000) or if very large pores or throat aspects are considered (Lenormand, 1990).

2.2 Discussion of Concept

Two-phase displacement experiments on reservoir rock samples (core flooding) can easily be performed with water and oil as the two liquid phases. Depending on the wettability of the rock and on the injected liquid, the experiment represents either drainage or imbibition and the injected liquid creates a particular shape of the invading fluid front as described. If we perform our experiments in a certain range with respect to the capillary number and viscosity ratio, we can expect the fluid front to propagate in a stable fashion in the imbibition case but to develop strong fingering as a result of percolation effects in the drainage case. Observations of the arriving fluid front then instantly reveal the wettability of the rock sample. Figure 1 shows this concept for water injection in an oil-saturated core sample: In a water-wet core we expect to see the propagation of a fairly flat fluid front; in an oil-wet core we expect to observe strong fingering since nonwetting water follows only the path along the largest pores (least resistance) according to percolation theory. Let us consider water ($\mu = 1$ cP) and a reasonably light oil ($\mu < 100$ cP) as fluid pair, which gives a viscosity ratio in the range of $M = 10^{-2}, \dots, 10^{2}$. In the drainage case we can then choose injections speeds yielding capillary numbers up 10^{-4} and still observe capillary fingering (drainage, regime i) (Lenormand et al., 1988), (Xu et al., 1998), while in the imbibition case we can have capillary numbers as low as 10^{-6} while still observing a fairly flat advancing front (imbibition, regime II) (Hughes & Blunt, 2000), (Vizika et al., 1994), (Melean et al., 2003). In conclusion, if we select an

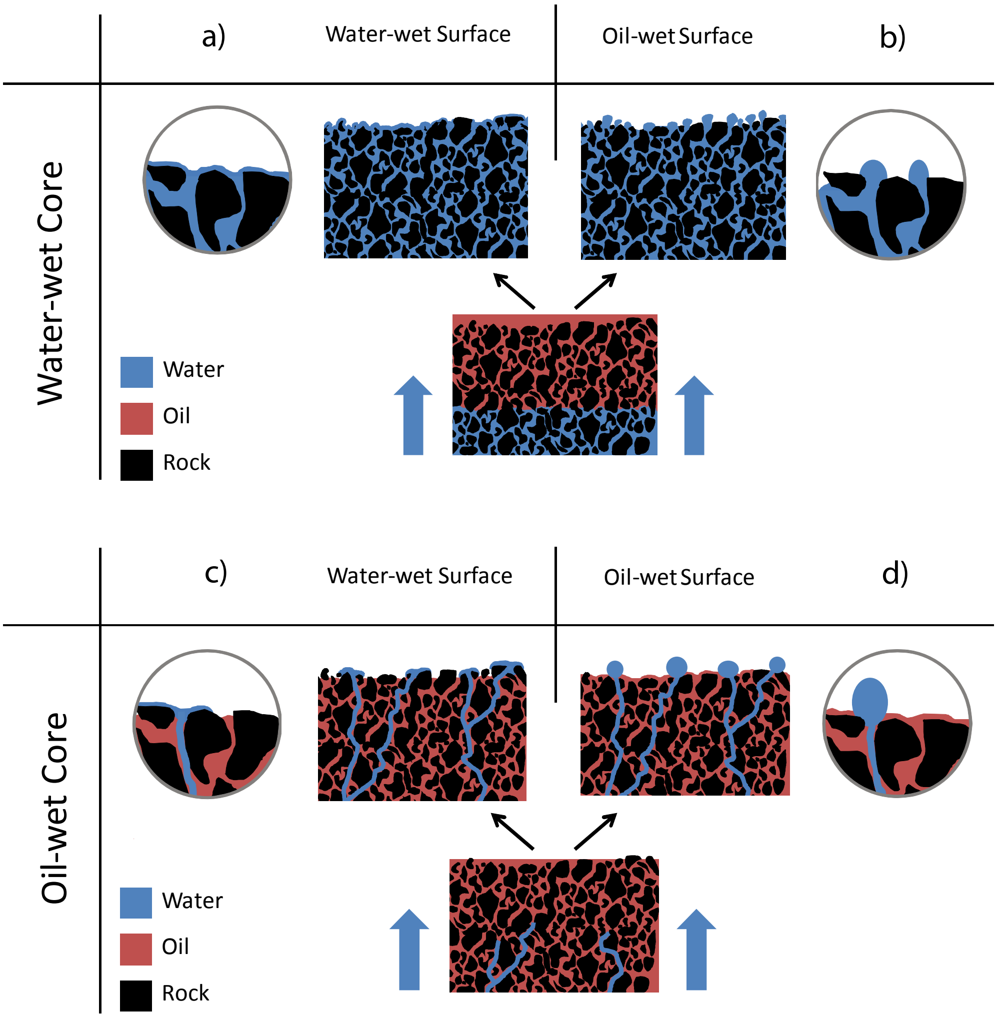

Figure 1: Schematic description of the injection concept: For a particular range of capillary numbers distinct fluid fronts are expected to develop. (a,b) flat fluid front is expected for imbibition, and (c,d) capillary fingering is expected for drainage. Surface wettability causes different behavior upon breakthrough; i.e., spreading over grains (a,c) or droplet formation (c,d).

injection speed yielding a capillary number around 10^{-5}, we can expect fluid propagation, shown in Figure 1, as a function of the wettability of the rock.

Wettability of reservoir rock is in many cases governed by surface contaminations inside the pore space and not by the wetting properties of the clean minerals. Therefore, the outer surface of a core sample does not always accurately represent the true (bulk) wettability of the sample. In cases where the bulk wettability is significantly changed by aging, wettability measurements on the surface of a freshly cut core sample (e.g., by the sessile drop method) would yield significant discrepancies. However, by considering the shape of the arriving fluid front and not the shape of droplets from individual pores, our measurement technique is independent of the surface conditions. For bulk wettability of the injected fluid (e.g., water), a fairly flat front is expected to arrive at the surface (Figure 1). Depending on the surface wettability, the arriving fluid (water) might then either emerge as a thin film and quickly spread over the grains (Figure 1a) or emerge as individual droplets from the pores, repelled by the nonwetting surface (Figure 1b). Independent of the surface condition, fluid arrival at a large number of pores reveals the internal (bulk) wetting state of the rock. For the opposite case (drainage case), the nonwetting fluid (e.g., water) is expected to arrive at only a few distinct spots at the surface as a result of capillary fingering. Whether the emerging fluid (water) spreads on the surface (Figure 1c) because of different surface wettability or is repelled by an oil-wet surface (Figure 1d), bulk wettability of the rock again is revealed by the arrival of the fluid at only a few distinct pores.

3 Material and Methods

3.1 Rock Preparation

The main part of the study used limestone samples from St Maximin, France. These rocks are clean, quarried rocks that have never been in contact with any crude oil. The samples are fairly homogeneous and have a high porosity of about 40% with an average grain size of 100 µm, an apparent density of about 1600 kg/m^3, and are strongly hydrophilic (Rocamat, 2008). Some additional rock samples were used for the study related to optical contrast between crude oil, water, and rock. As a representative for sandstone, Berea 500 samples were used, and additional limestone from Sireuil, France, was used as well. Cylindrical core samples of size Ø45 × 50 mm^2 were extracted from the rocks, which were large enough for the particular textures to assume homogeneity between samples. Porosity values were verified for each core in-house with a pycnometer and were found to be constant among samples and in agreement with the provided values.

Some of the rock samples were rendered oil-wet with a commercial silanization product (Anderson, 1986). It was diluted in low viscosity mineral oil (20%) and centrifuged into the rock at 4,500 rpm during one night. Then, another centrifuge run was used to drain the excess product from the rock and the sample was dried in an oven. Porosity of the core sample was measured with the pycnometer before and after the treatment and no measurable change in porosity due to the treatment was detected. Alternative wettability modification by aging in crude oil as reported in literature (Anderson, 1986), (Cuiec, 1975), (Donaldson et al., 1969) was also performed as a reference. In this case, a heavy, asphaltene-rich crude oil was centrifuged into the core for several hours at 4,500 rpm and then put to age in an oven at 70°C during several days (Anderson, 1986). At the end of the process excess oil was drained from the core via centrifugation.

The surface wettability of some samples was altered independently from their bulk wettability properties. We used a fuming technique that employs a cyanoacrylate based glue (Czekanski et al., 2006) to produce and oil-wet surface and while keeping the bulk part remains water-wet. This glue is a strongly hydrophobic (oil-wet) polymer resulting from the polymerization of the monomer cyanoacrylate with water. Our technique evaporated the glue to condense on the rock surface as thin hydrophobic coating. The rock sample and a cup with water were put on an aluminum foil inside an oven at 70°C, and covered by a plastic beaker. After a few minutes pre-heating and temperature stabilization, several drops of the glue were added and the system was left for an 1 h. The rock was then removed for cooling.

Wettability measurement of the rock samples and the verification of the treatment effects used USBM-index measurements. USBM index is a quantitative method developed by Donaldson et al.

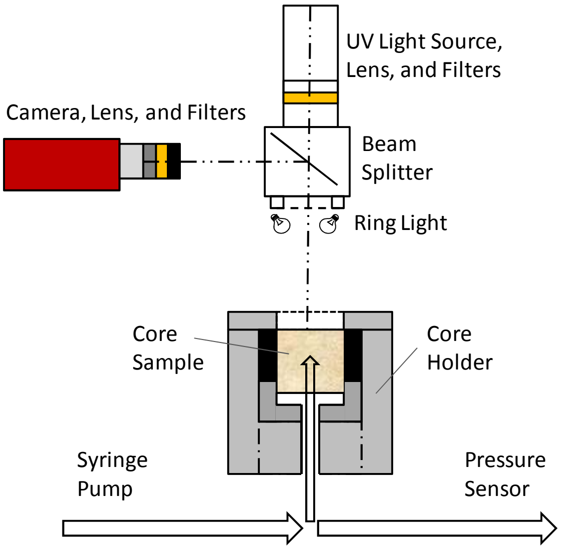

Figure 2: Schematic description of optical setup and core-holder assembly.

(Donaldson et al., 1969), (Anderson, 1986), (Djebbar & Donaldson, 2004). It compares the areas under the two capillary curves (capillary pressure against water saturation). These areas are related to the work needed for one fluid to displace the other, and then directly related to wettability. A negative index signifies an oil-wet rock, and a positive index a water-wet rock. The first saturation curve was measured by centrifuging water in a rock saturated with mineral oil. The second was made by centrifuging oil in the water-saturated rock. The saturation speed was 4,500 rpm and the saturation curve was measured in steps of 500 rpm. Sample cells were custom-designed for the experiments and allowed for drainage or imbibition experiments depending on the rock placement and the particular fluid pair.

3.2 Optical Setup

The imaging setup was a modification of previously reported work (Schneider et al., 2009): A fiber-optic ring-light illuminator powered by a halogen lamp provides white-light illumination under oblique angles (Figure 2). The reflected light from the rock sample is deflected by a short-pass dichroic beam splitter, which guides the rock images toward the camera-lens assembly. A 4-megapixel CCD camera with a Bayer-type color filter was used together with a matched macrolens. Fluorescence excitation is stimulated by an additional UV light source. A matched set of emission and excitations filters provided fluorescence excitation in the UV-A range (325–375 nm) and suppressed reflected UV before reaching the CCD detector.

The rock samples were mounted in a custom-designed core-holder, which allowed for fluid injection through the bottom face of the rock and for observation of the upper surface. The core samples were placed inside a soft rubber sleeve (NBR 40SH). The cell was tightened, compressing the rubber and forming a tight seal around the rock. During injection experiments raw video data were recorded at 30 fps onto a computer and processed after the experiment with appropriate software packages.

3.3 Fluid Injection Experiments

The fluids used were G232H oil with a viscosity of 3 cP, and water with a viscosity of 1 cP. This particular fluid pair provides a viscosity ratio of $M = 1/3$ for water injection and $M = 3$ for oil injection. An oil-soluble fluorescent dye was added to the oil mimicking the natural florescence of crude oil. Water was dyed red with a stain in some experiments. Each rock sample was used only once to avoid unwanted wettability alterations, in particular from the dyes, which might precipitate in small quantities during the experiment (Tuck et al., 2003).

Fluids were injected with a syringe pump, and fluid volumes injected into the core sample were obtained directly from the piston movement of the syringe-pump under consideration of the existing dead volume. Pressure was monitored during injection at the fluid inlet. Prior to each injection experiment the rocks were saturated with the initial fluid. Initial saturation was achieved by flooding the core at 20 mL/min for about 10 min. The injection experiments themselves were performed at an injection rate of 0.5 mL/min, which yielded a capillary number in the desired range ($Ca \approx 10^{-5}$). Two different experiments were performed for all different rock types: injection of oil in a rock saturated with water, and injection of water in a rock saturated with oil.

4 Results and Discussion

4.1 Visibility and Contrast of Fluid Phases

Sufficient contrast is required for visual (microscopic) observations of a fluid emerging from porous rock. During the transient time window when the emerging fluid just arrives at the surface, one of two principal scenarios occurs: (1) If the emerging fluid is wetting the rock with respect to the displaced phase, it will appear as a thin film spreading over the grains of the rock. (2) If the emerging fluid is the nonwetting fluid, it will break through to the surface via distinct pores and appear in the shape of individual drops. For proper visual observations it is therefore crucial to have sufficient contrast between the two fluid phases as well as good contrast between fluid and rock for at least one of the fluid phases. Petroleum applications commonly include water, oil, and gas, where typically water (brine) as the emerging liquid is fairly transparent (filtrate). Previous work (Schneider et al., 2009) shows that black crude oil gives excellent contrast; it is clearly distinguishable from clear water or gas and from the rock. Only water and gas also give good contrast. In this particular case the contrast is provided by the significant difference in the refraction index between the fluids (Schneider et al., 2009). However, detecting the presence of light crude oils solely by white-light imaging can be challenging because they may blend in with the colors of the rock as a result of their faint coloration.

In addition to white-light imaging, we used fluorescence imaging to enhance visibility for light crude oils. Fluorescence is excited with an additional UV light source at 365 nm and can be applied either simultaneously to white-light exposure or in alternating mode, which is shown in Figure 3 on a St Maximin sample. Figure 3a shows the dry sample under white-light illumination. In Figure 3b the injected liquid emerging from the rock can be observed, but from the while-light image alone the light crude oil might be confused with water because of its faint coloration. However, additional UV excitation instantly identifies the oil as strong, naturally occurring blue fluorescence (Figure 3d). In contrast, the fluorescence signal of the dry rock sample is negligible (Figure 3b).

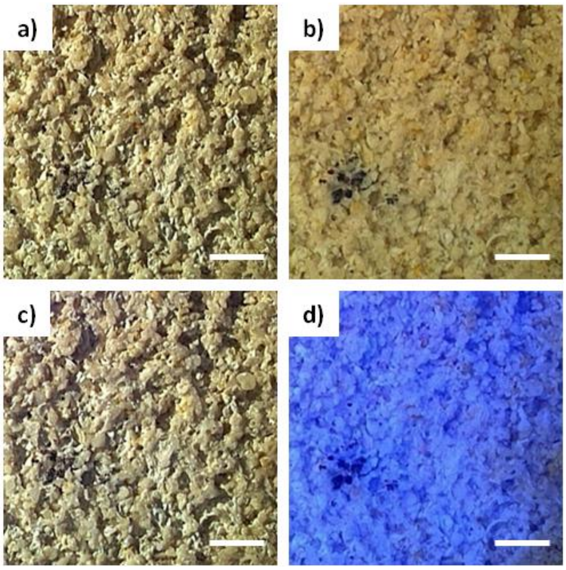

Figure 3: Visual contrast for (a,b) white-light imaging only, and (c,d) combined with fluorescence excitation. Dry samples (a,c) are compared with oil-saturated samples (b,d). White bars equal 1 mm.

Figure 4a–c show an example of a sandstone sample, saturated with water, in which the same light crude oil is injected. In this case the crude oil is the nonwetting phase and appears on the surface as droplets emerging from distinct pores. In this second case, as well, the appearance of the oil is easily missed in white-light only (Figure 4a); its faint color blends in with some of the brown grains while the fluorescence imaging overlay instantly reveals the oil-producing pores (Figure 4b). For comparison, Figure 4c shows the fluorescence

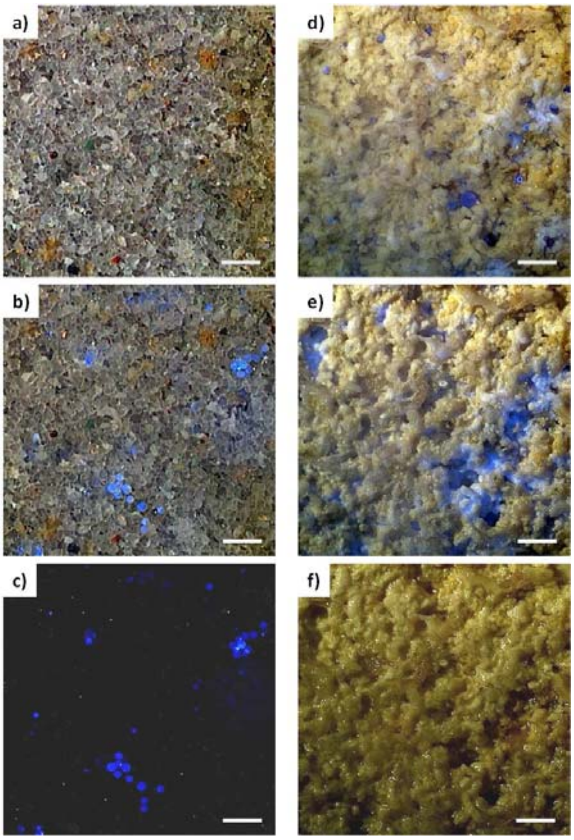

Figure 4: (a-c) Oil injection into water-saturated sandstone sample with (a) white-light only, (b) combined with fluorescence, and (c) fluorescence only. (d-f) Oil injection into water-saturated limestone sample until first oil breakthrough (d) and after draining of liquids (e,f). (e,f) compare combined white-light and fluorescence (e) with white-light imaging only (f). White bars equal 1 mm.

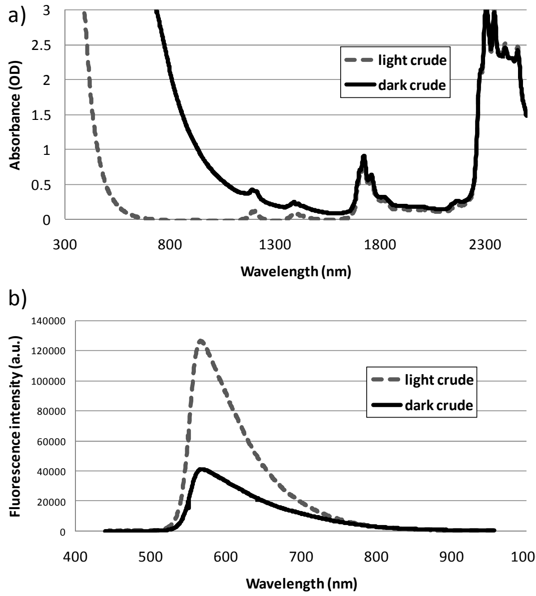

Figure 5: (a) Absorption spectra of light and dark crude oils for 2-mm path length. (b) Fluorescence spectra of the same samples for 470-nm excitation.

image only, without white-light illumination. In another experiment, shown in Figure 4d–f, the light crude was injected into a water-saturated Sireuil sample. Minute quantities of oil arriving in individual pores can be observed in great detail with combined white-light and fluorescence imaging (Figure 4d). In this particular experiment, fluid flow was reverted and both water and oil were drained from the rock. While white-light imaging only reveals a residual liquid film on the grains (Figure 4f), fluorescence imaging provides a detailed view of localized residual oil films at high contrast (Figure 4e).

Fluorescence imaging is particularly powerful because crude oils exhibit significant natural fluorescence and are thereby readily and easily distinguishable from water or gas. Although fluorescence intensity varies significantly among different crude oil samples as a function of their composition, almost all crude oils contain enough fluorescent species (mainly small aromatic molecules) to potentially yield intense fluorescence. However, the effective fluorescence yield is also governed by the amount of quenchers in the crude oil, which are mainly polycyclic aromatic hydrocarbons (PAH). Since PAHs, the heavy components in the crude oil, are also responsible for the coloration of the crude oil, there exists an inverse relation between crude oil color and fluorescence intensity (Andrews et al., 2008), (Mullins, 1998). This inverse relationship is ideal for our optical imaging technique: While dark oils are easily observed in the white-light images, light, weakly colored crude oils clearly distinguish themselves by intense fluorescence. As an example, Figure 5a shows the absorption spectrum of the light crude oil used in the paper compared with that of a typical dark crude oil. While the dark oil shows complete absorption in the visible-light range (400–700 nm), the light crude oil is still partially transparent. Fluorescence spectra for the same oil samples are shown in Figure 5b, which shows the inverse relationship: The fluorescence intensity of the light crude oil is significantly higher than that of the dark oil. Some limestones are also known to exhibit natural fluorescence (Wang et al., 1997), (Bezouska et al., 1998). Though weak, it might interfere with weak fluorescence signals from very dark crude oils. However, our optical imaging technique employs white-light imaging to detect dark oils by color, and fluorescence images are used to detect light, intensely fluorescent oils. Hence, the visual imaging technique is unaffected by the weak fluorescence background of some rock samples.

4.2 Fluid Injection Experiments

We carried out fluid injection experiments of water-oil systems in rock samples of different wettability to investigate the predicted regimes. We used St Maximin samples both in their native wettability state (hydrophilic) and in a hydrophobic state, altered by silanization as described. Bulk wettability was verified by the USBM method: All native rocks samples were found to be strongly water-wet with an index around +1; samples subjected to the silanization treatment were strongly and consistently oil-wet with indices between –1 and –1.5. Clear evidence for the particular cases of bulk wettability was also given by the pressure evolution during initial saturation, as shown in Figure 6a. When water reaches the water-wet rock sample (position: 0%, black markers), the pressure drops since capillary forces actively ”soak up” water by spontaneous imbibition. When the core sample is completely imbibed (position: 100%), an external pressure buildup is required for the fluid to exit the rock and to establish a constant flow, as described by Darcy’s law. On the other hand, if water reaches the oil-wet rock sample (dark gray markers), pressure buildup is instantly required to drive a flow through the sample. The driving pressure in this case is significantly higher than in the wetting case. The wettability of a reference sample was altered by aging in a heavy crude oil, and a subsequent USBM measurement revealed hydrophobic bulk wettability (index –1) similar to that experienced after the silanization treatment. However, for the following experiments only silanization treatment was employed since it was much less time-consuming.

Our study particularly focused on the injection cases in which surface wettability of the rock samples differs from their bulk wettability. Therefore, rock samples with modified surface wettability were prepared and tested as well. One modification consisted of fuming the rock surface with cyanoacrylate. This technique renders the fumed surface strongly hydrophobic (water-repellant), while the bulk rock retains its hydrophilicity. Another method consisted of a silanization treatment with subsequent grinding of the surface. While the silanization treatment rendered the rock sample entirely hydrophobic, the grinding step exposed again some of the hydrophilic minerals on the surface. The resulting surface state with this technique was mixed-wet; it consisted of a mix of silanized, hydrophobic pore throats and freshly exposed hydrophilic grains.

The wettability state of the surface was verified with contact angle measurements on a water droplet in air (Borysenko et al., 2009).The fumed surface was found to be strongly hydrophobic, as expected. Grinding of the fumed surface with subsequent contact angle measurement as well as USBM measurement confirmed that the bulk wettability remained hydrophilic. Also, if a hydrophilic rock is saturated with red-dyed water and left to dry, most of the dye is carried by the liquid water phase during drying to the outer surface of the rock where the evaporating water causes accumulation of the dye (Figure 7a). For a fumed sample, however, the outer surface is rendered strongly hydrophobic, repelling liquid water effectively. In this case water needs to evaporate within the rock and escape through the last layer of grains as vapor, which causes the dye to accumulate just underneath the treated surface (Figure 7b). Further evidence of the wettability state is given by the pressure profile during the experiment, as shown in Figure 6b: The two rock samples show identical pressure profiles, indicating identical bulk wettability, and the exit surface of one sample (dotted line) was rendered hydrophobic by fuming.

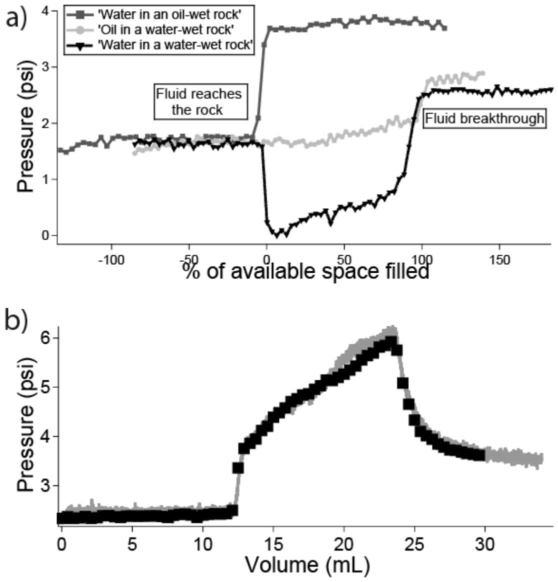

Figure 6: (a) Evolution of the pressure during injection of fluids in different dry rocks (0.5 mL/min). (b) Injection of oil in a water-saturated water-wet rock and cyanoacrylate-treated rock (dots)

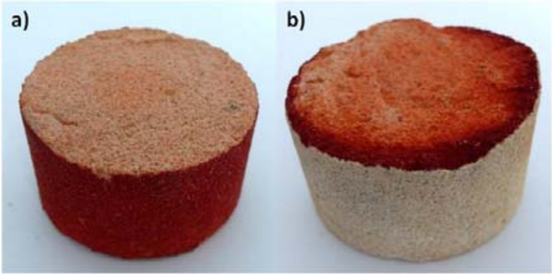

Figure 7: Core samples cut in half after flooding with red-dyed water and drying. (a) Hydrophilic sample: Red dye accumulated at the outer surface during water evaporation. (b) Hydrophilic sample with hydrophobic surface treatment (cyanoacrylate fuming): Dye accumulated within the rock just underneath the outer (treated) layer.

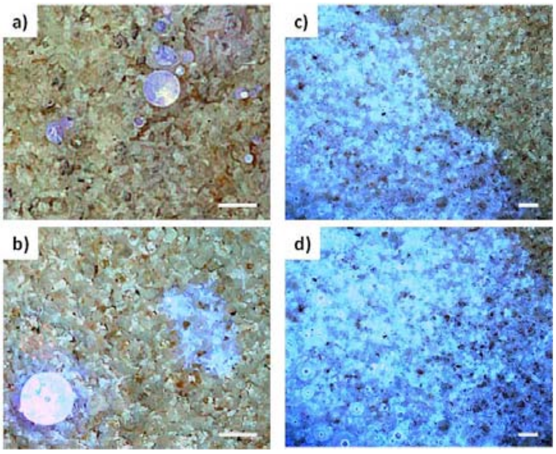

Figure 8: Oil injection (blue fluorescence) into water-saturated samples: (a) water-wet sample, (b) water-wet sample with oil-wet surface, (c,d) oil-wet sample. White bars equal 1 mm.

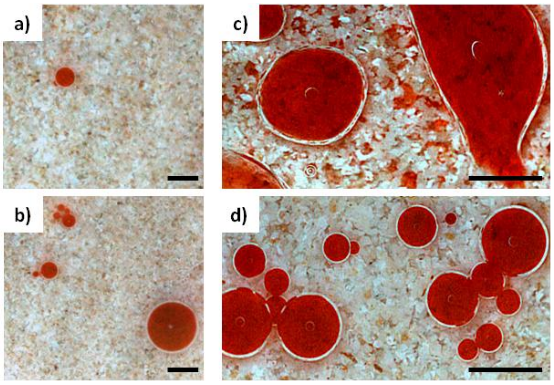

Figure 9: Water injection (dyed red) in oil-saturated sample: (a,b) oil-wet sample, (c) water-wet sample, (d) water-wet sample with oil-wet surface. Black bars equal 2 mm.

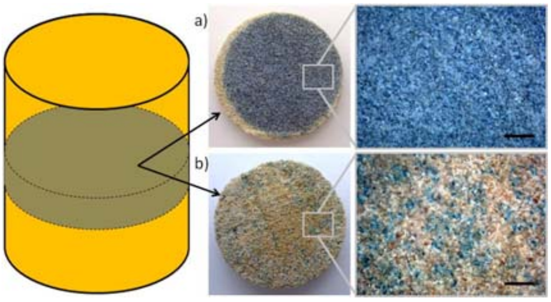

Figure 10: Aqueous stain precipitation (blue) during water-injection in oil-saturated sample for (a) water-wet and (b) oil-wet sample. Black bars equal 2 mm.

With confidence established in the wetting states of the prepared samples, we could carefully interpret the observed fluid-rock interactions by visual imaging: Figure 8 shows image examples during oil injection. A fluorescent dye was added to the transparent model oil to mimic the natural fluorescence in crude oils. If oil is injected into a water-wet rock, fingering occurs as predicted (Figure 1d) and oil emerges at the surface from a few distinct pores, as shown in Figure 8a. Even if the surface wettability differs (e.g., oil-wet surface), oil still arrives at a few distinct spots on the surface (Figure 8b) because fingering occurs in the water-wet core (Figure 1c). On the other hand, if oil is injected into an oil-wet core, a homogeneous imbibition front will propagate through the core sample and arrive at the surface (Figure 1a–b). Figure 8c–d show a time sequence of oil arriving at the surface. Although the fluid front shows some tilt with respect to the surface, the oil-wet nature of the rock can instantly be identified. Examples for water injection into oil-saturated cores are shown in Figure 9. Figure 9a–b show a time series of water injected into an oil-wet rock. Again, due to internal fingering, water arrives at the surface only through a few very distinct pores with significant spacing. In the wetting case, however, water arrives through almost all pores, spreads as a film, and gathers in large drops eventually (Figure 9c). Even if the surface has a different wettability (hydrophobic) and water cannot be observed spreading on the surface, the water-wet bulk properties of the rock are still apparent because water arrives through a large number of pores at the surface (Figure 9d).

The different types of fluid propagation through the rock samples depending on wettability (fingering vs. flat front) were also confirmed by the injected volumes. Table 1 lists the volumes injected into the core sample until first breakthrough at the surface. Volume fractions are calculated according to (Ovdat & Berkowitz, 2007): $f = 4V_{\text{inj}}/\phi\, hd^2$, where V_{inj} is the injected volume until first breakthrough, ϕ is the porosity, and h and d are height and diameter of the core sample. Table 1 illustrates that breakthrough of the nonwetting liquid occurs consistently early with only small amounts of injected fluid (less than 10%). On the other hand, much larger injection volumes for the wetting fluid are needed before breakthrough at the surface is observed, which clearly indicates a homogeneous front.

4.3 Length Scale Considerations

An additional experiment helped visualize the shape of the invading fluid front within the core sample and to gain further confidence in the proposed method: Water was injected into oil-saturated samples of different wettability. A blue ionic dye (methylene blue) was added to the water phase at high concentrations. This particular dye has a strong tendency to adhere to the mineral surface of the rock, even after a wettability-altering treatment. Injection was stopped at first breakthrough and the rock sample was cut in slices perpendicular to the direction of injection. Pores and throats where water has passed by are revealed by the blue stain. Figure 10 shows cross sections both for imbibition and drainage. For the imbibition case (Figure 10a), water invades the hydrophilic rock uniformly and fills almost all the available pore space. In the drainage case (Figure 10b), on the other hand, severe capillary fingering occurs, as clearly revealed by the punctual staining of the cross section, preferentially around large pore throats as expected from IP theory. These experiments clearly confirm the expected difference in flow regime as a function of bulk

Table 1: Measured volumes during injection experiments: Saturation volume indicates the amount of initial phase in the rock prior to injection. Injected volume indicates the amount of injected phase until first breakthrough is observed. Drainage experiments are highlighted in gray and imbibition experiments are in white.

	Oil Injection in Water-Saturated Sample			**Water Injection in Oil-Saturated Sample**		
	Saturation Volume, mL	**Injected Volume, mL**	**Volumetric Fraction, %**	**Saturation Volume, mL**	**Injected Volume, mL**	**Volumetric Fraction, %**
Fresh rock (water-wet)	22,5	2,5	8	33,0	12,0	38
Fresh rock, fumed surface (water-wet core, oil-wet surface)	25,8	2,8	9	30,0	10,0	31
Silanized rock (oil-wet)	35,0	16,0	50	24,0	3,0	9

wettability. The drainage case shown in Figure 10b also gives indications for required length scales: The full cross section of the core (about 16 cm^2 of surface area) shows a large number of fingers, indicating that a smaller observation area would be sufficient. The detailed view of an area with high finger density shows that even in those areas the spacing between fingers is several pores apart, allowing for clear distinction between fingering and flat frontal advance.

The minimal required observation area for the rock surface was identified by statistical analysis determining an average number of drops per area: For water injection into an oil-wet rock (drainage case, Figure 1c–d) 0.7 ± 0.3 fingers per cm^2 could be observed in average. For oil injection into a water-wet rock (drainage) 1.3 ± 0.4 fingers per cm^2 could be observed. Since the measurement technique requires the observation of at least one finger, a minimal observation area of several cm^2 is required for this rock type. Statistical analysis for the imbibition case with nonwetting surface (c.f. Figure 1b) shows an average of 7 ± 2 drops per cm^2 for water injection, clearly distinct from the drainage case.

5 CONCLUSION

Optical visualization combining white-light and fluorescence imaging clearly distinguishes water, oil, and rock at sufficiently high contrast. With established confidence in the optical imaging technique, fluid injection experiments were performed on core samples. All injection experiments were performed on St Maximin samples, a hydrophilic limestone with 100-µm average grain size and 40% porosity. A low-viscosity mineral oil with a fluorescent dye was used as substitute for a light crude oil. Treatments were established to alter bulk wettability and surface wettability independently between hydrophilic and hydrophobic. Confidence in the wettability treatments was established by several independent measurements such as USMB index measurement and the monitoring of injection pressure and injected volumes during experiments. All experiments were performed for capillary numbers around 10^{-5} and all observations clearly confirmed the distinct difference in the shape of the invading fluid front as a function of core wettability, hence confirming our measurement concept.

We successfully showed that wettability can be determined by visual observation of the emerging liquid from the rock sample during injection experiments. The measurement is based on the shape of the fluid front of the injected phase and is independent of the wetting state of the rock surface.

REFERENCES

Al-Maamari, R.S.H. & Buckley, J.S., 2003. Asphaltene Precipitation and Alteration of Wetting: The Potential for Wettability Changes During Oil Production. *SPE Reservoir Evaluation and Engineering*, p.SPE 84938.

Anderson, W.G., 1986. Wettability Literature Survey-Part 1: Rock/Oil/Brine Interactions and the Effects of Core Handling on Wettability. *Journal Of Petroleum Technology*, 38(10), pp.1125-44.

Anderson, W.G., 1986. Wettability Literature Survey-Part 2: Wettability Measurement. *Journal of Petroleum Technology*, 38(11), pp.1246-62.

Anderson, W.G., 1987. Wettability Literature Survey-Part 4: Effects of Wettability on Capillary Pressure. *Journal of Petroleum Technology*, 39(10), pp.1283-00.

Anderson, W.G., 1987. Wettability Literature Survey-Part 5: The Effects of Wettability on Relative Permeability. *Journal of Petroleum Technology*, 39(11), pp.1453-68.

Andrews, A.B. et al., 2008. Fluorescence Methods for Downhole Fluid Analysis of Heavy Oil Emulsions.

Journal of Dispersion Science and Technology, 29, pp.171-83.

Bezouska, J.R., Wang, J. & Mullins, O.C., 1998. Origin of Limestone Fluorescence. *Applied Spectroscopy*, 52, pp.1606-13.

Blunt, M.J. & Scher, H., 1995. Pore-level modeling of wettability. *Rhysical Review E*, 52, pp.6387-403.

Borysenko, A. et al., 2009. Experimental investigations of the wettability of clays and shales. *Journal of Geophysical Research*, 114, p.B07202.

Buckely, J.S., Liu, Y. & Monsterleet, S., 2003. Mechanisms of Wetting Alteration by Crude Oils. *SPE Journal*, p.SPE 37230.

Cuiec, L.E., 1975. Restoration of the Natural State of Core Sample. In *SPE Annual Technical Conference and Exhibition*., 1975.

Czekanski, P., Fasola, M. & Allison, J., 2006. A Mechanistic Model for the Superglue Fuming of Latent Fingerprints. *Journal of Forensic Sciences*, 51(6), pp.1623-28.

Djebbar, T. & Donaldson, E.C., 2004. *Petrophysics, Theroy and Practice of Measuring Reservoir Rock and Fluid Transport Properties 2nd Edition*. Elsevier.

Donaldson, E.C., Thomas, R.D. & Lorenz, P.B., 1969. Wettability Determination and Its Effect on Recovery Efficiency. *Journal of Petroleum Technology*, 9(1), pp.13-20.

Hirasaki, G.J., 1991. Wettability: Fundamentals and Surface Forces. *SPE Formation Evaluation*, 6(2), pp.217-26.

Hughes, R.G. & Blunt, M.J., 2000. Pore Scale Modeling of Rate Effects in Imbibition. *Transport in Porous Media*, 40, pp.295-322.

Lenormand, R., 1986. Pattern Growth and Fluid Displacements Through Porous Media. *Physica*, 140A, pp.114-23.

Lenormand, R., 1990. Liquids in porous media. *Journal of Physics: Condensed Matter*, 2, pp.SA79-88.

Lenormand, R., Touboul, E. & Zarcone, C., 1988. Numerical models and experiments on immiscible displacements in porous media. *Journal of Fluid Mechanics*, 189, pp.165-87.

Melean, Y., Broseta, D. & Blossey, R., 2003. Imbibition fronts in porous media: effects of initial wetting fluid saturation and flow rate. *Journal of Petroleum Science and Engineering*, 39, pp.327-36.

Mullins, O.C., 1998. Optical interrogation of aromatic moieties in crude oils and asphaltenes. In O.C. Mullins & E.Y. Sheu, eds. *Structures and Dynamics of Asphaltenes*. New York: Plenum.

Ovdat, H. & Berkowitz, B., 2007. Pore-scale imbibition experiments in dry and prewetted porous media. *Advances in Water Resources*, 30, pp.2373-86.

Rocamat, 2008. Datasheet - Limestones. p.downloaded from: www.rocamat.fr.

Sahimi, M., 1993. Flow phenomena in rocks: from continuum models to fractals, percolation, cellular automata, and simulated annealing.pdf. *Review of Modern Physics*, 65, pp.1393-534.

Schneider, M.H. et al., 2009. Novel microscopic imger instrument for rock and fluid imaging. *Geophysics*, 74, pp.E251-62.

Tuck, D.M., Iversen, G.M. & Pirckles, W.A., 2003. Organic Dye Effects on Dense Non Aqueous Phase Liquids (DNAPL) Entry Pressure in Water Saturated Porous Media. *Water Ressources Research*, 39(8), pp.1208-21.

Vizika, O., Avraam, D.G. & Payatakes, A.C., 1994. On the Role of the Viscosity Ratio during Low-Capillary-Number Forced Imbibition in Porous Media. *Journal of Colloid and Interface Science*, 165, pp.386-401.

Wang, J., Wu, X. & Mullins, O.C., 1997. Fluorescence of Limestones and Limestone Components. *Applied Spectroscopy*, 51, pp.1890-95.

Xu, B., Yortsos, Y.C. & Salin, D., 1998. Invasion percolation with viscous forces. *Physical Review E*, 57, pp.739-51.

Zhou, X., Morrow, N.R. & Ma, S., 2000. Interrelationship of Wettability, Initial Water Saturation, Aging Time and Oil Recovery by Spontaneous Imbibition and Waterflooding. *SPE Journal*, 5(2), pp.199-207.

3.2 Microscopic Grain Imager Instrument

Optical imaging and detailed visual observations of rock/fluid interactions at a pore level is a powerful tool to determine a variety of significant rock and fluid properties essential to the oil industry [**217**]. A novel technique for wettability assessment by visual imaging during fluid injection in a core sample was presented in the previous sub–section (3.1.3). This novel technique probes the wettability of the bulk sample independent of the wettability state of the surface. However, an overall clean surface with clear, unclogged pores is beneficial. Other measurements based on optical imaging also rely on a clean, well–defined rock surface, such as petrographic image analysis (PIA) for geological feature analysis [**218**], [**219**]. In many cases, however, rock samples are recovered in less–than–ideal conditions. In particular the exposed surfaces are frequently subjected to various alterations, both mechanical and chemical. The surface might show significant coarseness due to cutting grooves or chipped–off material, the surface might be oxidized, or the pores on the surface might be clogged due to fine deposits from the drilling mud (mudcake) [**94**], [**199**], [**220**].

A novel method and apparatus was developed which provides access to a clean, well–defined rock surface to an optical microscopic imager device, by drilling a small sampling hole through the damaged surface into the fresh rock. Method and apparatus have been published in *Geophysics* and are presented in sub–section 3.2.1. The versatility of such a microscopic imager instrument was demonstrated for both static and dynamic imaging applications. Static imaging refers to the capture of high–resolution still images, which are used for geological analysis (e.g. PIA) in order to determine rock properties such as texture and porosity [**221**], [**222**], [**223**]. Dynamic imaging refers to the continuous imaging of the emerging fluids from the pores during fluid injection, which can provide additional rock properties such as wettability or permeability of the rock sample. The dynamic imaging concept is demonstrated by locally probing permeability, another essential rock property [**224**], [**225**].

A detailed evaluation of the microscopic imager optical performance is provided in Appendix C.

3.2.1 *Article:* ***Novel Microscopic Imager Instrument for Rock and Fluid Imaging***

GEOPHYSICS, VOL. 74, NO. 6 (NOVEMBER-DECEMBER 2009); P. E251–E262, 23 FIGS.
10.1190/1.3261801

Novel microscopic imager instrument for rock and fluid imaging

Marc H. Schneider[1,2], Patrick Tabeling[2], Fadhel Rezgui[1], Martin G. Lüling[1], and Aurelien Daynes[2]

ABSTRACT

Core analysis from reservoir rock plays an important role in oil and gas exploration as it can provide a large number of rock properties. Some of these rock properties can be extracted by image analysis of microscopic rock images in the visible light range. Such properties include the size, shape, and distribution of pores and grains, or more generally the texture, mineral distribution, and so on. A novel laboratory instrument and method allows for easy and reliable core imaging. This method is applicable even when the core sample is in poor shape. The capabilities of this technique can be verified by core images, image interpretation, and dynamic measurements of rock samples during flooding. A microscopic imager instrument is operated in video acquisition mode and can measure additional properties, such as fluid mobility, by detecting the emergence of injected fluids across the core sample.

INTRODUCTION

In oil and gas exploration, laboratory core analyses continue to play an important role to determine the "final truth" about a rock. Remote formation-evaluation measurements by logging while drilling or wireline provide rapid surveys of large intervals along a borehole. On the other hand, they do not offer a detailed textural analysis of rocks down to the grain level. Such an analysis is not practical for the formation evaluation of an entire well, but it is very valuable in well-specified zones of interest.

Traditionally, thin sections have been used routinely to determine the size and shape distribution of the rock grains. A rock-core sample is dried and cleaned, then flushed to saturation with an epoxy resin, and machine cut to thin slices of a few hundred microns in thickness. These slices then are examined and characterized by visual inspection under a microscope. This process is proven and well established, but its multiple preparation steps render it quite cumbersome and expensive (American Petroleum Institute, 1998, RP40, section 7).

Alternately, electron microscopy permits characterization of rocks to the ten-micron level (Krinsley et al., 1998). This method is particularly useful with shales, which tend to be mechanically unstable. Similarly to thin sections, electron microscopy is well established, but requires the installation and operation of the complex apparatus of the electron microscope with its sample preparation.

The preparation of rock samples entails some risks. In particular, rock-core samples that have been stored for an extended time will be altered at the surface, providing an incorrect picture of the reservoir rock in situ. In such a situation, an observational sample from deeper inside the core offers a more accurate picture. Furthermore, a rock sample saturated with multiple fluid phases could offer a more authentic picture if it has not been cleaned by artificial means but left, at worst, to dry out at the surface.

The challenge of such a rock-core analysis is to access the interior of the core, possibly with the connate fluids still present, and to analyze the rock texture and the pore structure with its surface wettability properties while the core still is in reasonably pristine condition (American Petroleum Institute, 1998, RP40, section 2). This desired method must be easy to use, rapid to execute, and comparatively inexpensive to compete with the established laboratory methods. Developing such a laboratory method and device is no simple task.

This study introduces a prototype laboratory device that provides a simple, repetitive laboratory procedure to examine the rock with optical means. A rock sample, preferably a barrel core, is drilled with a precision milling machine to a moderate, operator-controlled depth; in the machined hole a sapphire optical probe with an integrated conical mirror is inserted, which illuminates the freshly exposed surface and records a digital image with about a ten-micron resolution (Figure 1a). In a postprocessing step, the distortion induced by the mirror is removed by an "unwrapping" image-processing algorithm, and the individual images are combined to create a

---

Manuscript received by the Editor 10 February 2009; revised manuscript received 28 May 2009; published online 8 December 2009.
[1] Études et Production Schlumberger, Clamart, France. E-mail: mschneider@slb.com; frezgui@clamart.oilfield.slb.com; MLuling@clamart.oilfield.slb.com.
[2] École Supérieure de Physique et de Chimie Industrielles (ESPCI), Laboratory for Microfluidics, MEMS and Nanostructures (MMN), Paris, France. E-mail: patrick.tabeling@espci.fr; aurelien.daynes@bde.espci.fr.

single coherent image (Figure 1b). This digital image can be computer processed to extract semiautomatically the grain size, shape, and orientation information as well as fluid mobility properties.

Investigation of this particular imaging technique also serves as a research concept study toward a downhole measurement.

The second section of this study presents the laboratory installation and basic measurement procedure for the rock texture analysis. Section three presents several examples of rock images and their analysis/interpretation. In section four, the fluid mobility is studied by combining the optical measurement with controlled pressure gradients across the core sample. The concluding section summarizes the description of laboratory apparatus and procedure and the discussion of the first results.

EXPERIMENTAL SETUP

The proposed instrument, referred to as the microscopic grain imager (MGI), has been implemented in a first step as a laboratory setup, which provided all images and measurements presented in this study. Figure 2 schematically shows the optical components of the instrument. It consists of a camera plus lens, an oblique illumination device, and a sapphire probe. The camera was a PIKE F-421C from Allied Vision Technologies featuring a 4-megapixel charge-coupled device (CCD) chip and a Firewire B connection with data transmission rates as high as 100 MB/s. The camera was combined with an Apo-Componon 4.5/90 objective from Schneider Kreuznach, which performs extremely well at the required magnification range of about 1:1.

The oblique illumination device used in the laboratory setup was realized by a fiber-optic ring light illuminator connected to a KL1500 halogen reflector lamp from Schott. The ring light illuminator injects light into the sapphire probe at angles between 35° and 90° normal to the surface of the sapphire with the major intensity at 70°. It leaves a clear aperture of more than 20 mm; hence it provides an unobstructed view of the sapphire probe to the camera. Figure 2 also shows an optional linear polarizer, which is required to compensate for any birefringence in the sapphire probe. The angled design of the optical train was chosen to limit the overall system height and implement a compact system.

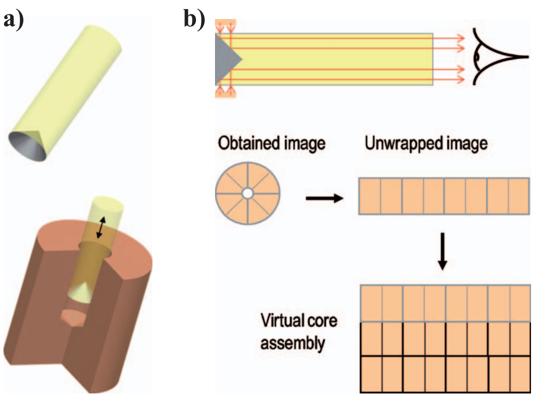

Figure 1. Sapphire probe and digital core-imaging principle. (a) Model of the optical probe (sapphire with conical mirror) as it is deployed in the cored hole. (b) Sketch of the coring process: At each position of the optical probe, an image of a ring of rock surface can be obtained as a circular distorted image. Unwrapping and assembly of the raw images are shown schematically as well.

The sapphire probe is a specifically manufactured, synthetically grown mono-crystal shaped as a rod with a 12-mm diameter. Sapphire was chosen as the probe material for its excellent optical transmission properties in the visible range combined with its outstanding mechanical properties, such as high strength and abrasion resistance (Schmid et al., 1997; Schmid et al., 1999; Wakaki et al., 2007). The only other candidate that could match the high durability of sapphire, diamond, was not considered because of its excessive cost. The end of the probe toward the camera has a flat, polished surface. The probe tip includes a conically shaped cavity with a full opening angle of 90°. The conical surface is highly polished with a silver coating, which renders it highly reflective as a conical mirror.

This sapphire probe is inserted into a machined, cored hole within the rock sample (Figure 1a). Because of the conical mirror, the probe provides a 360° view of the sidewalls of the cored hole at a certain depth. The raw images show the rock surface highly distorted; this distortion is corrected by an "unwrapping" image-processing algorithm (Figure 1b). The probe obtains images at several depths in the cored hole. These raw images are combined in a postprocessing step to create a single coherent image, the "digital core" (Figure 1). The maximum achievable surface area of the digital core for a given probe diameter depends on the effective penetration length of the sapphire probe. We had two probe lengths available with effective penetration lengths of 30 mm and 70 mm yielding maximum observation areas of 1110 mm^2 and 2600 mm^2, respectively.

The rock samples can be placed below the optical probe on a vertical elevator. The vertical elevator permits a precision movement in the axial direction between the rock sample and the optical probe.

Optical performance

Looking down the sapphire probe along the cylinder axis toward the conical mirror provides a right-angle view to the sidewall of the probe. For axis-parallel rays, the refractive angle is exactly 90° because the full opening angle of the cone is 90° as well. Although the mirror induces significant distortion, the optical path lengths stay the same as compared to a sapphire probe with a flat tip. This path is indicated by the orange ray in Figure 3. Therefore, except for the distortion, the image seen by the camera could be located also at the end of a flat sapphire tip, which will be referred to as a substituted object. The substituted object, a disk of diameter 12 mm, needs to be projected fully on the image sensor with a 2048×2048 pixel square matrix. In this case, each pixel corresponds to an area of less than $6 \times 6\ \mu m^2$ in the substituted object plane, yielding a theoretical resolution of 83 lp/mm (image line pairs per mm) according to the Nyquist-Shannon sampling theorem (Shannon, 1998).

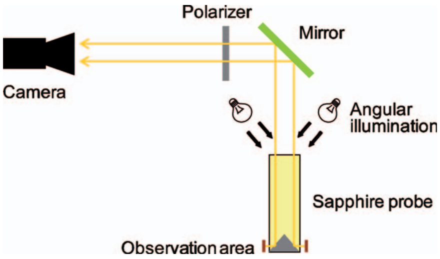

Figure 2. Sketch of the laboratory setup showing the optical path starting at the observation area and going through the sapphire probe, mirror, and polarizer toward the camera. The ring light illumination is indicated also.

Significant distortion is induced by the conical mirror in the sapphire probe, although the original dimensions can be restored with a postprocessing algorithm, referred to as unwrapping. However, the effective resolution varies significantly over the unwrapped image depending on the vertical and radial position (Figure 3). The object can be divided in rings with incremental extent in the vertical direction. Then each of these rings is projected to a corresponding ring on the conical mirror, which is seen by the camera. The diameters of the projected rings on the mirror decrease for increasing vertical position but still represent a full ring of diameter 12 mm in the real object plane. Therefore, the resolution is the highest for the area close to the tip (purple rays in Figure 3) of the sapphire, and it decreases significantly higher up in the vertical direction (turquoise rays). This distortion effect applies only to the radial direction; in the vertical direction, the projection theoretically is free of distortion.

The effective resolution was assessed experimentally with a T-20 microscopy resolution test chart that provides bar patterns with different numbers of black and white line pairs per mm. The contrast transfer function then was estimated by measuring and calculating the contrast c of several bar patterns according to the contrast equation (Hecht, 1988)

$$c = \frac{C_{\max} - C_{\min}}{C_{\max} + C_{\min}}, \tag{1}$$

where $C_{\max}$ and $C_{\min}$ are the gray values of the maximum and minimum, respectively.

The achievable contrast across the probe for three distinct test patterns is shown in Figure 4. The lower diagram shows that the contrast and hence the resolution in vertical (lateral) direction are fairly constant with respect to the vertical position. The contrast and resolution in the radial direction, however, decrease significantly at increasing vertical positions as the upper diagram in Figure 4 shows. Both observations are consistent with theoretical predictions.

According to Figure 4, the best contrast and therefore the highest resolution can be achieved at a vertical position of about 0.5 mm. The contrast transfer function was determined at this position by measuring the contrast of several distinct resolution patterns between 15 lp/mm and 55 lp/mm for the radial and lateral directions. At a spatial frequency of 50 lp/mm, the achievable contrast was 25% and 15% for the radial and lateral directions, respectively. With these percentages set as critical values for the contrast limit, the effective (experimentally determined) resolution of the device is 20 μm. According to this definition, objects at the resolution limit still show a contrast of 25% and 15% for the radial and lateral directions, respectively. A 20-μm object is represented by 3 pixels in the captured image, which corresponds to a pixel resolution of less than 7 μm. Therefore, features smaller than 20 μm still can be picked up by the system at certain conditions, i.e., if a very dark spot (pore edge) clearly distinguishes itself from a bright background.

The illumination technique of choice is an oblique illumination. Because of the dark-field illumination effect, the surface structure of the rock sample is enhanced and a depth perception is created that can help distinguish pore space from black mineral inclusions. The illumination light is provided under oblique angles by a fiber-optic ring light illumination and coupled into the sapphire rod. The rod acts as a light guide and delivers the light to the object plane. The primary condition for efficient light delivery is total internal reflection on the cylinder wall of the sapphire rod. The flat end of the sapphire, where the light is coupled in, is located inside the apparatus. Therefore, coupling always is realized through an air-sapphire interface.

By contrast, during a measurement, the lower part of the sapphire can be submerged in liquids such as water and oil, which changes the conditions for total internal reflection. Figure 5 shows the calculated critical coupling angle α_1 (cf. Figure 3) as a function of the index of refraction of the surrounding fluid. If light is coupled into the sapphire rod at angles larger than α_1, then these light rays are not guided and will escape the sapphire probe. As can be seen from Figure 5, for typically occurring liquids such as water and mineral oil the sapphire rod acts as a perfect light guide. Even in the rare situation of performing measurements while submerged in a synthetic high-refractive-index oil ($n = 1.5$), there still exists a large fraction of light that is guided by the sapphire probe. Therefore, the sapphire probes do not require an additional coating of the cylinder surface to act as light guides with adequate efficiency.

The light source reaches an illuminance of the object between 20 and 150 klx depending on the power setting at the lamp. These values were obtained by measurements with a 545 Luxmeter from Testo.

ROCK IMAGING

The milled hole provides access to a clean, well-defined rock surface for the optical probe. If the milling-bit geometry, as well as cutting speed and feed rate, is chosen properly, the lateral surface of the hole will provide an accurate representation of texture and pores. Furthermore, defined by the size of the bit, the milled hole can be created repeatedly and reliably with the internal diameter being only slightly larger than the outer diameter of the sapphire probe, hence leaving only a very narrow gap between probe and rock surface in

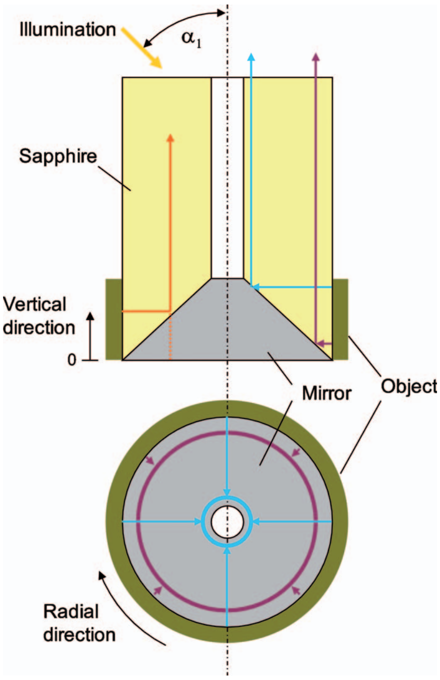

Figure 3. Schematic image of the sapphire tip. Selected raypaths in the sapphire probe are shown for the imaging part. For simplification purposes, the "object" is drawn to fit the sapphire probe tightly. Definitions for vertical and radial directions are given.

the order of a few hundred micrometers. Because the depth of field (DOF) of the MGI can be controlled by the aperture of the internal objective and typically is set to be at least 500 μm, the obtained images always are in focus. The resulting rock images or digital cores permit the extraction of a variety of features related to porosity and texture by means of petrographic image analysis (PIA), such as the size, shape, and distribution of pores and grains (Anselmetti et al., 1998; Layman and Ahr, 2004).

Image processing

The digital core-imaging experiments followed a specific protocol. The imaging process started with the sapphire probe at its most forward-deployed position, at which system parameters such as exposure time and illumination intensity were adjusted. A series of images then was taken while retracting the optical probe from the milled hole at intervals between 0.5 and 1 mm. After all rock images were obtained, a last frame was taken of a white, ideally diffusing object, which served as the white reference. An image-processing routine then was applied to the image sequence to obtain the digital core image.

The image-processing routine was created within the image-treatment software Inspector 8 from Matrox, which is built on the Matrox Imaging Library (MIL) algorithms. The image-processing routine consisted of three main steps. First the distortion induced by the conical mirror was corrected by means of an image-unwrapping algorithm. The unwrapping algorithm transforms a selected annulus region in the source image to a rectangular target image.

Besides the source image itself, the inner and outer radius and center coordinates of the annulus, as well as a starting angle, are passed to the unwrapping algorithm. The algorithm then cuts the annulus at the specified starting angle and unwraps the data into a rectangular image. Although the outermost circle of the annulus is mapped pixel by pixel to the top line of the target image, smaller circles toward the inner limit of the annulus lack the appropriate number of pixels and need to be interpolated when mapped to a line in the target image. As the diameter of the optical probe is known and the circumference of the probe itself can be seen in each image (cf. Figure 6), this “built-in” reference is used to calibrate pixel-dimensions with real dimensions.

In a second step, brightness gradients were subtracted from each frame with the aid of the white reference image to obtain an even-intensity distribution. This step is crucial, and care must be taken to obtain a proper white reference. If nonideal conditions exist (e.g., a slight misalignment in the white reference), a subtle brightness gradient remains, which causes the appearance of “stripes” (sudden steps in brightness) in the final digital core image.

In a third step, the individual images were combined to create a single, coherent digital core image. A pattern recognition algorithm was used on each image to identify its position with respect to the preceding image. Each image then was placed in the global digital core image according to the position identified by the pattern recognition algorithm. This particular assembly approach yields accurately assembled digital core images independent of the mechanical accuracy in the step size.

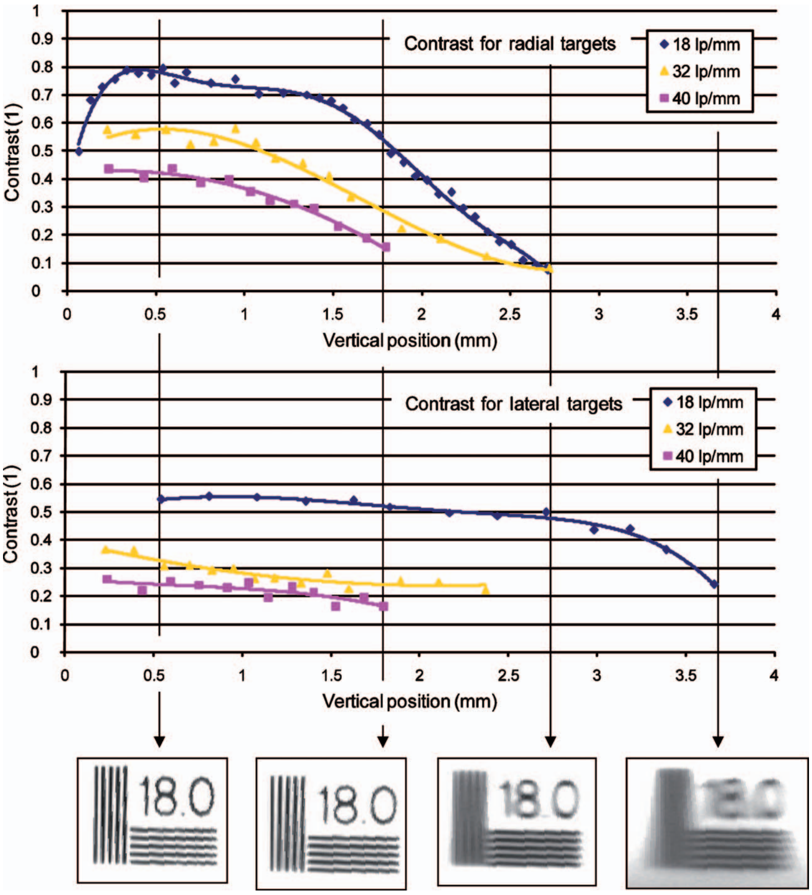

Figure 4. Measured contrast across the probe area for three resolution patterns. The upper diagram shows the results for radial resolution; the lower diagram shows the results for lateral (vertical) resolution. In the bottom part of the figure, samples of measurements with the 18 lp/mm pattern are shown. The left part of the pattern determines radial and the bottom part lateral (vertical) resolution.

Digital core imaging

Figure 6 shows an example of a digital core image from a rock sample featuring distinct channel porosity. One of the raw images obtained by the sapphire probe is shown in the upper left part of the figure. A section of the assembled digital core image (cf. Figure 1) covering roughly 400 mm^2 of rock surface is shown in the lower part of the figure. As shown in the zoom view, pore throats as small as a few tenths of microns in diameter, as well as different grains and textures, can be distinguished easily from the digital core image.

Additional examples of digital cores are shown in Figure 7 for a limestone sample and a sandstone sample. In the left (Part a) of the figure, the digital core image clearly identifies pores as small as a few tenths of microns. In addition, the sandstone example clearly distinguishes individual grains.

Figure 8 shows a comparison between different optical imaging techniques. The digital core image shown in Figure 8a was obtained by milling a hole into the rock sample and using the MGI for imaging. A detail view of the core image is shown in Figure 8b. In a subsequent step, the rock sample was cut in half and the inside of the milled hole was inspected under a stereomicroscope SZX12 from Olympus. Images were taken with a ColorView 3 camera from Olympus connected to the microscope, which can provide 5 -megapixel color images. Figure 8c shows an image of the rock surface under highly oblique illumination from a fiber-optic light source; the image in Figure 8d shows the same rock surface obtained with the microscope's internal axial illumination. The two images obtained with the microscope, as well as the detail view of the MGI image (Figure 8b-d), show the same rock-surface area.

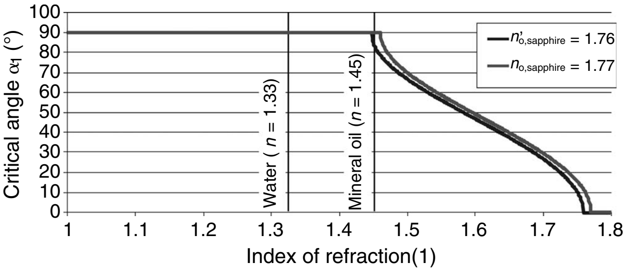

Figure 5. Critical coupling angle in terms of the index of refraction of the surrounding fluid. The actual coupling angle must be equal to or smaller than the given values.

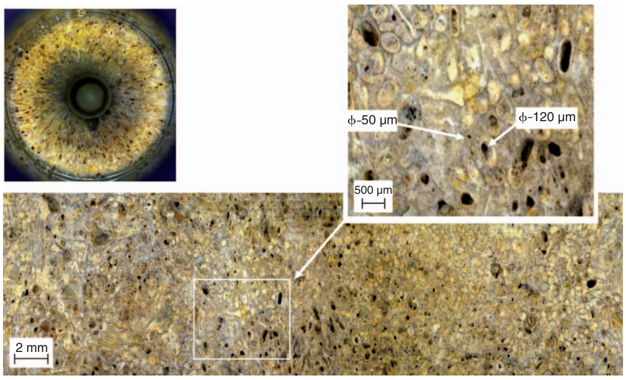

Figure 6. Example of a "digital core" obtained from a rock sample with a strongly heterogeneous pore structure covering about 400 mm^2 of rock surface. One of the raw images as obtained during the digital core-imaging process is shown in the upper left corner. A magnification of a selected area is given in the upper right corner showing grain and pore features as small as a few tenths of microns.

As can be seen in Figure 8c, oblique illumination provides excellent contrast between pits (pores) and the reference surface. This high-relief contrast occurs mainly because the pits appear as dark shadows cast by the surrounding grains as a result of light incident under highly oblique angles. In comparison, the image taken with axial illumination (Figure 8d) does not provide any depth perception or relief information because the incident light easily can reach the bottom of the pits and no shadows are cast in the image. However, perpendicular surface illumination (axial illumination) provides a much better contrast between surface colors, which helps distinguish different minerals, whereas for highly oblique illumination, detail information about the surface composition is lost. As can be seen in Figure 8b, the MGI image with its oblique illumination at moderate angles provides a good compromise between the two extremes. Although deep pits can be distinguished clearly, enough color contrast still is present to analyze the surface composition.

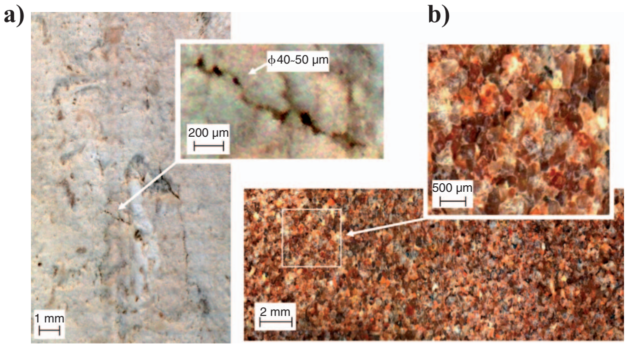

Figure 7. Examples of digital cores from two rock samples. (a) Digital core image obtained from a white chalky carbonate rock. (b) Digital core image obtained from sandstone. Additional zoom views of distinct features are shown for both digital cores highlighting the true resolution of the images.

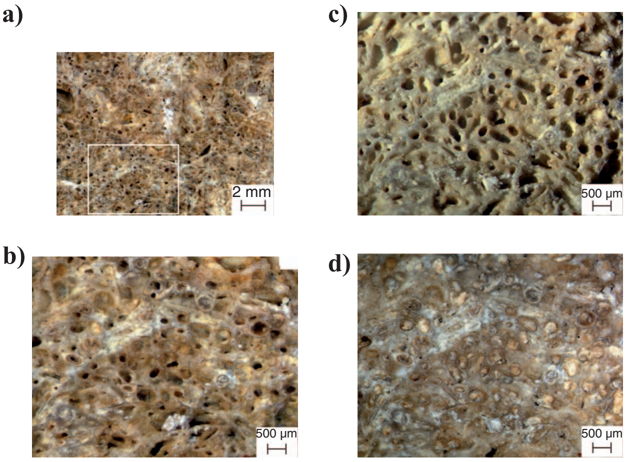

Figure 8. Comparison of rock-imaging techniques. (a) A digital core image obtained with the MGI, and (b) a detail view of the same image. Parts c and d show images of the same rock section as in Part b, obtained with a stereo microscope. Part c shows an image obtained with highly oblique illumination; Part d was obtained with axis-parallel illumination.

An image of the same rock sample taken with a scanning electron microscope (SEM) is shown in Figure 9. It is apparent that SEM images can reveal the surface topology in much greater detail. However, surface topology (depth information) is the only information retrieved by the SEM, whereas optical images provide color information as an additional property.

The digital core images presented above were obtained in air. However, rock-grain images can be acquired also in the presence of liquids. The narrow gap size between the sapphire probe and the rock surface, as mentioned above, offers another significant advantage: It permits images to be obtained even in the presence of dark attenuating liquids, such as crude oil.

An experiment was conducted on a limestone rock with a cored hole of 12.3 mm in diameter, hence resulting in a gap of approximately 150 μm. First an image was obtained of the dry sample. Then another image was obtained with the sample soaked in water. Finally, after drying, a third image was obtained of the sample saturated with a light crude oil. Sections of each digital core image from the same region of the rock are shown in Figure 10 for comparison. Because clean water is entirely transparent in the visible light range, the digital core image obtained in water is very similar to the one obtained in air. Both images were taken with identical exposure times. The only difference is that the digital core image obtained in water shows slightly less relief information because of the higher refraction index of water.

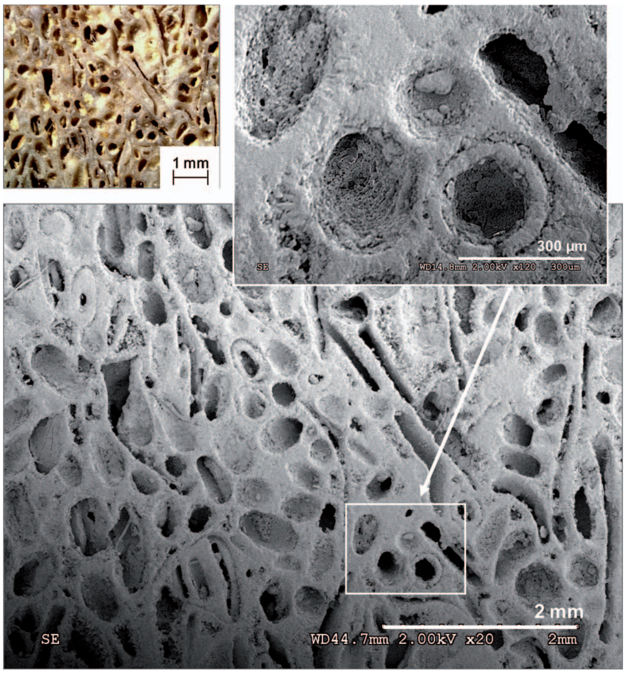

Figure 9. An SEM image of a rock sample similar to the one in Figure 8. A photograph of the sample section taken with visible light under oblique illumination is shown in the upper left corner. The upper right part shows a detail view of the SEM image.

The digital core image obtained in crude oil required an increased exposure time (a factor of 2.5) to compensate for absorption losses in the liquid; it resulted in an image with a reddish touch. Figure 11 shows that light attenuation in crude oil increases for decreasing wavelengths, hence featuring the red shades in the transmitted image. This effect can be corrected easily by means of a postprocessing color correction (Figure 10). Compared to absorption spectra of other crude oils published in the literature (Mullins et al., 2007; Andrews et al., 2008; Venkataramanan et al., 2008), the sample used corresponds to a light crude oil or to a heavy crude oil diluted by a transparent solvent. Although a few color nuances are missing in the digital core image obtained in crude oil, all the relief and pore information is clearly visible, which demonstrates the capability of the MGI to obtain digital cores even in the presence of an optically absorbing liquid.

a) Image obtained in air

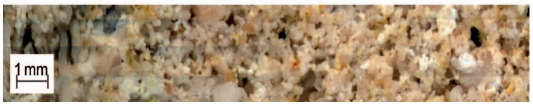

b) Image obtained in water

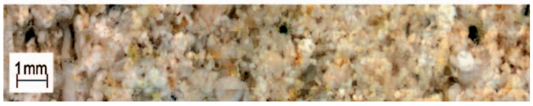

c) Image obtained in a light crude oil (raw)

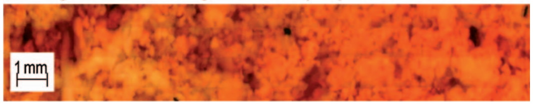

d) Image obtained in a light crude oil (color corrected)

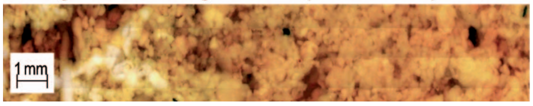

Figure 10. Rock images obtained from the same sample at the same spot while immersed in (a) air, (b) water, and (c), (d) a light crude oil. Image (c) in crude oil was taken with an exposure elevated by a factor of 2.5. Part d image shows image (c) after applying a color correction to compensate the reddish color of crude oil. The rock structure and pores are clearly visible in all images despite the surrounding fluid.

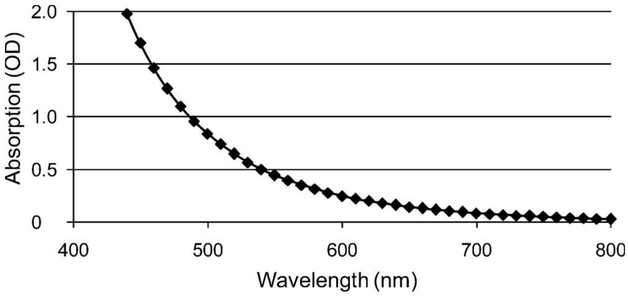

Figure 11. Absorption spectrum of the light crude oil measured with a laboratory grade spectrometer for an optical path length of 2 mm. The absorption is given as optical density (OD).

Image interpretation example

Image analysis software Inspector and MIL from Matrox was used on the sample shown in Figure 6 to analyze the channel porosity. Pores with an area greater than 1000 μm^2 were identified and classified with a blob analysis algorithm. This particular threshold for the pore area corresponds to a pore diameter of about 35 μm in the case of a circular pore aperture, which corresponds to macroporosity as defined by Eberli et al. (2004). Figure 12a shows the rock-grain image with the identified pores shaded in blue.

The pore-size (area) distribution is given in Figure 12b, and Figure 12c shows the distribution of the dimensionless pore-shape factor γ (Anselmetti et al., 1998):

$$\gamma = \frac{P}{2\sqrt{\pi A}}, \qquad (2)$$

where P and A are the perimeter and area of the pore, respectively.

The macroporosity retrieved by the PIA technique represents a certain fraction of the overall rock porosity, neglecting the finer pores excluded by the area threshold as well as micropores that are not visible by means of optical imaging (Cunningham et al., 2004). Precisely this macroporosity fraction dominates the rock's permeability properties (Eberli et al., 2004), which makes it a property of significant interest. By considering only the rock's macroporosity, or more precisely the pore-shape factor γ of the macroporosity, the uncertainty in the porosity-permeability correlation can be reduced by two orders of magnitude (Eberli et al., 2004). If the analysis of multiple sampling points is combined, the uncertainty of the estimated permeability decreases even further (Kameda et al., 2006). In addition, if grain-size analysis is performed on the image, these data can be used to verify and strengthen the detected pore-size information by means of a grain-size to effective pore-size transformation (Glover and Walker, 2009). Obtaining such properties by analyzing MGI digital core data for several different rocks has shown to be very powerful and promising. However, the intent of this section is briefly to highlight the value and importance of the static imaging part of the MGI.

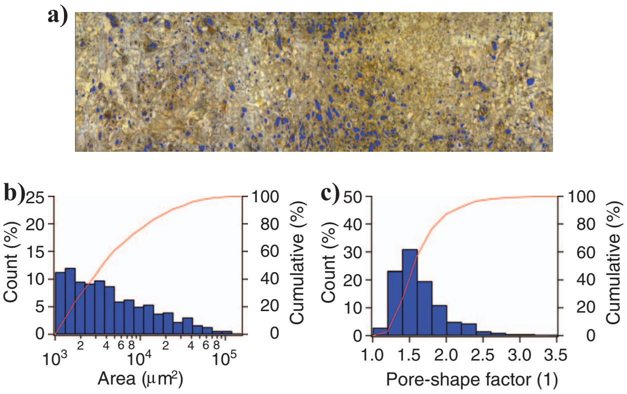

Figure 12. Pore space identification example of digital core data. (a) Digital core image with identified pore areas highlighted in blue. (b) Pore-size distribution chart (histogram) including the cumulative size function (red). (c) Pore-shape distribution chart (histogram) including the cumulative shape function (red).

DYNAMIC MEASUREMENTS

In addition to the application of static digital core imaging, the MGI can be used also to observe dynamic fluid movements as they emerge from the rock. For these dynamic measurements, the optical probe typically is placed at a desired fixed depth. The camera is operated in video acquisition mode to observe fluid movement over time. A series of such dynamic measurements was conducted to investigate permeability phenomena.

Setup modifications

For the dynamic fluid measurements, the same MGI setup configuration was used; however, the camera typically was operated in a subsampling mode to increase the achievable frame rate. The experiments were carried out with two limestone samples, Sireuil and Saint-Maximin Sebastopol from central and southern France. The samples were obtained as cylindrical cores of the diameter 45 mm and length 50 mm. Whereas the Saint-Maximin was representative of a strongly water-wet sample, the Sireuil showed signs of an intermediate wettability state.

A specific sample cell was designed for the fluid experiments, which allows the rock sample to be mounted centrally in a way that fluid access is provided on the outside to the bottom surface as well as to a large fraction of the lateral surface (Figure 13). Each rock sample was bonded to an individual adapter ring to facilitate the exchange of the samples. By means of an additional silicone sleeve, fluid access to the rock surface could be restricted further, e.g., access to the bottom or lateral surface only. The applied pressure gradients were measured with differential pressure sensors from the Honeywell 26PC series directly in the sample cell. Fluids were injected at constant flow rates using syringe pumps from New Era Pumping Systems.

For air injection experiments, the air was given access to the entire available rock surface with the rock sample initially saturated with water. This type of experiment corresponds to a drainage case. For water injection experiments, the lateral surface of the rock sample was sealed with a silicone sleeve to provide fluid access to the bottom surface only. Two fundamentally different measurement approaches were used: (1) water injection in a dry sample and fluid imaging with the MGI as close to the bottom of the cored hole as possible (Figure 14a and 2) water injection in an already saturated sample and fluid imaging with the MGI close to the top surface (Figure 14b).

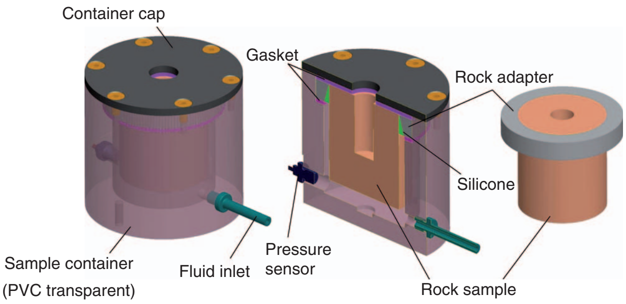

Figure 13. Sample holder with rock sample. The rock sample is glued to an adapter ring, which allows for rapid sample changes. The sample is held in a transparent sample cell, which also provides a fluid inlet and a pressure sensor.

Theoretical background

Two main cases, imbibition and drainage, need to be considered, depending on whether the injected fluid is wetting the rock with respect to the other fluid or vice versa.

Imbibition case

In the case of imbibition, for instance, water imbibing a water-wet (i.e., hydrophilic) rock sample, the liquid first invades the lower part of the sample, which was initially dry (cf. Figure 14a). Then it penetrates into the milled hole by forming films between the sapphire probe and the rock sample, which rapidly grow, coalesce, and form a meniscus, which moves upward and eventually floods the entire space left between the optical probe and the sidewall of the hole. This process is shown schematically in Figure 15.

In this case, we measure the position of the meniscus in real time as it passes the observation area of the sapphire probe. From the known frame rate, we determine the velocity V_f of the fluid front and further calculate the corresponding flow rate Q according to the relation

$$Q = V_f \cdot A_{\text{gap}}, \tag{3}$$

where A_{gap} is the cross-sectional area of the annular space between the sapphire probe and the sidewall of the cored hole. For the experiments presented in this study, the inner diameter of the cored hole d and hence the resulting A_{gap} have been measured with a three-point internal micrometer at several depths after drilling to obtain maximum accuracy. In general, however, with a well-characterized drill bit the resulting diameter can be assumed from its geometry with sufficient accuracy.

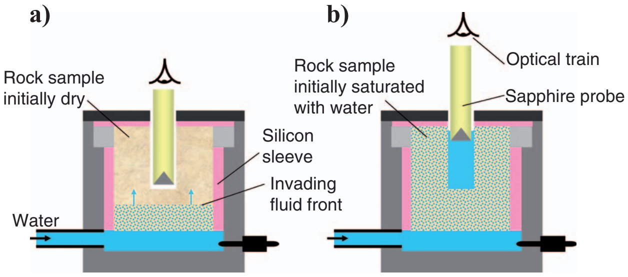

Figure 14. Setup for fluid injection experiments. (a) True imbibition case whereby water is injected into an initially dry rock sample, hence providing a transient state measurement. (b) Steady state measurement, whereby water is pushed through an already saturated rock sample.

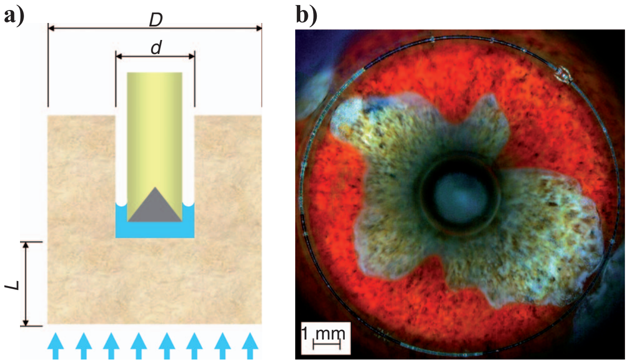

Figure 15. Measurement principle for the water injection experiments (imbibition case). General sample dimensions are indicated. (b) Typical image as obtained during a measurement. Red-dyed water is emerging from the bottom (outer ring) and rising upward (toward the center).

The permeability of a bulk material is defined by the Darcy relation

$$\kappa = \frac{\mu L}{\Delta P} q, \tag{4}$$

where μ is the fluid viscosity; L is the effective length over which the pressure drop ΔP is applied; and q is the magnitude of the fluid flux, i.e., the flow rate per unit area.

The flux magnitude q is related to the flow rate Q by the reciprocal of an effective area. For the sample geometry used in this study, the effective area is expressed as the cross-sectional area of the cylindrical sample multiplied by a correction factor β that considers the flow restrictions near the cored hole. Hence the flux magnitude can be defined as

$$q = \frac{4\beta}{\pi D^2} Q, \tag{5}$$

where D is the outer diameter of the cylindrical sample as shown in Figure 15a.

The correction factor β was determined by a finite-element method (FEM) flow simulation with ANSYS (software by ANSYS, Inc.). The simulation was carried out for a fully saturated model with outer cylinder diameter D, inner diameter d of the cored hole, and effective length L between the bottom of the cored hole and the bottom cylinder surface (cf. dimensions in Figure 15a). The mathematical basis for the simulation was the more general form of Darcy's law (Wyckoff et al., 1934; Whitaker, 1966; Bear, 1972; Scheidegger, 1974):

$$q = -\frac{\kappa}{\mu} \nabla P, \tag{6}$$

where ∇P is the pressure gradient. Permeability κ and viscosity μ were set equal to one to obtain normalized results. The simulated flow patterns are shown in Figure 16, which also indicate the boundary conditions reproducing the conditions in the real sample mount.

Simulations were performed with dimensions normalized with respect to the outer cylinder diameter, i.e., d/D and L/D covering a wide range of aspect ratios around the real samples. The aspect ratio of cored-hole depth versus outer diameter was kept at the constant value of 0.57 as given by the used sample. Figure 17 shows the simulation results as the ratio between the real flow rate and the flow rate found in a corresponding cylinder of length L with no restrictions, which is by definition the correction factor β. The results for our particular sample geometry are indicated by the black diamonds.

Evaluation of the simulated flow pattern showed that in a steady state situation, 50% of the flow emerges from the bottom part and the lowest 3 mm of the sidewall of the hole (red arrows in Figure 16). Because the tip of the sapphire probe is protected by a metal cap of 3-mm thickness, the region visible by the probe starts 3 mm away from the bottom of the hole. In the case of a water injection experiment with an initially dry rock sample (Figure 14a) where the probe is deployed fully into the hole, the water that is passing by the visible area of the probe has accumulated from the bottom part and the lowest 3 mm of the sidewall of the hole, and therefore corresponds to 50% of the overall flow rate in the rock sample. This is in contrast to the observations in experiment 2 (Figure 14b) with a fully saturated sample, where the probe was deployed close to the top of the sample and the observed flow rate was equal to the overall flow rate in the rock sample.

Drainage case

In the case of drainage (e.g., air flowing through the water-wet rock sample initially saturated with water), the fluid invades the porous medium in a more complex way: Depending on the viscosity ratio and the invasion speed, fingering can occur. Even in the absence of fingering, the front moving through the porous medium develops complex patterns typical for percolation processes. As the front reaches the cored hole (initially filled with water), bubbles (or drops) form, expand, fill the gap, and eventually, after pinching off, rise up vertically and collapse at the water surface. Bubble-interface velocities can be measured as they emerge from the pores of the rock sample. The principle of the measurement along with a real image is shown in Figure 18.

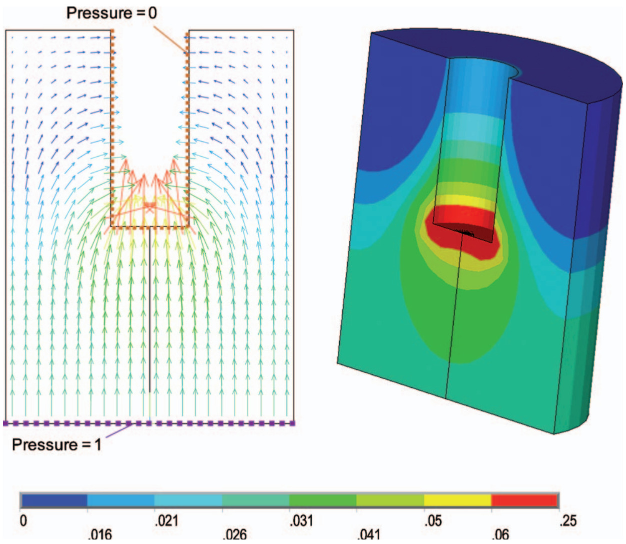

Figure 16. An ANSYS simulation of the flow pattern for a fully saturated rock sample. Results are shown as a vector plot (left side) and a contour plot (right side). The applied boundary conditions are indicated in the left plot. Edges with no conditions applied were treated as walls.

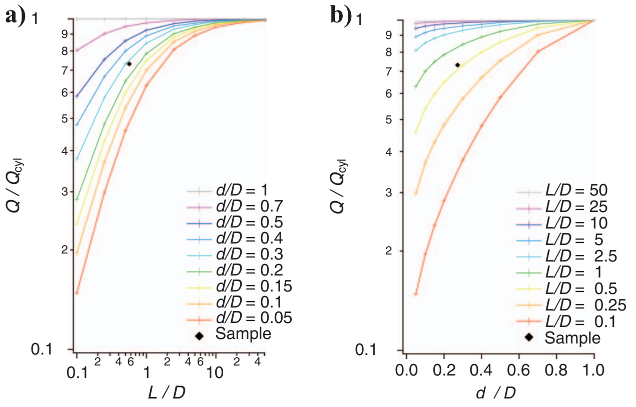

Figure 17. Simulation results for the correction factor β for different aspect ratios of the sample. The correction factor $\beta = Q/Q_{\mathrm{cyl}}$ relates the flow rate to the sample with a cored hole to the flow rate of a cylindrical sample without the annulus section. (a) Diagram shows the correction factor as a function of the cylinder length. (b) Diagram shows the correction factor as a function of the cored-hole diameter.

This measurement is fundamentally different from the previous case because only a fraction of the flow can be observed at a time, whereas in the imbibition case Q was directly accessible by observing the advancing fluid front. Without direct access to the flow rate, Q has to be determined via an average pore-fluid velocity:

$$\bar{V}_{\mathrm{P}} = \frac{q}{\varphi_{\mathrm{eff}}}. \tag{7}$$

Here φ_{eff} is the effective porosity of the connected pores, which can be accessed by the fluid, given as the dimensionless ratio of pore space to bulk volume. The average pore-fluid velocity needs to be determined by a sufficient number (ideally all) of local pore-fluid velocities V_{P}. If only a small fraction of active pores can be observed, the resulting average pore-fluid velocity $\bar{V}_{\mathrm{P}}$ and hence the flux magnitude q suffer from significant error.

RESULTS AND DISCUSSION

Wetting fluid injected in saturated sample

We first consider water injection into a saturated sample according to Figure 14b: Figure 19 shows the evolution of the water flow rate Q with the applied pressure difference ΔP for the strongly water-wet rock sample Saint-Maximin. The plot shows that the flow rate is proportional to the applied pressure as predicted by Darcy's law. Not only the advancing but also the retracting fluid front was measured after inverting the pumping direction. These data points appear in Figure 19 as negative flow rates at negative pressures.

The permeability was calculated from the data shown in Figure 19 according to equations 4 and 5, with the correction factor $\beta = 0.70$ for the sample geometry in use according to Figure 17. The result of 336 ± 57 mD for the permeability as calculated from all 21 data points provides a reasonable precision, and it further corresponds well with the permeability to air of 353 ± 4 mD as found in a reference measurement using an airflow, which was conducted on the bulk cylinder prior to drilling the cored hole. The measurement

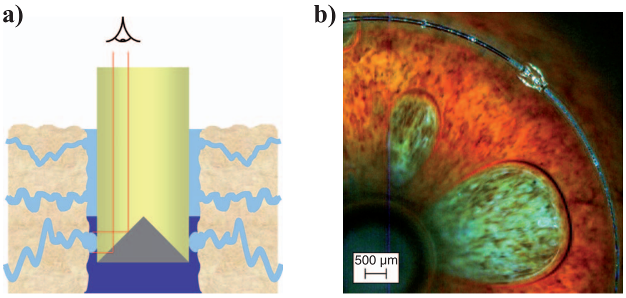

Figure 18. Measurement principle for the air injection experiments (drainage case). As the schematic shows, the optical probe is observing the fluid bubbles as they emerge from the pores and grow until they detach and rise to the surface. (b) Section of a typical image as obtained during a measurement. Two air bubbles are emerging from pore channels and displace the red-dyed water.

shows that the MGI measuring technique could determine permeability with sufficient precision and accuracy for this particular sample.

Another set of measurements was conducted on the Sireuil sample as shown in Figure 20. Again, the permeability of 94 ± 22 mD as calculated from 26 data points provides a reasonable precision. Because the Sireuil sample shows signs of intermediate wettability, water saturation was only partial in this case. The permeability measured by water injection is therefore the partial permeability of the rock for water, which has to be smaller than the absolute permeability as the nonwetted pores are not contributing to the throughput (Tiab and Donaldson, 2004). Indeed, the absolute permeability was found to be 253 ± 4 mD in the reference measurement using an airflow.

Wetting fluid injected in dry sample: Imbibition case

Experiments were conducted also for the imbibition case, in which the samples were completely dry prior to the water injection, as shown in Figure 14a. Measured flow rates as functions of the applied pressure difference are given in Figure 21 for both rock samples. The figure shows that the relation between the measured flow rate and the applied pressure for these particular experiments is not linear. Whereas for small pressure differences the detected flow rates are much smaller than expected, a converging behavior toward the predicted flow rates can be observed for increasing pressure differences. The undersized flow rates at small pressures can be explained by spontaneous imbibition. Spontaneous imbibition describes the fluid uptake driven by capillary forces, which depends strongly on the rock-fluid contact angle, interfacial tension, and pore size. For increased applied pressures and therefore increased flow rates, forced imbibition becomes the dominant mechanism, and the effects of spontaneous imbibition become increasingly negligible.

A detailed examination of the images obtained during these measurements has shown that the MGI observes a "dark shadow" preceding the observed fluid front. This "dark shadow" corresponds to a fluid front inside the rock sample that causes the rock to appear darker after the grains have been wet by a film of water. For small flow rates, this internal fluid front, driven by spontaneous imbibition, precedes significantly the fluid front in the observation gap, which is driven by forced imbibition.

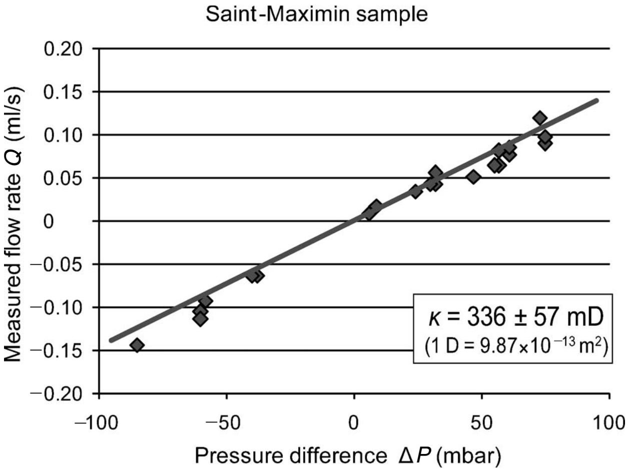

Figure 19. Measured flow rate versus applied pressures for the strongly water-wet Saint-Maximin sample. The sample was saturated initially with water, and the measurements were performed close to the top of the cored hole (cf. Figure 14b). The measured data points are shown as diamonds, which align well with the expected evolution of the flow rate (straight line) according to the reference permeability.

Air injected in wet sample: Drainage case

Another set of data was obtained with air injection into a water-wet sample initially saturated with water. We operate in this case in a drainage regime in which the fluid front is likely to develop instabilities because the displacing fluid (air) is of lower viscosity than the displaced fluid (water). Pore-level measurements of the flow rate are shown in Figure 22, in which each asterisk represents a measurement of an individual bubble at a certain pressure. The calculated average pore-fluid flow rates are indicated by the dark diamonds, including their standard deviation. A trend of increasing pore-fluid flow rates for increasing pressures is visible even though the few pores that were observed represent only a fraction of the producing pores. However, variations from the linear fit are significant, which add significant uncertainty to an absolute permeability value determined from these data.

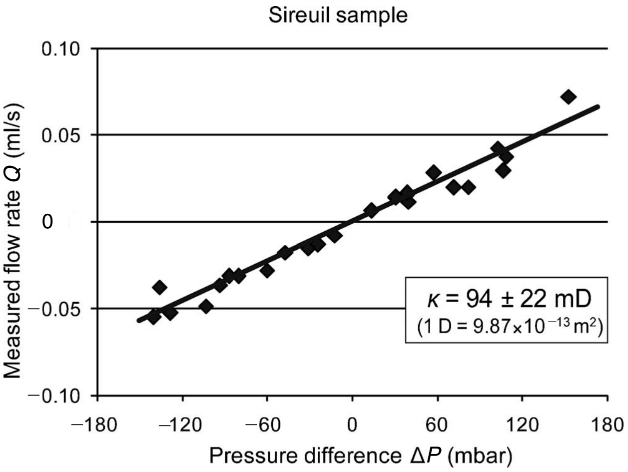

Figure 20. Measured flow rate versus applied pressures for the mixed-wet Sireuil sample. The sample was initially saturated with water, and the measurements were performed close to the top of the cored hole (cf. Figure 14b). The measured data points are shown as diamonds; the straight line shows the best linear fit to this data.

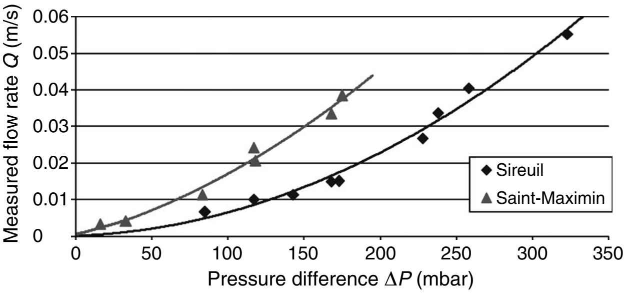

Figure 21. Measured flow rates versus applied pressures for the Saint-Maximin sample and the Sireuil sample. The samples were dry prior to each measurement, and transient imbibition measurements were performed with the optical probe close to the bottom of the cored hole (cf. Figure 14a).

Nevertheless, because of the capability of the MGI to observe percolation on the pore scale, various kinds of valuable information can be extracted from the measurements, such as number and size of the contributing pores. As an example, Figure 23 shows two image sequences of sections around a percolating pore. A section of the unwrapped image of the rock sample is shown in the upper half of each frame. The lower half shows the differential image of two consecutive frames, which clearly outlines the moving fluid interface. For demonstration purposes, the water has been dyed red to improve visibility. Figure 23 shows static bubbles, which do not correspond to a percolating pore. As these bubbles are not moving, their interfaces do not appear in the differential images; this fact makes this technique even more valuable for this particular image analysis.

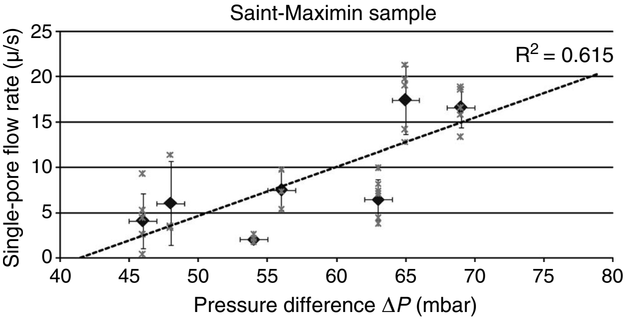

Figure 22. Measured single-pore flow rates at various applied pressures in the drainage case. At each pressure step, all visible bubbles/pores have been evaluated. Each asterisk corresponds to a measurement from an individual bubble. The calculated average is shown as a dark diamond for each pressure step, with the error bar denoting one standard deviation. The dashed trend line shows a linear trend according to a linear best fit.

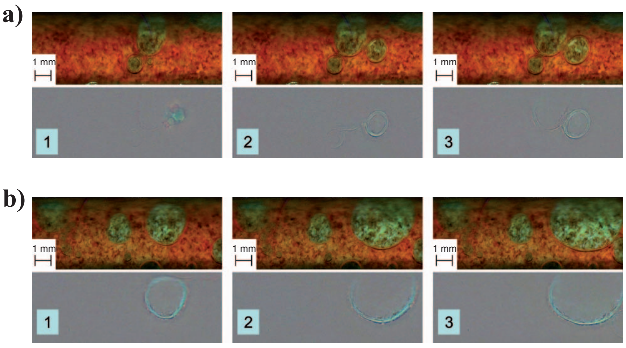

Figure 23. Image series from an air injection measurement performed with the Saint-Maximin sample initially saturated with red-dyed water. The two series (a) and (b) show three frames each at intervals of one second from a chronological series showing the evolution of a bubble emerging from a percolating pore. The upper part of each frame shows a section of the rock image where the air bubbles appear in the original rock color as they displace the red-dyed water. The lower part (gray background) shows the corresponding differential image, i.e., the difference in the image between two consecutive frames. Whereas the real images show several bubbles, the differential images show only the growing bubbles with moving interfaces.

From fluid mobility toward rock permeability

The dynamic measurements of the grain imager in the presence of external pressure clearly show fluid moving out of the pores at the exposed surface. This observation raises the hope that the present measurement might lead to a direct observation of rock permeability. However, it would be premature to promise quantitative permeability estimation from this optical measurement alone.

Extensive laboratory observations on several rock samples, repeated for each sample several times, show a repeatable process of first fluid breakthrough. There tends to be a single macroscopic pore or a small number of distinct pores that show fluid arrival, whereas the majority of the pores are lagging behind. The permeability is dominated by these pores. At the same time, the optical image alone cannot be used to estimate permeability from such single pores: These pores represent a minuscule fraction of the exposed surface that statistically is not representative. If the overall reference surface was divided into smaller reference surfaces, the breakthrough pore size would not change; hence, the estimated permeability as the ratio of the breakthrough pore size to the exposed reference surface would be changed according to the arbitrary choice of reference surface. On the other hand, the timed image of the first breakthrough, along with the geometry and the hydraulic pressure dynamics of the rock-core cell, provides a quantitative lower bound for the fluid mobility estimate.

CONCLUSION

This study introduces a novel microscopic grain imager (MGI) instrument for rock imaging in the visible light range. Rock preconditioning by machining a hole proved very valuable. The images obtained with this technique showed clean, well-defined, and sharply focused rock surfaces, even in the presence of attenuating liquids. The optical performance of such a device was assessed carefully, and it could be shown that rock images can be obtained of somewhat large areas (more than 1 cm^2) at resolutions that are sufficiently high (better than 20 µm) to allow for lithographic and petrographic rock studies. The core image examples presented in the study show that the overall image quality is sufficiently high to identify individual grains and pores as well as to observe grain distribution. In particular, the comparison with images obtained by other imaging techniques shows that the MGI images provide a good compromise between relief contrast and color contrast. Thus the obtained images are well suited for interpretation regarding structural and compositional information.

In a second part, the capability of the MGI to observe and study fluid dynamics on the pore scale was demonstrated successfully. It was shown that the MGI is capable of repeatedly measuring accurate flow values on the microscale and determining localized permeability values within reasonable accuracy. Although upscaling of these locally measured permeability values will not be possible in heterogeneous rock, a variety of observations can be made, such as observations of fluid breakthrough on the pore level and the number of producing pores with pressure, which are related to fluid mobility.

NOMENCLATURE

Definition	Dimensions	Units
A = area	L^2	m^2
A_{gap} = area of annular gap	L^2	m^2
c = contrast	n	1
C = gray value	n	1
d = inner diameter	L	m
D = outer diameter	L	m
L = length	L	m
n = index of refraction	n	1
P = perimeter	L	m
q = flux magnitude (filter velocity)	L/t	m/s
Q = flow rate	L^3/t	m^3/s
V_f = fluid front velocity	L/t	m/s
V_P = pore velocity	L/t	m/s
α_1 = critical coupling angle	n	°
β = coefficient	n	1
ΔP = differential pressure	m/Lt^2	Pa [mbar]
φ = porosity	n	1
γ = pore-shape factor	n	1
κ = permeability	L^2	m^2 [mD]
μ = viscosity	m/Lt	kg/ms [cP]
∇P = pressure gradient	$1/Lt^2$	Pa/m

REFERENCES

American Petroleum Institute, 1998, Recommended practices for core analysis: RP, 40, 2nd ed.: Copy reproduced under license from American Petroleum Institute by ILI INFODISK Inc., (www.ili-info.com).

Andrews, A. B., M. H. Schneider, J. Canas, E. Freitas, Y. Song, and O. C. Mullins, 2008, Fluorescence methods for downhole fluid analysis of heavy oil emulsions: Journal of Dispersion Science and Technology, **29**, 171–183.

Anselmetti, F. S., S. Luthi, and G. P. Eberli, 1998, Quantitative characterization of carbonate pore systems by digital image analysis: AAPG Bulletin, **82**, 1815–1836.

Bear, J., 1972, Dynamics of fluids in porous media: Dover Publications.

Cunningham, K. J., J. I. Carlson, and N. F. Hurley, 2004, New method for quantification of vuggy porosity from digital optical borehole images as applied to the karstic Pleistocene limestone of the Biscayne aquifer, southeastern Florida: Journal of Applied Geophysics, **55**, 77–90.

Eberli, G. P., G. T. Baechle, R. Weger, and J.-L. Massaferro, 2004, Quantitative discrimination of effective porosity using digital image analysis — Implications for porosity-permeability transformation: Presented at the 66th Annual Conference and Exhibition, EAGE, accessed 12 October 2009, http://mgg.rsmas.miami.edu/students/greg/EAGE2004.pdf.

Glover, P. W. J., and E. Walker, 2009, Grain-size to effective pore-size transformation derived from electrokinetic theory: Geophysics, **74**, no., 1, E17–E29.

Hecht, E., 1988, Optics: Addison-Wesley Publishing.

Kameda, A., J. Dvorkin, Y. Keehm, A. Nur, and W. Bosl, 2006, Permeability-porosity transforms from small sandstone fragments: Geophysics, **71**, no., 1, N11–N19.

Krinsley, D. H., K. Pye, S. Boggs, and N. K. Tovey, 1998, Backscattered scanning electron microscopy and image analysis of sediments and sedimentary rocks: Cambridge University Press.

Layman, J., and W. Ahr, 2004, Porosity characterization utilizing petrographic image analysis: Implications for rapid identification and ranking of reservoir flow units, Happy Spraberry Field, Garza County, Texas: Presented at the AAPG International Conference, Abstract A88927.

Mullins, O. C., S. S. Betancourt, M. E. Cribbs, F. X. Dubost, J. L. Creek, A. B. Andrews, and L. Venkataramanan, 2007, The colloidal structure of crude oil and the structure of oil reservoirs: Energy and Fuels, **21**, 2785–2794.

Scheidegger, A. E., 1974, The physics of flow through porous media: University of Toronto Press.

Schmid, F., C. P. Khattak, H. H. Rogers, D. M. Felt, J. Askinazi, and R. V. Wientzen, 1999, Current status of very large sapphire crystal growth for optical applications: Proceedings of the SPIE, **3705**, 70–76.

Schmid, F., C. P. Khattak, M. B. Smith, and D. M. Felt, 1997, Current status of sapphire for optics: Proceedings of the SPIE, **CR67**, 137–158.

Shannon, C. E., 1998, Communication in the presence of noise: Proceedings of the IEEE, **86**, 447–457.

Tiab, D., and E. C. Donaldson, 2004, Petrophysics: Theory and practice of measuring reservoir rock and fluid transport properties: Gulf Professional Publishing.

Venkataramanan, L., H. Elshahawi, D. McKinney, M. Flannery, M. Hashem, and O. C. Mullins, 2008, Downhole fluid analysis and fluid comparison algorithm as an aid to reservoir characterization: SPE Reservoir Evaluation and Engineering, **11**, 535–543.

Wakaki, M., K. Kunda, and T. Shibuya, 2007, Physical properties and data of optical materials: CRC Press.

Whitaker, S., 1966, The equations of motion in porous media: Chemical Engineering Science, **21**, 291–300.

Wyckoff, R. D., H. G. Botset, M. Muskat, and D. W. Reed, 1934, Measurement of permeability of porous media: AAPG Bulletin, **18**, 161–190.

Chapter 4

Conclusion

4.1 Wettability Patterning in PDMS

Microfluidic systems made of PDMS are used with great success for a large number of applications in chemistry, life science, etc. However, many applications require modified surface wettability of the micro–channels, in particular applications where water/oil multiphase flows need to be precisely guided through the system in both, continuous flow and digital, droplet–based microfluidics. However, patterning of wettability, in particular within enclosed microfluidic structures, has been challenging in the past.

In this work, an improved method has been developed which allows for altering the surface wettability in enclosed PDMS micro–channels by surface–directed UV–induced graft polymerization of PAA. This method presents significant improvements in terms of wettability contrast and spatial resolution of the patterned structures as compared to recent literature. Every step of the treatment process was rigorously investigated and key parameters for a stable and reliable treatment of high quality were identified. The influence of each parameter was carefully investigated and recommended values were provided, supported by experiments. Many of those parameters have been overlooked, neglected or misinterpreted in previous works. In particular the role and behavior of the photo–initiator benzophenone (BP) was studied in detail. This detailed understanding of the treatment process and the effects of the critical parameters on it allowed for significant improvements of the treatment process in terms of quality and reliability. Several application examples were presented, which clearly outline the high quality of the treatment. Special interest was focused on patterned wettability within complex micro–channel networks (micromodels) as it is of major interest to the oil industry to investigate multiphase flow properties in porous media of heterogeneous wettability with the aid of such systems.

The progress in wettability patterning allowed for the first time the fabrication of micromodels with well controlled wettability patterns down to a pore level. An experimental study on multiphase flow behavior in such micromodels of fractional wettability revealed astonishing results: flow patterns drastically deviate from either the wetting or non–wetting homogeneous case and entirely new flow regimes emerge. More detailed studies will be required to map the new flow regimes in more detail, but the great potential of these results to better understand mixed– and fractional–wet porous media on a pore–scale is already apparent, in particular for the oil industry.

4.2 Applications for the Oil Industry

A novel method for wettability assessment was developed and proven successful. The method employs visual observations to observe the arriving fluid front at the exit face of a rock sample during fluid injection. Based on the shape of the arriving front the bulk wettability within the rock can be inferred, independent of the surface wettability state. A key part of the method is the appearance of distinct flow regimes (fingering, flat frontal advance) as established by micromodel experiments, thus revealing the rock's wettability state. Experiments were successfully conducted on grainy limestone samples of fairly homogeneous pore structure. Wettability could be clearly identified during fluid injection of an oil/water fluid pair at moderate viscosity ratio. While the wetting phase clearly showed a flat frontal advance, the non–wetting phase was revealed by the development of distinct finger structures.

The novel microscopic grain imager instrument proved essential for reliable rock and fluid imaging at high resolution with preconditioning of the rock surface. The optical train of the imager was characterized in detail and optimized to provide maximal quality within the given design restrictions. The imaging concept was successfully demonstrated for both methods: static imaging (virtual coring) for rock characterizations and dynamic imaging of rock/fluid interactions for fluid–based measurements such as permeability and wettability.

Optical imaging and pore–level observations of a rock sample during fluid injection is an incredibly versatile technique as it allows for a large number of quantities to be measured and extracted. The basic concept was proven successful in the present work by various experiments. With some additional work towards the measurements on more heterogeneous samples and with more viscous oils, the method might someday become a routine laboratory test and rival current standard techniques.

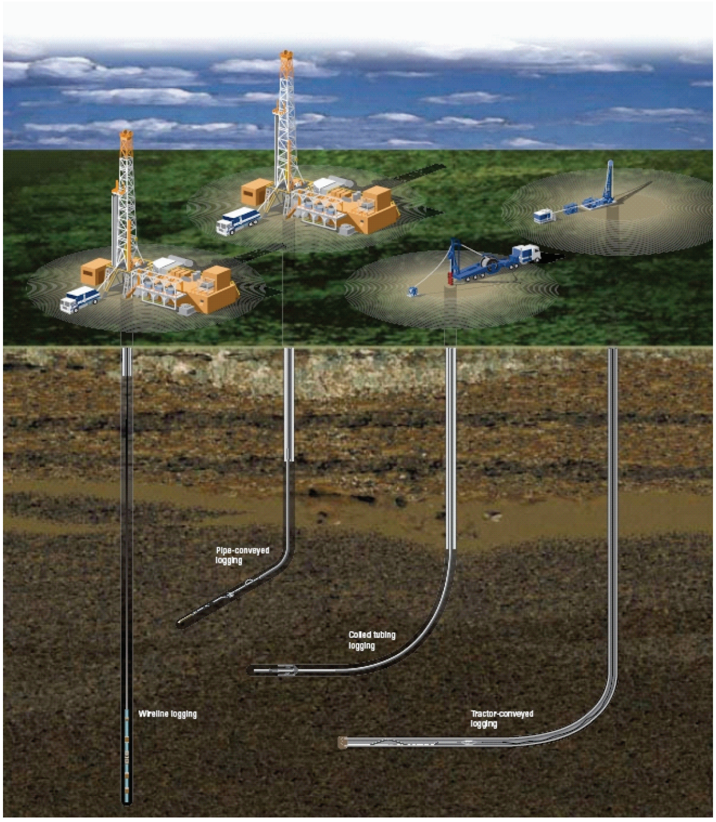

Figure 4.1: Various scanner tools and methods for in–situ downhole reservoir evaluation [**226**].

Current downhole scanners and imagers (Figure 4.1) for the oil industry do not provide sufficient resolution for pore–level imaging. However, if one day a downhole deployable microscope becomes available the presented method might be applied for in–situ wettability assessment.

Appendices

Appendix A

Photoinitiator Benzophenone

A detailed study was performed on the interaction between the photoinitiator BP and PDMS during BP solution injection (priming) of a surface treatment process. The effective diffusion coefficient of BP for acetone–swollen PDMS was experimentally determined and data showed BP to migrate surprisingly fast into the PDMS matrix. The data revealed that BP concentration profiles can significantly change across the PDMS matrix in a short timeframe, and in particular BP concentration at the channel surfaces quickly depletes. These findings, surprisingly high migration speeds of photoinitiator within PDMS, are essential to graft–polymerization treatment on PDMS and need to be carefully considered and implemented in order to achieve proper surface functionalization at reliably high quality.

In addition, a novel visualization technique was developed, which allows for in situ observation of reacted BP within the PDMS matrix. The method was proven vital to observe graft initiation in situ and to identify zones of local photoinitiation inhibition, e.g. due to oxygen quenching.

This work on BP diffusivity in PDMS will be published in *Langmuir* as presented in the following section.

A.1 Article: Benzophenone Absorption and Diffusion in PDMS and its Role in Graft Photo–Polymerization for Surface Modification

Langmuir
Article
pubs.acs.org/Langmuir

Benzophenone Absorption and Diffusion in Poly(dimethylsiloxane) and Its Role in Graft Photo-polymerization for Surface Modification

Marc H. Schneider,*[†,§] Yvette Tran,[‡] and Patrick Tabeling[†]

[†]Microfluidique, MEMS & Nanostructures, UMR 7083 Gulliver CNRS-ESPCI, Paris, France,
[‡]Physico-chimie des Polymères et des Milieux Dispersés, UMR 7615 CNRS-ESPCI, Paris, France, and
[§]Etudes et Production Schlumberger, 1 rue Henri Becquerel, 92140 Clamart, France

Received August 22, 2010. Revised Manuscript Received December 13, 2010

Following the great success of traditional microfluidic devices across many disciplines, a new class of microfluidic systems emerged in recent years, which features finely tuned, localized surface modifications within the microstructures in order to keep up with the demand for devices of ever increasing complexity (lab on chip, assay on chip, etc.). Graft photopolymerization has become a powerful tool for such localized surface modifications particularly in combination with poly(dimethylsiloxane) (PDMS) devices, as it is compatible with many functional monomers and allows for high spatial resolution. However, application within enclosed PDMS microstructures and in particular well-controlled surface-directed polymerization remains challenging. Detailed understanding of the interaction between photoinitiator, benzophenone (BP), and polymer matrix is needed. We have developed a visualization technique, which allows for observation of reacted BP in situ within the PDMS matrix. We present a detailed study on solvent-driven BP diffusion providing results essential to successful surface treatment. We also identified and investigated photoinitiator inhibition by oxygen and provide appropriate mitigation strategies.

Introduction

The field of microfluidics has seen great progress in recent years with a large number of novel applications based on surface patterning, i.e., surface functionalization with high spatial control. New applications reach from on-chip immunoassays, cell attachment and growth, selective protein adsorption, electrophoretic separation, and so forth[1-4] in the field of biology and biochemistry to application in chemical analysis such as multiple emulsion synthesis, liquid−liquid extraction, and so forth,[5-7] all requiring well-controlled functionalized surfaces. Despite recent success, surface patterning is still a new technology in the field of microfluidics. Most currently available techniques and protocols for patterned surface functionalization cannot match geometrical resolution and reliability of the host microfluidic device; significant progress is needed before microfluidic chips can harness the full potential provided by surface patterning of high quality at high spatial resolution. Very recently great progress was reported on surface patterning and functionalization of paper-based microfluidic devices.[8,9] However, devices made of poly(dimethylsiloxane) (PDMS) remain by far the primary choice for inexpensive microfluidic applications due to fast and easy manufacturing routines[10,11] and great versatility in applications as analytical systems for chemical and biological studies as well as for fundamental research.[12-14] Several different techniques are available, such as graft photopolymerization, in order to adjust the surface properties of PDMS systems to particular needs.[15-17] Grafting of functional monomers using UV radiation is a very powerful tool to modify surface properties locally and tailor them to specific needs.[18-22] Benzophenone (BP) plays a key role in such processes since its photochemically produced triplet state can abstract hydrogen atoms from almost all polymers, thus generating radicals, which can be produced locally at high concentrations, e.g., close to the surface, without interfering with the bulk properties of the polymer.[23] Such grafting techniques allow for localized modifications at high spatial control and are applicable not only to open surfaces but to enclosed microfluidic capillaries and structures as well.[24,25] For example, locally grafted

---

*Corresponding author.

(1) El-Ali, J.; Sorger, P. K.; Jensen, K. F. *Nature* **2006**, *442*, 403–411.
(2) Fiddes, L. K.; Chan, H. K. C.; Lau, B.; Kumacheva, E.; Wheeler, A. R. *Biomaterials* **2010**, *31*, 315–320.
(3) Wang, Y.; Lai, H.-H.; Bachman, M.; Sims, C. E.; Li, G. P.; Allbritton, N. L. *Anal. Chem.* **2005**, *77*, 7539–7546.
(4) Hu, S.; Ren, X.; Bachman, M.; Sims, C. E.; Li, G. P.; Allbritton, N. *Electrophoresis* **2003**, *24*, 3679–3688.
(5) Hennequin, Y.; Pannacci, N.; Pulido de Torres, C.; Tetradis-Meris, G.; Chapuliot, S.; Bouchaud, E.; Tabeling, P. *Langmuir* **2009**, *25*, 7857–7861.
(6) Pannacci, N.; Bruus, H.; Bartolo, D.; Etchart, I.; Lockhart, T.; Hennequin, Y.; Willaime, H.; Tabeling, P. *Phys. Rev. Lett.* **2008**, *101*, 164502-1–164502-4.
(7) Tokeshi, M.; Minagawa, T.; Uchiyama, K.; Hibara, A.; Sato, K.; Hisamoto, H.; Kitamori, T. *Anal. Chem.* **2002**, *74*, 1565–1571.
(8) Carrilho, E.; Martinez, A. W.; Whitesides, G. M. *Anal. Chem.* **2009**, *81*, 7091–7095.
(9) Martinez, A. W.; Phillips, S. T.; Whitesides, G. M.; Carrilho, E. *Anal. Chem.* **2010**, *82*, 3–10.
(10) Duffy, D. C.; McDonald, J. C.; Schueller, O. J. A.; Whitesides, G. M. *Anal. Chem.* **1998**, *70*, 4974–4984.
(11) Xia, Y.; Whitesides, G. M. *Annu. Rev. Mater. Sci.* **1998**, *28*, 153–184.
(12) McDonald, J. C.; Duffy, D. C.; Anderson, J. R.; Chiu, D. T.; Wu, H.; Schueller, O. J. A.; Whitesides, G. M. *Electrophoresis* **2000**, *21*, 27–40.
(13) Ng, J. M. K.; Gitlin, I.; Stroock, A. D.; Whitesides, G. M. *Electrophoresis* **2002**, *23*, 3461–3473.
(14) Sia, S. K.; Whitesides, G. M. *Electrophoresis* **2003**, *24*, 3563–3576.
(15) Nie, Z.; Kumacheva, E. *Nat. Mater.* **2008**, *7*, 277–290.
(16) Makamba, H.; Kim, J. H.; Lim, K.; Park, N.; Hahn, J. H. *Electrophoresis* **2003**, *24*, 3607–3619.
(17) Wong, I.; Ho, C.-M. *Microfluid. Nanofluid.* **2009**, *7*, 291–306.
(18) Yang, W.; Ranby, B. *J. Appl. Polym. Sci.* **1996**, *62*, 533–543.
(19) Yang, W. T.; Ranby, B. *J. Appl. Polym. Sci.* **1997**, *63*, 1723–1732.
(20) Li, Y.; Desimone, J. M.; Poon, C.-D.; Samulski, E. T. *J. Appl. Polym. Sci.* **1997**, *64*, 883–889.
(21) Chun, H. J.; Cho, S. M.; Lee, Y. M.; Lee, H. K.; Suh, T. S.; Shinn, K. S. *J. Appl. Polym. Sci.* **1999**, *72*, 251–256.
(22) Flores-Gallardo, S. G.; Sanchez-Valdes, S.; Ramos de Valle, L. F. *J. Appl. Polym. Sci.* **2001**, *79*, 1497–1505.
(23) Wouters, M.; Castell Muixi, P. Wettability aspects and the improvement of adhesion of UV curable powder coatings on polypropylene substrates. In *Contact Angle, Wettability and Adhesion*; VSP: Leiden, Netherlands, 2008; Vol. *5*.
(24) Liu, J.; Lee, M. L. *Electrophoresis* **2006**, *27*, 3533–3546.
(25) Abate, A. R.; Krummel, A. T.; Lee, D.; Marquez, M.; Holtze, C.; Weitz, D. A. *Lab Chip* **2008**, *8*, 2157–2160.

DOI: 10.1021/la103345k

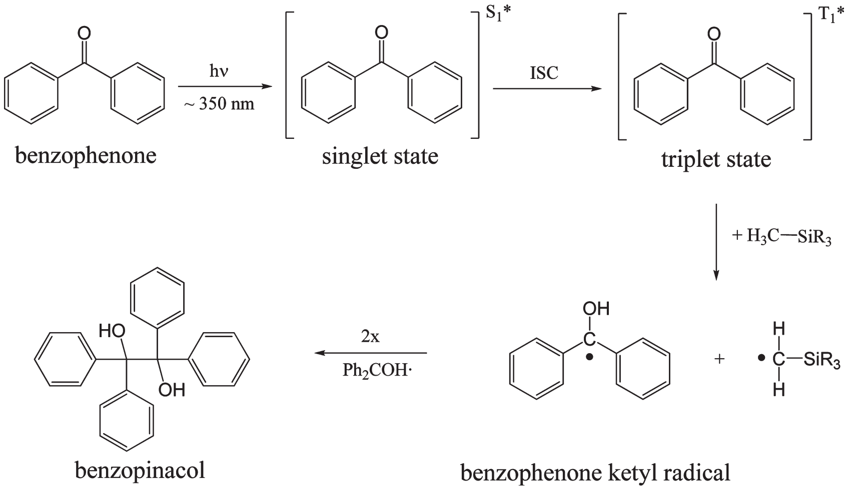

Figure 1. Reaction schematic of the dominant pathway for graft photoinitiation with BP: Triplet BP is produced via absorption of a photon and subsequent $S_1 \rightarrow T_1$ transition via ISC. Triplet BP then abstracts an H-atom from a PDMS methyl-group to form the BP ketyl radical. While the methyl radical can serve as an initiator for AA polymerization, BP ketyl radicals combine with each other to form benzopinacol eventually.

poly(acrylic acid) (PAA) in PDMS microstructures yields strongly hydrophilic areas, while untreated parts of the system remain hydrophobic, hence allowing for spatial control of wettability in the microfluidic device.[26] Grafting of various polymers within enclosed PDMS microstructures has been performed in recent years.[2,25,27,28] Despite this recent progress, the achievable yield and quality of many of the published protocols remains surprisingly low. Many details and important parameters seem to be neglected, not reported, or significant contradictions exist. In particular, the role of BP and its interaction with the PDMS matrix during graft photopolymerization have not been carefully investigated so far.

In this paper we present a detailed study of BP behavior and interaction with PDMS with particular focus on surface graft polymerization processes. Typically, the first step of a surface graft polymerization treatment consists in priming the system with photoinitiator, i.e., application of BP solution and BP diffusion into the polymer matrix of the target surface. In a second step, functional monomer solution is applied to the surface, and graft photopolymerization is initiated by exposure to UV light.[26,27] The presence of BP at appropriate concentrations and with homogeneous distribution in proximity to the polymer surface is a key factor for successful grafting. A detailed understanding of required concentrations and time scales of the solvent-driven BP diffusion is therefore essential in order to design a reliable, optimized grafting process. We have developed a technique based on the photoluminescence of reacted BP to study the spatial distribution of the photoinitiator as a function of time. From our experiments we estimate an effective diffusion coefficient for solvent-driven BP diffusion into PDMS. We also employ UV spectroscopy to measure the stationary diffusion coefficient of BP in acetone-swollen PDMS. Our results show diffusion time scales for BP diffusion in PDMS, which need careful consideration in the preparation of a graft polymerization surface treatment. We also discuss photoinitiation inhibition due to diffusing oxygen and introduce an appropriate mitigation strategy. We have identified BP diffusion as a crucial parameter in surface graft polymerization processes acting on many levels. Our detailed studies provide significant improvements of the grafting process in terms of reliability and quality.

Background

BP as Photoinitiator. The predominant reaction scheme of BP during photo initiation[29−32] is shown in Figure 1. Upon absorption of a photon, BP is excited into a singlet state, undergoes conversion to a triplet state by intersystem crossing (ISC) and relaxes from the triplet state by a hydrogen abstraction reaction. Abstraction of hydrogen from a reaction partner (e.g., methyl group of PDMS) creates a radical site at the reaction partner and leaves a BP ketyl radical.[33] BP ketyl radicals then combine to form benzopinacol as a reaction product.[34−37] Figure 2 shows a simplified Jablonski diagram for the first and second excited singlet and triplet states of BP, with estimates of the excited state energies expressed in terms of their wavenumber.[38−41] A first absorption peak appears at around 345 nm, which corresponds to an n → π^* transition in the carbonyl group.[42,43] While the radiative lifetime of the first excited singlet state (S_1) is on the order of 100 ns,[44] population of the first excited triplet state (T_1)

---

(26) Schneider, M. H.; Willaime, H.; Tran, Y.; Rezgui, F.; Tabeling, P. *Anal. Chem.* **2010**, *82*, 8848–8855.

(27) Hu, S.; Ren, X.; Bachman, M.; Sims, C. E.; Li, G. P.; Allbritton, N. *Anal. Chem.* **2004**, *76*, 1865–1870.

(28) Ebara, M.; Hoffman, J. M.; Stayton, P. S.; Hoffman, A. S. *Radiat. Phys. Chem.* **2007**, *76*, 1409–1413.

(29) Yang, W.; Ranby, B. *Macromolecules* **1996**, *29*, 3308–3310.

(30) Pan, B.; Viswanathan, K.; Hoyle, C. E.; Moore, R. B. *J. Polym. Sci., Part A: Polym. Chem.* **2004**, *42*, 1953–1962.

(31) Deng, J.; Wang, L.; Liu, L.; Yang, W. *Prog. Polym. Sci.* **2009**, *34*, 156–193.

(32) Dorman, G.; Prestwich, G. D. *Biochemistry* **1994**, *33*, 5661–5673.

(33) Kawai, A.; Hirakawa, M.; Abe, T.; Obi, K.; Shibuya, K. *J. Phys. Chem. A* **2001**, *105*, 9628–9636.

(34) Goda, T.; Konno, T.; Takai, M.; Moro, T.; Ishihara, K. *Biomaterials* **2006**, *27*, 5151–5160.

(35) Coyle, J. D. *Introduction to Organic Photochemistry*; John Wiley & Sons: Chichester, U.K., 1986; Chapter 4, pp 115−119.

(36) Qu, B.; Xu, Y.; Ding, L.; Ranby, B. *J. Polym. Sci., Part A: Polym. Chem.* **2000**, *38*, 999–1005.

(37) Poston, P. E.; Harris, J. M. *J. Am. Chem. Soc.* **1990**, *112*, 644–650.

(38) Beckett, A.; Porter, G. *Trans. Faraday Soc.* **1963**, *59*, 2051–2057.

(39) Dilling, W. L. *J. Org. Chem.* **1966**, *31*, 1045–1050.

(40) Hutchinson, J. A.; DiBenedetto, J.; Rentzepis, P. M. *J. Am. Chem. Soc.* **1986**, *108*, 6517–6521.

(41) Klessinger, M.; Michl, J. *Excited States and Photochemistry of Organic Molecules*; VCH Verlagsgesellschaft: Weinheim, Germany, 1995; Chapter 5, pp 243−276.

(42) Cai, X.; Sakamoto, M.; Fujitsuka, M.; Majima, T. *Chem.—Eur. J.* **2005**, *11*, 6471–6477.

(43) Georg, H. C.; Coutinho, K.; Canuto, S. *J. Chem. Phys.* **2007**, *126*, 034507.

(44) Beckett, A.; Porter, G. *Trans. Faraday Soc.* **1963**, *59*, 2038–2050.

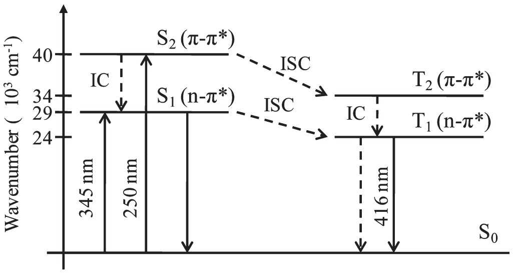

Figure 2. Simplified Jablonski diagram of BP ground state (S_0) as well as first and second excited singlet (S_1, S_2) and triplet (T_1, T_2) states. Excited state energies are indicated in terms of their wavenumber as approximate values. Solid lines indicate radiative transitions, while dashed lines indicate nonradiative transitions. IC and ICS processes are labeled as well.

occurs after only 100 ps[44] or less.[45−47] Therefore the yield for BP triplet states is almost 100%, and direct relaxation from S_1 to the ground state S_0 via fluorescence almost never occurs.[48] On the other hand, the long radiative lifetime of T_1 of about 100 μs promotes the nonradiative decay from T_1 to S_0 via hydrogen abstraction, which can occur 100 times faster than phosphorescence if a suitable H-donor is available.[32] These BP n,π* triplets (T_1) are very effective for hydrogen abstraction and are known to preferentially react with unreactive C−H bonds such as the methyl groups in PDMS,[32,49] while the π,π* triplets (T_2) show little or no reactivity toward hydrogen abstraction[50,51] and have to undergo internal conversion (IC) to T_1 first before hydrogen abstraction can occur. If no suitable H-donor is available excited BP can relax from T_1 to S_0 via emission of a phosphorescence photon and is readily available again for photo activation. Such Norrish type II reaction[49] is very beneficial since BP is not depleted by UV exposure directly but only those molecules which undergo a reaction with a reaction partner are consumed. Therefore, for BP at sufficiently high concentration, depletion effects become negligible.

BP is well soluble in many organic solvents such as acetone and ethanol. Figure 3a shows absorption spectra for the different BP concentrations in ethanol. Both the first absorption peak at around 345 nm corresponding to the n → π* transition ($S_0 \rightarrow S_1$) and the second absorption peak at around 250 nm corresponding to the $\pi \rightarrow \pi$* transition ($S_0 \rightarrow S_2$) are clearly visible in the figure. As can be seen, the lower energy absorption peak (S_1) is much weaker than the higher energy absorption peak (S_2). Nevertheless, due to the triplet conversion with almost unity yield and the high-yield hydrogen abstraction process, photoinitiation through S_1 excitation is a very efficient process. It shall be noted that the actual peak positions in Figure 3a are shifted with respect to the values given in Figure 2. The $S_0 \rightarrow S_1$ absorption peak is blue-shifted to 333 nm, and the $S_0 \rightarrow S_2$ absorption peak is red-shifted to 252 nm, which is a well-known effect caused by the solvent polarity of ethanol.[39] Figure 3b shows absorption spectra for BP dissolved in acetone. Due to the absorption peak of acetone at 280 nm and the cutoff toward lower energies at about 335 nm[52] the absorption band of BP is masked over a broad region by the presence of the solvent. Nevertheless, around the mercury i-line (365 nm), acetone is completely transparent, but BP still provides a significant absorption peak (S_1).

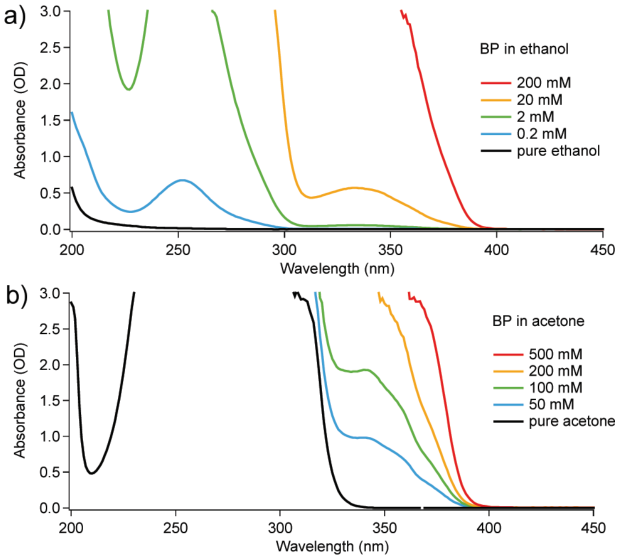

Figure 3. UV absorption spectra of BP dilution series in ethanol (a) and acetone (b).

Experimental Section

Materials. Sylgard 184 Silicone Elastomer Kit was purchased from Dow Corning (Midland, MI). P-type boron silicon wafers were purchased from Wafer World, Inc. (West Palm Beach, FL), and SU8 2000 series photo resist was obtained from MicroChem Corp. (Newton, MA). BP was purchased from Sigma-Aldrich Chimie (Lyon, France) and used without further purification. Organic solvents and lab supplies were purchased from VWR International (Strasbourg, France). Deionized (DI) water was produced in-house (Resistivity ≥18.2 MΩcm) by a Synergy Ultrapure water system from Millipore SAS (Guyancourt, France). Benzopinacol was synthesized in-house by reacting BP with isopropanol under UV light and subsequent filtration.[53,54]

Device Fabrication and Sample Preparation. Cross-linked PDMS samples were prepared by mixing Sylgard 184 PDMS base with curing agent at a ratio of 10:1 (w/w) unless stated otherwise. In order to reach a desired sheet thickness of typically 2 mm, appropriate quantities of PDMS mix were poured into disposable Petri dishes and degassed under vacuum. The casts were allowed to cross-link at 65 °C for 2 h before they were removed from the Petri dishes and stored for use. PDMS samples containing microfluidic channel structures were prepared in a similar fashion but with an appropriate mold placed as an insert into the Petri dish. The molds were created in-house by a photolithography patterning process of SU8 photoresist on a silicon waver. In order to obtain enclosed microfluidic channel structures, the PDMS sample containing the microfluidic structures on its surface was bonded against a flat counterpart by a plasma bonding technique. Bonding was achieved by activating the surfaces of the two halves with oxygen plasma in a Harrick Plasma Cleaner (Ithaca, NY) for

---

(45) Coyle, J. D. *Introduction to Organic Photochemistry*; John Wiley & Sons: Chichester, U.K., 1986; Chapter 1, pp 9−37.

(46) Shah, B. K.; Rodgers, A. J.; Neckers, D. C. *J. Phys. Chem. A* **2004**, *108*, 6087–6089.

(47) Aloise, S.; Ruckebusch, C.; Blanchet, L.; Rehault, J.; Buntinx, G.; Huvenne, J.-P. *J. Phys. Chem. A* **2008**, *112*, 224–231.

(48) Hochstrasser, R. M.; Lutz, H.; Scott, G. W. *Chem. Phys. Lett.* **1974**, *24*, 162–167.

(49) Klessinger, M.; Michl, J. *Excited States and Photochemistry of Organic Molecules*; VCH Verlagsgesellschaft: Weinheim, Germany, 1995; Chapter 7, pp 395−404.

(50) Wagner, P. J.; Kemppainen, A. E.; Schott, H. N. *J. Am. Chem. Soc.* **1973**, *95*, 5604–5614.

(51) Cizmeciyan, D.; Sonnichsen, L. B.; Garcia-Garbay, M. A. *J. Am. Chem. Soc.* **1997**, *119*, 184–188.

(52) Pretsch, E.; Buehlmann, P.; Affolter, C. *Structure Determination of Organic Compounds - Tables of Spectral Data*, 3rd ed.; Springer Verlag: Heidelberg, Germany, 2000; Chapter 8, pp 385−404.

(53) Lu, H.; Schmidt, M. A.; Jensen, K. F. *Lab Chip* **2001**, *1*, 22–28.

(54) Filipescu, N.; Minn, F. L. *J. Am. Chem. Soc.* **1968**, *90*, 1544–1547.

30 s at a 400 mTorr oxygen atmosphere. Both halves were brought into contact immediately after the plasma treatment in order for irreversible bonds to form at the interface, hence sealing the device permanently. The devices were annealed in an oven at 90 °C for 2 days in order to reverse the plasma-induced surfaces changes and recover the native water contact angle of PDMS of 108°.[10]

BP Diffusion Study. The presence of BP in PDMS was indirectly visualized by exposure with UV light from the mercury i-line and simultaneous observation in the visible light range. The samples were mounted on a DMIL inverted microscope with a 100 W mercury arc lamp illuminator from Leica Microsystems, GmbH (Wetzlar, Germany). A custom-made fluorescence filter cube from Chroma Technology Corp. (Bellows Falls, VT) with a 365 nm narrowband excitation filter for the mercury i-line and a 420 nm long-pass emission filter was used to detect photoluminescence. Images were captured through the microscope by a Pike F-100C color camera from Allied Vision Technologies, GmbH (Stadtroda, Germany) with a single charge-coupled device (CCD) and Bayer filter design. The camera provides color images at a resolution of 1 MP.

BP diffusion was studied on flat PDMS samples, on closed PDMS microchannels primed according to the regular protocol, as well as on microchannels during priming. For the latter, a flow of BP solution was applied to the microfluidic system with a syringe pump directly on the microscope.

In some cases, photoluminescence was monitored in situ during a graft polymerization treatment. In these cases, the microfluidic system was observed during UV exposure with the Pike F-100C camera through a Z16 APO macroscopic zoom lens from Leica pointing at the system under a 45° angle from above. As a UV light source, a Lightningcure LC8 lamp with a 200 W mercury–xenon arc lamp optimized for the mercury i-line (365 nm) from Hamamatsu was used. An additional 365 nm band-pass filter was added to the optical path to further restrict the optical output to the desired wavelength. A UV screening filter was placed between sample and lens in order to protect the camera from overexposure by scattered UV light. The entire setup was placed in a dark room, shielded from visible light, in order to observe the faint photoluminescence signal.

UV Spectroscopy. UV absorption measurements were conducted on an 8453 UV–visible spectrometer from Agilent Technologies (Massy, France). Spectral data for each sample were recorded between 190 and 1100 nm at a resolution of 1 nm. Liquid samples were introduced into the spectrometer in a quartz cuvette with 2 mm path length. A background reference spectrum was taken prior to each measurement with the empty cuvette in the beam path. PDMS samples were introduced directly into the spectrometer as flat strips of 2 mm thickness. Background reference spectra for these samples were taken with an empty sample chamber. PDMS samples were typically handled as larger pieces during sample preparation, e.g., during immersion in BP solution. A center part was then cut out afterward and used for spectroscopic analysis in order to avoid artifacts caused by additional imbibition along the original edges of the sample.

Theory

Fick's first law of diffusion describes a diffusive flux J as the result of a gradient in the concentration c as[55,56]

$$J = -D\frac{\partial c}{\partial x} \tag{1}$$

with the diffusion coefficient D for a single dimension x.

From eq 1 and mass balance considerations, Fick's second law can be derived:

$$\frac{\partial c}{\partial t} = D\frac{\partial^2 c}{\partial x^2} \tag{2}$$

assuming a constant diffusion coefficient D.

Let us consider a scenario where we prepare a large (infinite) bath of solution with initial dopant concentration c_0. At time $t = 0$, a sheet of polymer, presoaked with solvent, is inserted into the bath. For a sheet much larger than its thickness L, the edges can be neglected, and a one-dimensional model for dopant diffusion can be derived from eq 2 with the initial conditions

$$c(x,0) = \begin{cases} 0 & 0 \le x \le L \\ c_0 & \text{otherwise} \end{cases} \tag{3}$$

With these particular initial conditions (eq 3) the following solution for eq 2 can be found:

$$c(x,t) = c_0 - c_0\left[\frac{1}{2}\operatorname{erf}\left(\frac{x}{\sqrt{4Dt}}\right) + \frac{1}{2}\operatorname{erf}\left(\frac{L-x}{\sqrt{4Dt}}\right)\right] \tag{4}$$

Equation 4 describes the concentration profile across the thickness of the sheet at each instant of time. If we are interested in the amount of absorbed dopant per unit area C we need to integrate eq 4 across the sheet:

$$C(t) = \int_0^L c(x,t)\,\mathrm{d}x$$

$$= \frac{c_0}{\pi}\left[\pi L + 2\sqrt{\pi D t} - \pi L \cdot \operatorname{erf}\left(\frac{L}{2\sqrt{Dt}}\right) - 2\sqrt{\pi D t}\cdot \mathrm{e}^{L^2/4Dt}\right] \tag{5}$$

Now, let us consider a simple case of dopant diffusion from a solution of constant concentration c_0 into a sufficiently thick block of polymer (assuming infinite thickness). If we define the interface between polymer and dopant solution at $x = 0$, we find the following solution for eq 2:

$$c(x,t) = c_0\operatorname{erfc}\left(\frac{x}{2\sqrt{Dt}}\right) \tag{6}$$

Equation 6 describes a concentration profile within the polymer block as a result of dopant diffusion from a constant source. If we consider another case where we remove the constant source after an initial time t_0, then the concentration profile at time t_0 according to eq 6 serves as initial condition for the new model:

$$c(x,0) = c_0\operatorname{erfc}\left(\frac{x}{2\sqrt{D_0 t_0}}\right) \tag{7}$$

Instead of a constant concentration at $x = 0$, we now apply the following zero-flux condition to the boundary:

$$\frac{\partial c(0,t)}{\partial x} = 0 \tag{8}$$

A solution for eq 2 on the interval $(0,\infty)$, which satisfies the initial condition according to eq 7 and the boundary condition according to eq 8 is given by

$$c(x,t)$$

$$= \frac{c_0}{2\sqrt{\pi D t}}\int_0^\infty \left(\mathrm{e}^{-(x-y)^2/4Dt} + \mathrm{e}^{-(x+y)^2/4Dt}\right)\operatorname{erfc}\left(\frac{y}{2\sqrt{D_0 t_0}}\right)\mathrm{d}y \tag{9}$$

---

(55) Crank, J. *The Mathematics of Diffusion*, 2nd ed.; Oxford University Press: Oxford, 1975.

(56) Cussler, E. L. *Diffusion, Mass Transfer in Fluid Systems*, 3rd ed.; Cambridge University Press: Cambridge, U.K., 2009.

although integration cannot be performed in closed form and eq 9 needs to be evaluated numerically.

Results and Discussion

Typical graft polymerization techniques employ a two-step protocol: In the first step, the photoinitiator BP is applied to the polymer matrix (priming) of the PDMS device, and in the second step a functional monomer solution is applied and graft photopolymerization is initiated. The two-step protocol ensures that BP and monomer meet only along the surface where graft polymerization is desired and parasitic polymerization in the bulk solution is suppressed, an essential feature in particular for application within capillaries or enclosed microstructures. BP is applied as a solution, typically in acetone. If treatment is performed on open PDMS membranes or devices, the samples are typically dipped into a reservoir of BP solution for a certain time. For treatment within enclosed microfluidic systems, BP solution is flown through the capillaries for a given time. By means of such priming process, BP as the photoinitiator can be effectively implanted within the PDMS matrix for subsequent graft polymerization initiation.

Solvent-enhanced diffusion of functional molecules has recently also been successfully employed for other applications such as microfluidic permeation printing of self-assembled monolayer (SAM) gradients[57,58] or enhanced dye diffusion in polymer thin films for LED applications.[59,60]

Acetone Diffusion in PDMS. It is well know that the presence of solvents lowers the glass transition temperature of the polymer[60,61] and thereby promotes the diffusion of a dopant such as BP into the polymer matrix significantly.[59] In the case of cross-linked PDMS, small molecule solvent such as acetone can easily diffuse into the polymer matrix and is quickly absorbed[62,63] as a result of the highly flexible PDMS backbone structure and its resulting large free volume.[64] Acetone is a solvent, which can diffuse particularly fast into PDMS, with an effective diffusion coefficient of about 30 × 10^{-11} m^2/s.[65] During the priming process, acetone quickly penetrates the PDMS matrix, hence providing increased BP diffusion. Figure 4 shows the evolution of PDMS samples imbibed with acetone for 10 min and then taken out of solution where acetone starts to diffuse out and evaporate. Figure 4a shows attenuated total reflection−Fourier transform infrared (ATR-FTIR) spectra of the samples. The diminishing absorption peak of acetone[66] at 1715 cm^{-1} shows the evaporation of acetone. Since the ATR probe is only sensitive to compounds present within the first micrometer underneath the surface, the results indicate that, after about 20 min, acetone has evaporated below the detection limit close to the surface. However, acetone is present longer in the bulk, as revealed by the UV absorption spectra in Figure 4b. Although large quantities of acetone evaporate within the first 30 min, acetone in the PDMS sample can still be detected after 1 h. Due to its high vapor pressure at room temperature, evacuation does not significantly improve the evaporation rate (c.f. Figure 4b).

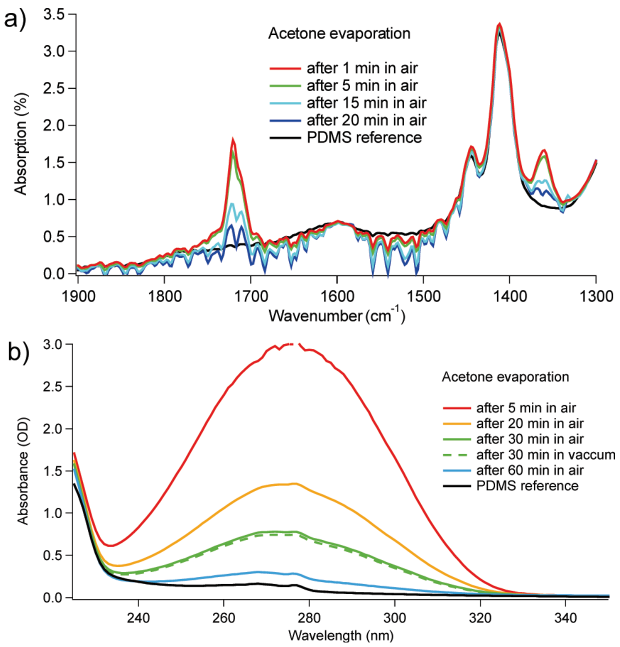

Figure 4. (a) FTIR-ATR spectra around the acetone absorption band (1715 cm^{-1}) showing an acetone-imbibed PDMS sample and acetone evaporated from the surface layer over time. (b) UV absorption spectra of an acetone-imbibed PDMS sample showing vanishing acetone concentration from bulk PDMS over time.

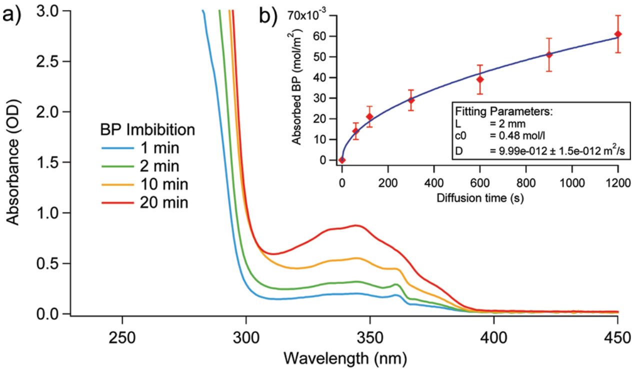

Figure 5. (a) UV absorption spectra of PDMS imbibed with BP. PDMS samples were saturated with acetone prior to diffusion experiments and then immersed in a 10 wt % BP solution in acetone for the indicated times. (b) Amounts of absorbed BP determined via UV absorption (markers) and curve fit (solid line) as a function of diffusion time.

Stationary BP Diffusion in PDMS. The uptake of photoinitiator was studied by immersion of PDMS samples into an acetone solution containing 10 wt % BP for various times. Samples were analyzed by UV spectroscopy (Figure 5a), and the BP absorbance at the 345 nm peak was evaluated in order to determine BP concentration according to Beer−Lambert law:[45]

$$A = \varepsilon l c \tag{10}$$

where A is the measured absorbance, ε is the molar extinction coefficient, l is the sample path length, and c is the concentration of the absorbing species. The molar extinction coefficient was

---

(57) Lamb, B. M.; Park, S.; Yousaf, M. N. *Langmuir* **2010**, *26*, 12817–12823.

(58) Lamb, B. M.; Barrett, D. G.; Westcott, N. P.; Yousaf, M. N. *Langmuir* **2008**, *24*, 8885–8889.

(59) Graves-Abe, T.; Pschenitzka, F.; Jin, H. Z.; Bollman, B.; Sturm, J. C.; Register, R. A. *J. Appl. Phys.* **2004**, *96*, 7154–7163.

(60) Pschenitzka, F.; Sturm, J. C. *Appl. Phys. Lett.* **2001**, *78*, 2584–2586.

(61) Khang, D.-Y.; Lee, H. H. *Appl. Phys. Lett.* **2000**, *76*, 870–872.

(62) Duineveld, P. C.; Lilja, M.; Johansson, T.; Inganas, O. *Langmuir* **2002**, *18*, 9554–9559.

(63) Lue, S. J.; Tsai, C. L.; Lee, D.-T.; Mahesh, K. P. O.; Hua, M. Y.; Hu, C.-C.; Jean, Y. C.; Lee, K.-R.; Lai, J.-Y. *J. Membr. Sci.* **2010**, *349*, 321–332.

(64) Zhao, C.; Li, J.; Jiang, Z.; Chen, C. *Eur. Polym. J.* **2006**, *42*, 615–624.

(65) Singh, A.; Freeman, B. D.; Pinnau, I. *J. Polym. Sci., Part B: Polym. Phys.* **1998**, *36*, 289–301.

(66) Pretsch, E.; Buehlmann, P.; Affolter, C. *Structure Determination of Organic Compounds - Tables of Spectral Data*, 3rd ed.; Springer Verlag: Heidelberg, Germany, 2000; Chapter 6, pp 286−303.

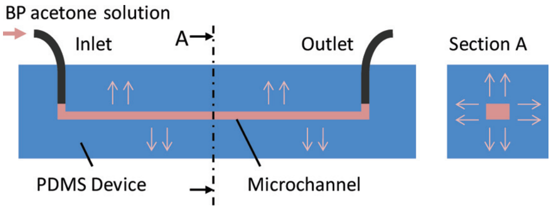

Figure 6. Schematic of a simple PDMS device containing a single microchannel. Acetone and BP diffusion into the PDMS matrix during injection is indicated.

determined from UV spectroscopy on a dilution series of BP in ethanol (Figure 3a). Results are shown in Figure 5b. The amount of absorbed BP as a function of diffusion time is expressed as integral values over the sample thickness per surface area. The experimental results are represented by markers, while a least-squares fit of the model (eq 5) is shown as a solid line. With the known sample thickness $L = 2 \pm 0.1$ mm and the known initial concentration $c_0 = 480$ mol/m^3, the effective diffusion coefficient for BP diffusion in acetone-swollen PDMS can be determined from the model fit to $D_{\mathrm{eff}} \approx 1 \times 10^{-11}$ m^2/s. Data from a second set of experiments confirms the value for the diffusion coefficient within a 10% error margin.

In Situ Visualization of BP Diffusion during Priming. The diffusion coefficient as determined in the last section applies to BP freely diffusing into acetone-swollen PDMS. However, during priming of an enclosed microfluidic system, the situation is somewhat different: BP solution is pumped into the microfluidic channels in order to establish a constant flow for a given amount of time. Acetone can imbibe through the channel wall into the PDMS chip, diffuse, and evaporate into ambient atmosphere (Figure 6), which establishes a constant stream of acetone through the PDMS matrix. BP is therefore expected to be carried into the PDMS matrix significantly faster than predicted by stationary diffusion. We conducted a qualitative study of BP diffusion during priming in order to gain a better understanding of local concentrations and the specific solvent-driven diffusion behavior of BP. We developed an indirect visualization technique based on photoluminescence of BP reaction product, which allows for an in situ study of the process, as described in the following.

In pure BP crystals the $T_1 \rightarrow S_0$ decay via phosphorescence[67] at 416 nm (c.f. Figure 2) could be observed on the microscope as shown in Figure 7a, since phosphorescence is known to be favored in hard or very viscous media. However, in solution or in PDMS, nonradiative decay dominates,[68,69] and phosphorescence is suppressed beyond the detection limit; therefore BP can not be detected by visualization directly. If on the other hand triplet BP relaxes by hydrogen abstraction and BP ketyl radicals are formed, a weak photoluminescence signal can be detected[70] in the green wavelength range (~550 nm). This photoluminescence signal is in the wavelength range of the first electronic transition of the BP ketyl radical (545 nm[33,71]), while the second electronic transition at about 332 nm[71] is still close enough to be excited at a low yield by the used UV light.[72] The observed photoluminescence might therefore either be phosphorescence of the BP ketyl radicals themselves or of the reaction production of the ketyl radicals, "isobenzopinacol", an unstable intermediary toward the final arrangement of the stable benzopinacol,[73] with chromophores close to those of the ketyl radicals themselves. The appearance of such isobenzopinacol intermediates (In) toward the formation of stable benzopinacol on longer time scales is well-known in the literature.[36,37,73,74] Spectral data of a PDMS sample primed with BP (Figure 8b) shows that, immediately after UV exposure, an additional absorption peak between 310 − 340 nm appears, which then diminishes significantly throughout the first hour after exposure. These results are in excellent agreement with spectral data of In presented in literature.[54] Absorption at this additional peak diminishes over time, as the end product benzopinacol has no significant absorption in this wavelength range (see Figure 8a). However, cleavage of benzopinacol can be easily induced[72] even by UV exposure at long wavelengths above the intrinsic absorption, which produces BP ketyl radicals and In[74] and yields again phosphorescence at this particularly large red-shift in the green wavelength range.[75] This UV-induced benzopinacol cleavage and subsequent phosphorescence of In was demonstrated on the microscope on dry benzopinacol crystals (Figure 7b). In summary, the results show that, due to the very large and particular red-shift of In phosphorescence, we can clearly identify and visualize sites that contain reacted BP (i.e., BP that underwent hydrogen abstraction).

Solvent-Driven Diffusion Study. We employed the photoluminescence visualization technique to study solvent-driven BP diffusion on systems with a simple microchannel (c.f. Figure 6). The channels were 200 μm wide and 100 μm high, and a solution of 10 wt % BP in acetone was continuously injected at a rate of 200 μL/min. Observations were performed from the bottom of the system revealing a view of the 200 μm wide channel and the BP diffusion through the 100 μm high side walls as depicted in Figure 9a. At each instant of time, a photoluminescence intensity profile across the PDMS chip is plotted as a vertical line (c.f. Figure 9a) and shown as a time evolution plot in Figure 9c. Evolution over time is shown along the horizontal axis while the vertical axis indicates the spatial location across the chip, and the measured intensity is given as a color code. Actual fluorescence images at distinct time steps are shown as examples in Figure 9b. The solution-carrying microchannel is indicated by a gray shade in Figure 9b,c.

As can be seen from the figure, BP is carried deep into the PDMS matrix, even at short time scales. Besides regular PDMS prepared with 10% curing agent, imbibition studies have also been conducted on "soft" PDMS prepared with 8% curing agent and "hard" PDMS prepared with 12% curing agent, where the different amounts of curing agent give rise to different stiffnesses of the PDMS matrix. Penetration depth of the detectable phosphorescence signal, which corresponds to a BP concentration of about 15 mol/m^3, is plotted in Figure 9d as a function of diffusion time. As the plot shows, imbibition rates differ significantly for different stiffnesses of the PDMS matrix. As a simplified approach we can model the experimental results with the linear diffusion model according to eq 6. If we set the concentration $c(x,t)$ equal to the detectable concentration limit and solve eq 6 for the diffusion time, we obtain a model for the experimental data

---

(67) Turek, A. M.; Krishnamoorthy, G.; Phipps, K.; Saltiel, J. *J. Phys. Chem. A* **2002**, *106*, 6044–6052.

(68) Ramseier, M.; Senn, P.; Wirz, J. *J. Phys. Chem. A* **2003**, *107*, 3305–3315.

(69) Du, Y.; Xue, J.; Li, M.; Phillips, D. L. *J. Phys. Chem. A* **2009**, *113*, 3344–3352.

(70) Sakamoto, M.; Cai, X.; Fujitsuka, M.; Majima, T. *J. Phys. Chem. A* **2006**, *110*, 118000–111808.

(71) Hayon, E.; Ibata, T.; Lichtin, N. N.; Simic, M. *J. Phys. Chem.* **1972**, *76*, 2072–2078.

(72) Rogowski, J.; Zielonka, J.; Marcinek, A.; Gebicki, J. *J. Phys. Chem. A* **2003**, *107*, 810–814.

(73) Minn, F. L.; Trichilo, C. L.; Hurt, C. R.; Filipescu, N. *J. Am. Chem. Soc.* **1970**, *92*, 3600–3610.

(74) Schenck, G. O.; Cziesla, M.; Eppinger, K.; Matthias, G.; Pape, M. *Tetrahedron Lett.* **1967**, *3*, 103–198.

(75) Mel'nik, V. I.; Nelipovich, K. I.; Faidysh, A. N.; Yangkovskaya, L. B. *J. Appl. Spectrosc.* **1980**, *33*, 1075–1080.

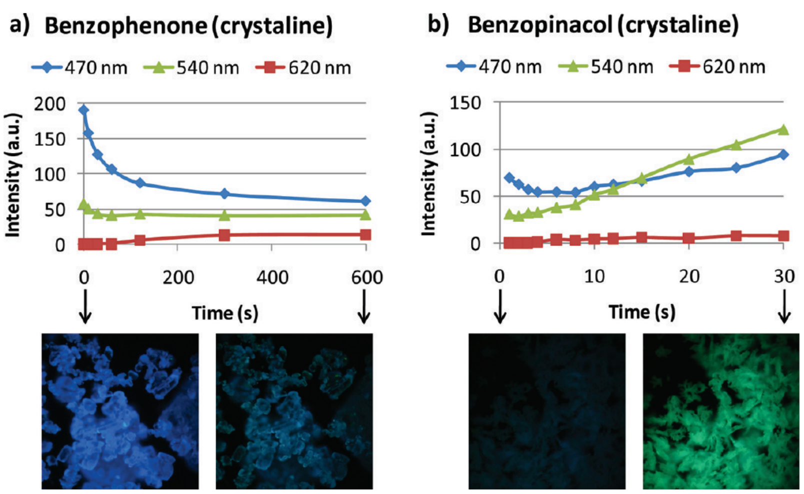

Figure 7. Photoluminescence signals observed during UV exposure of dry crystals of (a) BP and (b) benzopinacol.

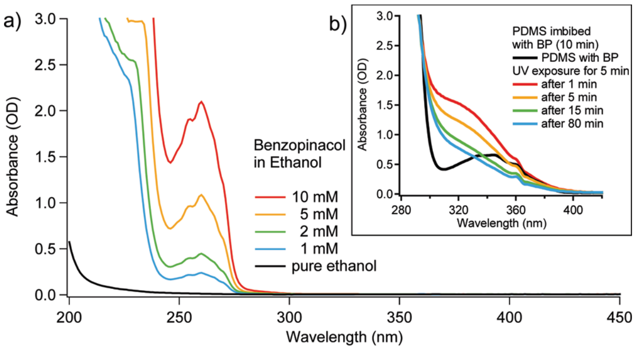

Figure 8. (a) UV absorption spectra of benzopinacol dissolved in ethanol. (b) UV absorption spectra of PDMS imbibed with BP before and after UV treatment. The spectral series shows the appearance and evolution over time of the intermediate species In with characteristic absorption at around 320 nm.

shown in Figure 9d. From a least-squares fit we obtain (13 ± 3) × 10^{-11} m^2/s for soft PDMS, (8.5 ± 0.5) × 10^{-11} m^2/s for regular PDMS, and (6 ± 1) × 10^{-11} m^2/s for hard PDMS. The values are based on three individual experiments each. It shall be noted, however, that our simplified model does not consider the influence of the diffusing acetone; the reported values therefore need to be interpreted as equivalent diffusion coefficients specific to our experimental setup. As these numbers show compared to the value for the stationary diffusion coefficient ($D_{\mathrm{eff}} \approx 1 \times 10^{-11}$ m^2/s for regular PDMS), during priming of a microchannel BP migrates into the PDMS matrix at much higher rates since the equivalent diffusivity is almost one order of magnitude higher in this case.

Diffusion of BP during the drying step immediately after priming was investigated with a second set of experiments on simple channel systems (regular PDMS). First, priming was performed for a certain period of time as described above, and BP solution was removed from the channel by a jet of air afterward. The systems were then left to dry, and the concentration profile was probed after 1 min, half an hour, and 1 h, respectively. The results are listed in Table 1. While shortly after imbibition BP is already present in significant quantities at depths of about 260 and 580 μm for 1 and 10 min of imbibition, respectively, BP diffusion continues at significant speeds during the drying period. After a waiting time of 30 min, BP was detected already at twice the initial depth and continued to diffuse inside the PDMS. With a fixed initial amount of adsorbed BP, this diffusion causes BP concentration to decrease significantly over

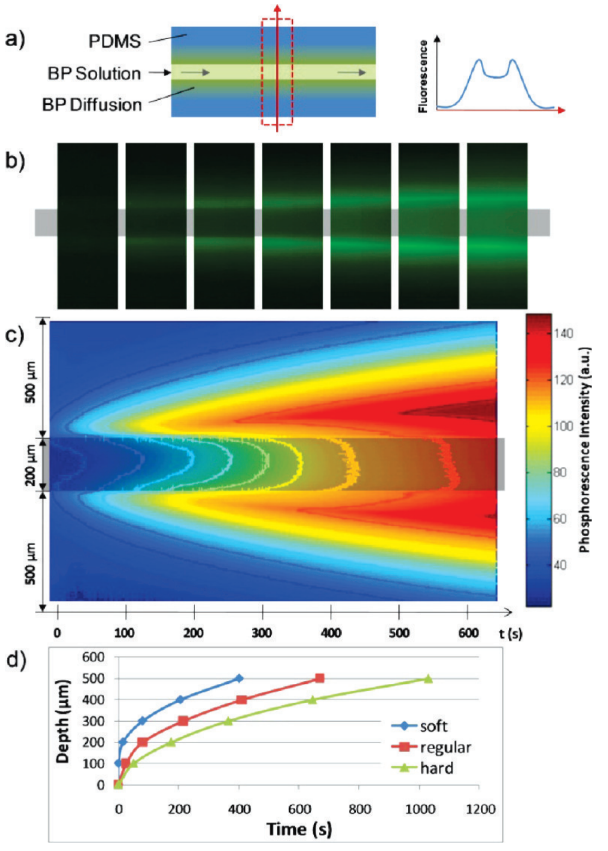

Figure 9. (a) Schematic depiction of the experiment: Photoluminescence is measured as a line profile across the channel. (b,c) Time evolution of BP imbibition into PDMS as observed by phosphorescence of In. BP (10 wt%) in acetone solution was driven through a 200 μm wide and 100 μm deep channel in a closed PDMS system. The outline of the channel is indicated by the gray bars. (b) Real images at discrete time steps as obtained by the microscope. (c) The line profile of the phosphorescence intensity across the channel is plotted versus time. (d) Depth penetration plotted over time is plotted for varying stiffness of the PDMS matrix. Different mounts of curing agent, 8%, 10%, and 12% (wt) were used to achieve the different stiffnesses.

Table 1. Evolution of BP Concentration in a Simple Microchannel PDMS System during Drying Period after Initial Priming

	priming (imbibition) time	
drying time (min)	1 min	10 min
1	262 ± 14 μm	582 ± 42 μm
30	659 ± 31 μm	1061 ± 81 μm
60	899 ± 86 μm	1328 ± 46 μm

time. For diffusion times longer than 1 h the concentration was typically so low that photoluminescence almost vanished. A simplified model based on linear diffusion for this particular experiment is given by eq 9, where the initial concentration profile is described by the diffusion model during priming (c.f. eqs 6 and 7). We need to assume that during the drying period a different equivalent diffusivity applies compared to the priming process, since the acetone source is removed. Setting the value for the initial diffusivity equal to 8.5×10^{-11} m^2/s as determined above, eq 9 was evaluated iteratively in order to match the experimental data. Figure 10 shows the calculated BP concentration profile at various time steps (solid lines) as well the experimental data (markers). For an assumed equivalent diffusivity of 4×10^{-11} m^2/s during drying, the model lines up well with the experimental data for both experiments. Again, the equivalent diffusivity is a value particular to the experimental setup, but it highlights the speed of the migrating BP as significant. The results clearly outline that the waiting time between priming and graft initiation in a surface treatment protocol is a critical parameter, which needs to be well controlled and kept at short time intervals in order to ensure a sufficiently high BP concentration close to the surface.

Quenching by Oxygen. The presence of molecular oxygen significantly lowers or completely inhibits the hydrogen abstraction of BP and hence the photopolymerization[76,77] due to various mechanisms such as quenching of triplet BP,[78,79] photobleaching of BP,[40,80] or the formation of chain terminating peroxide molecules.[81,82] However, oxygen is consumed during this process at a significant rate as well.[81,83] If BP is present at sufficiently high concentrations, it acts as an oxygen scavenger during initial exposure until oxygen is depleted and PDMS radicalization through hydrogen abstraction can start. However, this oxygen sink along the PDMS surface is constantly replenished by fresh oxygen diffusing in from the surrounding, both by diffusion through the bulk PDMS as well as through the monomer solution. PDMS is known for its high permeability toward oxygen.[82,84] The diffusion coefficient of oxygen in PDMS is typically reported around 50−80 × 10^{-11} m^2/s,[85,86] about twice the value of acetone vapor. With the ability of oxygen to diffuse quickly through PDMS toward the oxygen sink, it is certainly causing constant radicalization inhibition in a border area. However, the oxygen influx through the bulk PDMS can be easily stopped if BP is implanted at sufficient concentration deep below the surface within the PDMS matrix in order to screen the arriving oxygen well before reaching the photopolymerization sites. More critical, on the other hand, is the presence of dissolved oxygen in the monomer solution, as in this case the oxygen limits or inhibits PDMS radicalization right at the surface where graft polymerization is desired. In Figure 9 for example, BP is imbibing into PDMS from a continuous flow of BP solution through the channel (channel indicated by gray background). Although BP concentration has to be the highest in direct vicinity of the wall, maximum photoluminescence (PDMS radicalization) occurs several tenths of micrometers within the PDMS matrix, which is caused by radicalization inhibition due to dissolved oxygen in the BP solution. It shall be noted that, in this case, the influence of oxygen is particularly severe since solubility of oxygen in acetone solution is 5 times higher than that in aqueous solutions,[87] and no measures were taken to remove oxygen from the BP carrying acetone solution. In summary, we want to point out that the presence of oxygen significantly affects and disturbs the efficiency of PDMS radicalization (graft initiation). While the removal of dissolved oxygen from solution through vacuum degassing or bubbling with nitrogen is relatively simple, the prevention of atmospheric oxygen entering the PDMS matrix cannot easily be realized in a simple benchtop process and would require the treatment to be performed, e.g., under nitrogen atmosphere. However, our results show that removal of atmospheric oxygen is not necessary if BP is implanted at sufficient concentrations and in sufficient depth into the PDMS matrix to act as an oxygen scavenger.

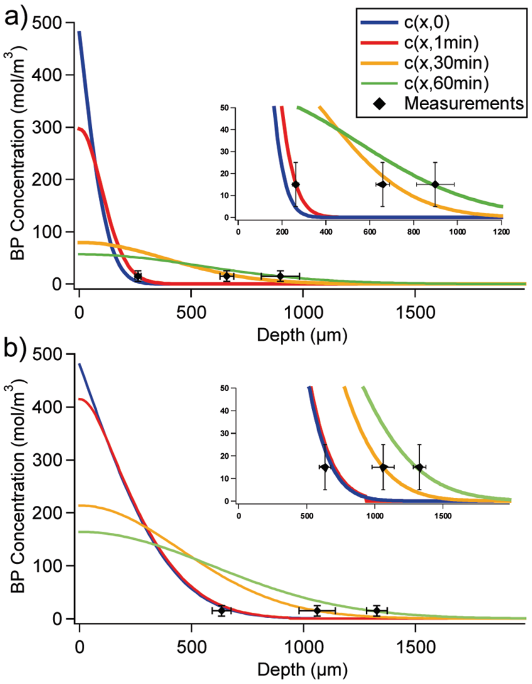

Figure 10. BP concentration profiles during the drying period at discrete time steps calculated according to linear diffusion are plotted as solid lines. Black markers show experimental data. Initial priming was performed with a flow of 10 wt % BP in acetone for (a) 1 min and (b) 10 min.

In Situ Monitoring. The monitoring of reacted BP via photoluminescence can also be easily employed in situ during a graft photopolymerization process. These observations are

---

(76) Gorman, A. A.; Rodgers, M. A. J. *J. Am. Chem. Soc.* **1986**, *108*, 5074–5078.

(77) Drake, J. M.; Levitz, P.; Turro, N. J.; Nitsche, K. S.; Cassidy, K. F. *J. Phys. Chem.* **1988**, *92*, 4680–4684.

(78) Arai, T.; Nishimura, Y.; Sasaki, M.; Fujita, H.; Matsuo, I.; Sakuragi, H.; Tokumaru, K. *Bull. Chem. Soc. Jpn.* **1991**, *64*, 2169–2173.

(79) Nau, W. M.; Scaiano, J. C. *J. Phys. Chem.* **1996**, *100*, 11360–11367.

(80) Coyle, J. D. *Introduction to Organic Photochemistry*; John Wiley & Sons: Chichester, U.K., 1986; Chapter 2, pp 69−72.

(81) Decker, C.; Jenkins, A. D. *Macromolecules* **1985**, *18*, 1241–1244.

(82) Dendukuri, D.; Panda, P.; Haghgooie, R.; Kim, J. M.; Hatton, T. A.; Doyle, P. S. *Macromolecules* **2008**, *41*, 8547–8556.

(83) Goerner, H. *Photochem. Photobiol.* **2006**, *82*, 801–808.

(84) Oh, S.-J.; Zurawsky, W. P. *J. Membr. Sci.* **1996**, *120*, 89–99.

(85) De Bo, I.; Van Langenhove, H.; Pruuost, P.; De Neve, J.; Pieters, J.; Vankelecom, I. F. J.; Dick, E. *J. Membr. Sci.* **2003**, *215*, 303–319.

(86) Shiku, H.; Saito, T.; Wu, C.-C.; Yasukawa, T.; Yokoo, M.; Abe, H.; Matsue, T.; Yamada, H. *Chem. Lett.* **2006**, *35*, 234–235.

(87) Golovanov, I. B.; Zhenodarova, S. M. *Russ. J. Gen. Chem.* **2005**, *75*, 1795–1797.

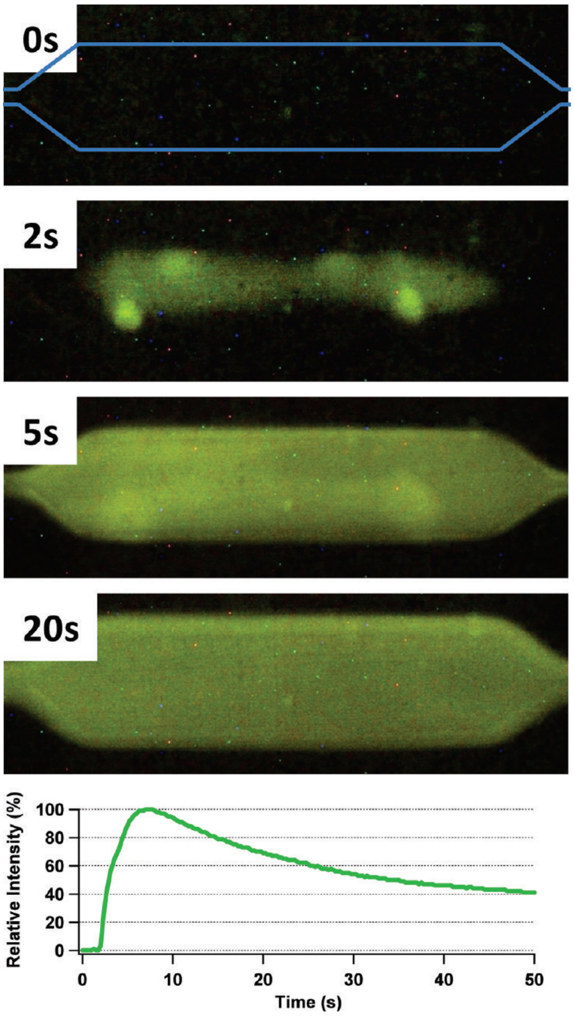

Figure 11. In situ monitoring of reacted BP phosphorescence during graft polymerization of a cavity structure enclosed in PDMS. The shape of the cavity is outlined in blue in the first frame. Images at various time steps are given. The evolution of the average phosphorescence intensity over the first 50 s is shown on the bottom.

valuable in order to verify that a sufficient amount of BP was homogeneously implanted during the priming process, which is particularly helpful during the development of a new surface treatment protocol. An example for in situ monitoring is given in Figure 11: graft polymerization of PAA was performed within a microfluidic cavity structure enclosed in PDMS. The detailed treatment protocol is given elsewhere;[26] briefly, the system was primed with a solution of 10 wt % BP in acetone for 5 min and allowed to dry for 10 min. The system was then filled with a degassed solution of 10 wt % acrylic acid in water and exposed to UV light at 365 nm (mercury i-line) for 3 min at an intensity of 65 mW/cm^2 yielding a thick coating of PAA within the cavity structure. The microstructure as shown in Figure 11 is a 15 × 5 mm^2 wide and 250 μm high cavity with inlet and outlet channel. Images of the cavity during exposure showing the green photoluminescence of reacted BP are shown in Figure 11 as well as an average phosphorescence intensity plot over time for the first 50 s. During the first two seconds, almost no light is emitted since the process is dominated by oxygen quenching. Once oxygen is depleted in the reaction zone, uniform phosphorescence can be observed, and the intensity reaches its maximum (after about 5 s). During the remainder of the exposure, phosphorescence around the cavity walls remains uniform since the oxygen influx from the surrounding is screen by BP deep within the PDMS matrix. However, overall intensity diminishes slowly as BP is used up during the graft polymerization initiation (c.f. Figure 11).

Conclusion

We have developed and presented a visualization method for the detection of reacted BP (benzophenone ketyl radical), which is easily applicable on standard laboratory microscopes. The presented visualization method was proven vital to observe graft initiation in situ and to identify zones of local photoinitiation inhibition, e.g., due to oxygen quenching. Based on the visualization technique, we studied solvent-driven BP migration during BP solution injection (priming) into a typical PDMS microchannel device. We have also determined the effective diffusion coefficient of BP in acetone-swollen PDMS ($D_{\mathrm{eff}} \approx 1 \times 10^{-11}$ m^2/s). Although the measured diffusion coefficient already shows fast BP diffusion, BP migration during priming was shown be up to 10 times faster. These results clearly demonstrate that, for time frames on the order of minutes, the BP concentration profile can significantly change across the PDMS matrix, and in particular BP concentration at the channel surface quickly depletes. These findings, surprisingly high migration speeds of photoinitiator within PDMS, are essential to any graft-polymerization treatment on PDMS and need to be carefully considered and implemented in order to achieve proper surface functionalization at reliably high quality.

Appendix B

Microfluidic Networks (Micromodels)

Detailed sets of experiments were conducted on two–phase flow in micromodels of patterned wettability with the objective being to identify and study the influence of fractional wettability on the resulting flow patterns. The different types of micromodels employed in the study as well as experimental protocols are presented and discussed in detail below. Results and details on the study itself are presented in the main text, section 2.3.

B.1 Micromodel Design

Micromodels with three different network designs were used for the main set of experiments (c.f. Figure 2.15). Network type I was designed as a regular lattice with uniform channels in crisscross arrangement (Figure B.1). Crisscross arrangement was chosen to avoid any preferential direction with respect to the fluid inlet. The uniform channel size allows for surface–related flow phenomena to emerge undisturbed by channel geometry. Network type II provided a regular rectangular network with channel size distribution as well as vacancy size distribution (Figure B.2). ‘Vacancy’ refers to the void space around the node, typically larger than the adjacent channels. In a vacancy/channel arrangement the vacancies can be thought to represent the pores while the channels represent the pore throats of grain–based porous media. Network type III was also based on a regular node arrangement with vacancy and channel size distribution (Figure B.3). Compared to type II the node spacing is wider in type III and both vacancies (in the shape of squares) and channels are placed at a small, random offset with respect to the node positions. A list of detailed properties and design parameters for the three network types is provided in Table B.1.

The figures (Figure B.1, Figure B.2, Figure B.3) also show the fluid inlet and outlet channels as well as additional alignment structures. During micromodel fabrication, via holes were punched through the circular pads at the end of the inlet and outlet channels in order to provide fluid connections to the exterior. The additional inlet and outlet ports served as access ports for a differential pressure sensor.

Typical experiments started with the micromodels initially saturated with clear water. The index of refraction for water is $n = 1.33$ and $n = 1.43$ for PDMS [**227**]. With large field–of–view optics the difference in the refractive index is too small to provide contrast between PDMS and water; hence water–filled channels appear invisible at the beginning of the experiment. It was therefore essential to integrate clearly visible alignment structures in the microcmodel for proper alignment in the optical imaging setup. Network types II and III (Figure B.2, Figure B.3) contain air pockets in square shape while network type I (Figure B.1) contains a dummy channel, which can be filled with a colored liquid.

Table B.1: Network properties and design rules for the three network types (I, II, and III) as employed in this work

	I	**II**	**III**
Lattice Type	uniform, crisscross	uniform, rectangular	uniform, rectangular
Network Dimensions (mm^2)	24 × 18	24 × 18	24 × 18
Porosity (%)	60	70	50
Number of Nodes (Vacancies)	9740	10800	4800
Number of Channels	19200	21300	9400
Node Spacing (µm)	$150 \times \sqrt{2}$	200	300
Channel Width (µm)	80	50, 60, 80, 100, 120 (20% each)	50, 60, 80, 100, 120 (20% each)
Node Vacancy Dimensions (μm^2)	80 × 80	70^2, 90^2, 110^2, 130^2, 140^2 (20% each)	70^2, 90^2, 110^2, 130^2, 140^2 (20% each)
Off-center Channels and Vacancies	No	no	yes

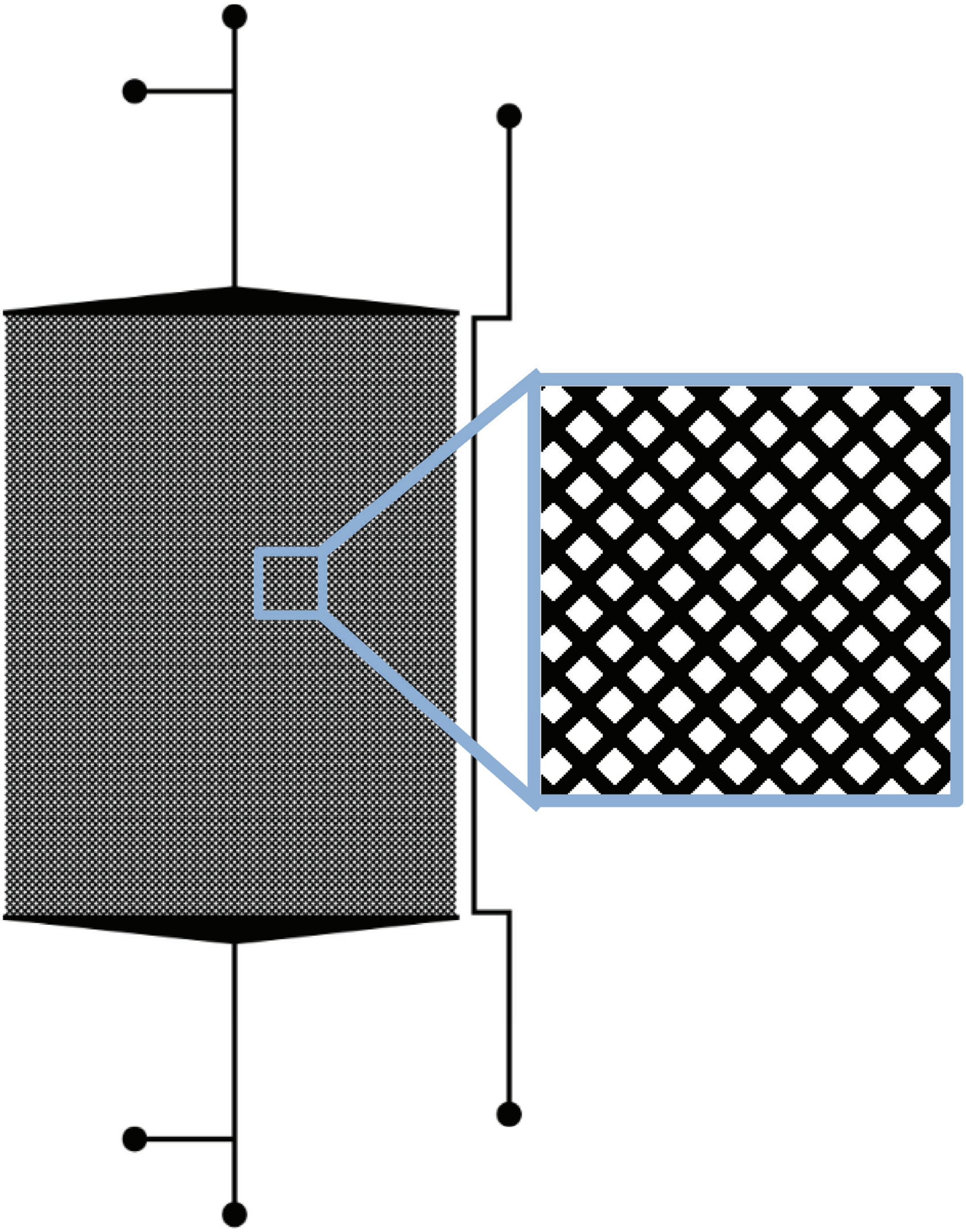

Figure B.1: Network type I.

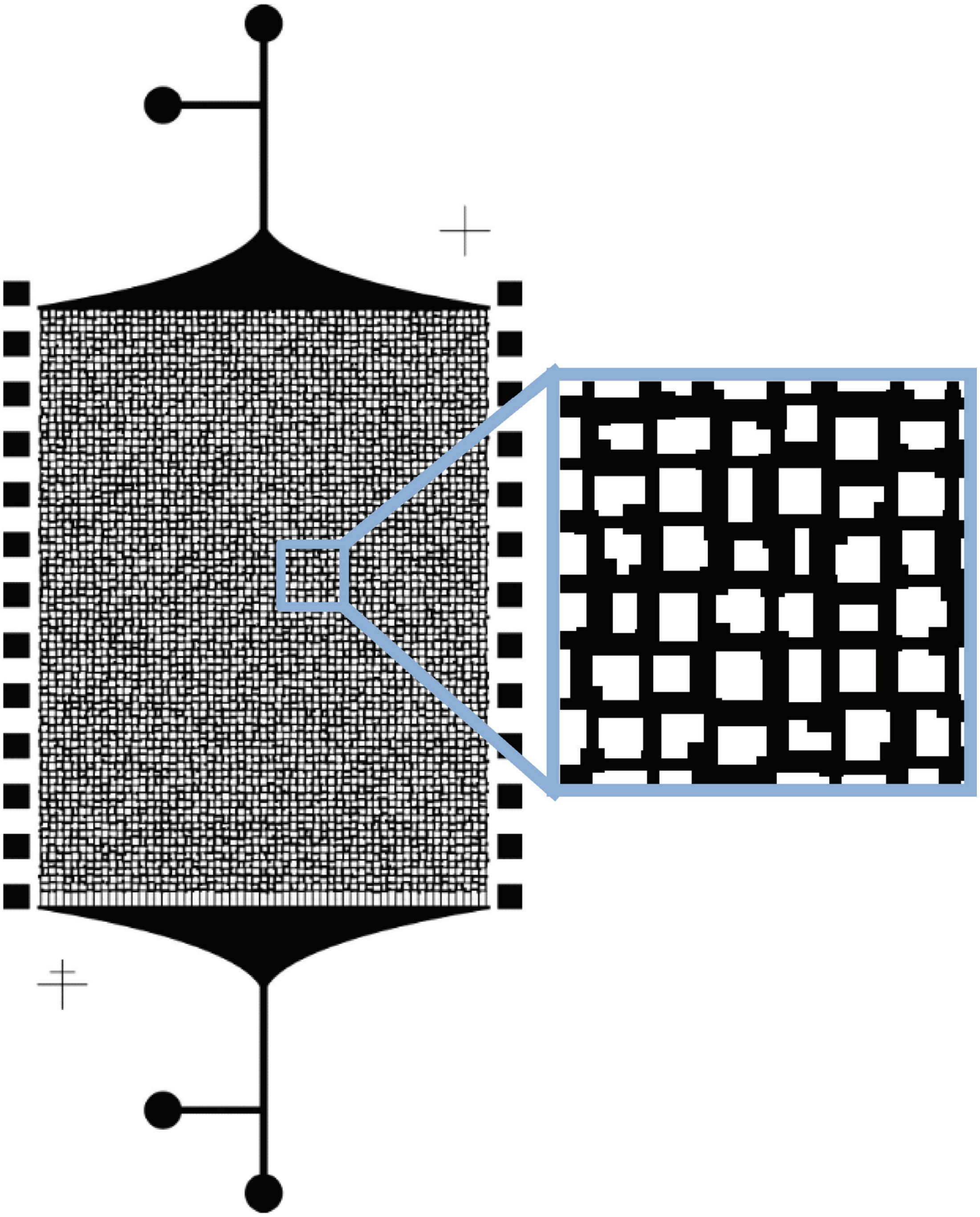

Figure B.2: Network type II.

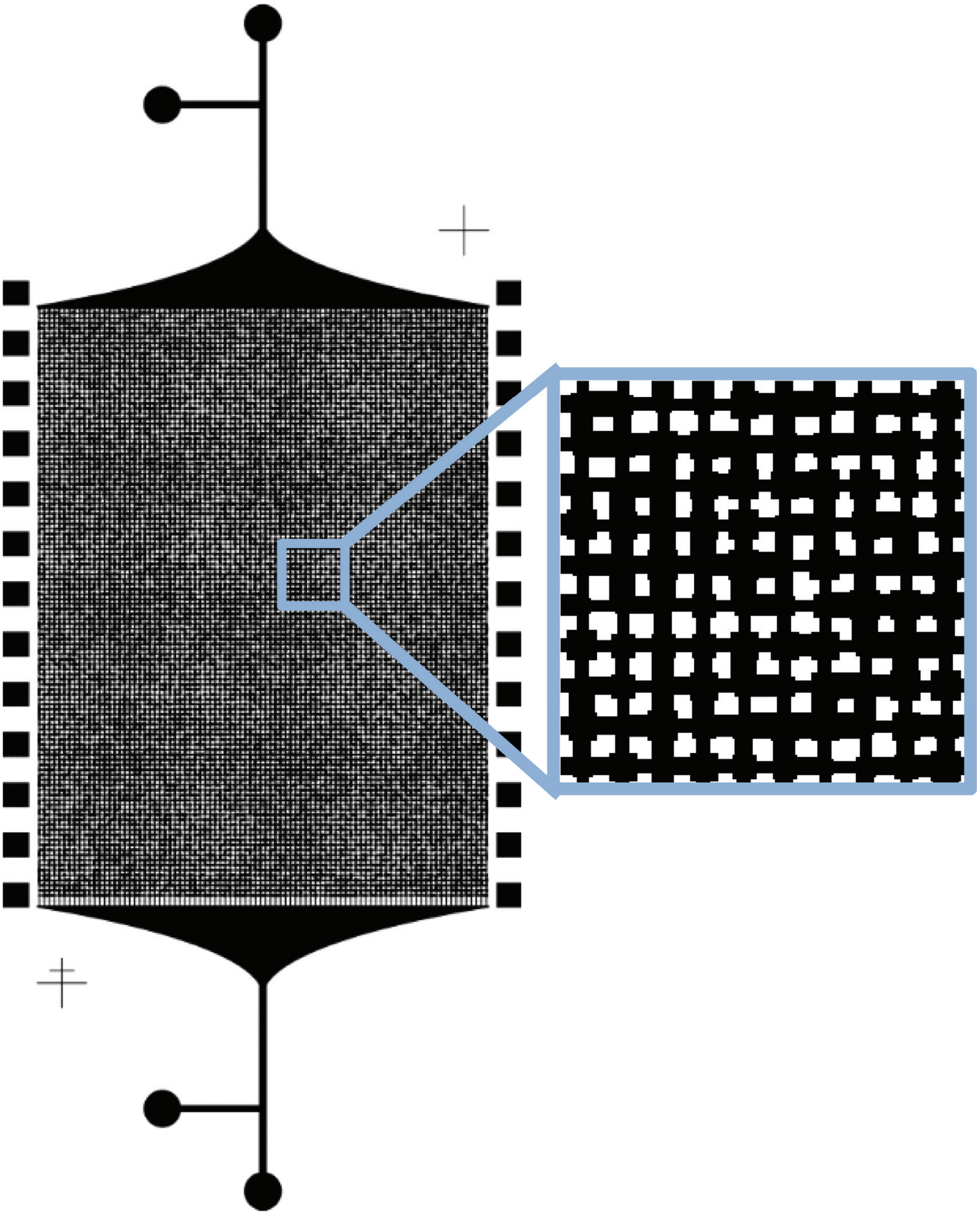

Figure B.3: Network type III.

B.2 Wettability Patterns

Wettability patterns in the micromodels were generated from random distribution patters of 500 × 500 μm^2 square blocks. UV exposure masks for the surface treatment process were designed to provide various ratios f_w between wetting and non–wetting parts.

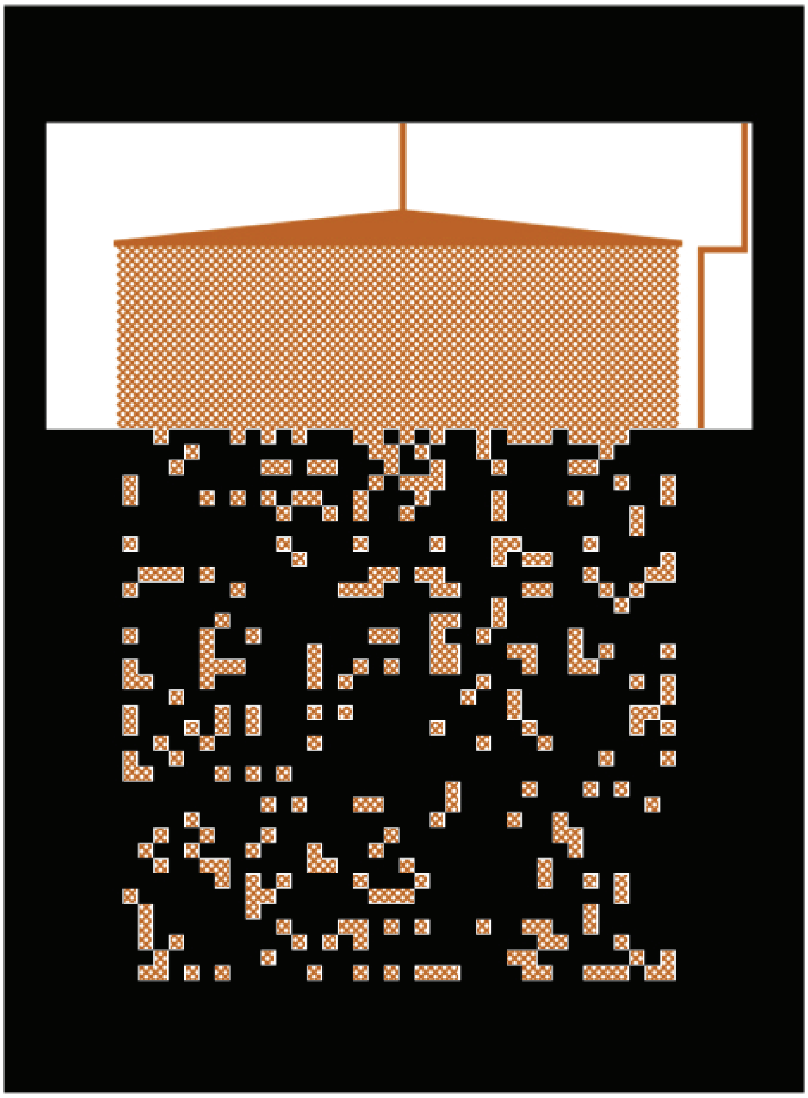

Figure B.4: UV exposure mask designed for wettability pattering with 20% water–wet area ($f_w = 0.2$). The top part of the mask provides a wide opening for full exposure. A micromodel (type I) is schematically shown in the background.

An example of an UV exposure mask is shown in Figure B.4. This particular mask was designed to yield 20% water–wet area (f_w = 0.2). The wide opening in the mask, providing complete water–wet treatment across the top part of the micromodel, prevents an early oil breakthrough and is not considered for the calculation of f_w. A micromodel of network type I is schematically shown behind the mask in Figure B.4, demonstrating the channels which would be subjected to surface treatment in this configuration.

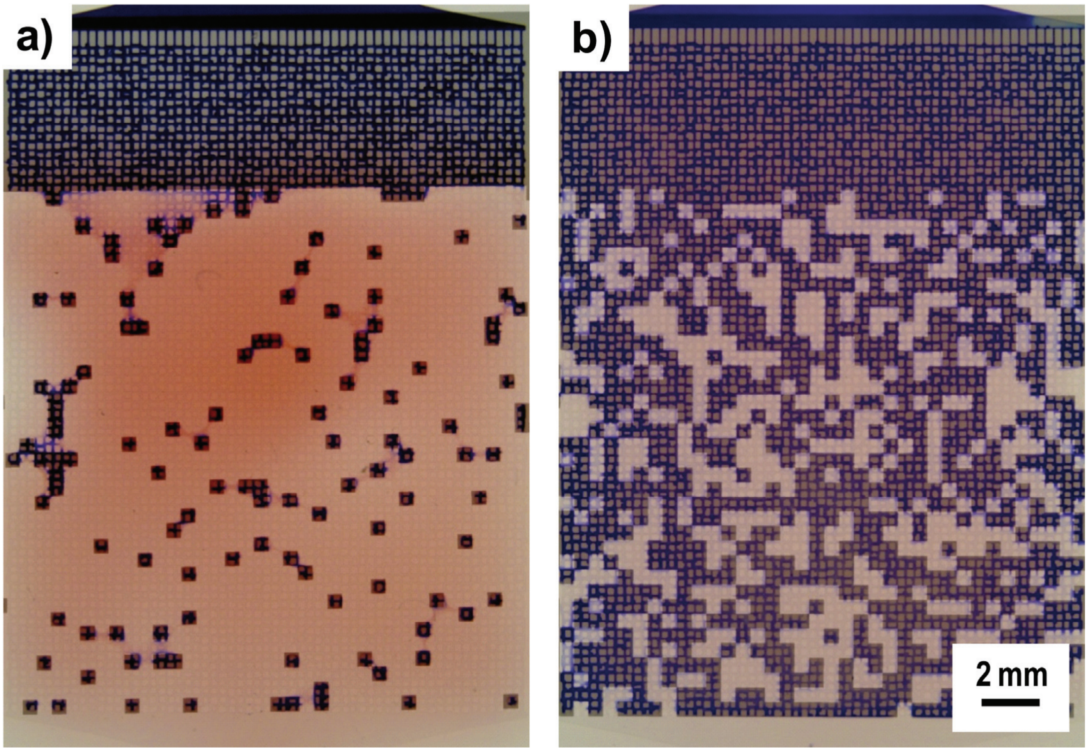

Figure B.5: Network type III micromodels with patterned surface treatment. Grafted areas (water–wet) are stained blue. Wettability patterns were created by random placement of 500 × 500 μm^2 patches to achieve (a) 10% water–wet zones (f_w = 0.1) and (b) 60% water–wet zones (f_w = 0.6). Both micromodels have an additional strip of continuous treatment across the top part. Images were taken after oil injection experiments were performed; residual red dye shed by the oil phase is still visible.

Figure B.5 shows photographs of PDMS micromodels with patterned wettability, revealed by staining with toluidine blue. The main part of each system shows a wettability pattern of randomly placed treatment spots of size 500 × 500 μm^2. Figure B.5a shows a micromodel where 10% of the network were rendered water–wet (f_w = 0.1); in Figure B.5b, 60% of the network were subjected to water–wet surface treatment (f_w = 0.6).

B.3 Experimental Protocol

Figure B.6 shows an outline of the experimental setup used for the two–phase flow experiments in micromodels. The micromodels were placed on a horizontal light table[16], which provided a diffuse homogeneous light source for transmitted–light illumination. Oil was injected into the water–saturated micromodel at a stable flow rate applied by a syringe pump[17]. A typical injection flow rate was 10 µL/min.

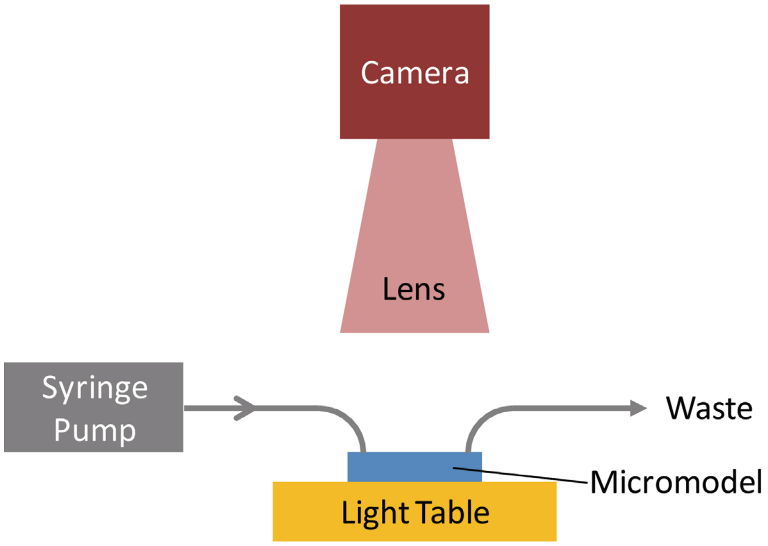

Figure B.6: Experimental Setup.

The flow evolution during injection was captured and recorded with a camera[18] and lens[19] assembly. The magnification of the lens was set to 0.6X in order to capture

---

[16] LPE 4, Waldmann GmbH & Co., Villingen-Schwenningen, Germany.
[17] neMESYS High Precision Syringe Pump, centoni GmbH, Korbussen, Germany.
[18] Color CMOS Camera PL-B782U, PixeLINK, Ottawa, Ontario.

the entire micromodel on the image sensor chip. Typically the image area was set to a size of 22 × 30 mm^2, slightly larger than the network in the micromodel (18 × 24 mm^2). The resolution of the image sensor was 2208 × 3000 pixels (6.6 Megapixel), thus providing a pixel resolution[20] of 10 µm. A 100 µm wide channel in the micromodel was therefore resolved by 10 pixels. The large resolution of the image sensor allowed for full–frame observation of the micromodel while still resolving fluid fronts in individual channels. The color capabilities of the camera based on a Bayer filter design further allowed for unambiguous fluid identification due to staining of the liquids. During the experiment, images were recorded at a rate of 3 frames per second (fps). The pressure difference between fluid inlet and outlet during injection was continuously measured with a differential pressure sensor[21] and recorded on a computer with a digitizer device[22].

B.4 Image Processing

Processing and automated evaluation of the acquired image and video material was a challenging task for two reasons: (1) large numbers of minute features, such as micrometric channels spanning over centimetric distances, needed to be properly analyzed, and (2) initial water saturation prevented the observation of any channel structure due to the close match of the refractive indices. A custom image treatment process was designed with the objective to provide a high level of reliable automated computer processing with only little user interaction. For the processing tasks the software Inspector[23] was used for full–frame operations while Matlab[24] was employed for individual pixel manipulations. A brief outline of the process is as follows.

---

[19] Leica Z16 APO, Leica Microsystems GmbH, Wetzlar, Germany.

[20] Pixel resolution refers to the length in the object plane represented by one pixel. In order to resolve a geometrical feature, a minimum of two pixels is required according to the Nyquist-Shannon sampling theorem [**235**].

[21] 26PC series, Honeywell International Inc., Morristown, New Jersey.

[22] NI 9239 & NI USB-9162, National Instruments Corporation, Austin, Texas.

[23] Inspector 8.0 & Matrox Imaging Library (MIL 8.0), Matrox Electronic Systems Ltd, Dorval, Quebec.

[24] Matlab R2007b, The MathWorks Inc., Natick, Massachusetts.

Figure B.7 outlines the main image treatment process. A white–reference image and a calibration image are recorded prior to each experiment (shown in green). During image processing each frame (image) of the recorded video data is individually subjected to image treatment (blue arrows denote a process applied to each frame). First, color correction is performed based on the recorded white–reference image and lens distortions are removed (image flattening) based on the recorded calibration image by automated steps in Inspector (indicated by blue circles). In a following step, the frames are aligned with the appropriate network model (c.f, Figure B.1, Figure B.2, or Figure B.3). User input is required (indicated by red color) to align one frame of choice with the network model and define the amount of rotation, translation, and scaling. The specified transformations are then automatically applied to all frames. Copies of the images are binarized (thresholding) showing red colors as black and others as white, and passed on to Matlab for further processing (indicated in orange).

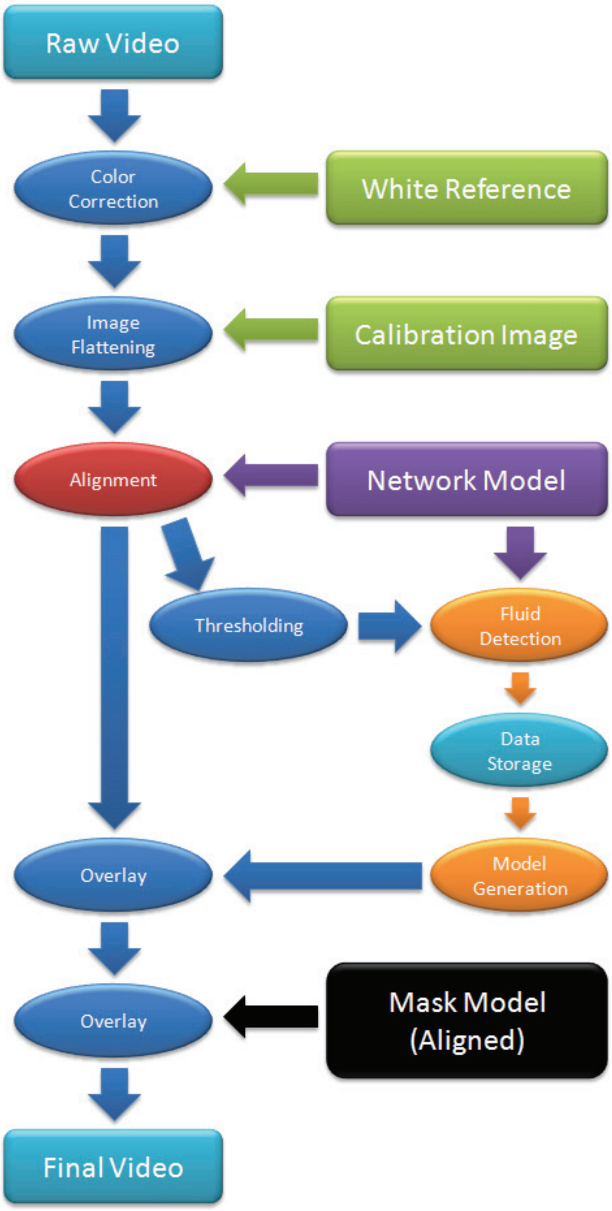

Figure B.7: Process diagram for main image processing sequence.

Based on the knowledge of the network geometry, a search algorithm was developed to identify oil–filled channels and vacancies in each frame and results were stored in a database for further analysis. Based on the database values, Matlab was used to generate idealized network images (oil–filled channels in red and water–filled channels in blue). Those idealized images were passed back to Inspector and blended into the recorded images, thus revealing the positions of the invisible water–filled channels. In a final step, a model of the mask as used during surface treatment was blended into the image to reveal the locations of water–wet and oil–wet zones. Special alignment between the mask model and the recorded images was required.

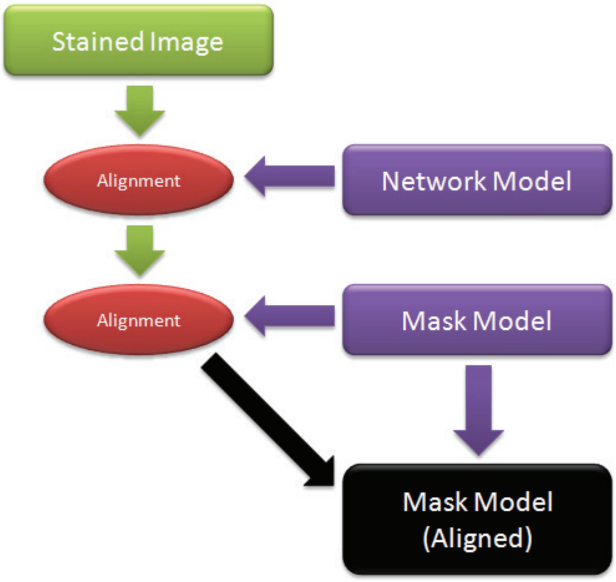

Figure B.8: Process diagram for mask calibration step.

Transparent surface treatment (PAA coating) was revealed by staining with toluidine blue after each experiment and an image of the stained network was recorded. However, during staining, the micromodel needed to be removed from the setup and therefore the calibration was lost. User input is therefore required to align the stained image with the network model, as indicated in Figure B.8. User input is also required to align the mask model with the stained patches in the stained image. With both sets of calibration data the mask model can then be blended in with the video data at its intended position (Figure B.7).

Output of the image treatment process is an image sequence (video) of improved quality with model feature overlay as well as a Matlab dataset of channel saturation for further processing.

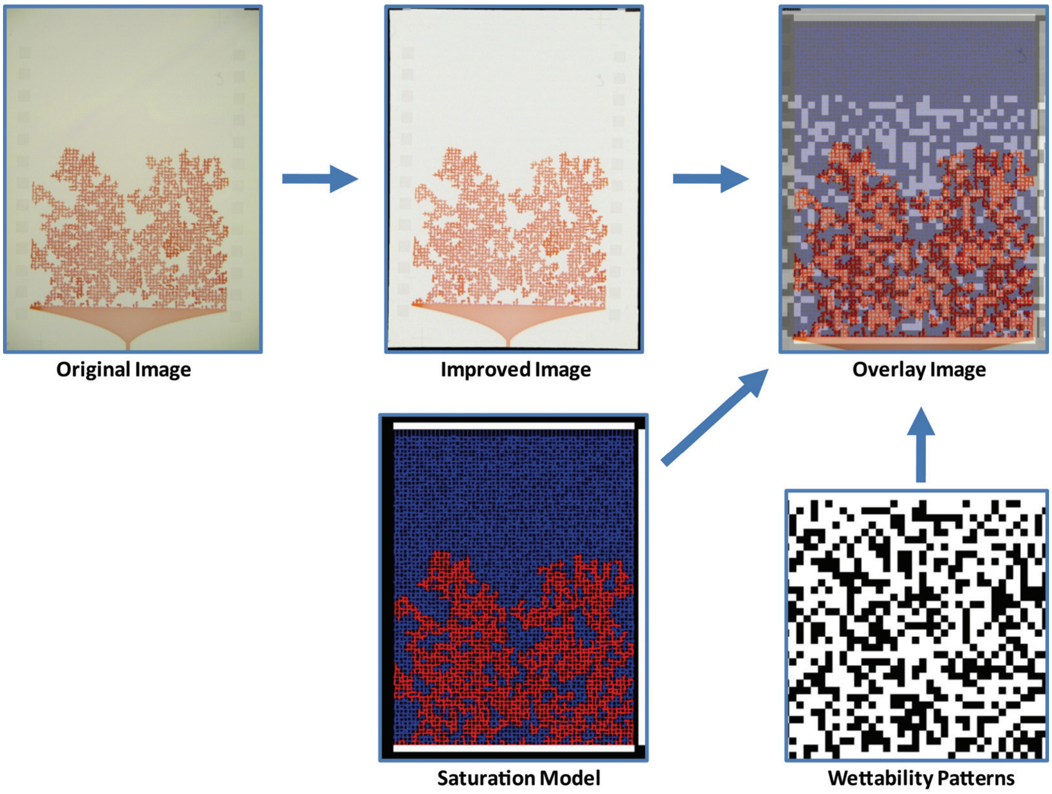

Figure B.9: Example images at various steps in the image treatment process

Example images for several steps throughout the image treatment process are shown in Figure B.9. The quality of the original images is significantly improved by white balance correction, image flattening and alignment. However, even in the improved image water-filled pores as well as regions containing surface treatment remain indistinguishable from the bulk PDMS due to their transparent nature. Therefore, saturation data as determined by the fluid detection algorithm are used to generate a saturation model image, where blue and red colors indicate water- and oil-filled pores, respectively. This saturation model is blended with the real image (improved image) in order to increase visibility and outline all channels. Additionally, the wettability patterns as applied by surface treatment are indicated by superimposing the wettability patterning mask with the final image. As a result a final overlay image is obtained, which shows the originally recorded image (with mainly the red oil phase being visible) together with the saturation model and the superimposed wettability patterns. Superimposing the black and wettability patterning mask causes different shades of brightness to appear in the final image and therefore highlights the different zones of wettability efficiently. Detailed views of the image examples are given in Figure B.10.

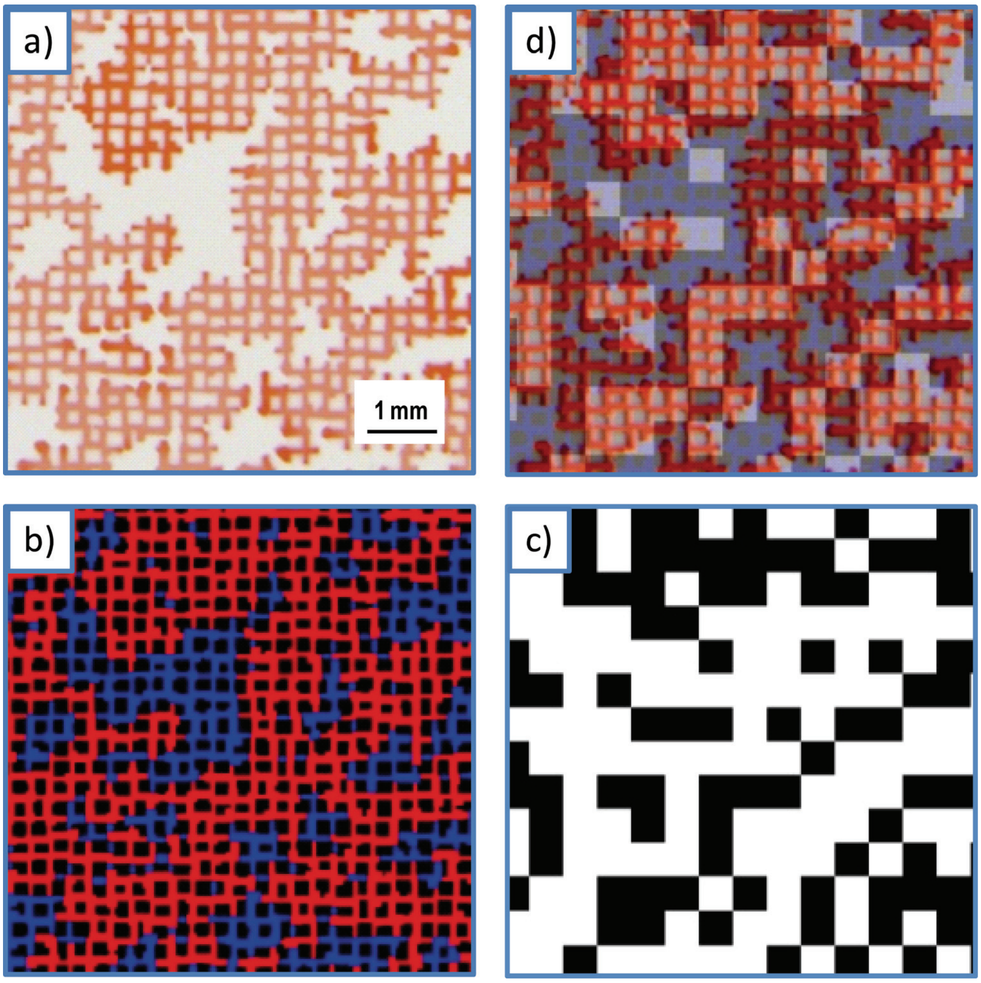

Figure B.10: Detail view of image examples. (a) Recorded image after flattening and white balance (improved image). (b) Network model showing oil-filled (red) and water-filled (blue) pores as identified by fluid detection algorithm (saturation model). (c) Wettability patters as applied to the micromodel. (d) Final overlay image, which is a blend of the individual images a-c.

Appendix C

Microscopic Imager Optics

The microscopic grain imager (MGI) instrument [**228**] is a novel device developed at Schlumberger. The MGI instrument and in particular its applications are described in section 3.2. In short, the MGI drills a sampling hole and employs an endoscope–like optical probe into a rock sample in order to gain access to a clean and well defined rock surface and to become independent of the potentially weathered, rough outer surface of the rock sample. The MGI can then be employed to obtain a high resolution 'virtual core' of the rock sample, i.e. a composite image of the sampling hole, which provides data for geological interpretation. If fluids are injected into the rock samples, the MGI can be employed in a dynamic imaging mode (video acquisition mode) in order to observe the emerging fluids on a pore level. Interpretation of these dynamic imaging data yield additional rock and fluid properties are discussed in section 3.2.

Optimal image quality of the MGI instrument is essential for successful application and reliable measurements in both the static imaging mode (virtual coring) and the dynamic imaging mode (fluid observations). The optical performance was carefully assessed and improved in order to provide an imaging system with optimal image quality and maximal confidence in the acquired data. The optical study of the MGI is presented in this appendix.

C.1 General Description

In order to investigate and improve the optical train of the MGI, a laboratory setup was designed and built for detailed study of the optical properties. It allows for thorough investigation of the individual optical components and consists of the following main parts: A CCD camera (including the objective), a beam splitter, the sapphire probe with conical mirror tip as well as two different illumination techniques, coaxial and angular illumination. The schematic of this setup is shown in Figure C.1.

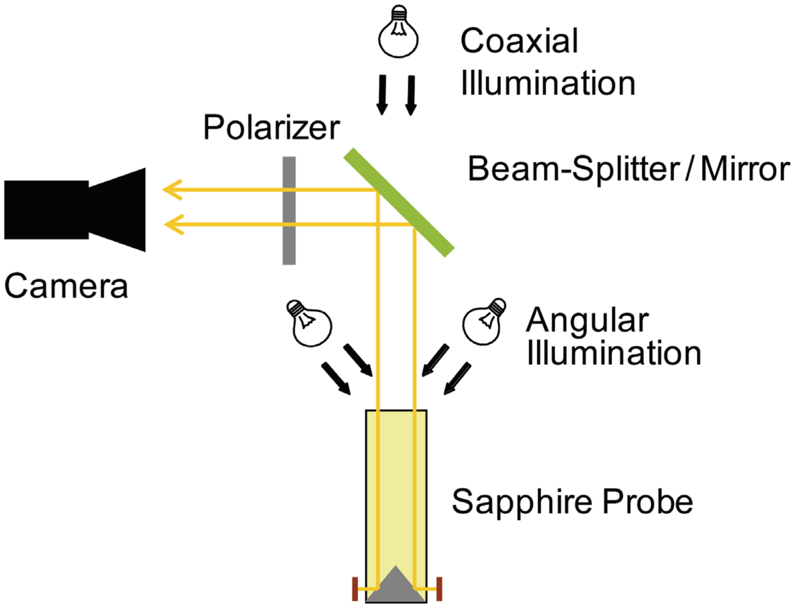

Figure C.1: Schematic of MGI laboratory setup.

A model of the actual setup is shown in Figure C.2. The camera[25] contains a 4 Megapixel color CCD chip of size 15 × 15 mm^2 chip with high sensitivity. The camera is connected to a PC via Firewire B providing data transmission rates up to 100 Mbyte/s. The camera further provides an extended set of on–board features such as partial scan, sub–sampling, etc, hence allowing for optimization regarding high resolution images as well as fast video capturing.

---

[25] PIKE F-421C, Allied Vision Technologies GmbH, Stadtroda, Germany.

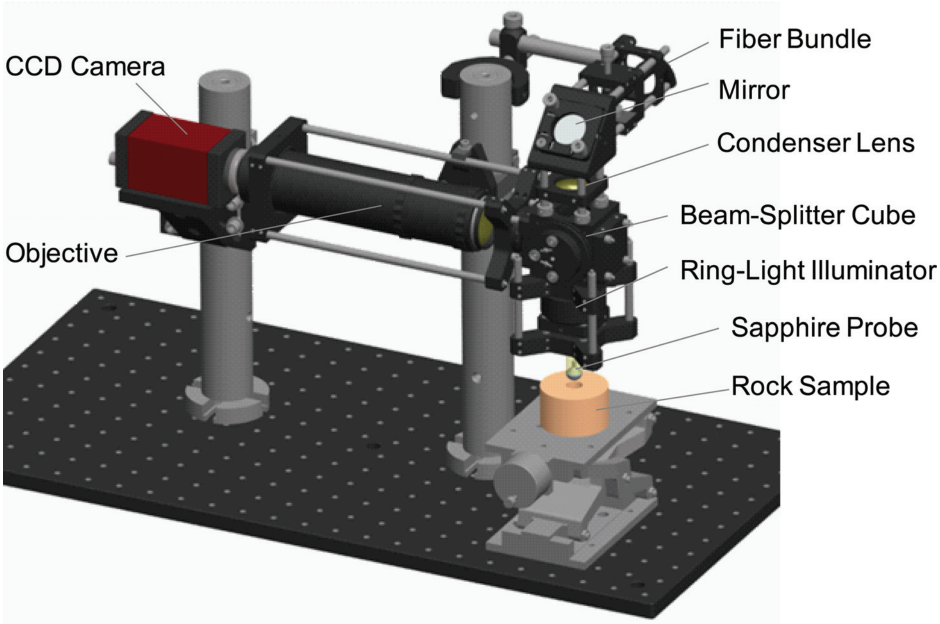

Figure C.2: MGI laboratory setup. The setup is comprised of the optical train including the imaging part and the two illumination options: angular illumination and coaxial illumination. The optics are mounted at a fixed height; the rock sample can be placed underneath on a precision jack and moved relative to the optical probe.

Since the available sapphire probes have an outer diameter of 12 mm, a camera objective[26] with a slight magnification was used to project the 12 mm sapphire fully onto the 15 mm camera chip, and which performs extremely well at this magnification range around 1:1.

Illumination is provided by a 1500 W halogen reflector lamp[27] plus corresponding fiber optics. The setup was designed in order to provide and evaluate two different types of illumination: coaxial and angular illumination. For the coaxial illumination, the light is delivered by a single–branch fiber–bundle and focused by a lens through a beam splitter into the sapphire probe. For the angular illumination a special ring–light

---

[26] Apo-Componon 4,5/90, Jos. Schneider Optische Werke GmbH, Bad Kreuznach, Germany.

[27] KL1500, Schott AG, Main, Germany.

illuminator is used, which is explained in more detail in section C.2. A detailed view of the optical components around the beam–splitter cube is given in Figure C.3.

The setup is built in a way so that the beam splitter can be replaced by a mirror with a quick–release technique for evaluation purposes. Additionally, a polarizer can be inserted in the optical train in order to evaluate polarization effects (see Figure C.1).

Figure C.3: Detail view of the MGI setup. The beam–splitter cube, sapphire probe and the functional components of the illumination systems are shown. Mechanical supports are not shown in the figure. The orientation is such that the camera can look through the polarizer into the beam–splitter cube.

C.1.1 Coaxial Illumination

A proper illumination technique is essential for high image quality. Therefore both angular and coaxial illumination with a white–light source where investigated and compared.

A coaxial illumination technique comprises two fundamental design issues:

- the need for an optical beam splitter and
- the presence of specular reflection,

which both need to be carefully addressed.

C.1.2 Beam Splitter

A schematic of the coaxial illumination and imaging system is shown in Figure C.4. The illuminating light is illustrated as single, bold, bright–orange arrows whereas the rays coming from the object plane are depicted as pairs of narrow dark–orange arrows. In general there are two major concerns regarding beam splitter optics:

- decreased light intensity due to the nature of beam splitting and
- induced optical aberrations by the beam splitter.

For a standard beam splitter with an equal splitting ratio (50r/50t), only half of the intensity from the light source is directed towards the object and again only half of the intensity reflected by the object finally arrives at the camera. If sufficient intensity is available, such as in the laboratory setup, then the decrease in intensity can be easily compensated. However, in terms of a given intensity, the intensity drop due to the beam splitter always demands longer exposure times in the camera, which potentially decreases the image quality due to vibrations, etc. The part of the illuminating light that is reflected by the beam splitter (arrow to the right in Figure C.4) is of no use for the imaging process. However, special care has to be taken in a real design that this light fraction is properly guided away or absorbed. Any specular reflections have to be avoided since those would be visible for the camera through the beam splitter and significantly obstruct the image.

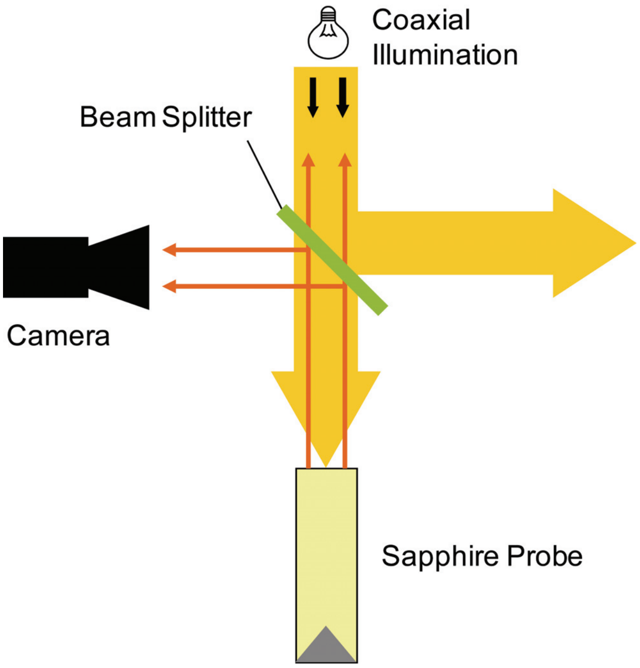

Figure C.4: Coaxial illumination with beam splitter.

Aberrations induced by the beam splitter are typically:

- chromatic aberrations for cubic beam splitters caused by the glass and
- ghost images for plate beam splitters caused by additional reflection on the second surface.

The aberration effects of a cubic beam splitter have been investigated and found to be very small so that they can be neglected in comparison to the aberrations induced by other components in the system. Two different plate beam splitters where tested in the laboratory setup, both performing well. Since these beam splitters are treated by default with an anti reflection coating and/or provide a slightly non–parallel second surface, no ghost images were observed.

If a polarizer is used in the optical train, care should be taken to align it properly in respect to the beam splitter for optimal intensity. Although the beam splitter used in the setup was specified as ‘non–polarizing’, a difference in intensity could be observed for the different polarizations as shown in Figure C.5. Both images were taken with identical settings aside from the orientation of the polarizer.

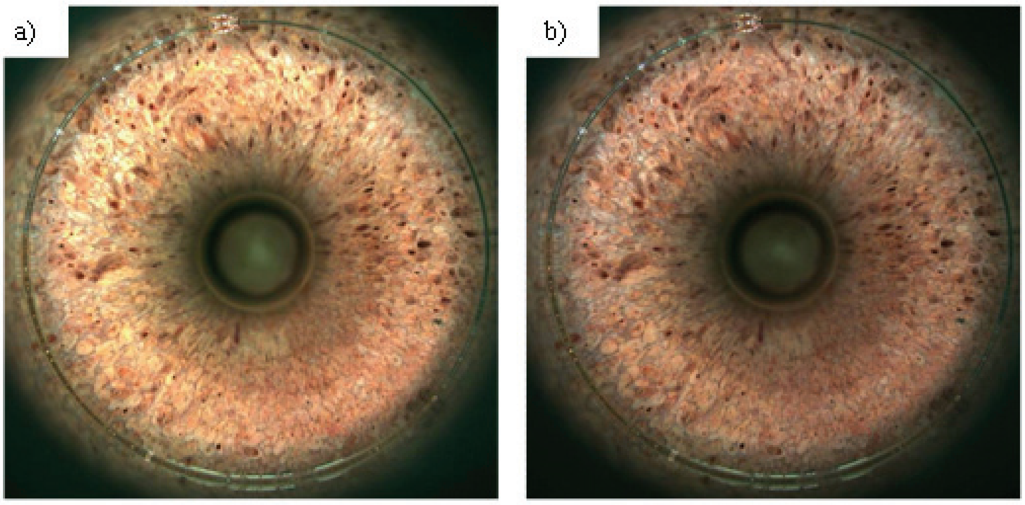

Figure C.5: Images of the same rock sample taken with a plate beam splitter and a polarizer. a) Polarizer at position X, b) Polarizer at position X + 90°.

By qualitative image inspection the performance of the employed beam splitter appears good, no obvious ghost image can be observed. However, if ring–light illumination is used (discussed in section C.2), the beam splitter can be replaced by a mirror (cf. Figure C.1). By these means the achievable image quality with beam splitter and mirror can be compared by taking images of a resolution target. Figure C.6 shows an image obtained with the beam splitter setup next to an image obtained with a high quality first surface mirror with enhanced aluminum coating. In the detail view it is obvious that the mirror yields superior quality. The lower image quality in case (a) might be caused by a lower surface quality of the beam splitter or by a longer exposure time as mentioned earlier, or most likely by a combination of both.

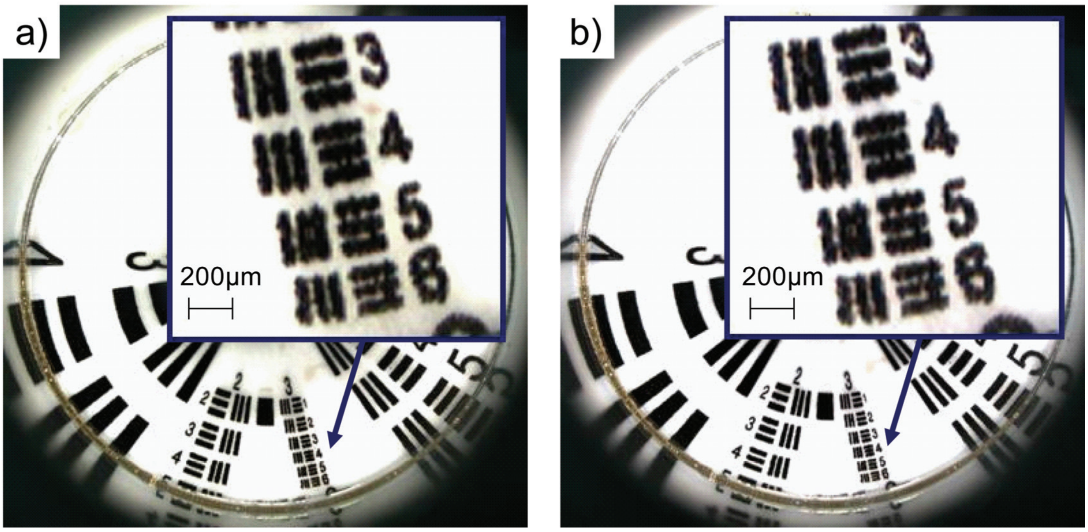

Figure C.6: Image of a resolution target obtained with a) beam splitter, b) mirror. The exposure time was adjusted to compensate for the lower intensity with the beam splitter setup.

The resolution for test element number 6 is 14.3 line pairs per mm. The observed graininess of the lines however is not cause by the imaging system but due to resolution limits of the printing process.

C.1.3 Reflections

Another point that needs to be considered is the appearance of reflections. Reflections occur on each interface between optical media with different indices of refraction and more light is reflected for an increasing difference in the indices of refraction according to the Fresnel equations [**229**]. The mismatch between the index of refraction for air of about $n_{\mathrm{air}} = 1$ and the ordinary index of refraction for sapphire $n_{o,\mathrm{sapphire}} = 1.77$ [**230**] at a wavelength $\lambda = 555$ nm is significant. In the setup under discussion both the entrance surface and the exit surface of the sapphire are parallel to the direction of propagation for coaxial illumination. The exit surface, which is a section of the cylinder surface, is parallel to the optical path because of the conical mirror with a cone angle (half opening angle) of 45° as shown in Figure C.7.

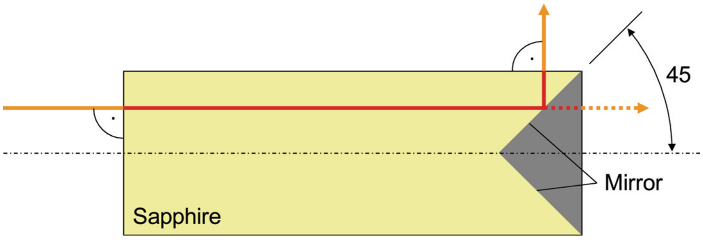

Figure C.7: Schematic beam path in the sapphire probe.

Assuming an ideal mirror for the following discussion, the exit surface can be substituted by a flat tip without changing the path length in the sapphire probe (c.f. Figure C.7).

For normal incidence the reflectivity R is independent of the polarization of the light and can be calculated as [**229**]:

$$R = \left(\frac{n_1 - n_2}{n_1 + n_2}\right)^2 \qquad (\text{C.1})$$

where n_1 and n_2 are the indices of refraction of the two media. The transmittance T is calculated as the remainder of the incident intensity by:

$$T = 1 - R \qquad (\text{C.2})$$

For the air–sapphire (*as*) interface, reflectivity and transmittance can be calculated as:

$$R_{as} = \left(\frac{1 - 1.77}{1 + 1.77}\right)^2 = 7.7\%$$
$$T_{as} = 1 - 0.077 = 92.3\% \qquad (\text{C.3})$$

Since visible range absorption in sapphire is negligible, the intensities relative to the incident intensity can be calculated as shown in Figure C.8. The calculation was stopped after the third interface since only 0.5% of the initial intensity was left. If the tip (surface 2) is surrounded by air as well then only about 85% of the initial intensity can pass the sapphire probe. The other 15% is reflected and superimposed with the light coming from the object. If the sapphire tip is immerged in a fluid with an index of refraction closer to the one of sapphire, then the transmittance will improve. However, the reflectance will always be at least 7.7% (I_{R_1}) since this is the sole contribution from the first surface.

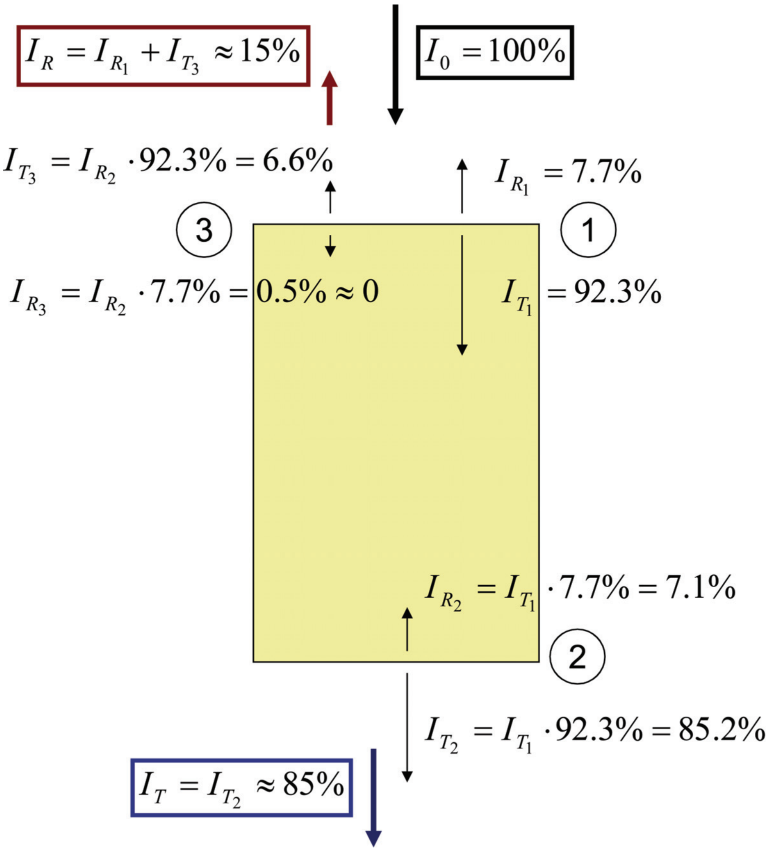

Figure C.8: Transmittance and reflection at the sapphire probe.

Images of a resolution target were taken with coaxial illumination. The actual images were entirely outshined by the reflection at the sapphire. Figure C.9 shows an image of a resolution target taken with the coaxial illumination cone out of center so that at least a fraction of the object becomes visible. From this image it becomes clear that coaxial illumination will not yield useful images in this setup.

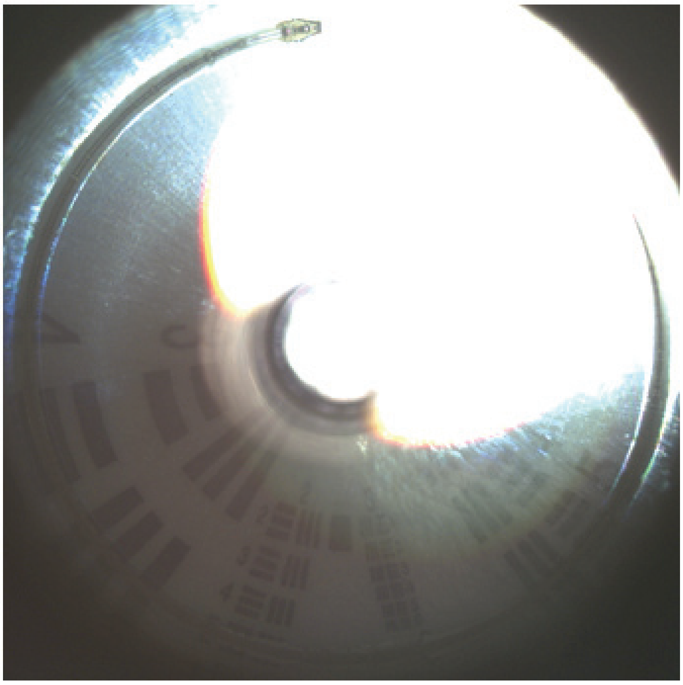

Figure C.9: Image of resolution target taken with coaxial illumination brought out of center.

C.2 Ring Light Illumination

For angular illumination the light is delivered from the light source by a fiber–bundle similar to the coaxial illumination, but in this case a particular fiber–bundle is used, which has its fibers split up and shaped into a ring on one side. Such a fiber is referred to as ring–light guide. Figure C.10 shows a schematic view of such a ring–light head. The individual fibers of the fiber bundle are homogeneously distributed along the ring and molded in a way so that the tips point towards the center axis under a certain angle ϑ. The ring light guide as used in this setup has a clear aperture of $CA = 22$ mm which is sufficiently large to provide a clear view of the sapphire tip to the camera. The ring light head emits light under angles from almost 0° up to 55° with the main intensity emitted at $\vartheta = 20°$.

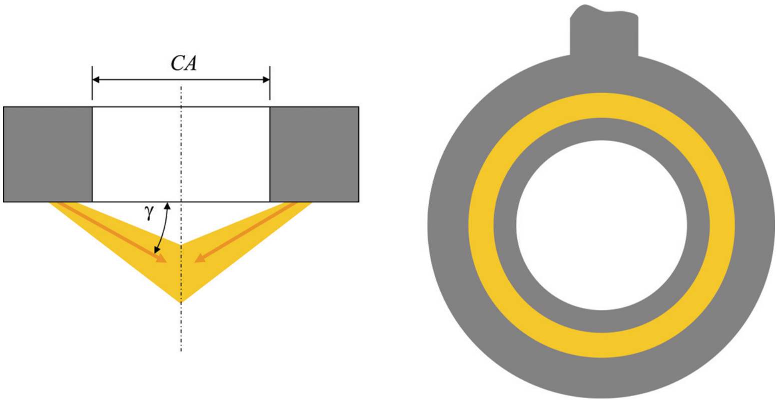

Figure C.10: Ring–light guide for angular illumination.

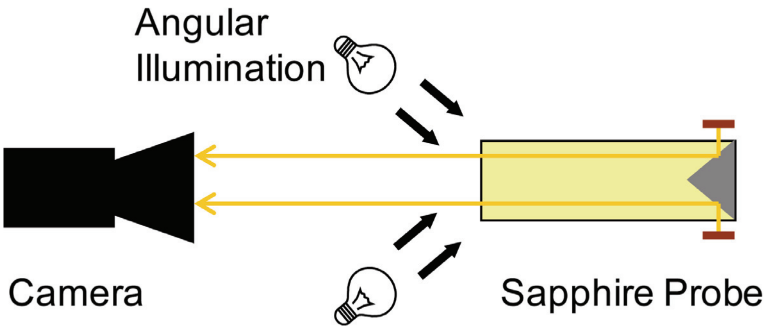

Figure C.11: Sketch of a simplified setup with ring light illumination.

By using such an illumination technique, a beam splitter becomes unnecessary. Therefore the beam splitter was replaced by a high quality mirror in the laboratory setup (cf. Figure C.1). Such a mirror provides increased light intensity at the camera and eventually obvious image quality improvements, as shown in Figure C.6. In general, the mirror can be entirely removed and a simplified setup can be arranged as shown in Figure C.11. However, in this case the general design of the laboratory setup was preserved (see Figure C.1) to keep the setup flexible for later tests involving fluorescence imaging.

With the given light source an illuminance of the object between 20 and 150 klx could be reached depending on the power setting of the lamp. These values were obtained by measurements with a lux meter[28]. As a comparison these values corresponds to the illuminance of direct sunlight on the surface of the earth [**231**]. The typical value used during rock imaging experiments in air and water was around 40 klx. Assuming an even (homogeneous) light distribution at the sapphire tip as well as homogeneous spectral distribution of the light source, the illuminance values given above correspond roughly to an optical power output at the sapphire tip between 5 and 50 mW.

C.2.1 Total Internal Reflection

In order for the angular illumination to work properly the sapphire has to act as a light guide and guide the injected light via total internal reflection towards the conical mirror. The conditions for total internal reflection need to be carefully considered since the side wall (cylinder surface) of the sapphire probe can come in contact with a variety of different fluids. Figure C.12 shows schematically a typical ray path and its significant angles.

---

[28] Testo 545 lux meter, Testo AG, Lenzkirch, Germany.

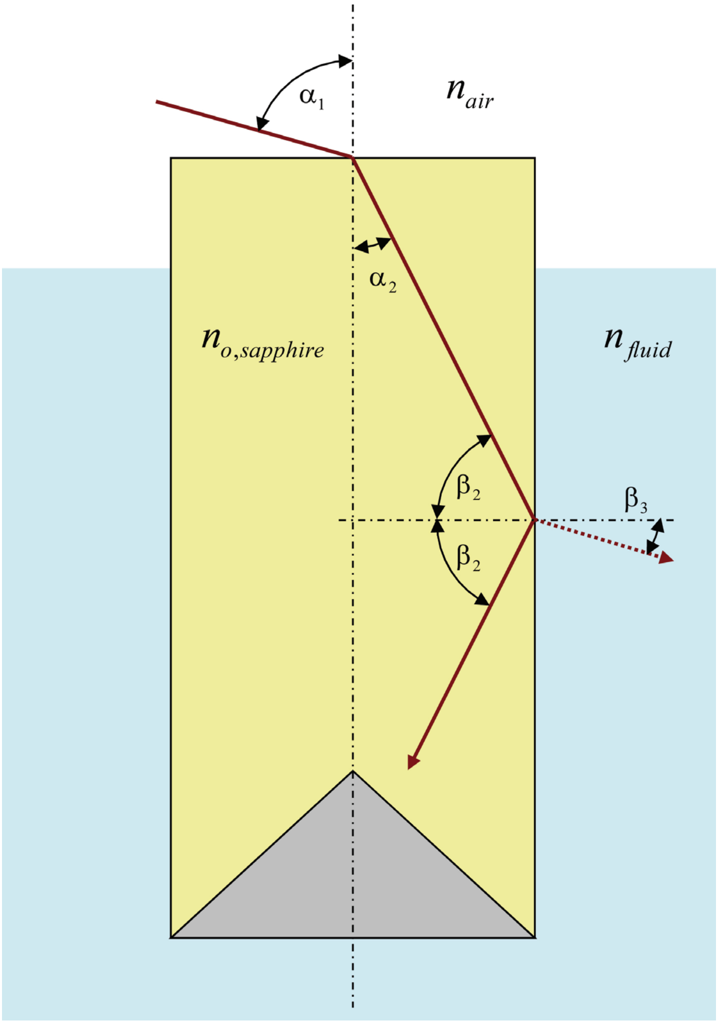

Figure C.12: Condition for internal reflection in the sapphire probe.

The illumination light is always coupled through an interface of air (n_{air}=1) and sapphire. According to Figure C.12, Snell's law can be written as:

$$n_{\mathrm{air}} \sin(\alpha_1) = n_{o,\mathrm{sapphire}} \sin(\alpha_2) \qquad (\text{C.4})$$

or in terms of β_2 as:

$$\alpha_1 = \arcsin\left(n_{o,\mathrm{sapphire}} \sin(90° - \beta_2)\right) \qquad (\text{C.5})$$

In order for total reflection to occur, β_2 has to be equal or larger than the critical angle:

$$\beta_2 \geq \arcsin\left(\frac{n_{\text{fluid}}}{n_{o,\text{sapphire}}}\right) \qquad (\text{ C.6 })$$

Substituting eqn. C.6 into eqn. C.5 yields the condition for the coupling angle α_1 in terms of the index of refraction of the surrounding fluids for which the sapphire probe properly serves as a light guide:

$$\alpha_1 \leq \arcsin\left(n_{o,\text{sapphire}}\sin\left(90° - \arcsin\left(\frac{n_{\text{fluid}}}{n_{o,\text{sapphire}}}\right)\right)\right) \qquad (\text{ C.7 })$$

Figure C.13 shows a plot of eqn. C.7. Sapphire has an ordinary index of refraction of $n_{o,\text{sapphire}}$ = 1.77 at the center of the visible range (λ=555 nm) [**230**]. However, at a wavelength of λ' = 800 nm the index of refraction has decreased to $n'_{o,\text{sapphire}}$ = 1.76 [**230**]. Results for both values are shown in Figure C.13.

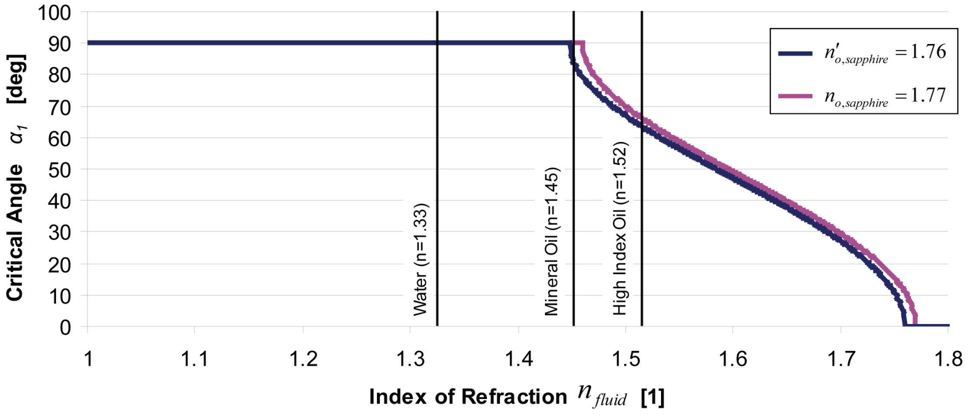

Figure C.13: Critical coupling angle in terms of the index of refraction of the surrounding fluid. The actual coupling angle has to be equal or smaller than the given values.

If light is coupled into the sapphire probe at angles equal or smaller than the indicated ones, then light is properly guided through the sapphire. As can be seen in Figure C.13, if the sapphire probe is surrounded by air or water then there are no restrictions to the coupling. Even for typical mineral oils such as Hydroseal[29] with an index of refraction of n = 1.45 [**232**] the coupling angle can still be up to almost 90°. For high–index oils (e.g. n = 1.52 [**233**]), which are unlikely to appear in oil wells, the maximal allowed coupling angle of about 65° falls in the range of the angular illumination provided by the used ring–light. The range of ring–light emitting angles between 0° and 55° as mentioned earlier corresponds to a range of coupling angles between 35° and 90°. In this case, a part of the light can escape through the cylinder surface of the sapphire probe and is lost, but there will still be a part of the illumination light that contributes to a proper illumination.

Judging from these findings, it seems valid to use the sapphire probe as light guide without any additional treatment of the cylinder surface.

C.2.2 Even Illumination

Even illumination of the sample is very important in order to obtain images with uniform brightness. This is especially important if the images are used to perform virtual coring. Virtual coring refers to the procedure of mapping a large fraction of the cylinder surface of the sample perforation by obtaining and assembling a series of images at different depths within the sample perforation. Figure C.14 shows the principle of such a virtual core assembly process. In order to obtain a seamless virtual core image it is crucial that the brightness values at the top of an image match the ones on the bottom of the following image and so forth.

---

[29] Hydroseal G 232 H, Total France, Puteaux, France.

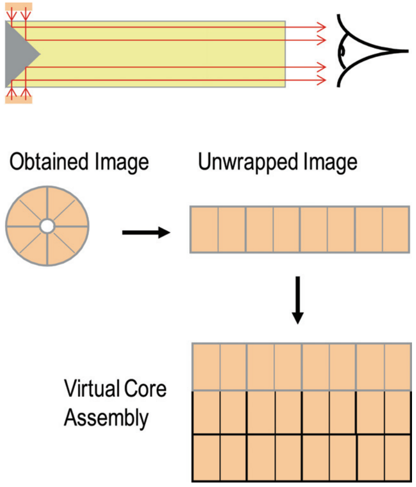

Figure C.14: Virtual core assembly.

Figure C.15 shows an example of a virtual core obtained from a real rock, which suffers from a discontinuous brightness profile. However, it shall be noted that the observed stripes are caused only by a mismatch in brightness and are not due to a misalignment of the individual images. Rock features such as the pores line up accurately across individual images.

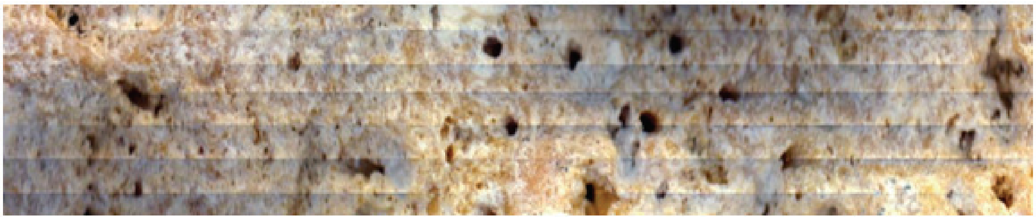

Figure C.15: Virtual core example 1.

In case of coaxial illumination with collimated light, one can easily imagine that the obtained image will possess an even brightness distribution if an ideal mirror or an ideal diffuser is wrapped around the sapphire probe. Following this train of thought, if there was a gap between the sapphire surface and the object, then depending on the case one of the following would happen: For the perfectly reflecting target, the brightness distribution would stay even and the image would not change as all light beams are reflected straight back into the sapphire probe. For the perfect diffuser, the brightness distribution would decrease towards the outer and inner ring having the maximal intensity left at the middle ring (reference is the wrapped image, cf. Figure C.14). This profile would be due to the fact that the diffuser redistributes each incoming straight light beam into an outgoing cone of large opening angle and with an increasing gap, the fraction of the light cone that 'misses' the sapphire probe increases as well.

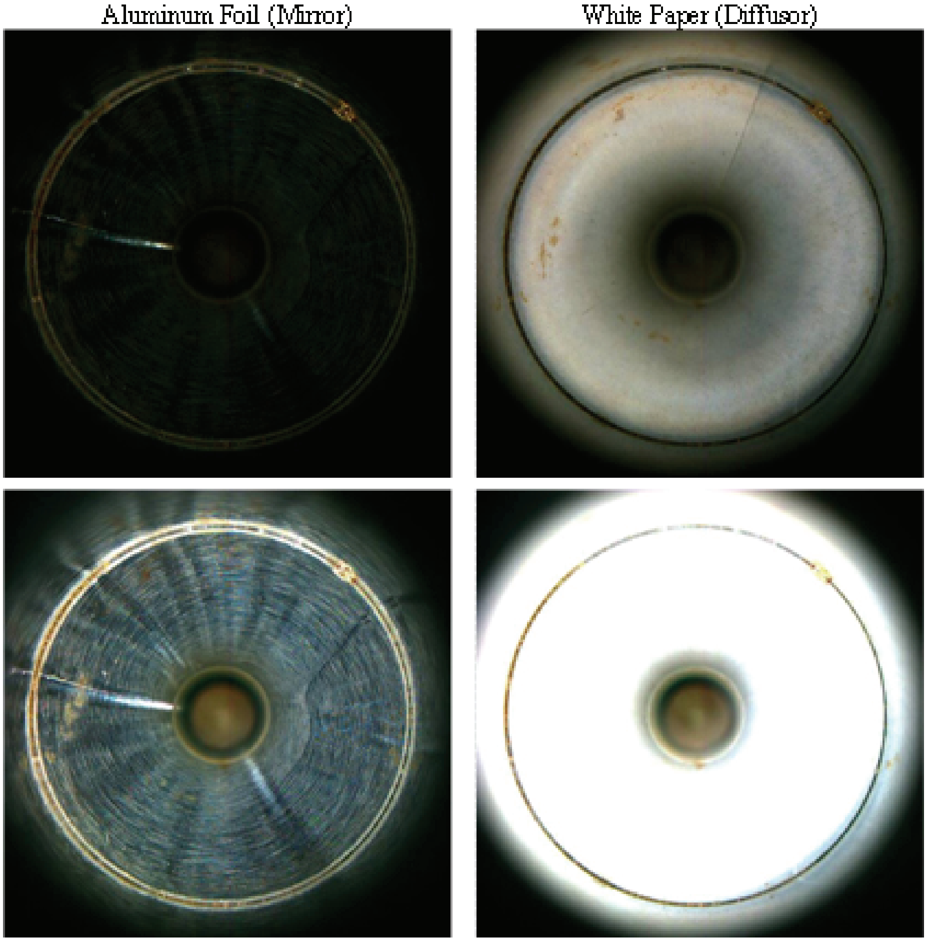

Figure C.16: Images obtained with the ring–light illumination setup for a sapphire probe surrounded by a mirror and a diffuser. Images in each row are taken with identical illumination intensity.

In the present case of ring–light illumination, the optical ray paths are more complicated since the outgoing light exits the sapphire probe already under a variety of oblique angles. Hence the even brightness distribution is not even given anymore for objects in direct contact with the sapphire probe. Figure C.16 shows images obtained with the ring–light illumination setup of the sapphire probe wrapped with highly reflective aluminum foil (left column) and with white paper (right column). The illumination light intensity of the two images in each row is the same. Whereas for coaxial illumination the light intensity seen by the camera would be much larger when reflective aluminum foil is present, in this setup the image with the aluminum reflector appears to be almost dark. This fact proves that the illuminating light leaves the sapphire probe under oblique angles and basically no coaxial components are present. The reflections of these oblique–angle rays most likely reenter the sapphire probe as schematically shown in the left–hand part of Figure C.17 but escape from the optical train at a later point and do not reach the camera. In the case of a diffusing object, parts of the illumination light are always reflected straight back in the probe independent of the incident light angle and can be captured by the camera. That is shown schematically in the right part of Figure C.17. Such an illumination technique is very powerful and extremely valuable for this rock imaging application as it significantly enhances the edge contrast and gives a good visual impression of different surface depths.

An ideal diffuser as mentioned above is also referred to as a Lambertian scatterer [**234**]. When illuminated, such a diffuser appears to possess equal brightness regardless of the observation angle. White paper follows the laws of a Lambertian scatterer in good approximation [**234**] and is therefore used as the diffuser target of choice.

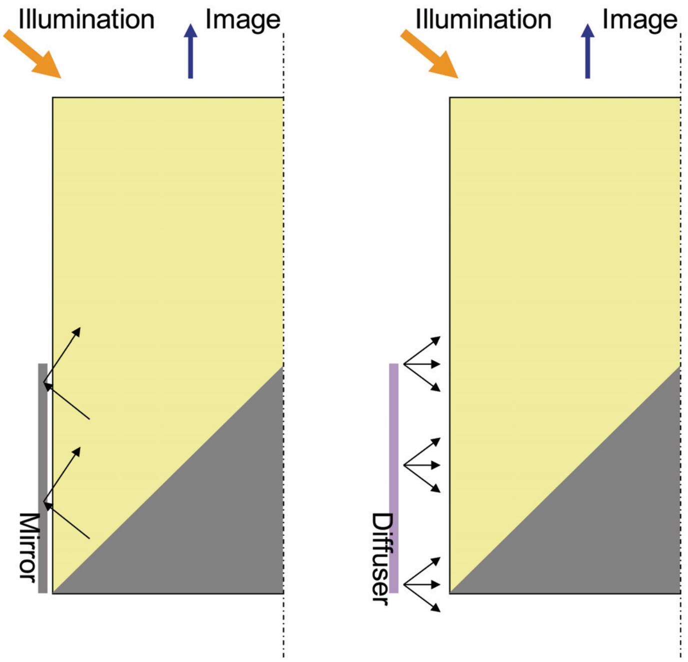

Figure C.17: Visibility of reflecting or diffusing object in the case of oblique angle illumination.

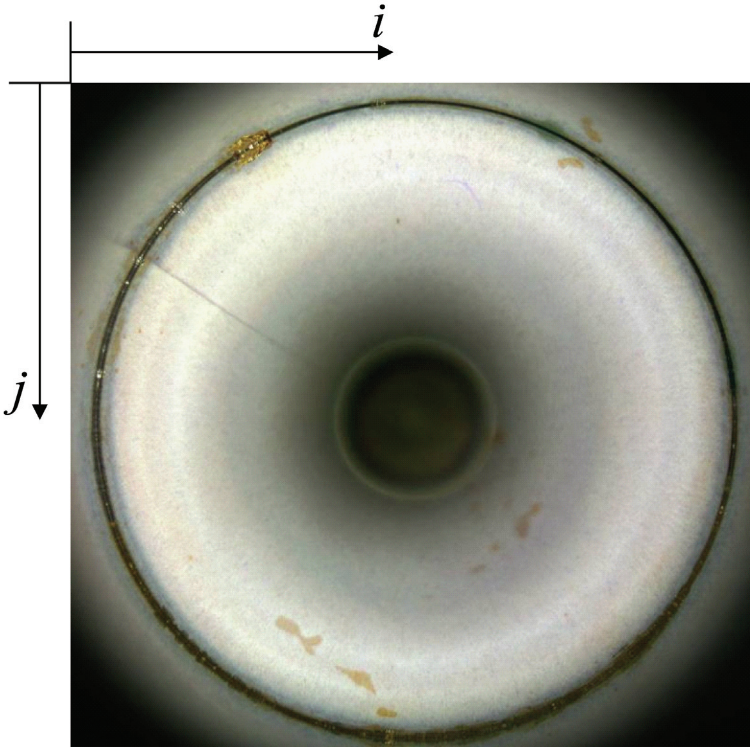

Figure C.18: White reference image.

Figure C.18 shows a white–reference image in the angular illumination case obtained by wrapping bright–white copier paper around the sapphire probe. As can be seen from the image, the illumination intensity is not evenly distributed over the image. However, if such a white–reference image is obtained prior to virtual coring, then the brightness distribution in the virtual core images can be corrected according to the following equation:

$$image_{ij} = \frac{original_{ij} \times \max\left(ref_{ij}\right)}{ref_{ij}} \qquad (\quad C.8 \quad)$$

The corrected image is referred to as $image$, $original$ and ref denote the raw core image from the camera and the white–reference image, respectively. The annotation with the indices ij shall indicate that eqn. C.8 has to be applied as a pixel–by–pixel operation.

Such an illumination correction has been performed on the images of the virtual core shown in Figure C.19. For this particular sample, heavy vibrations occurred at the drill bit causing a rough, non–circular sample perforation. As can be seen, the right half of the core image appears now to be seamless, as desired. This part of the rock was very close to or directly in contact with the sapphire rod, which can be concluded from the well focused and well illuminated appearance. In the left half of the image, however, a brightness mismatch can still be observed. This part of the rock surface seems to be located at a significant distance away from the sapphire probe surface since the illumination is weaker and the rock structure is unfocused.

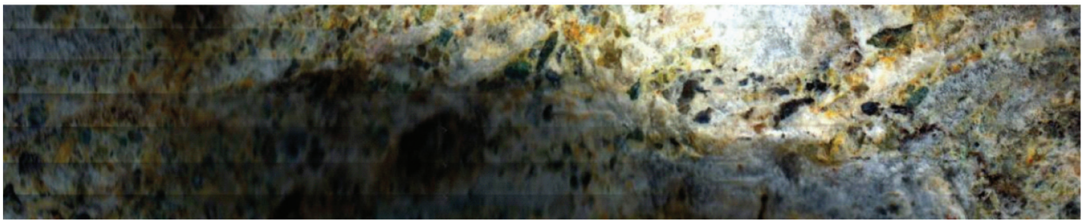

Figure C.19: Virtual core example 2.

The white reference image for example 2 has been taken with a paper wrapped directly around the sapphire probe. The brightness correction based on this reference image works well for the rock sections in close contact with the sapphire probe. For the regions where there is a significant gap between the rock surface and the sapphire probe, the image correction did not work sufficiently. This finding indicates a large dependency of the brightness distribution with distance. An experiment has been conducted with white paper targets wrapped in cylindrical shapes of various diameters. The results of this experiment are shown in Figure C.20. An image was obtained for each paper cylinder pressed against the sapphire probe from one side (from the left in Figure C.20) hence creating the maximal gap on the opposing side (on the right). Line profiles of the intensity were obtained from each image along the red line shown in the upper left image and plotted for comparison.

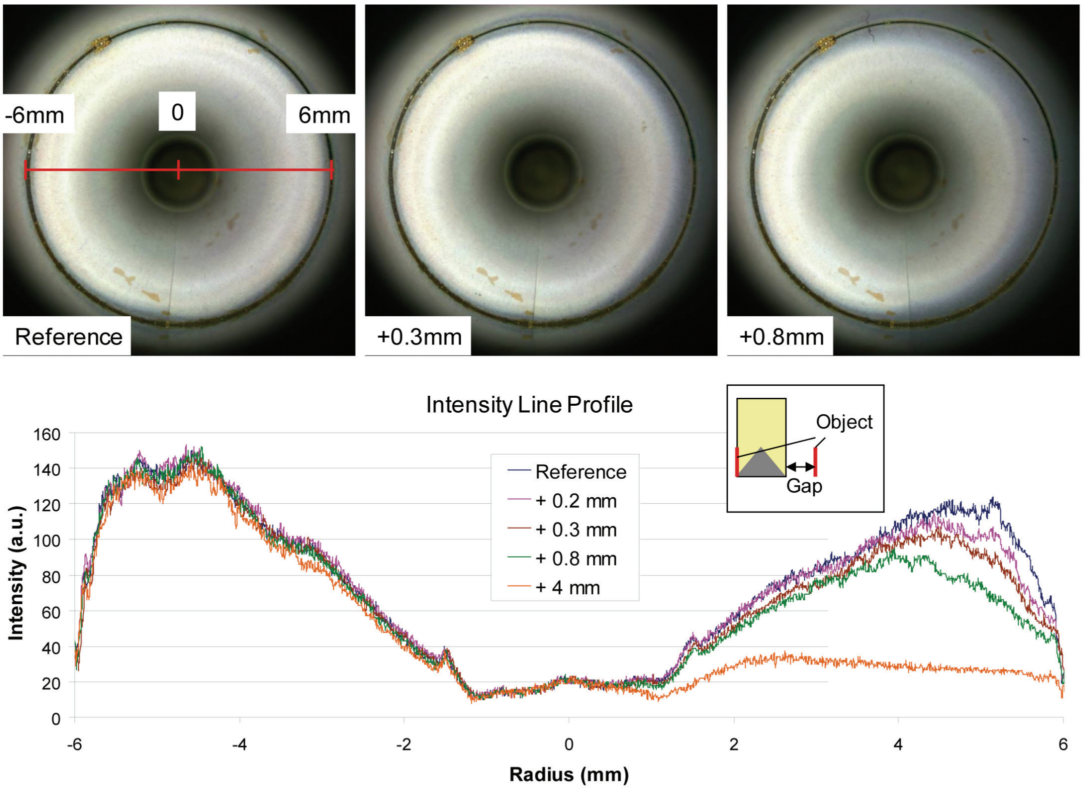

Figure C.20: Illumination intensity at different gap sizes.

Two facts can be established from Figure C.20, first, the brightness varies significantly over the radius, and second, the brightness drops quickly for increasing gap size. Fact number one can be easily corrected by means of white reference correction. However, the drop in brightness in the outer ring for increasing gap sizes has a significant impact on the quality of the virtual core image, especially since this outer ring region provides the highest resolution and is therefore the most valuable part.

It has to be mentioned that the virtual coring example in Figure C.19 represents an untypically bad result that can be easily avoided if proper care is taken during the drilling process. However, if vugs, pores or fractures of extended size are present, which cause a significant gap between the optical probe and their surface structure, then the unsteady brightness problem can occur locally in these regions. Also, a special white–reference target should be used, which resembles the real gap size as present in the sample perforation.

C.3 Resolution and Image Quality

Looking down the sapphire probe along the cylinder axis towards the conical mirror provides a right angle view to the side wall of the probe. For axis–parallel rays the refractive angle is exactly 90° since the full opening angle of the cone is also 90°. Although the mirror induces significant distortion, the optical path lengths stay the same as compared to a sapphire probe with a flat tip. This relation is indicated by the orange ray in Figure C.21. Therefore, besides the induced distortion, the image seen by the camera could also be located at the end of a flat sapphire tip, which shall be referred to as substituted object. The substituted object, a disk of diameter 12 mm needs to be fully projected on the image sensor. The CCD chip of the camera in the laboratory setup has a square matrix with 2048 x 2048 pixels. If the setup is carefully aligned so that the entire image sensor is filled with the area of interest, then each pixel would represent an area of less than 6 x 6 μm^2 in the object plane. In this case, however, slight movements of the sapphire tip would instantly lead to misalignment and image clipping. A more stable approach is to set the magnification in a way that the area of interest is slightly smaller than the image sensor. Leaving a safety border of 100 pixels on each side will provide an image in which each pixel corresponds to an area of 6.5 x 6.5 µm^2 in the object plane, yielding a theoretical resolution of 13 µm or 77 line pairs per millimeter (lp/mm).

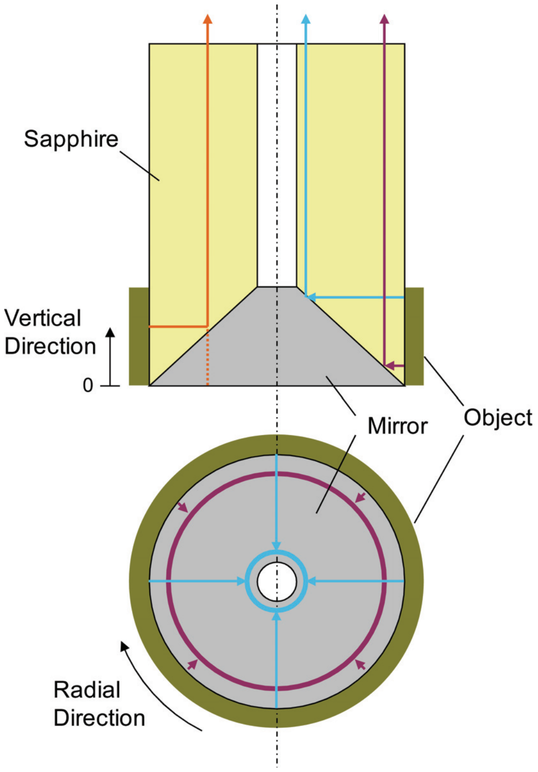

Figure C.21: Ray paths in the sapphire probe for the imaging part.

C.3.1 Distortion

Significant distortion is induced by the conical mirror in the sapphire probe, although the original dimensions can be restored with a post–processing algorithm, referred to as ‘unwrapping’. However, the effective resolution varies significantly over the unwrapped image. As indicated in Figure C.21 the two directions in the object plane shall be referred to as the radial direction along the circumference of the sapphire probe and the vertical direction parallel to the sapphire cylinder axis with its zero position at the tip of the sapphire. If one imagines the object to be divided in rings with incremental extend in vertical direction then each of these rings gets projected to a corresponding ring on the conical mirror, which is then seen by the camera. The projected rings decrease in diameter for increasing vertical position but still represent a full ring of diameter 12 mm in the object plane. Therefore, the resolution is the highest for the area closest to the tip of the sapphire and decreases significantly in the vertical direction. This is shown schematically in Figure C.21, where the purple rays correspond to the high resolution area and the turquoise rays correspond to an area of low resolution. It has to be mentioned that only the resolution in the radial direction decreases with increasing vertical position as the diameter of the projected rings get increasingly shrunk in respect to the original diameter, hence compressing features in this radial direction. In the vertical direction the projection is theoretically free of distortion as the width of each projected ring seen by the camera is the same as the width of it in the object plane.

The sapphire probe in use had an outer diameter of 12 mm and an additional central perforation of diameter 3 mm hence providing a reflective area in the vertical direction over 4.5 mm. Calculated pixel density and pixel size in the object plane are plotted in Figure C.22 as functions of the vertical position both for the radial and vertical directions. The theoretical resolution or upper resolution limit can be expressed as half the pixel density in lp/mm. Or, in other words, the smallest features that can be resolved according to the Nyquist–Shannon sampling theorem [**235**] needs to have an extension of twice the projected pixel size as given in the right–hand plot in Figure C.22.

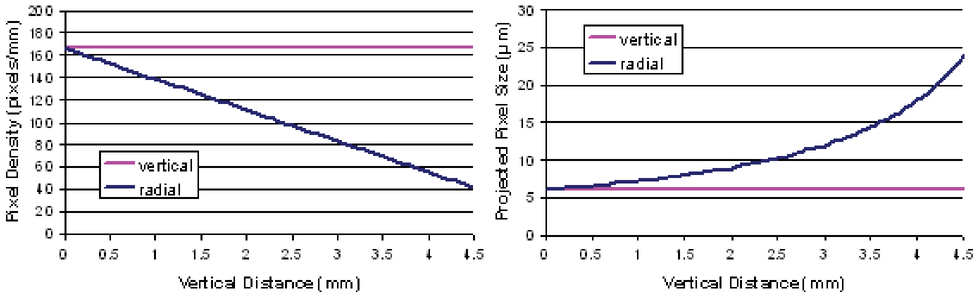

Figure C.22: Calculated upper resolution limit in radial and vertical direction in terms of pixels.

Figure C.23 shows an example of a distorted image of a rock sample as obtained by the camera on the left and the corresponding unwrapped image, clipped in the radial direction, on the right. As can be seen from the image the resolution decreases drastically towards the small part of the conical mirror (upper part in the unwrapped image). However, a vertical range of about 3 mm is available for rock observation with reasonable image quality. For virtual coring, however, the stepping can be chosen much smaller than 3 mm (1 mm or less) and hence only the stripes with the highest resolution are used for the virtual core assembly yielding the best possible image quality. It shall be noted that at very close distance to the probe tip (vertical position 0 mm) a dark stripe can be observed, which is caused by uneven illumination as discussed in section C.2.2.

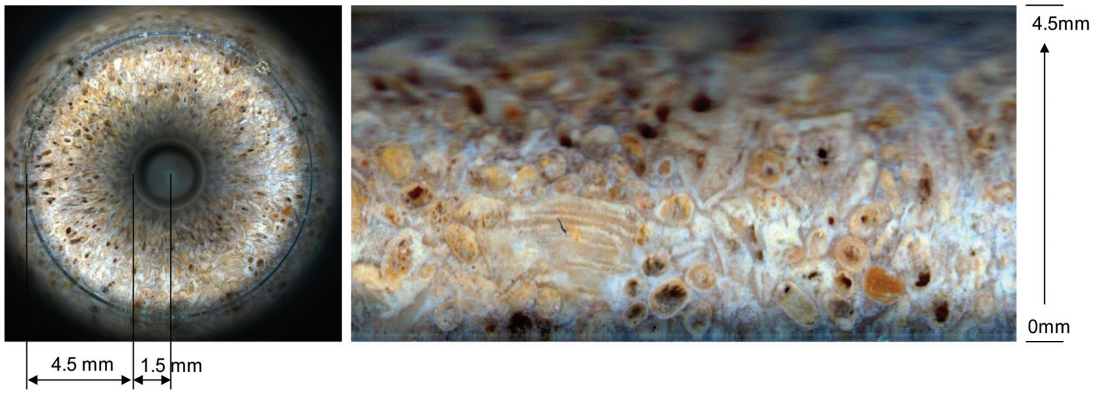

Figure C.23: Example of distorted and unwrapped image.

C.3.2 Effective Resolution

Effective resolution can be determined by obtaining images of a test chart and determining which bar patterns can still be resolved. A bar pattern composed of a certain number of black and white line pairs per millimeter (lp/mm) will not turn suddenly from clearly visible to completely unrecognizable but rather blur out gradually. In order to quantify the quality of a blurred test pattern, the contrast transfer function (CTF) [**236**]:

$$contrast = \frac{C_{\max} - C_{\min}}{C_{\max} + C_{\min}} \qquad (\text{ C.9 })$$

is typically used, where $C_{\max}$ and $C_{\min}$ are the gray values of the maximum and minimum, respectively.

In order to assess the resolution dependency on object position, experiments with resolution targets wrapped around the sapphire probe have been conducted. The resolution targets were moved along the sapphire probe and corresponding images were taken in a way so that the entire vertical distance was covered by the test patterns. The test patterns of choice had 18 lp/mm, 32 lp/mm and 40 lp/mm, which means that the width of each black or white line is about 28 µm, 16 µm, and 12 µm, respectively. The 18 lp/mm test pattern was provided on a T–10 microscopy resolution test chart on high quality white photo paper. The smaller targets were included in a T–20 microscopy resolution test chart on a transparent 8 mm film strip. The film strip was attached to a sheet of white paper in order to provide diffuse reflectivity. By applying eqn. C.9 to the test patterns in the unwrapped images, the contrast of the vertical and radial resolution patterns in dependency of the vertical position was obtained as shown in Figure C.24. Exemplary snapshots of the 18 lp/mm test pattern at distinct points are also shown.

Several observations can be made on the plot in Figure C.24. The radial resolution decreases quickly with an increasing vertical position as predicted. The vertical resolution varies only slightly with a vertical position over a broad range as predicted, but finally decreases as well in the upper region of the conical mirror. At distances very close to the sapphire tip the radial resolution decreases as well, which is due to improper illumination as previously mentioned.

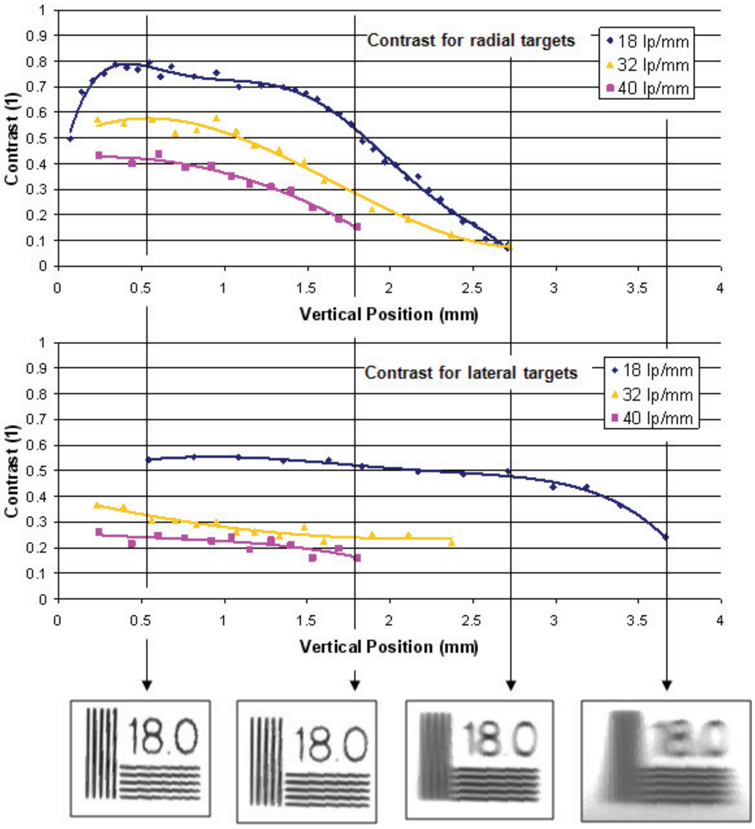

Figure C.24: Contrast transfer functions of several targets at several vertical positions.

According to Figure C.24 the best resolution is achieved at a vertical position of around 0.5 mm. Figure C.25 shows the CTF for various spatial frequencies between 15 lp/mm and 50 lp/mm, corresponding to resolutions of 65 µm and 20 µm, respectively. At a spatial frequency of 40 lp/mm the CTF is at least 25% in both, radial (40%) and lateral (25%) directions, which allows for proper distinction of features in the image. Therefore the resolution of the device is 25 µm. It shall be noted, however, that a test object of 88 µm extent was found to be represented by 13 pixel in the image, which proves the pixel size in the object plane to be 6.8 µm. Therefore features much smaller than 25 µm can still be picked up by the system in certain conditions, i.e. if a very dark spot (pore) clearly distinguishes itself from a bright background.

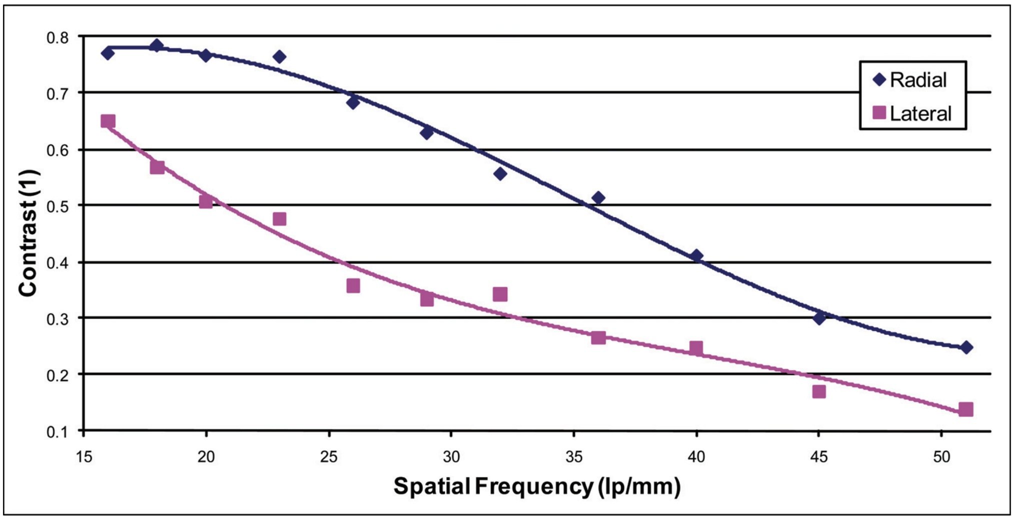

Figure C.25: Contrast transfer function for different spatial frequencies in radial and lateral direction.

The contrast measurements shown in Figure C.24 and Figure C.25 have been performed with resolution targets directly in contact with the sapphire probe. If a gap is present between the object and the sapphire probe then the resolution will decrease as the gap size increases. This decrease in resolution is partially due to decreasing pixel density in the radial direction in the object plane. The diameter of the ring projected on the conical mirror stays the same, while for increasing gap sizes the diameter of a ring in the wrapped object plane increases. More important, however, is the fact that the object simply moves out of focus with an increasing gap size. The depth of field (DOF) depends on the size of the aperture. If the aperture is closed down (large f–numbers) the DOF increases significantly, however, light intensity is significantly decreased as well, which needs to be adjusted for by means of more illumination light intensity or increased exposure time. An experiment has been conducted where the contrast of an 8 lp/mm test pattern was measured at different gap sizes and for different apertures. The results are shown in Figure C.26. If large gaps can occur in a measurement application then a small aperture (large f–number) should be chosen so that a good contrast is provided even for large gap sizes, as can be seen in Figure C.26. However, a small aperture demands more light intensity. This means that for a given illumination intensity the exposure time has to be increased. The exposure time needs to increase exponentially for increasing f–numbers as Figure C.27 shows. Longer exposure times in turn reduce the image quality due to increased sensitivity to vibrations and thermal noise. DOF and exposure time were selected to achieve a good compromise.

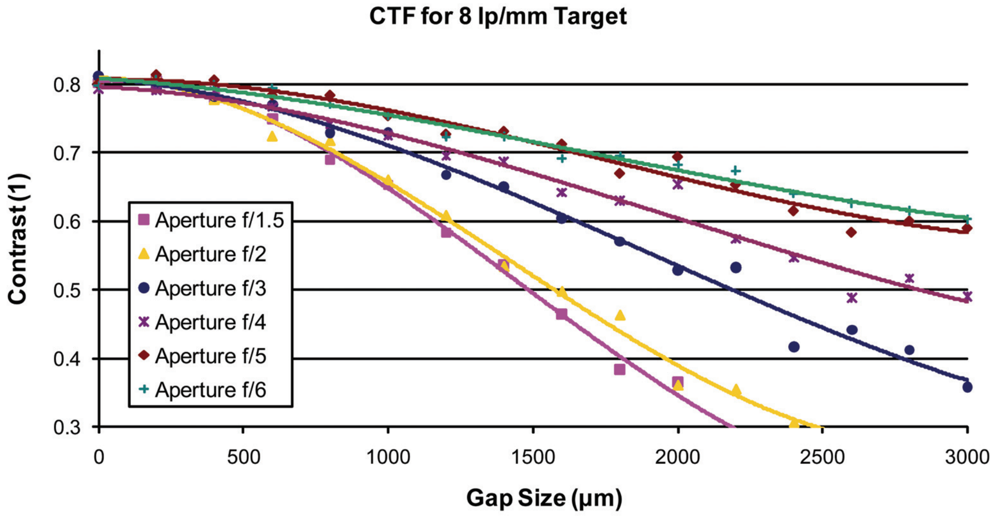

Figure C.26: Contrast transfer function for an 8 lp/mm target in radial direction for various gap sizes and apertures.

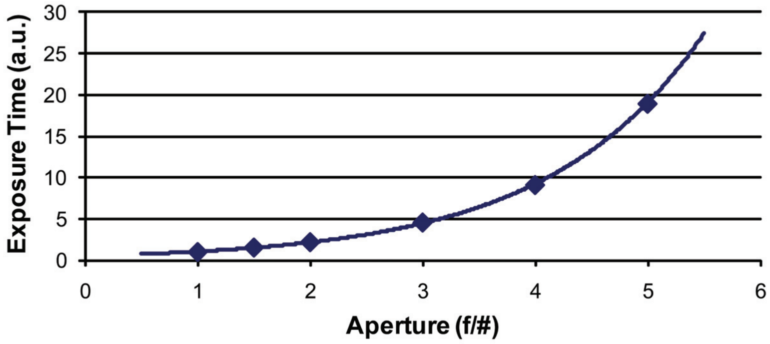

Figure C.27: Relation between aperture size (f–number) and exposure time. The measured data (dots) follow an exponential increase (solid line).

C.3.3 Birefringence

Sapphire crystals are birefringent, hence possessing different indices of refraction depending on the polarization in relation to the crystal axes. The birefringence of sapphire is uniaxial, meaning a single axis of anisotropy, and the so called optic axis can be identified. Optical waves in sapphire with polarization perpendicular to this axis experience an ordinary index of refraction n_o = 1.770 (at a wavelength λ = 555 nm). For polarization parallel to the optic axis the crystal possesses the extraordinary index of refraction n_e = 1.762 [**230**]. The birefringence magnitude is defined as [**229**]:

$$\Delta n = n_e - n_o \qquad (\text{C.10})$$

and takes on the value Δn = 0.008 for sapphire.

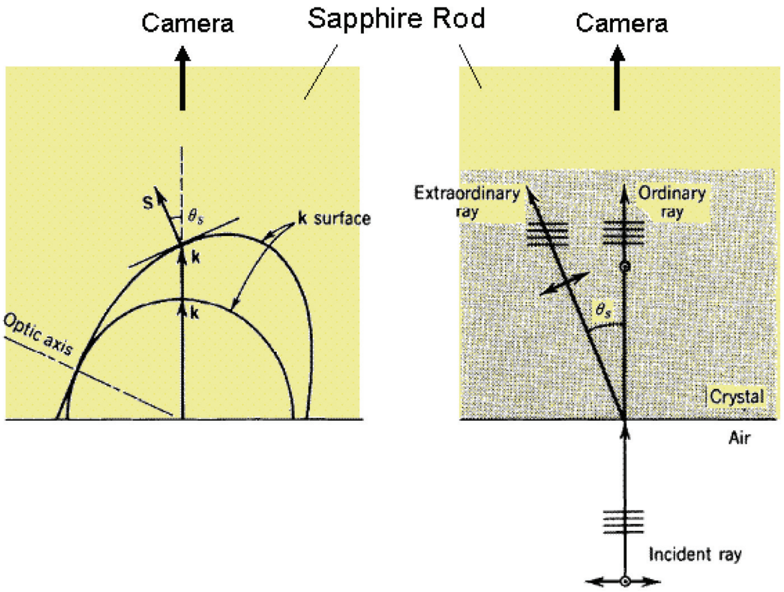

Figure C.28: Double refraction at normal incidence [**229**].

The effect of birefringence in the sapphire rod is shown schematically in Figure C.28, neglecting the conical mirror and assuming a flat–tip probe. In the schematic a ray coming from the object with arbitrary polarization enters the sapphire probe at normal incidence. The optic axis in this example lies in the sketch plane but is not parallel to the cylinder axis of the probe. The component of the incident ray with polarization normal to the sketch plane and hence perpendicular to the optic axis does not experience any anisotropy effect and therefore travels straight through the crystal as the ordinary ray. The other component of the incident ray with its polarization lying in the sketch plane experiences an anisotropy effect depending on the angle between the optic axis and the incident ray. As can be seen in the left part of Figure C.28, the Poynting vector S in this case deviates from the wavefront vector k due to the anisotropy effect, which causes the ray to shift ‘sidewards’ as it travels through the crystal while the original orientation of the wavefront is still preserved. Due to this effect, there will be two images of equal magnitude leaving the sapphire crystal where the extraordinary image is shifted sidewards by a certain amount with respect to the ordinary image, hence resulting in a blurred image. Since the polarizations of ordinary and extraordinary image are perpendicular to each other, one of the images can be blocked by a linear polarizer hence obtaining a sharp image with half the original intensity. Figure C.29 shows images of a rock sample for which birefringence occurred. For orientations 0° and 90° of the linear polarizer the extraordinary and ordinary image are suppressed, respectively, and a sharp image is obtained. For an intermediate orientation of the polarizer a mixture of both images is obtained which results in a blurred image as shown in the middle of Figure C.29. The same blurred image would be obtained without a polarizer but with twice the intensity.

If the sapphire crystal is cut in a way that the optic axis is parallel to the cylinder axis, then all the possible polarizations that enter the sapphire under normal incidence are normal to the optic axis as well, hence no birefringence occurs. This situation would be very advantageous since no care would have to be taken to align the polarizer with respect to the sapphire crystal. Or, if the polarizer is completely left out, twice the intensity can be obtained by the camera, which would reduce the required exposure time.

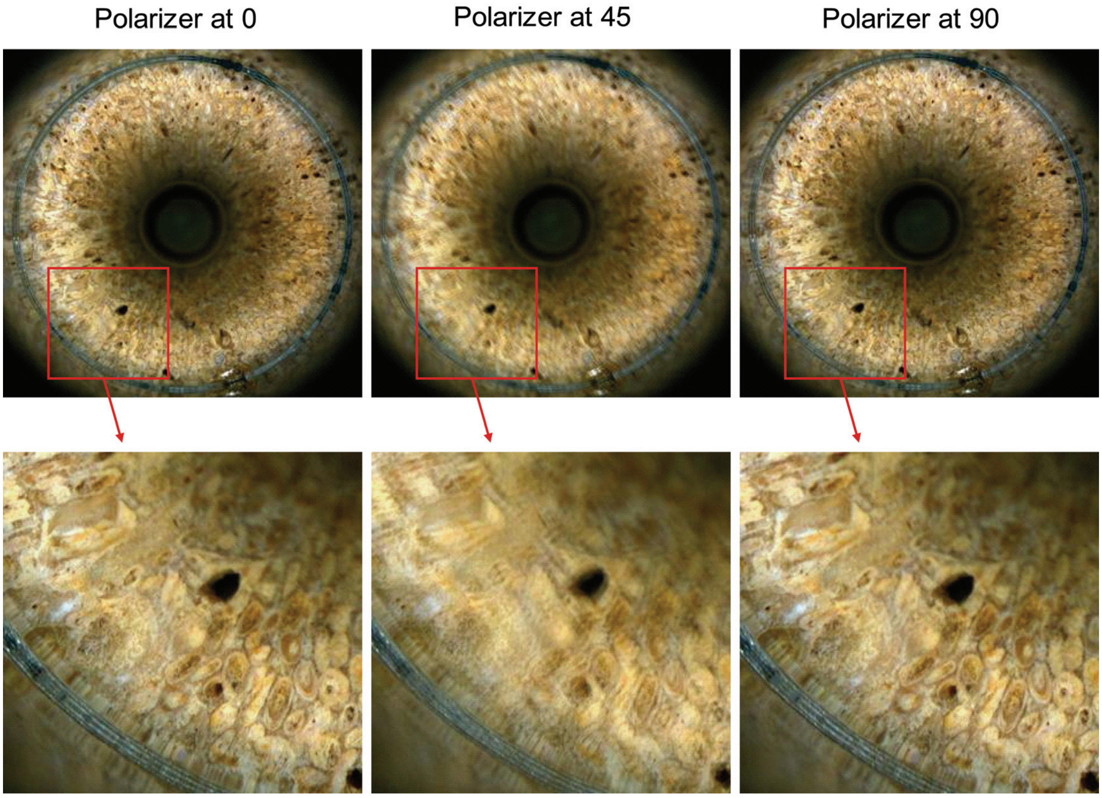

Figure C.29: Images obtained for different orientations of the polarizer.

C.4 Summary

C.4.1 Overview

The microscopic grain imager laboratory setup as described and discussed was used to evaluate different optical components, to evaluate the overall performance and to identify the most suitable system design. The final system was carefully characterized regarding resolution, image quality, etc.

The optimized system is comprised of a 4 Megapixel color CCD detector and an oblique angle ring–light illumination system. Although the coaxial illumination technique was discarded, a brief summary of the findings shall be given anyway. Introducing a beam–splitter was found to be unproblematic. Different beam–splitters were tested and the resulting loss in image quality was negligible. Light coupling into the sapphire was found to be critical. Due to the significant index of refraction mismatch between air and sapphire, 8 – 15% of the incident light is reflected back from the sapphire probe. In the case of coaxial illumination, this light component is captured by the camera and outshines the rock image completely.

C.4.2 Illumination

The preferable illumination technique was found to be the ring–light illumination. As oblique angle ring–light illumination injects the illumination light from a ring around the sapphire, it leaves a sufficiently large clear aperture in the center for the imaging train, rendering a beam splitter unnecessary. Further, outshining of the images does not occur due to the oblique angle light injection, as reflected light components leave the optical train and are not picked up by the camera. The ring–light illumination is also very advantageous in terms of image quality. Due to the oblique angle illumination the surface structure is enhanced, providing an increased level of relief information.

Problems identified with the ring–light illumination are an uneven or inhomogeneous illumination. As gradients in the brightness of each individual image can occur, the final virtual core image can be affected by an alternating brightness distribution in form of stripes. Although this effect is only superimposed and does not alter the resolution, it has a disturbing effect on the image analysis and interpretation and needs to be corrected by means of a software algorithm. The difference in brightness increases with an increasing gap size, which makes the image susceptible to an eccentric position of the sapphire probe.

C.4.3 Resolution

The resolution of the MGI setup was carefully assessed. Resolution varies over the lateral position along the sapphire probe but it was found that an optimal resolution can be obtained over a width of about 1 mm. Therefore, if a step size of

1 mm or smaller is chosen, the entire virtual core image can be obtained with optimal resolution.

The theoretical resolution is 13 µm, which corresponds to the width of two pixels in the object plane. The effective resolution was carefully determined with a contrast transfer function (CTF). At a resolution of 25 µm, the resulting contrast is still between 25 and 40%.

If the sapphire rod is cut in a way that its optic axis is carefully aligned with its cylinder axis, then birefringence can be entirely avoided. In general the birefringence effect can be easily eliminated by introducing a polarizer. However, the polarizer will cause a loss in light intensity of 50%.

Bibliography

---

[1] Digante Bhusan Das and S. M. Hassanizadeh, "Preface on Upscaling Multiphase Flow in Porous Media: From Pore to Core and Beyond," *Transport in Porous Media*, vol. 58, pp. 1-3, 2005.

[2] Muhammad Sahimi, "Flow phenomena in rocks: from continuum models to fractals, percolation, cellular automata, and simulated annealing.pdf," *Review of Modern Physics*, vol. 65, pp. 1393-1534, 1993.

[3] M. Ferer et al., "Two-Phase Flow in Porous Media: Predicting Its Dependence on Capillary Number and Viscosity Ratio," *Transport in Porous Media*, pp. DOI 10.1007/s11242-010-9619-3, 2010.

[4] Can Ulas Hatiboglu and Tayfun Babadagli, "Experimental and visual analysis of co- and counter-current spontaneous imbibition for different viscosity ratios, interfacial tensions, and wettability," *Journal of Petroleum Science and Engineering*, vol. 70, pp. 214-228, 2010.

[5] A. Bazylak, V. Berejnov, B. Markicevic, D. Sinton, and N. Djilali, "Numerical and microfluidic pore networks: Towards designs for directed water transport in GDLs," *Electrochimica Acta*, vol. 53, pp. 7630-7637, 2008.

[6] S. Litster, D. Sinton, and N. Djilali, "Ex situ visualization of liquid water transport in PEM fuel cell gas diffusion layers," *Journal of Power Sources*, vol. 154, pp. 95-105, 2006.

[7] Viatcheslav Berejnov, Ned Djilali, and David Sinton, "Lab-on-chip methodologies for the study of transport in porous media: energy applications," *Lab on a Chip*, vol. 8, pp. 689-693, 2008.

[8] Martin J. Blunt, "Flow in porous media - pore-network models and multiphase flow," *Current Opinion in Colloid & Interface Science*, vol. 6, pp. 197-207, 2001.

[9] Pierre M. Adler and Howard Brenner, "Multiphase Flow in Porous Media," *Annual Review of Fluid Mechanics*, vol. 20, pp. 35-59, 1988.

[10] S. G. Sayegh and D. B. Fisher, "Enhanced Oil Recovery by CO2 Flooding in Homogeneous and Heterogeneous 2D Micromodels," *Journal of Canadian Petroleum Technology*, vol. 48, pp. 30-36, 2009.

[11] R. Lenormand, C. Zarcone, and A. Sarr, "Mechanisms of the displacement of one fluid by another in a network of capillary ducts," *Journal of Fluid Mechanics*, vol. 135, pp. 337-353, 1983.

[12] Ronald Lenormand and Cesar Zarcone, "Invasion Percolation in an Eteched Network: Measurement of a Fractal Dimension," *Physical Review Letters*, vol. 54, pp. 2226-2229, 1985.

[13] Roland Lenormand and Cesar Zarcone, "Capillary Fingering: Percolation and Fractal Dimension," *Transport in Porous Media*, vol. 4, pp. 599-612, 1989.

[14] D. G. Avraam and A. C. Payatakes, "Flow regimes and relative permeabilities during steady-state two-phase flow in porous media," *Journal of Fluid Mechanics*, vol. 293, pp. 207-236, 1995.

[15] Norman R. Morrow and Geoffrey Mason, "Recovery of oil by spontaneous imbibition," *Current Opinion in Colloid and Interface Science*, vol. 6, pp. 321-337, 2001.

[16] Hanita Ovdat and Brian Berkowitz, "Pore-scale imbibition experiments in dry and prewetted porous media," *Advances in Water Resources*, vol. 30, pp. 2373-2386, 2007.

[17] Can Ulas Hatiboglu and Tayfun Babadagli, "Pore-scale studies of spontaneous imbibition into oil-saturated porous media," *Physical Review E*, vol. 77, p. 066311, 2008.

[18] Y. Melean, D. Broseta, and R. Blossey, "Imbibition fronts in porous media: effects of initial wetting fluid saturation and flow rate," *Journal of Petroleum Science and Engineering*, vol. 39, pp. 327-336, 2003.

[19] O. Vizika, D. G. Avraam, and A. C. Payatakes, "On the Role of the Viscosity Ratio during Low-Capillary-Number Forced Imbibition in Porous Media," *Journal of Colloid and Interface Science*, vol. 165, pp. 386-401, 1994.

[20] B. Xu, Y. C. Yortsos, and D. Salin, "Invasion percolation with viscous forces," *Physical Review E*, vol. 57, pp. 739-751, 1998.

[21] Roland Lenormand, "Liquids in porous media," *Journal of Physics: Condensed Matter*, vol. 2, pp. SA79-SA88, 1990.

[22] Roland Lenormand, "Pattern Growth and Fluid Displacements Through Porous Media," *Physica*, vol. 140A, pp. 114-123, 1986.

[23] Roland Lenormand, Eric Touboul, and Cesar Zarcone, "Numerical models and experiments on immiscible displacements in porous media," *Journal of Fluid Mechanics*, vol. 189, pp. 165-187, 1988.

[24] Richard G. Hughes and Martin J. Blunt, "Pore Scale Modeling of Rate Effects in Imbibition," *Transport in Porous Media*, vol. 40, pp. 295-322, 2000.

[25] Martin J. Blunt and Harvey Scher, "Pore-level modeling of wettability," *Rhysical Review E*, vol. 52, pp. 6387-6403, 1995.

[26] M. Ferer, Grant S. Bromhal, and Duane H. Smith, "Spatial distribution of avalanches in invasion percolation: their role in fingering," *Physica A*, vol. 311, pp. 5-22, 2002.

[27] Martin Blunt, Michael J. King, and Harvey Scher, "Simulation and theroy of two-phase flow in porous media," *Physical Review A*, vol. 46, pp. 7680-7699, 1992.

[28] Cornelis Johannes van Duijn, Hartmut Eichel, Rainer Helmig, and Iuliu Sorin Pop, "Effective equations for two-phase flow in porous media: the effect of trapping on the microscale," *Transport in Porous Media*, vol. 69, pp. 411-428, 2007.

[29] Eyvind Aker, Knut Jorgen Maloy, and Alex Hansen, "Simulating temporal evolution of pressure in two-phase flow in porous media," *Physical Review E*, vol. 58, pp. 2217-2226, 1998.

[30] S. G. Sayegh and D. B. Fisher, "Enhanced Oil Recovery by CO2 Flooding in Homogeneous and Heterogeneous 2D Micromodels," in *Canadian International Petroleum Conference (Petroleum Society of Canada)*, Calgary, 2008, pp. 2008-005.

[31] David Wilkinson, "Percolation effects in immiscible displacement," *Physical Review A*, vol. 34, pp. 1380-1391, 1986.

[32] M. Ferer, Grant S. Bromhal, and Duane H. Smith, "Two-phase flow in porous media: Crossover from capillary fingering to compact invasion for drainage," *Physical Review E*, vol. 71, p. 026303, 2005.

[33] Vanita Mani and K. K. Mohanty, "Pore-Level Network Modeling of Three-Phase Capilllary Pressure and Relative Permeability Curves," *SPE Journal*, vol. 3, pp. 238-248, 1998.

[34] Martin J. Blunt, Matthew D. Jackson, Mohammad Piri, and Per H. Valvatne, "Detailed physics, predictive capabilities and macroscopic consequences for pore-network models of multiphase flow," *Advances in Water Resources*, vol. 25, pp. 1069-1089, 2002.

[35] S. Geiger, S. Matthai, J. Niessner, and R. Helmig, "Black-Oil Simulations for Three-Component - Three-Phase Flow in Fractured Porous Media," *SPE Journal*, vol. 14, pp. 338-354, 2009.

[36] Erle C. Donaldson and Waqi Alam, *Wettability*. Houston, Texas: Gulf Publishing Company, 2008.

[37] Varvara Sygouni, Christos D. Tsakiroglou, and Alkiviades C. Payatakes, "Capillary pressure spectrometry: Toward a new method for the measurement of the fractional wettability of porous media," *Physics of Fluids*, vol. 18, p. 053302, 2006.

[38] V. Sygouni, C. D. Tsakiroglou, and A. C. Payatakes, "Using wavelets to characterize the wettability of porous media," *Physical Review E*, vol. 76, p. 056304, 2007.

[39] M. B. Alotaibi, R. A. Nasralla, and H. A. Nasr-El-Din, "Wettability Challenges in Carbonate Reservoirs," in *SPE Improved Oil Recovery Symposium*, Tulsa, Oklahoma, 2010, p. SPE 129972.

[40] William G. Anderson, "Wettability Literature Survey - Part 6: The Effects of Wettability on Waterflooding," *Journal of Petroleum Technology*, vol. 39, pp. 1605-1622, 1987.

[41] A. R. Kovscek, H. Wong, and C. J. Radke, "A Pore-Level Scenario for the Development of Mixed Wettability in Oil Reservoirs," *Environmental and Energy Engineering*, vol. 39, pp. 1072-1085, 1993.

[42] Munish Kumar, Andrew Fogden, Tim Senden, and Mark Knackstedt, "Investigation of Pore-Scale Mixed Wettability," in *SPE Improved Oil Recovery Symposium*, Tulsa, Oklahoma, 2010, p. SPE 129974.

[43] C. Laroche, O. Vizika, and F. Kalaydjian, "Network Modeling to Predict the Effect of Wettability Heterogeneities on Multiphase Flow," in *SPE Annual Technical Conference and Exhibition*, Houston, Texas, 1999, p. SPE 56674.

[44] M.I.J. van Dijke, M. Lorentzen, M. Sohrabi, and K. S. Sorbie, "Pore-Scale Simulation of WAG Floods in Mixed-Wet Micromodels," *SPE Journal*, vol. 15, pp. 238-247, 2010.

[45] A. V. Ryazanov, M.I.J. van Dijke, and K. S. Sorbie, "Pore-network Prediction of Residual Oil Saturation Based on Oil Layer Drainage in Mixed-wet Systems," in *SPE Improved Oil Recovery Symposium*, Tulsa, Oklahoma, 2010, p. SPE 129919.

[46] Mohammad Piri and Martin J. Blunt, "Three-dimensional mixed-wet random pore-scale network modeling of two- and three-phase flow in porous media. II. Results," *Physical Review E*, vol. 71, p. 026302, 2005.

[47] Matthew D. Jackson, Per H. Valvatne, and Martin J. Blunt, "Prediction of wettability variation and its impact on flow using pore- to reservoir-scale simulations," *Journal of Petroleum Science and Engineering*, vol. 39, pp. 231-246, 2003.

[48] Mohammad Piri and Martin J. Blunt, "Three-dimensional mixed-wet random pore-scale network modeling of two- and three-phase flow in porous media. I. Model description," *Physical Review E*, vol. 71, p. 026301, 2005.

[49] Munish Kumar et al., "Imaging of Pore Scale Distribution of Fluids and Wettability," *Petrophysics*, vol. 50, pp. 311-321, 2009.

[50] George F. Pinder and William G. Gray, *Essential of Multiphase Flow and Transport in Porous Media*. Hoboken, New Jersey: John Wiley & Sons, 2008.

[51] P. G. Saffman and G. Taylor, "The penetration of a fluid into a medium of hele-shaw cell containing a more viscous liquid," *Proceedings of the Royal Society of London, Series A - Mathematical and Physical Sciences*, vol. 245, pp. 312-129, 1958.

[52] P. G. De Gennes, "Wettability: statics and dynamics," *Reviews of Modern Physics*, vol. 57, pp. 827-863, 1985.

[53] Daniel Bonn, Jens Eggers, Joseph Indekeu, Jacques Meunier, and Etienne Rolley, "Wetting and spreading," *Reviews of Modern Physics*, vol. 81, pp. 739-805, 2009.

[54] T. Young, "An Essay on the Cohesion of Fluids," *Philosophical Transactions of the Royal Society of London*, vol. 95, pp. 65-87, 1805.

[55] William G. Anderson, "Wettability Literature Survey - Part 1: Rock/Oil/Brine Interactions and the Effects of Core Handling on Wettability," *Journal of Petroleum Technology*, vol. 38, pp. 1125-1144, 1986.

[56] Pierre-Gilles De Gennes, Francoise Brochard-Wyart, and David Quere, *Capillarity and Wetting Phenomena - Drops, Bubbles, Pearls, Waves*. New York, USA: Springer, 2003.

[57] Cedric P. Ody, "Capillary contributions to the dynamics of discrete slugs in microchannels," *Microfluid Nanofluid*, vol. 9, pp. 397-410, 2010.

[58] Hansang Cho, Ho-Young Kim, Ji Yoon Kang, and Tae Song Kim, "How the capillary burst microvalve works," *Journal of Colloid and Interface Science*, vol. 306, pp. 379-385, 2007.

[59] Patrick Tabeling and Yi-Kuen Lee, "Micro/Nanofluidic Processes," in *Micro/Nano Technology Systems for Biomedical Applications: Microfluidics, Optics, and Surface Chemistry*. New York: Oxford University Press, 2010, ch. 2, pp. 33-52.

[60] Patrick Tabeling, "A brief introduction to slippage, droplets and mixing in microfluidic systems," *Lab on a Chip*, vol. 9, pp. 2428-2436, 2009.

[61] Holger Becker and Laurie E. Locascio, "Polymer microfluidic devices," *Talanta*, vol. 56, pp. 267-287, 2002.

[62] Chang Liu, "Recent Developments in Polymer MEMS," *Advanced Materials*, vol. 19, pp. 3783-3790, 2007.

[63] J. Cooper McDonald and George M. Whitesides, "Poly(dimethylsiloxane) as a Material for Fabricating Microfluidic Devices," *Accounts of Chemical Research*, vol. 35, pp. 491-499, 2002.

[64] David C. Duffy, J. Cooper McDonald, Olivier J.A. Schueller, and George M. Whitesides, "Rapid prototyping of microfluidic systems in poly(dimethylsiloxane)," *Analytical Chemistry*, vol. 70, pp. 4974-4984, 1998.

[65] Petra S. Dittrich, Kaoru Tachikawa, and Andreas Manz, "Micro Total Analysis Systems. Latest Advancements and Trends," *Analytical Chemistry*, vol. 78, pp. 3887-3907, 2006.

[66] Remi Dreyfus, Patrick Tabeling, and Herve Willaime, "Ordered and Disordered Patterns in Two-Phase Flows in Microchannels," *Physical Review Letters*, vol. 90, p. 144505, 2003.

[67] Wei Li et al., "Screening of the Effect of Surface Energy of Microchannels on Microfluidic Emulsification," *Langmuir*, vol. 23, pp. 8010-8014, 2007.

[68] Herve Willaime et al., "Generating Double Emulsion W/O/W in a PDMS System by Controlling Locally the Wetting Properties of the Channel," in *Proceedings of the 1st European Conference on Microfluidics - Microfluidics 2008*, Bologna, 2008, pp. uFLU08-138.

[69] Adam R. Abata, Julian Thiele, Marie Weinhart, and David A. Weitz, "Patterning microfluidic device wettability using flow confinement," *Lab on a Chip*, vol. 10, pp. 1774-1776, 2010.

[70] Richard A. Dawe and Carlos A. Grattoni, "Experimental displacement patterns in a 2 x 2 quadrant block with permeability and wettability heterogeneities - problems for numerical modelling," *Transport in Porous Media*, vol. 71, pp. 5-22, 2008.

[71] M. Sohrabi, D. H. Tehrani, and G. D. Henderson, "Visualization of Oil Recovery by Water-Altering-Gas Injection Using High-Pressure Micromodels," *SPE Journal*, vol. 9, pp. 290-301, 2004.

[72] C. A. Grattoni, X. D. Jing, and R. W. Zimmerman, "Wettability alteration by aging of a gel placed within a porous medium," *Journal of Petroleum Science and Engineering*, vol. 33, pp. 135-145, 2002.

[73] C. Laroche, O. Vizika, and F. Kalaydjian, "Network modeling as a tool to predict three-phase gas injection in heterogeneous wettability porous media," *Journal of Petroelum Science and Engineering*, vol. 24, pp. 155-168, 1999.

[74] V. Bortolotti, P. Macini, and F. Srisuriyachai, "Wettability Index of Carbonatic Reservoirs and EOR: Laboratory Study to Optimize Alkali and Surfactant Flooding," in *SPE International Oil and Gas Conference and Exhibition in China*, Beijing, 2010, p. SPE 131043.

[75] G. J. Hirasaki, "Wettability: Fundamentals and Surface Forces," *SPE Formation Evaluation*, vol. 6, pp. 217-226, 1991.

[76] Bernard Montaron et al., "Shapes of Flood Fronts in Heterogeneous Reservoirs and Oil Recovery Strategies," in *SPE/EAGE Reservoir Characterization and Simulation Conference*, Abu Dhabi, UAE, 2007, p. SPE 111147.

[77] Norman R. Morrow, "Wettability and Its Effect on Oil Recovery," *Journal of Petroleum Technology*, vol. 42, pp. 1476-1484, 1990.

[78] M. K. Zahoor, Mohd. N. Derahman, and M. H. Yunan, "Wettability - Interpreting the Myth," *NAFTA*, vol. 60, pp. 367-369, 2009.

[79] Robert J.S. Brown and Irving Fatt, "Measurements Of Fractional Wettability Of Oil Fields' Rocks By The Nuclear Magnetic Relaxation Method," in *Fall Meeting of the Petroleum Branch of AIME*, Los Angeles, 1956, pp. 743-G.

[80] R. A. Salathiel, "Oil Recovery by Surface Film Drainage In Mixed-Wettability Rocks," *Journal of Petroleum Technology*, vol. 25, pp. 1216-1224, 1973.

[81] Chinedu Agbalaka, Abhijit Y. Dandekar, Shirish L. Patil, Santanu Khataniar, and James R. Hemsath, "The Effect of Wettability on Oil Recovery: A Review," in *SPE Asia Pacific Oil and Gas Conference and Exhibition*, Perth, 2008, p. SPE 114496.

[82] Wael Abdallah et al., "Fundamentals of Wettability," *Oilfield Review*, vol. 19, no. 1, pp. 44-61, 2007.

[83] E. M. Freer, T. Svitova, and C. J. Radke, "The role of interfacial rheology in reservoir mixed wettability," *Journal of Petroleum Science and Engineering*, vol. 39, pp. 137-158, 2003.

[84] Munish Kumar and Andrew Fogden, "Patterned Wettability of Oil and Water in Porous Media," *Langmuir*, vol. 26, pp. 4036-4047, 2010.

[85] M. Robin, "Interfacial Phenomena: Reservoir Wettability in Oil Recovery," *Oil & Gas Science and Technology - Revue de l'IFP Energies Nouvelles*, vol. 56, pp. 55-62, 2001.

[86] Michele Moisio Thomas, Jamie A. Clouse, and John M. Longo, "Adsorption of organic compounds on carbonate minerals: 1. Model compounds and their influence on mineral wettability," *Chemical Geology*, vol. 109, pp. 201-213, 1993.

[87] Bernard A. Baldwin and Peter R. Gray, "Fluid-Surface Interactions in Oil Reservoirs," Society of Petroleum Engineers , Research and Devlopment Report SPE 4925, 1974.

[88] Rashid S. H. Al-Maamari and Jill S. Buckley, "Asphaltene Precipitation and Alteration of Wetting: The Potential for Wettability Changes During Oil Production," *SPE Reservoir Evaluation and Engineering*, p. SPE 84938, 2003.

[89] Marc H. Schneider, A. Ballard Andrews, Sudipa Mitra-Kirtley, and Olliver C. Mullins, "Asphaltene Molecular Size by Fluorescence Correlation Spectroscopy," *Energy and Fuels*, vol. 21, pp. 2875-2882, 2007.

[90] J. S. Buckely, Y. Liu, and S. Monsterleet, "Mechanisms of Wetting Alteration by Crude Oils," *SPE Journal*, p. SPE 37230, 2003.

[91] M. Rahbar, S. Ayatollahi, and M. H. Ghatee, "The Roles of Nano-Scale Intermolecular Forces on the Film Stability During Wettability Alteration Process of the Oil Reservoir Rocks," in *Trinidad and Tobago Energy Resources Conference*, Port of Spain, 2010, p. SPE 132616.

[92] Chandra S. Vijapurapu and Dandina N. Rao, "Compositional effects of fluids on spreading, adhesion and wettability in porous media," *Colloids and Surfaces A: Physicochemical and Engineering Aspects*, vol. 241, pp. 335-342, 2004.

[93] Mun-Hong Hui and Martin J. Blunt, "Effects of Wettability on Three-Phase Flow in Porous Media," *Journal of Physical Chemistry B*, vol. 104, pp. 3833-3845, 2000.

[94] American Petroleum Institute, *Recommended practices for core analysis: RP 40*, 2nd ed. Paramus, NJ, USA: Copy reproduced under license from American Petroleum Institute by ILI INFODISK Inc., 1998.

[95] William G. Anderson, "Wettability Literature Survey - Part 2: Wettability Measurement," *Journal of Petroleum Technology*, vol. 38, pp. 1246-1262, 1986.

[96] John S. Huang and Ramesh Varadaraj, "Colloid and interface science in the oil industry," *Current Optinion in Colloid and Interface Science*, vol. 1, pp. 535-539, 1996.

[97] E. Tzimas, A. Georgakaki, C. Garcia Cortes, and S. D. Peteves, "Enhanced Oil Recovery using Carbon Dioxide in the European Energy System," Institute for Energy, Petten, The Netherlands, Report EUR 21895 EN ISBN 92-79-01044-1, 2005.

[98] Larry W. Lake, *Enhanced Oil Recovery*, 1st ed. Upper Saddle River, NJ, USA: Prentice Hall, 1996.

[99] S. Thomas, "Enhanced Oil Recovery - An Overview," *Oil and Gas Science and Technology - Revue d'IFP Energies nouvelles*, vol. 63, pp. 9-19, 2008.

[100] Norman R. Morrow, Hau T. Lim, and Jill S. Ward, "Effect of Curde-Oil-Induced Wettability Changes on Oil Recovery," *SPE Formation Evaluation*, vol. 1, pp. 89-103, 1986.

[101] A. B. Dixit, S. R. McDougall, K. S. Sorbie, and J. S. Buckley, "Pore-Scale Modeling of Wettability Effects and Their Influence on Oil Recovery," *SPE Reservoir Evaluation and Engineering*, vol. 2, pp. 25-36, 1999.

[102] Paul D. Torrey, "Modern Practice in Water-flooding of Oil Sands in the Bradford and Allegany Fields," *Transactions of the Society of Petroleum Engineers of the American Institute of Mining, Metallurgical and Petroleum Engineers, Inc. (AIME)*, vol. 86, pp. 295-276, 1930.

[103] T. F. Lawry, "Flowing vs. Pumping operations in Water Flooding," *Drilling and Production Practice (API)*, pp. 35-42, 1943.

[104] Tandem Terminal. (2010, September) Oil recovery factor improvement. [Online]. http://tandem-terminal.ru/oil_recovery/index.htm

[105] William G. Anderson, "Wettability Literature Survey - Part 5: The Effects of Wettability on Relative Permeability," *Journal of Petroleum Technology*, vol. 39, pp. 1453-1468, 1987.

[106] K. K. Mohanty, H. T. Davis, and L. E. Scriven, "Physics of Oil Entrapment in Water-Wet Rock," *SPE Reservoir Engineering*, vol. 2, pp. 113-128, 1987.

[107] S. H. Raza, L. E. Treiber, and D. L. Archer, "Wettability of Reservoir Rocks and Its Evaluation," *Producers Monthly*, vol. 32, pp. 2-7, 1968.

[108] William G. Anderson, "Wettability Literature Survey - Part 4: Effects of Wettability on Capillary Pressure," *Journal of Petroleum Technology*, vol. 39, pp. 1283-1300, 1987.

[109] J. C. Melrose and C. F. Brandner, "Role of Capillary Forces in Determining Microscopic Displacement Efficiency for Oil Recovery by Waterflooding," *Journal of Canadian Petroleum Technology*, vol. 13, pp. 54-62, 1974.

[110] P. Zhang and T. Austad, "Waterflooding in Chalk - Relationship Between Oil Recovery, New Wettability Index, Brine Composition and Cationic Wettability Modifier," in *SPE Europec/EAGE Annual Conference*, Madrid, Spain, 2005, p. SPE 94209.

[111] A. Graue and T. Bogno, "Wettability Effects on Oil Recovery Mechanisms in Fractured Reservoirs," in *SPE Annual Technical Conference and Exhibition*, Houston, TX, 1999, p. SPE 56672.

[112] Shouxiang Ma, Norman R. Morrow, and Xiaoyun Zhang, "Generalized scaling of spontaneous imbibition data for strongly water-wet systems," *Journal of Petroleum Science and Engineering*, vol. 18, pp. 165-178, 1997.

[113] E. N. Iwankow, "A Correlation of Interstitial Water Saturation and Heterogeneous Wettability," *Producers Monthly*, vol. 24, pp. 18-26, 1960.

[114] Irving Fatt and Waldemar A. Klikoff, "Effect of Fractional Wettability on Multiphase Flow Through Porous Media ," *Journal of Petroleum Technology*, vol. 11, pp. 71-76, 1959.

[115] Arne Skauge, Kristine Spildo, Linda Hoiland, and Bartek Vik, "Theoretical and experimental evidence of different wettability classes," *Journal of Petroleum Science and Engineering*, vol. 57, pp. 321-333, 2007.

[116] Benyamin Yadali Jamaloei and Riyaz Kharrat, "Analysis of Microscopic Displacement Mechanisms of Dilute Surfactant Flooding in Oil-wet and Water-wet Porous Media," *Transport in Porous Media*, vol. 81, pp. 1-19, 2010.

[117] Darwin R. Reyes, Dimitri Iossifidis, Pierre-Alain Auroux, and Andreas Manz, "Micro Total Analysis Systems. 1. Introduction, Theory, and Technology," *Analytical Chemistry*, vol. 74, pp. 2623-2636, 2002.

[118] Pierre-Alain Auroux, Dimitri Iossifidis, Darwin R. Reyes, and Andreas Manz, "Micro Total Analysis Systems. 2. Analytical Standard Operations and Applications," *Analytical Chemistry*, vol. 74, pp. 2637-2652, 2002.

[119] George M. Whitesides, "The origin and the future of microfluidics," *Nature*, vol. 44, pp. 368-373, 2006.

[120] George M. Whitesides, Emanuele Ostuni, Shuichi Takayama, Xingyu Jiang, and Donald E. Ingber, "Soft Lithography in Biology and Biochemistry," *Annual Review of Biomedical Engineering*, vol. 3, pp. 335-373, 2001.

[121] David J. Beebe, Glennys A. Mensing, and Glenn M. Walker, "Physics and Applications of Microfluidics in Biology," *Annual Review of Biomedical Engineering*, vol. 4, pp. 261-286, 2002.

[122] Jamil El-Ali, Peter K. Sorger, and Klavis F. Jensen, "Cells on chips," *Nature*, vol. 442, pp. 403-411, 2006.

[123] Chih-Ming Ho, *Micro/Nano Technology Systems for Biomedical Applications: Microfluidics, Optics, and Surface Chemistry*. New York: Oxford University Press, 2010.

[124] Terence G. Henares, Fumio Mizutani, and Hideaki Hisamoto, "Current development in microfluidic immunosensing chips," *Analytica Chimica Acta*, vol. 611, pp. 17-30, 2008.

[125] Todd M. Squires and Stephen R. Quake, "Microfluidics: Fluid physics at the nanoliter scale," *Reviews of Modern Physics*, vol. 77, pp. 977-1026, 2005.

[126] H. A. Stone, A. D. Stroock, and A. Ajdari, "Engineering Flows in Small Devices: Microfluidics Towards a Lab-on-a-Chip," *Annual Review of Fluid Mechanics*, vol. 36, pp. 381-411, 2004.

[127] Patrick Tabeling, *Introduction to Microfluidics*. Oxford: Oxford Univeristy Press, 2006.

[128] David Erickson and Dongqing Li, "Integrated microfluidic devices," *Analytica Chimica Acta*, vol. 507, pp. 11-26, 2004.

[129] J. Cooper McDonald et al., "Fabrication of microfluidic systems in poly(dimethylsiloxane)," *Electrophoresis*, vol. 21, pp. 27-40, 2000.

[130] Jessamine M. K. Ng, Irina Gitlin, Abraham D. Stroock, and George M. Whitesides, "Components for integrated poly(dimethylsiloxane) microfluidic systems," *Electrophoresis*, vol. 23, pp. 3461-3473, 2002.

[131] Samuel K. Sia and George M. Whitesides, "Microfluidic devices fabricated in poly(dimethylsiloxane) for biological studies," *Electrophoresis*, vol. 24, pp. 3563-3576, 2003.

[132] Robin L. Garrell and Heather D. Maynard, "Surface Molecular Property Control," in *Micro/Nano Technology Systems for Biomedical Applications: Microfluidics, Optics, and Surface Chemistry*. New York: Oxford University Press, 2010, ch. 11, pp. 395-423.

[133] Ali Khademhosseini, Robert Langer, Jeffrey Borenstein, and Joseph P. Vacanti, "Microscale technologies for tissue engineering and biology," *Proceedings of the National Academy of Sciences of the United States of America*, vol. 103, pp. 2480-2487, 2006.

[134] Honest Makamba, Jin Ho Kim, Kwanseop Lim, Nokyoung Park, and Jong Hoon Hahn, "Surface modification of poly(dimethylsiloxane) microchannels," *Electrophoresis*, vol. 24, pp. 3607-3619, 2003.

[135] Jinwen Zhou, Amanda Vera Ellis, and Nicolas Hans Voelcker, "Recent developments in PDMS surface modification for microfluidic devices," *Electrophoresis*, vol. 31, pp. 2-16, 2010.

[136] Ieong Wong and Chih-Ming Ho, "Surface molecular property modifications for poly(dimethylsiloxane) (PDMS) based microfluidic devices," *Microfluidics and Nanofluidics*, vol. 7, pp. 291-306, 2009.

[137] Panittamat Kumlangdudsana, Stephan T. Dubas, and Luxsana Dubas, "Surface modification of microfluidic devices," *Journal of Metals, Materials and Minerals*, vol. 17, pp. 67-74, 2007.

[138] Yoshikimi Uyama, Koichi Kato, and Yoshito Ikada, *Surface Modification of Polymers by Grafting*. Heidelberg, Germany: Springer Verlag, 1998, vol. 137.

[139] Koichi Kato, Emiko Uchida, En-Tang Kang, Yoshikimi Uyama, and Yoshito Ikada, "Polymer surface with graft chains," *Progress in Polymer Science*, vol. 28, pp. 209-259, 2003.

[140] Christine Seguin, Jessica M. McLachlan, Peter R. Norton, and Francois Lagugne-Labarthet, "Surface modification of poly(dimethylsiloxane) for microfluidic assay applications," *Applied Surface Science*, vol. 256, pp. 2524-2531, 2010.

[141] Jianping Deng, Lifu Wang, Lianying Liu, and Wantai Yang, "Developments and new applications of UV-induced surface graft polymerization," *Progress in Polymer Science*, vol. 34, pp. 156-193, 2009.

[142] Domingo He, Heru Susanto, and Mathias Ulbricht, "Photo-irradiation for preparation, modification and stimulation of polymeric membranes," *Progress in Polymer Science*, 2008.

[143] Nele De Smet, Monika Rymarczyk-Machal, and Etienne Schacht, "Modification of Polydimethylsiloxane Surfaces Using Benzophenone," *Journal of Biomaterials Science*, vol. 20, pp. 2039-2053, 2009.

[144] Jikun Liu and Milton L. Lee, "Permanent surface modification of polymeric capillary electrophoresis for protein peptide analysis," *Electrophoresis*, vol. 27, pp. 3533-3546, 2006.

[145] Guodong Sui et al., "Solution-Phase Surface Modification in Intact Poly(dimethylsiloxane) Microfluidic Channels," *Analytical Chemistry*, vol. 78, pp. 5543-5551, 2006.

[146] Zhihong Nie and Eugenia Kumacheva, "Pattering surfaces with functional polymers," *Nature Materials*, vol. 7, pp. 277-290, 2008.

[147] Younan Xia and George M. Whitesides, "Soft Lithography," *Angewandte Chemie - International Edition*, vol. 37, pp. 550-575, 1998.

[148] Younan Xia and George M. Whitesides, "Soft lithography," *Annual Review of Materials Science*, vol. 28, pp. 153-184, 1998.

[149] Jessamine Ng Lee, Cheolmin Park, and George M. Whitesides, "Solvent Compatibility of Poly(dimethylsiloxane)-Based Microfluidic Devices," *Analytical Chemistry*, vol. 75, pp. 6544-6554, 2003.

[150] Marc A. Unger, Hou-Pu Chou, Todd Thorsen, Axel Scherer, and Stephen R. Quake, "Monolithic Microfabricated Valves and Pumps by Multilayer Soft Lithography," *Science*, vol. 288, pp. 113-116, 2000.

[151] Philippe Nghe, "Ecoulements de fluides complexes en géométries microfluidiques," Université Pierre & Marie Curie - Paris 6, Paris, PhD Thesis 2009.

[152] MicroChem, "Datasheet - SU-8 2000 Permanent Epoxy Photoresist - Processing Guidelines for SU-8 2100 and SU-8 2150," pp. downloaded from: www.microchem.com, 2007.

[153] Attila Olah, Henrik Hillborg, and Julius G. Vancso, "Hydrophobic recovery of UV/ozone treated poly(dimethylsiloxane): adhesion studies by contact mechanics and mechanism of surface modification," *Applied Surface Science*, vol. 239, pp. 410-423, 2005.

[154] Antoine Pallandre, Bertrand de Lambert, Rafaele Attia, Alain M. Jonas, and Jean-Louis Viovy, "Surface treatment and characterization: Perspectives to electrophoresis and lab-on-chip," *Electrophoresis*, vol. 27, pp. 584-610, 2006.

[155] Shuwen Hu et al., "Surface modification of poly(dimethylsiloxane) microfluidic devices by ultraviolet polymer grafting," *Analytical Chemistry*, vol. 74, pp. 4117-4123, 2002.

[156] Shuwen Hu et al., "Cross-linked coatings for electrophoretic separations in poly(dimethylsiloxane) microchannels," *Electrophoresis*, vol. 24, pp. 3679-3688, 2003.

[157] Shuwen Hu et al., "Tailoring the surface properties of poly(dimethylsiloxane) microfluidic devices," *Langmuir*, vol. 20, pp. 5569-5574, 2004.

[158] Shuwen Hu et al., "Surface-directed graft polymerization within microfluidic channels," *Analytical Chemistry*, vol. 76, pp. 1865-1870, 2004.

[159] H. Kusumaatmaja, C. M. Pooley, S. Girardo, D. Pisignano, and J. M. Yeomans, "Capillary filling in patterned channels," *Physical Review E*, vol. 77, p. 067301, 2008.

[160] Tzong-Shyng Leu and Pei-Yu Chang, "Pressure barrier of capillary stop valves in micro sample separators," *Sensors and Actuators A*, vol. 115, pp. 508-515, 2004.

[161] Alain Gliere and Cyril Delattre, "Modeling and fabrication of capillary stop valves for planar microfluidic systems," *Sensors and Actuators A*, vol. 130-131, pp. 601-608, 2006.

[162] Helene Andersson, Wouter van der Wijngaart, Patrick Griss, Frank Niklaus, and Goran Stemme, "Hydrophobic valves of plasma deposited octafluorocyclobutane in DRIE channels," *Sensors and Actuators B*, vol. 75, pp. 136-141, 2001.

[163] A. L. Hook, N. H. Voelcker, and H. Thissen, "Patterned and switchable surfaces for biomolecular manipulation," *Acta Biomaterialia*, vol. 5, pp. 2350-2370, 2009.

[164] Yi Sun, Yingyi Liu, Weisi Qu, and Xingyu Jiang, "Combining nanosurface chemistry and microfluidics for molecular analysis and cell biology," *Analytica Chimica Acta*, vol. 650, pp. 98-105, 2009.

[165] Manabu Tokeshi et al., "Continuous-flow chemical processing on a microchip by combining microunit operations and a multiphase flow network," *Analytical Chemistry*, vol. 74, pp. 1565-1571, 2002.

[166] Arata Aota, Akihide Hibara, and Takehiko Kitamori, "Pressure balance at the liquid-liquid interface of micro countercurrent flows in microchips," *Analytical Chemistry*, vol. 79, pp. 3919-3924, 2007.

[167] Arata Aota, Masaki Nonaka, Akihide Hibara, and Takehiko Kitamori, "Countercurrent laminar microflow for highly efficient solvent extraction," *Angewandte Chemie International Edition*, vol. 46, pp. 878-880, 2007.

[168] Arata Aota, Kazuma Mawatari, and Takehiko Kitamori, "Parallel multiphase microflows: fundamental physics, stabilization methods and applications," *Lab on a Chip*, vol. 9, pp. 2470-2476, 2009.

[169] Akihide Hibara, Manabu Tokeshi, Kenji Uchiyama, Hideaki Hisamoto, and Takehiko Kitamori, "Integrated Multilayer Flow System on a Microchip," *Analytical Sciences*, vol. 17, pp. 89-93, 2001.

[170] Todd Thorsen, Sebastian J. Maerkl, and Stephen R. Quake, "Microfluidic Large-Scale Integration," *Science*, vol. 298, pp. 580-584, 2002.

[171] Liang-Yin Chu, Andrew S. Utada, Rhutesh K. Shah, Jin-Woong Kim, and David A. Weitz, "Controllable monodisperse multiple emulsions," *Angewandte Chemie International Edition*, vol. 46, pp. 8970-8974, 2007.

[172] Nicolas Pannacci et al., "Equilibrium and nonequilibrium states in microfluidic double emulsions," *Physical Review Letters*, vol. 101, 2008.

[173] A. R. Abate and D. A. Weitz, "High-order multiple emulsions formed in poly(dimethylsiloxane) microfluidics," *Small*, vol. 5, pp. 2030-2032, 2009.

[174] Luis M. Fidalgo, Chris Abell, and Wilhelm T. S. Huck, "Surface-induced droplet fusion in mirofluidic devices," *Lab on a Chip*, vol. 7, pp. 984-986, 2007.

[175] Mark B. Romanowsky et al., "Functional patterning of PDMS microfluidic devices using integrated chemo-masks," *Lab on a Chip*, vol. 10, pp. 1521-1524, 2010.

[176] Ken Tore Tallakstad et al., "Steady-state, simultaneous two-phase flow in porous media: An experimental study," *Physical Review E*, vol. 80, p. 036308, 2009.

[177] Olav Inge Frette, Knut Jorgen Maloy, and Jean Schmittbuhl, "Immiscible displacement of viscosity-matched fluids in two-dimensional porous media," *Physical Review E*, vol. 55, pp. 2969-2975, 1997.

[178] A.-L. Barabasi and H. E. Stanley, *Fractal Concepts in Surface Growth*. Cambridge, UK: Cambridge University Press, 1995.

[179] T. A. Witten and L. M. Sander, "Diffusion-limited aggregation," *Physical Review B*, vol. 27, pp. 5686-5697, 1983.

[180] D. Stauffer, "Scaling theory of percolation clusters," *Physics Reports*, vol. 54, pp. 1-74, 1979.

[181] M. Ferer, Grant S. Bromhal, and Duane H. Smith, "Fractal dimension and avalanches of invasion percolation: the effect of aspect ratio," *Physica A*, vol. 334, pp. 22-38, 2004.

[182] Adrian P. Sheppard, Mark A. Knackstedt, W. V. Pinczewski, and Muhammad Sahimi, "Invasion percolation: new algorithms and universality classes," *Journal of Physics A: Mathematical and Theoretical*, vol. 32, pp. L521-L529, 1999.

[183] Grunde Lovoll, Yves Meheust, Renaud Toussaint, Jean Schmittbuhl, and Knut Jorgen Maloy, "Growth activity during fingering in a porous Hele-Shaw cell," *Physical Review E*, vol. 70, p. 026301, 2004.

[184] Knut. J. Maloy, Jens Feder, and Torstein. Jossang, "Viscous Fingering Fractals in Porous Media," *Physical Review Letters*, vol. 55, pp. 2688–2691 , 1985.

[185] M. M. Sharma and R. W. Wunderlich, "The Alteration of Rock Properties Due to Interactions With Drilling Fluid Components," in *SPE Annual Technical Conference and Exhibition*, Las Vegas, Nevada, 1985, p. SPE 14302.

[186] Frank G McCaffery, "Measurement of Interfacial Tensions And Contact Angles At High Temperature And Pressure," *Journal of Canadian Petroleum Technology*, vol. 11, pp. 72-03-03, 1972.

[187] F. G. McCaffrey and N. Mungan, "Contact Angle And Interfacial Tension Studies of Some Hydrocarbon-Water-Solid Systems," *Journal of Canadian Petroleum Technology*, vol. 9, pp. 70-03-04, 1970.

[188] O. S. Hjemeland and L. E. Larrondo, "Experimental Investigation of the Effects of Temperature, Pressure, and Crude Oil Composition on Interfacial Properties," *SPE Reservoir Engineering*, vol. 1, pp. 321-328, 1986.

[189] R. O. Leach, O. R. Wagner, H. W. Wood, and C. F. Harpke, "A Laboratory and Field Study of Wettability Adjustment in Water Flooding," *Journal of Petroleum Technology*, vol. 14, pp. 206-212, 1962.

[190] L. E. Treiber, D. L. Archer, and W. W. Owens, "A Laboratory Evaluation of the Wettability of Fifty Oil-Producing Reservoirs," *SPE Journal*, vol. 12, pp. 531-540, 1972.

[191] D. N. Rao and M. G. Girard, "A New Technique For Reservoir Wettability Characterization," *Journal of Canadian Petroleum Technology*, vol. 35, pp. 31-39, 1996.

[192] A. B. D. Cassie and S. Baxter, "Wettability of Porous Surfaces," *Transactions of the Faraday Society*, vol. 40, pp. 546-550, 1944.

[193] Artem Borysenko et al., "Experimental investigations of the wettability of clays and shales," *Journal of Geophysical Research*, vol. 114, p. B07202, 2009.

[194] Hasan O. Yildiz, F. Bahar Oztorun, and Ayhan A. Sirkeci, "Determination of Reservoir Rock Wettability by Thin Layer Wicking Approach," in *SPE/DGS Saudi Arabia Section Technical Symposium and Exhibition*, Al-Khobar, Saudi Arabia, 2010, p. SPE 136936.

[195] B. H. Rayes, T. Pernyeszi, and J. Toth, "Comparative Study of Asphaltene Adsorption on Formation Rocks under Static and Dynamic Conditions," in *International Symposium on Oilfield Chemistry*, Houston, TX, 2003, p. SPE 80265.

[196] L. E. Cuiec, "Restoration of the Natural State of Core Samples," in *Fall Meeting of the Society of Petroleum Engineers of AIME*, Dallas, Texas, 1975, p. SPE 5634.

[197] Louis Cuiec, "Study of Problems Related to the Restoration Of the Natural State of Core Samples," *Journal of Canadian Petroleum Technology*, vol. 16, pp. 68-80, 1977.

[198] Dennis M. Grist, Gordon O. Langley, and Ernst L. Neustadter, "The Dependence of Water Permeability On Core Cleaning Methods In the Case of Some Sandstone Samples," *Journal of Canadian Petroleum Technology*, vol. 14, pp. 48-52, 1975.

[199] Preston L. Gant and William G. Anderson, "Core Cleaning for Restoration of Native Wettability ," *SPE Formation Evaluation*, vol. 3, pp. 131-138, 1988.

[200] J. A. Burkhardt, M. B. Ward, and R. H. McLean, "Effect of Core Surfacing and Mud Filtrate Flushing on Reliability of Core Analysis Conducted on Fresh Cores," in *Fall Meeting of the Society of Petroleum Engineers of AIME*, Houston, TX, 1958, p. SPE 1139.

[201] M. E. Crocker and L. M. Marchin, "Evaluation and Determination of Cross Correlations Between Wettability Methods. Status Report.," National Inst. for Petroleum and Energy Research, Bartlesville, OK, Technical report NIPER-183, 1986.

[202] D. N. Rao and Z. A. Bassiouni, "A New Technique to Confidently Characterize Wettabilty Alterations Induced by Drilling/Completion/Workover Fluids," in *SPE/DOE Improved Oil Recovery Symposium*, Tulsa, Oklahoma, 2000, p. SPE 59516.

[203] Earl Amott, "Observations Relating to the Wettability of Porous Rock," *Petroleum Transactions of the American Institute of Mining,Metallurgical, and Petroleum Engineers*, vol. 216, pp. 156-162, 1959.

[204] D. F. Boneau and R. L. Clampitt, "A Surfactant System for the Oil-Wet Sandstone Of the North Burbank Unit," *Journal of Petroleum Technology*, vol. 29, pp. 501-507, 1977.

[205] Erle C. Donaldson, Rex D. Thomas, and Philip B. Lorenz, "Wettability Determination and Its Effect on Recovery Efficiency," *SPE Journal*, vol. 9, pp. 13-20, 1969.

[206] Nick P. Valenti, R. M. Valenti, and L. F. Koederitz, "A Unified Theory on Residual Oil Saturation and Irreducible Water Saturation," in *SPE Annual Technical Conference and Exhibition*, San Antonio, Texas, 2002, p. SPE 77545.

[207] Djebbar Tiab and Erle C. Donaldson, *Petrophysics: theroy and practice of measuring reservoir rock and fluid transport properties*, 2nd ed. Burlington, MA, USA: Gulf Professional Publishing, 2004.

[208] Kishore. K. Mohanty and Stephen. J. Salter, "Multiphase Flow in Porous Media: III. Oil Mobilization, Transverse Dispersion, and Wettability ," in *SPE Annual Technical Conference and Exhibition*, San Francisco, CA, 1983, p. SPE 12127.

[209] J. D. Eick, R. J. Good, and A. W. Neumann, "Thermodynamics of Contact Angles: II. Rough Solid Surfaces," *Journal of Colloid and Interface Science*, vol. 53, pp. 235-248, 1975.

[210] R. E. Johnson and R. H. Dettre, "Wettability and Contact Angles," in *Surface and Colloid Science, E*. New York City: Wiley Interscience, 1969, pp. 85-153.

[211] S.-Y. Yang, G. J. Hirasaki, S. Basu, and R. Vaidya, "Mechanisms for contact angle hysteresis and advancing contact angles," *Journal of Pretroleum Science and Engineering*, vol. 24, pp. 63-73, 1999.

[212] Jacob Bear, *Dynamics of fluids in Porous Media*. New York : Dover Publications, 1972.

[213] Philip H. Stauffer, "Flux Flummoxed: A Proposal for Consistent Usage," *Ground Water*, vol. 44, pp. 125-128, 2006.

[214] Zhangxin Chen, Guanren Huan, and Yuanle Ma, *Computational Methods for Multiphase Flows in Porous Media*. Philadelphia, PA: Society for Industrial and Applied Mathematics, 2006.

[215] J. G. Richardson, F. M. Perkins, and J. S. Osoba, "Differences in Behavior of Fresh and Aged East Texas Woodbine Cores," *Petroleum Transactions, AIME*, vol. 204, pp. 86-91, 1955.

[216] T. M. Geffen, W. W. Owens, D. R. Parrish, and R. A. Morse, "Experimental Investigation of Factors Affecting Laboratory Relative Permeability Measurements," *Petroleum Transactions, AIME*, vol. 192, pp. 99-110, 1951.

[217] M. M. Honarpour, N. R. Nagarajan, and K. Sampath, "Rock/Fluid Characterization and Their Integration - Implications on Reservoir Management," *Journal of Petroleum Technology*, vol. 58, pp. 120-130, 2006.

[218] R. M. Gies and Jon McGovern, "Petrographic Image Analysis: An Effective Technology for Delineating Reservoir Quality," in *SPE Gas Technology Symposium*, Calgary, Alberta, Canada, 1993, p. SPE 26147.

[219] Gao Yaming, Shen Pingping, and Tu Fuhua, "A Study of Pore Structure by Image Processing Method and Its Application," in *International Meeting on Petroleum Engineering*, Beijing, China, 1986, p. SPE 14872.

[220] Yongsheng Zhang, D. A. Bell, Guangyu Chen, R. Morrow N., and J. S. Buckley, "Cleaning Cores after Contamination with Synthetic Oil-Based Mud Components," in *9th International Symposium on Evaluation of Wettability and Its Effect on Oil Recovery*, Bergen, Norway, 2006, pp. A-12.

[221] Flavio S. Anselmetti, Stefan Luthi, and Gregor P. Eberli, "Quantitative Characterization of Carbonate Pore Systems by Digital Image Analysis," *AAPG Bulletin*, vol. 82, pp. 1815-1836, 1998.

[222] Kevin J. Cunningham, Janine I. Carlson, and Neil F. Hurley, "New method for quantification of vuggy porosity from digital optical borehole images as applied to the karstic Pleistocene limestone of the Biscayne aquifer, southeastern Florida," *Journal of Applied Geophysics*, vol. 55, pp. 77-90, 2004.

[223] Lars Oyno et al., "Prediction of Petrophysical Parameters Based on Digital Video Core Images ," *SPE Reservoir Evaluation & Engineering*, vol. 1, pp. 82-87, 1998.

[224] R. D. Wyckoff, H. G. Botset, M. Muskat, and D. W. Reed, "Measurement of Permeability of Porous Media," *Bulletin of the American Association of Petroleum Geologists*, vol. 18, pp. 161-190, 1934.

[225] C. L. Dinwiddie, "The Small-Drillhole Minipermeameter Probe for In-Situ Permeability Measurement," *SPE Reservoir Evaluation & Engineering*, vol. 8, pp. 491-501, 2005.

[226] Mark Alden et al., "Advancing Downhole Conveyance," *Oilfield Review*, vol. 16, no. 3, pp. 30-43, 2004.

[227] Florian Schneider, Jan Draheim, Robert Kamberger, and Ulrike Wallrabe, "Process and material properties of polydimethylsiloxane (PDMS) for Optical MEMS," *Sensors and Actuators A: Physical*, vol. 151, pp. 95-99, 2009.

[228] Marc H. Schneider, Patrick Tabeling, Fadhel Rezgui, Martin G. Luling, and Aurelien Daynes, "Novel microscopic imger instrument for rock and fluid imaging," *Geophysics*, vol. 74, pp. E251-E262, 2009.

[229] Bahaa E. A. Saleh and Malvin Carl Teich, *Fundamentals of Photonics*, 2nd ed. New York: Wiley and Sons, 2007.

[230] A. C. DeFranzo and B. G. Pazol, "Index of refraction measurement on sapphire at low temperatures and visible wavelengths," *Applied Optics*, vol. 32, pp. 2224-2234, 1993.

[231] Ana Perez-Burgos, Argimiro de Miguel, and Julia Bilbao, "Daylight illuminance on horizontal and vertical surfaces for clear skies. Case study of shaded surfaces," *Solar Energy*, vol. 84, pp. 137-143, 2010.

[232] Total, "Datasheet - Hydroseal G 232 H," pp. downloaded from: www.totalfluides.fr, 2010.

[233] Victor R. Jayalakshamma and Rajangam Ssayee, "Cost effective, qualitative immersion oil for microscopy," *Journal of the Anatomical Society of India*, vol. 54, pp. 1-9, 2005.

[234] Stephen H. Westin, Hongsong Li, and Kenneth E. Torrance, "A Comparison of Four BRDF Models," *Eurographic Symposium on Rendering*, pp. 1-10, 2004.

[235] Claude E. Shannon, "Communication in the Presence of Noise," *Proceedings of the IEEE*, vol. 86, pp. 447-457, 1998.

[236] Gregory Hallock Smith, *Camera Lenses: From Box Camera to Digital*. Washington: SPIE - The International Soceiety for Optical Engineers, 2006.

Résumé substantiel

Motivation

La compréhension détaillée des écoulements multiphasiques dans les milieux poreux est très importante pour de nombreuses applications industrielles et écologiques à diverses échelles spatiales et temporelles [**1**]. Les processus de déplacement dans les milieux poreux naturels tels les réservoirs de pétrole ou de gaz jouent un rôle crucial dans la mise en œuvre des techniques de récupération assistée du pétrole ou de séquestration du dioxyde de carbone [**2**], [**3**]. De plus, les processus de déplacement dans les aquifères et dans les réservoirs géothermique sont des sujets importants tant pour les sciences de la terre que pour l'hydrologie [**2**], [**4**]. Les exemples d'écoulements multiphasiques dans les milieux poreux de type synthétique vont des applications pour la chimie classique [**2**] comme la filtration dans des colonnes avec garnissage, au transport de fluides dans une pile à combustible [**5**], [**6**], [**7**]. Il est donc nécessaire d'identifier et d'étudier les processus d'écoulements multiphasiques à l'échelle microscopique pour quantifier leur manifestation à l'échelle macroscopique.

Depuis les années 1980, les réseaux micro fluidiques (micro-modèles) sont fréquemment utilisés comme modèles de milieux poreux pour l'identification et l'étude détaillée des phénomènes d'écoulements multiphasiques [**8**], [**9**]. Ces micro-modèles, typiquement fabriqués avec des matériaux en verre ou en polymère transparent, permettent une observation optique détaillée des phases fluidiques et leur propagation à travers les pores et canaux micro fluidiques [**7**], [**10**], [**11**]. Les études détaillées des micro-modèles permettent l'identification des diagrammes de phase, qui fournissent les prédictions pour les motifs d'écoulements fonction du nombre capillaire et de la viscosité [**21**], [**22**], [**23**]. Des expériences avec ces micro-modèles ont révélé les principes physiques sous-jacents des déplacements de fluides dans les pores, et ont permis, à l'aide des données expérimentales collectées de développer et de valider les outils de simulation [**24**], [**25**], [**26**], [**27**], [**28**], [**29**].

Cependant, malgré ce progrès, les études et applications ont été limitées aux systèmes et aux cas possédant des propriétés de surface (c'est-à-dire de mouillabilité) homogènes et uniformes. La mouillabilité qualifie l'adhérence relative entre un fluide et une surface solide. Dans un milieu poreux, en présence de deux fluides non miscibles la mouillabilité est la mesure de la tendance préférentielle d'un des deux fluides à mouiller la surface du milieu poreux [**36**]. L'hypothèse des propriétés de surfaces uniformes appliquée à l'ensemble du milieu poreux donne seulement des prédictions d'écoulements de fluides, en accord avec les deux cas fondamentaux : le drainage et l'imbibition, le mouillage partiel est négligé.

L'industrie pétrolière a récemment considéré qu'une mouillabilité partielle ou mixte est un facteur important car l'efficacité de déplacement de fluides, et finalement la quantité de pétrole récupéré grâce aux fluides d'injection (l'eau, par exemple) est imposée par la mouillabilité de la roche-réservoir [**39**], [**40**], [**41**]. Augmenter la récupération des hydrocarbures connus est un des défis de l'industrie pétrolière. Bien que l'injection d'eau soit pratiquée depuis plusieurs décennies pour la récupération du pétrole, les mécanismes de la récupération à l'échelle des pores restent incertains [**42**]. Par conséquent, il devient évident que la compréhension détaillée des mécanismes d'écoulements multiphasiques à l'échelle des pores pour une mouillabilité mixte est essentielle [**48**]. Toutefois le manque d'une technologie appropriée empêchait toutes investigations expérimentales détaillées des écoulements multiphasiques dans les milieux poreux à mouillabilité texturée [**42**], [**49**].

Un besoin d'étude détaillée du comportement d'écoulements multiphasiques dans les milieux poreux est nécessaire tant comme contribution scientifique dans les domaines de la physique et de la mécanique de**s** fluides que pour les applications dans l'industrie pétrolière. De telles études demandent un progrès technologique significatif, permettant la fabrication et la préparation des micro-modèles à mouillage texturé de type complexe fournissant une haute qualité de surface ainsi qu'une haute résolution spatiale. Ce travail se focalise sur la technologie de fabrication et de préparation des micro-modèles ainsi que l'étude d'écoulements dans les milieux poreux à mouillabilité texturée, en vue d'applications liées à l'industrie pétrolière.

Mouillabilité texturée dans les systèmes micro fluidiques.

Les études de mouillabilité texturée ont été centrées sur les écoulements multiphasiques dans des micro-modèles possédant une mouillabilité partielle. Cependant, la modification de la mouillabilité par un traitement de surface dans des systèmes micro fluidiques est en elle-même de très grande importance. Les puces micro fluidiques sont typiquement fabriquées dans des matériaux comme le verre ou le silicium [**61**]. Il y a un intérêt croissant pour l'utilisation de polymères dû à des prix fortement réduits ainsi qu'une fabrication plus rapide et moins complexe [**62**]. Le poly(dimethylsiloxane) (PDMS), en particulier, est un polymère fréquemment utilisé, pour les applications micro fluidiques [**129**], [**130**], [**131**]. Dans de nombreux cas les propriétés des matériaux des puces micro fluidiques ne suffisent pas pour les applications et il est nécessaire d'en modifier les propriétés de surface et de les fonctionnaliser pour les tâches bien précises [**132**], [**133**]. Par exemple, les systèmes micro fluidiques fabriqués en PDMS, qui est un matériel hydrophobe, ont fréquemment besoin de modifications de surface pour obtenir des canaux avec une surface hydrophile.

Nous avons développé un traitement de surface qui permet d'obtenir une mouillabilité texturée à l'intérieur de structures micro fluidiques en PDMS avec une grande résolution et une haute qualité. Nous avons utilisé une méthode spécifique de greffe par polymérisation de poly(acide acrylique) (PAA) à PDMS, initialisée par la lumière ultraviolette (UV) et dirigée vers la surface. Cette technique est fondée sur un protocole en deux étapes publié par Hu et al. [**158**]. Nous avons fait des améliorations considérables qui nous permettent de texturer la mouillabilité avec une grande résolution spatiale. Cette technique est ainsi applicable dans les systèmes micro fluidiques de type complexe. Le traitement de surface se compose de deux étapes majeures : l'amorçage et le greffage. L'étape d'amorçage consiste à déposer du photo amorceur le long des parois des micro-canaux en PDMS. Pour ce faire, le photo amorceur benzophenone (BP) est dissout dans l'acétone et la solution obtenue est injectée dans les micro canaux. Cela permet aux molécules de BP de diffuser dans le PDMS polymère et de former un réservoir de photo amorceur près des parois de canaux. Lors de la deuxième étape, les canaux sont remplis d'une solution aqueuse d'acide acrylique (AA) et la puce micro fluidique est insolée par lumière UV. Pendant l'insolation par UV, les molécules de BP sont excitées et ensuite relaxent par enlèvement d'hydrogène, typiquement des groupes méthyles de PDMS, et donc créent des radicaux libres. La polymérisation d'AA commence de ces sites radicaux et le PAA se développe sur et dans les parois en PDMS. Après nettoyage des canaux, une fine couche de PAA reste sur les parois de canaux micro fluidiques, qui est attachée au PDMS par les liaisons covalentes. Contrairement au PDMS non traité qui est hydrophobe, la couche PAA est fortement hydrophile et présente un bon contraste pour la mouillabilité (c'est-a-dire l'énergie de surface). Les deux étapes du protocole assurent que la photo amorceur et les AA monomères se mettent seulement le long des parois où le traitement de surface est désiré. Par cette stratégie le problème de la polymérisation dans le volume de canaux qui interférait avec le traitement de surface est maintenant éliminé. Nous avons publié les détails de cette méthode dans *Analytical Chemistry* (voir l'article dans le sous-chapitre 2.2.1).

Mouillabilité texturée dans les modèles pour les réservoirs de pétrole.

La mouillabilité de la roche est un facteur majeur pour la récupération du pétrole, qui contrôle la localisation, l'écoulement et la distribution des fluides dans le réservoir. La mouillabilité influe la plupart des propriétés pétrophysiques de la roche-réservoir dont les pressions capillaires, les perméabilités relatives, le comportement pendant l'injection d'eau, les propriétés électriques et la récupération assistée du pétrole [**74**], [**75**], [**76**]. La mouillabilité de la roche-réservoir peut être soit homogène, soit hétérogène. Dans le cas d'une mouillabilité homogène, la surface entière de la roche présente une mouillabilité uniforme, laquelle peut être pour l'eau, pour l'huile ou une mouillabilité intermédiaire [**41**], [**55**], [**78**]. Dans le cas d'une mouillabilité hétérogène, des régions de surface différentes présentent des mouillabilités différentes et la roche peut avoir une mouillabilité partielle ou mixte [**36**].

Les roches-réservoirs ont des structures complexes et sont composées d'une variété de minéraux différents où chaque minéral peut présenter une mouillabilité différente [**82**]. De plus, la mouillabilité de surface peut être modifiée par l'adsorption de molécules polaires ou par dépôt de couches minces de matériaux organiques [**55**], [**81**], [**83**], [**84**]. Les molécules qui peuvent modifier la mouillabilité des roches correspondent à la partie lourde du pétrole brut, à savoir les asphaltènes [**88**], [**89**]. Les réservoirs de pétrole évoluent par une migration de pétrole dans les espaces poreux de la roche qui possèdent initialement une mouillabilité en eau et sont saturés par de la saumure [**41**]. Le pétrole qui est la phase non-mouillante envahit préférentiellement les pores les plus grands tandis que la saumure reste dans les petits pores et en couche fine sur la surface des minéraux. En fonction de la rugosité de surface de la roche et de la composition de la saumure, les couches résiduelles d'eau peuvent collapser, permettant le contact direct entre la roche et le pétrole. Ce contact direct entre la roche et le pétrole peut entraîner une modification permanente de la mouillabilité [**93**]. En même temps, l'eau reste dans les petits pores et dans les coins aigus et évite le contact entre roche et pétrole, donc permettra de conserver les conditions de mouillabilité en eau initiales dans ces régions. Par ces mécanismes une mouillabilité partielle ou mixte peut se développer dans les réservoirs de pétrole [**41**], [**80**], [**36**].

L'une des applications principales de la mouillabilité texturée dans les micro-modèles de type complexe est l'étude de comportement d'écoulements multiphasiques dans ces systèmes pour la fraction des micro-canaux traités. Nos expériences dans les micro-modèles avec une mouillabilité texturée ont révélé des nouveaux régimes d'écoulements suivant la fraction de mouillabilité en eau, avec l'apparition de nouveaux phénomènes de piégeage amené par la digitation due à la mouillabilité texturée. Ces résultats ont permis d'obtenir des éclaircissements sur l’impact de la texturation de la mouillabilité sur le comportement d’écoulements multiphasiques et ont montré des comportements entièrement différents par rapport aux cas homogènes (mouillabilité uniforme en eau ou en huile). Une publication de cette étude expérimentale est en cours de préparation (voir l’article présenté dans le sous-chapitre 2.3.2).

La mesure de la mouillabilité dans l’industrie pétrolière.

L’extraction et la récupération de pétrole d’un réservoir sont classifiées en trois stades principaux : récupérations primaire, secondaire et tertiaire. Durant la récupération primaire, typiquement 5 – 15% du pétrole originellement présent dans la roche-réservoir est produit par les puits forés dans le réservoir à l’aide d’une surcharge de pression. 15 à 30% supplémentaires peuvent être produits par injection d’eau, technique appelée ‘par inondation d’eau’ ou ‘récupération secondaire [**96**], [**97**]. Une variété de techniques supplémentaires (récupération assistée du pétrole ou récupération tertiaire), est disponible pour extraire 5 – 15% supplémentaires de pétrole et obtenir ainsi une récupération totale entre 30% et 60% [**93**], [**97**].

La connaissance détaillée de l’état de mouillabilité du réservoir est cruciale pour le développement de stratégies de production optimale au cours des trois phases de récupération. Toutefois, l’évaluation de la mouillabilité est difficile et les conclusions définitives restent souvent insaisissables, en particulier dans le cas d’une mouillabilité hétérogène [**42**], [**90**]. La mouillabilité du réservoir est déterminée par analyse en laboratoire des échantillons de carottes [**94**]. Une altération de la mouillabilité des carottes de roche peut se produire pendant le coupage, la récupération et les manipulations subséquentes. Les raisons de cette altération sont variées : contamination par les fluides de coupage, oxydation, séchage. Les effets des réductions en température et en pression sur la composition du pétrole, la précipitation des asphaltènes ou les dépôts de cire ont également une incidence forte sur les propriétés de mouillabilité [**77**], [**88**]. Plusieurs méthodes sont disponibles pour mesurer la mouillabilité d’échantillons de roche en fonction de la mesure de l’angle de contact ou de la pression capillaire [**94**], [**95**]. Les techniques de mesure qui sont basées sur la pression capillaire utilisent des cycles d'imbibition et de drainage afin d'évaluer la mouillabilité de l'échantillon et de fournir un indice de mouillabilité entre une mouillabilité d'eau forte et une mouillabilité d'huile forte. Les mesures d'angle de contact, telles que la technique de la goutte sessile, sont difficiles à appliquer sur les surfaces brutes et poreuses, et la validité de l'état de mouillage de la surface de la roche fraîchement coupée est discutable. La connaissance détaillée de la mouillabilité de la roche est un élément clé mais reste souvent difficile à atteindre [**42**], [**90**].

Une nouvelle méthode pour l'évaluation de la mouillabilité dans des échantillons de roche a été développée, permettant la mesure de la mouillabilité indépendamment de l'état de surface des roches. Cette nouvelle méthode est basée sur l'observation des interactions fluide-roche par microscopie optique. Les fluides injectés dans les milieux poreux suivent un schéma d'écoulement particulier pour une certaine gamme de nombres capillaires (c'est-à-dire dans une gamme particulière de vitesses d'injection). Ces schémas d'écoulement dépendent de la mouillabilité du milieu poreux. Dans le cas d'un milieu non-mouillant l'invasion par percolation crée des structures distinctes de digitation sur une échelle locale. Par contre, l'imbibition d'un fluide mouillant avance en présentant un front de fluide assez plat. Après l'émergence du fluide injecté à la surface de sortie de l'échantillon de roche, le front de fluide peut être observé par coupe transversale. Cette nouvelle technique permet de déterminer la mouillabilité à l'intérieur de la roche indépendamment de son état de surface actuel. Nous avons combiné l'imagerie traditionnelle en lumière blanche avec l'observation de la fluorescence naturelle dans le pétrole brut, ce qui nous a permis d'améliorer considérablement le contraste optique et de pouvoir détecter des quantités infimes de pétrole. Nos expériences ont montré que la mouillabilité peut être déterminée avec succès par observation visuelle du liquide sortant de l'échantillon de roche pendant l'injection. Les détails de la méthode et les résultats expérimentaux on été soumis pour publication dans le *Journal of Petroleum Science and Engineering* (voir l'article dans le sous-chapitre 3.1.3).

Nous avons développé un nouvel instrument d'imagerie microscopique qui permet de réaliser des observations optiques entre la roche et les fluides à l'échelle des pores.

L’imageur a été conçu pour fournir des images de haute qualité des échantillons de roches et pour surmonter les défis d’imagerie qui sont liés aux conditions difficiles dans les échantillons de roche afin de réaliser de nouvelles mesures optiques, permettant l’évaluation de la mouillabilité.

L’imagerie optique et les observations visuelles détaillées des interactions entre la roche et les fluides à l’échelle des pores est un outil puissant pour la détermination des propriétés de la roche et des fluides dont la connaissance est essentielle à l’industrie pétrolière [**217**]. Notre nouvelle technique pour l’évaluation de la mouillabilité par l’imagerie visuelle au cours de l’injection de fluide permet d’identifier la mouillabilité à l’intérieur de l’échantillon, indépendamment de l’état de mouillabilité de la surface. Néanmoins, une surface propre sans bouchage des pores est bénéfique pour cette mesure. D’autres mesures basées sur l’imagerie optique requièrent également une surface propre et bien préparée de la roche. C’est le cas de l’analyse pétrographique d’images (petrographic image analysis, PIA) permettant d’accéder aux caractéristiques géologiques [**218**], [**219**]. Toutefois, dans de nombreux cas, les carottes de roche sont récupérées dans des conditions déficientes. En particulier, les surfaces qui sont exposées à des conditions difficiles, sont souvent soumises à diverses modifications mécaniques et chimiques. La surface peut ainsi parfois posséder une rugosité importante en raison des rainures de coupage ou du matériel ébréché. De plus, la surface peut être oxydée, ou les pores de la surface peuvent être bouchés par des dépôts fins de boue de forage (mudcake) [**94**], [**199**], [**220**].

Nous avons développé un nouvel instrument et une nouvelle méthodologie permettant d’obtenir une surface de roche propre et bien préparée pouvant ainsi être étudiée par imagerie optique microscopique. Cette nouvelle méthode est basée sur le perçage d’un petit trou d’exploration dans la roche immaculée à travers la surface endommagée. La polyvalence d’un tel instrument d’imagerie microscopique a été démontrée pour les applications d’imagerie statique ainsi que pour les applications d’imagerie dynamique. L’imagerie statique est la capture d’images fixes de haute résolution qui sont utilisées pour l’analyse géologique (par PIA, par exemple) afin de déterminer les propriétés des roches telles que texture et porosité [**221**], [**222**], [**223**].

Par contre, l'imagerie dynamique décrit l'imagerie continue des fluides émergeant des pores des roches lors de l'injection de fluide. Ces données peuvent fournir des informations supplémentaires sur les propriétés de la roche, telles que la mouillabilité ou la perméabilité de l'échantillon de roche. Le concept d'imagerie dynamique est démontré par un sondage de la perméabilité locale, autre propriété essentielle des roches [**224**], [**225**]. Cette nouvelle méthode et l'instrument développé ont été décrits dans un article publié dans *Geophysics* (voir l'article dans le sous-chapitre 3.2.1).

Abstract / Résumé

Wettability Patterning in Microfluidic Systems and Applications in the Petroleum Industry

Fractional or patterned wettability in porous media has a significant impact on multiphase flow behavior. It is believed that most of the world's oil reservoirs are characterized by heterogeneous wettability properties. Detailed investigations on the influence of fractional wettability on flow behavior in microfluidic porous medium models (micromodels) are therefore of great interest for both the study of fundamental concepts as well as application oriented research.

A wettability patterning technique was developed, which allowed for the first time selective changes of surface wettability in enclosed microfluidic systems of complex geometry made of poly(dimethylsiloxane) (PDMS) at high resolution and high quality. Based on this progress in surface treatment the influence of fractional wettability on two-phase flow behavior in micromodels was studied and new flow regimes were revealed.

Based on the emergence of different flow regimes depending on the wettability of a porous medium, a new technique was developed to assess wettability of a rock core sample by optical imaging and successfully demonstrated. The concept of flow measurements by optical imaging on pore scale was further extended and a novel microscopic imaging device was developed.

Keywords: wettability, microfluidics, surface treatment, porous medium, wettability patterning, mixed wettability, enhanced oil recovery.

Mouillabilité texturée dans les systèmes micro fluidiques et applications dans l'industrie pétrolière

La mouillabilité mixte ou partielle dans les milieux poreux influe considérablement sur le comportement des écoulements diphasiques. Dans le monde, la plupart des réserves pétrolières se situent dans des réservoirs possédant une mouillabilité hétérogène. Des études détaillées de l'influence de la mouillabilité partielle sur le comportement des écoulements dans les milieux poreux de type modèle micro fluidique sont par conséquent d'un intérêt majeur, tant pour la recherche fondamentale que pour les études appliquées.

Nous avons développé une nouvelle technique permettant pour la première fois la modification et la structuration de la mouillabilité de surface dans les systèmes micro fluidique de type complexe, système d'une grande homogénéité et de haute qualité fabriqué en poly(dimethylsiloxane) (PDMS). Ces progrès obtenus dans le traitement des surfaces, nous ont permis d'étudier l'influence de la mouillabilité partielle sur le comportement des écoulements diphasiques et d'observer de nouveaux régimes d'écoulements.

L'observation des régimes d'écoulement particuliers en fonction de la mouillabilité dans des carottes de roche nous a permis de développer une nouvelle technique de détection basée sur une visualisation optique de celle-ci. Ce concept de mesure d'écoulements par visualisation optique à l'échelle du pore fut étendu et un nouvel outil d'imagerie microscopique a été développé.

Mots clés: mouillabilité, micro fluidique, traitement de surface, milieu poreux, mouillabilité texturée, mouillabilité mixte, récupération assistée du pétrole.

Wettability Patterning in Microfluidic Systems and Applications in the Petroleum Industry

Fractional or patterned wettability in porous media has a significant impact on multiphase flow behavior. It is believed that most of the world's oil reservoirs are characterized by heterogeneous wettability properties. Detailed investigations on the influence of fractional wettability on flow behavior in microfluidic porous medium models (micromodels) are therefore of great interest for both the study of fundamental concepts as well as application oriented research.

A wettability patterning technique was developed, which allowed for the first time selective changes of surface wettability in enclosed microfluidic systems of complex geometry made of poly(dimethylsiloxane) (PDMS) at high resolution and high quality. Based on this progress in surface treatment the influence of fractional wettability on two-phase flow behavior in micromodels was studied and new flow regimes were revealed.

Based on the emergence of different flow regimes depending on the wettability of a porous medium, a new technique was developed to assess wettability of a rock core sample by optical imaging and successfully demonstrated. The concept of flow measurements by optical imaging on pore scale was further extended and a novel microscopic imaging device was developed.

Keywords: wettability, microfluidics, surface treatment, porous medium, wettability patterning, mixed wettability, enhanced oil recovery.

Mouillabilité texturée dans les systèmes micro fluidiques et applications dans l'industrie pétrolière

La mouillabilité mixte ou partielle dans les milieux poreux influe considérablement sur le comportement des écoulements diphasiques. Dans le monde, la plupart des réserves pétrolières se situent dans des réservoirs possédant une mouillabilité hétérogène. Des études détaillées de l'influence de la mouillabilité partielle sur le comportement des écoulements dans les milieux poreux de type modèle micro fluidique sont par conséquent d'un intérêt majeur, tant pour la recherche fondamentale que pour les études appliquées.

Nous avons développé une nouvelle technique permettant pour la première fois la modification et la structuration de la mouillabilité de surface dans les systèmes micro fluidique de type complexe, système d'une grande homogénéité et de haute qualité fabriqué en poly(dimethylsiloxane) (PDMS). Ces progrès obtenus dans le traitement des surfaces, nous ont permis d'étudier l'influence de la mouillabilité partielle sur le comportement des écoulements diphasiques et d'observer de nouveaux régimes d'écoulements.

L'observation des régimes d'écoulement particuliers en fonction de la mouillabilité dans des carottes de roche nous a permis de développer une nouvelle technique de détection basée sur une visualisation optique de celle-ci. Ce concept de mesure d'écoulements par visualisation optique à l'échelle du pore fut étendu et un nouvel outil d'imagerie microscopique a été développé.

Mots clés: mouillabilité, micro fluidique, traitement de surface, milieu poreux, mouillabilité texturée, mouillabilité mixte, récupération assistée du pétrole.